



# Amélioration de la modélisation spectrale des états de mer par un calcul quasi-exact des interactions non-linéaires vague-vague

Elodie Gagnaire-Renou

## ► To cite this version:

Elodie Gagnaire-Renou. Amélioration de la modélisation spectrale des états de mer par un calcul quasi-exact des interactions non-linéaires vague-vague. Océan, Atmosphère. Université du Sud Toulon Var, 2009. Français. NNT: . tel-00595353

**HAL Id: tel-00595353**

<https://theses.hal.science/tel-00595353>

Submitted on 24 May 2011

**HAL** is a multi-disciplinary open access archive for the deposit and dissemination of scientific research documents, whether they are published or not. The documents may come from teaching and research institutions in France or abroad, or from public or private research centers.

L'archive ouverte pluridisciplinaire **HAL**, est destinée au dépôt et à la diffusion de documents scientifiques de niveau recherche, publiés ou non, émanant des établissements d'enseignement et de recherche français ou étrangers, des laboratoires publics ou privés.

# **UNIVERSITE DU SUD TOULON VAR**

Ecole Doctorale Sciences Fondamentales et Appliquées

## **THESE**

pour l'obtention du

## **GRADE DE DOCTEUR**

**Spécialité : Sciences de l'Univers**

**Mention : Océanographie Physique**

présentée par

**Elodie Gagnaire-Renou**

## **AMELIORATION DE LA MODELISATION SPECTRALE DES ETATS DE MER PAR UN CALCUL QUASI-EXACT DES INTERACTIONS NON-LINEAIRES VAGUE-VAGUE**

Thèse soutenue publiquement le 24 novembre 2009,

devant un jury composé de :

M. REY Vincent	Pr., Univ. du Sud Toulon Var	Président du jury
M. ARDHUIN Fabrice	HDR, IFREMER (Brest)	Rapporteur
M. MONBALIU Jaak	Pr., K.U.Leuven (Belgique)	Rapporteur
M. KHARIF Christian	Pr., Ecole Centrale Marseille	Examinateur
M. FORGET Philippe	CR CNRS, HDR, Univ. du Sud Toulon Var	Directeur de thèse
M. BENOIT Michel	HDR, EDF R&D LNHE (Chatou)	Co-directeur de thèse
M. BADULIN Sergei	Dr., Institut P.P.Shirshov (Moscou)	Membre invité



# Remerciements

Je tiens tout d'abord à remercier les deux rapporteurs de ma thèse, le Docteur Fabrice Arduuin (SHOM jusqu'à fin 2009, puis IFREMER, Brest) et le Professeur Jaak Monbalju (Katholieke Universiteit Leuven), qui ont pris le temps de relire et de faire de (nombreux !) commentaires sur mon travail, malgré des délais assez courts, et en dépit de leurs nombreuses obligations. Merci pour vos précieux conseils et suggestions.

Je suis très reconnaissante envers le Professeur Vincent Rey, de l'Université du Sud Toulon Var, qui m'a fait l'honneur de présider le jury de thèse.

Mes remerciements s'adressent également au Professeur Christian Kharif (Ecole Centrale Marseille, IRPHE), pour avoir accepté d'être examinateur de ce travail.

Je remercie chaleureusement mes deux directeurs de thèse pour avoir encadré mon travail au long de ces trois années : le Docteur Philippe Forget, chargé de recherche CNRS au LSEET (Université du Sud Toulon Var), pour son aide, sa disponibilité (les nombreuses relectures !), son optimisme et ses encouragements, et Michel Benoit, chercheur-senior à EDF R&D et directeur du Laboratoire Saint-Venant, pour ses nombreux enseignements et explications, pour son aide et son soutien dans les moments les plus délicats.

J'ai eu le plaisir de collaborer avec le Docteur Sergei Badulin (Institut Shirshov, Moscou), qui s'est déplacé de Moscou pour venir assister à ma soutenance. Je tiens à le remercier tout particulièrement pour ses conseils, sa patience, ses nombreuses explications, pour m'avoir accueillie en février 2009 dans son laboratoire... et pour m'avoir permis de connaître Moscou en hiver : magnifique !

Les travaux de thèse ont été menés dans le cadre d'une convention CIFRE entre EDF R&D et le LSEET. J'adresse ainsi tous mes remerciements aux personnes du laboratoire LSEET, celles que j'ai pu croiser, avec qui j'ai pu discuter pendant mes séjours à Toulon. Je tiens particulièrement à exprimer ma reconnaissance au Professeur Philippe Fraunié, directeur du LSEET, pour ses conseils et sa gentillesse.

J'ai eu la chance de travailler au LNHE, dans un cadre privilégié pour effectuer une thèse. Je remercie mes collègues du LNHE, je ne pourrai pas tous les citer ici, mais j'ai une pensée particulière pour tout le groupe P74, Chi-Tuan, Vanessa, Didier, Reza, Marilyne, Emile, Damien, Nathalie, Giovanni, Sylvain, Thierry, Marc, Clément, Guy-Michel, Jean-Michel, Bruno, l'équipe POMPHY, Soizic et Cécile, toutes les personnes du laboratoire Saint-Venant, Florence, qui n'est plus au LNHE maintenant, pour la bonne ambiance

qu'ils font régner au sein du groupe, pour leurs conseils, les discussions que nous avons pu avoir. Je remercie bien sûr les autres thésards, Antoine, pour ses petits coups de pouce en Anglais, Etienne, Cédric, les post-docs et stagiaires, anciens et nouveaux, Florent, qui est maintenant maître de conférence à l'INSA de Toulouse, Amélie, Laetitia, Algiane...

Je tiens aussi à exprimer tous mes remerciements à Clarisse Fil, Laurent Perotin et Jean-Daniel Mattei, pour m'avoir permis de continuer à travailler à EDF et pour m'avoir laissé un peu de temps pour finir sereinement ma thèse.

Je remercie mes amis d'école, les thésards tout d'abord, Agathe, Nico, Charlotte, Xav, Sam, avec qui j'ai pu partager mes angoisses et questionnements ! que de soirées et discussions passées autour de la thèse ! je souhaite au passage bon courage à celles qui n'ont pas encore fini ! et ceux qui n'ont pas eu cette chance ;-) Flo, Guigui, Amandine, Cathy, Micka, MF.

Un grand merci à l'Orignal pour avoir été un digne représentant de vous tous le jour de ma soutenance ! Il a bien fait son travail (les photos en attestent) et bien sûr à Bernhard pour être venu m'accueillir au retour à la gare de Lyon !!

Merci aux anciens de Charlemagne, Céline, Sylvain, Oscar, Yi, Fabrice, Marie, Alexis, Sophie, et Thomas bien sûr, pour m'avoir encouragée à faire une thèse, m'avoir soutenue dans ses débuts. Plusieurs docteurs, chercheurs ou futurs docteurs parmi eux également.

Je remercie Anne et Amel, mes amies de lycée, avec qui je suis heureuse de pouvoir toujours garder le contact.

J'adresse des remerciements tout particuliers à Martin, pour son aide, son soutien chaque jour, ses encouragements, pour m'avoir supportée ces derniers temps (et ça ne devait pas toujours être facile !) pour ses conseils sur ma présentation, pour son soutien dans les moments de stress les derniers jours avant la soutenance.

Je remercie mes parents, ma mère, qui me supporte dans tous mes projets, m'a toujours encouragée, est toujours présente pour moi ; mon père, qui m'a envoyé plein d'ondes positives pour ma soutenance depuis Uzes ;-) pour ses encouragements et son soutien. Un grand merci aussi aux autres membres de ma famille, à ma petite soeur qui grandit, finira-t-elle aussi par faire une thèse ?

J'ai une pensée émue pour mon cousin Gabriel, un docteur lui aussi, et pour mon oncle et ma tante, Monique et Rémi.

# Résumé

Les modèles numériques d'état de mer de troisième génération ont été développés au cours des 20 dernières années, depuis la création du modèle WAM (WAMDI Group, 1988). Ils décrivent l'évolution du spectre d'énergie de l'état de mer sous l'action conjointe de plusieurs processus physiques qui apportent, dissipent ou transfèrent de l'énergie. Sur la base de retours d'expérience sur l'utilisation de ces modèles, notamment à l'occasion de campagnes de mesures *in situ*, certaines limitations ont pu être établies par plusieurs équipes de recherche. La modélisation de certains processus physiques pose question, et notamment la prise en compte des transferts non-linéaires d'énergie au sein du spectre des vagues. En grande et moyenne profondeur d'eau, ces transferts d'énergie s'effectuent principalement sous l'effet d'interactions résonnantes entre quadruplets de composantes spectrales.

Une meilleure prise en compte de ces interactions non-linéaires est essentielle à l'amélioration des modèles d'état de mer. En effet, depuis les travaux de Hasselmann (1962) et Zakharov (1999), le modèle mathématique décrivant ces mécanismes est connu et il a été établi que ces interactions jouent un rôle déterminant dans l'évolution spatio-temporelle du spectre d'énergie d'un état de mer (Young & Van Vledder, 1993). Cependant, le calcul numérique du terme d'interaction est très complexe et demande des ressources informatiques importantes, si bien que son évaluation exacte n'est aujourd'hui réalisée que dans quelques modèles de recherche. La méthode DIA (« Discrete Interaction Approximation ») de Hasselmann et al. (1985) est l'algorithme le plus souvent employé dans les codes opérationnels, mais elle apparaît aujourd'hui trop simplifiée et approximative (Benoit, 2005).

Sur la base d'une approche proposée par Lavrenov (2001), nous avons développé et optimisé une méthode de calcul quasi-exacte des interactions non-linéaires vague-vague en grande profondeur d'eau. Cette approche, nommée GQM (« Gaussian Quadrature Method »), est basée sur l'utilisation de quadratures de Gauss, et permet d'obtenir des estimations très précises du terme de transfert non-linéaire à des coûts de calcul raisonnables.

A l'aide de cette méthode, nous nous sommes d'abord intéressés à la modélisation de l'évolution temporelle du spectre des vagues dans un cas homogène et sans forçage (ni vent, ni dissipation). Le spectre évolue alors seulement sous l'effet des interactions non-linéaires, jusqu'à atteindre une forme d'équilibre, notamment dans les hautes fréquences. On retrouve également les résultats d'auto-similarité du spectre issus de la théorie de turbulence faible (Badulin et al., 2005). L'analyse détaillée du spectre directionnel fait apparaître une structure complexe, bimodale (deux directions principales de propagation), à la fois sur la partie hautes fréquences et sur la partie basses fréquences. Cette structure

est observée, au moins partiellement, sur des mesures *in situ* récentes effectuées avec des instruments sophistiqués (Hwang et al., 2000a,b).

Dans un second temps, l'introduction de différents termes de forçage par le vent (Snyder et al., 1981; Yan, 1987; Janssen, 1991) et de dissipation par moutonnement (Komen et al., 1984, 1994; Van der Westhuysen et al., 2007) nous a permis de montrer la sensibilité du spectre des vagues aux modèles choisis, notamment dans les hautes fréquences, et au niveau de sa structure directionnelle.

Des situations plus proches de la réalité mais conservant une géométrie simple ont ensuite été modélisées en prenant en compte la propagation spatiale des vagues. Les cas étudiés sont les conditions de « fetch limité » (vent constant et homogène, soufflant perpendiculairement à une côte rectiligne) et de « fetch oblique » (vent soufflant obliquement).

Les résultats de simulation du cas de « fetch limité » pour une large gamme de vitesses de vent sont examinés par une approche classique, où les paramètres traditionnels décrivant l'état de mer (énergie, fréquence de pic) sont adimensionnés par la vitesse du vent (Kitaigorodskii, 1962). Cette étude montre une forte dispersion de ces paramètres adimensionnels selon les modèles de forçage par le vent utilisés d'une part, et selon la vitesse du vent d'autre part. Une analyse comparative est alors effectuée dans le cadre de la théorie de la turbulence faible (Zakharov, 2005; Badulin et al., 2007), faisant ressortir certaines caractéristiques du développement des vagues qui ne dépendent pas du choix particulier des modèles de génération par le vent et de dissipation. Plusieurs stades de développement des vagues sont alors identifiés et caractérisés.

Dans le cas d'un « fetch oblique », l'incidence du vent entraîne une augmentation de la hauteur significative des vagues et une diminution de leur fréquence de pic, en particulier à faible distance de la côte. De plus, la présence du rivage influence fortement le spectre directionnel de l'état de mer. Les vagues de faibles fréquences sont déviées par la présence de la côte et ont tendance à se propager le long de la côte plutôt que dans la direction du vent (« wave steering »). Les vagues de plus hautes fréquences se propagent dans une direction plus proche de celle du vent. Ces simulations sont comparées avec des mesures de la campagne SHOWEX (Ardhuin et al., 2007).

Les travaux effectués confirment d'une part la nécessité de modéliser de façon précise les interactions non-linéaires dans les modèles spectraux d'états de mer et montrent d'autre part la faisabilité de ces améliorations (y compris en termes de temps de calcul), grâce à la méthode GQM et l'algorithme de calcul mis au point au cours de la thèse.

# Abstract

Third generation numerical wave models have been developed during the last 20 years since the elaboration of the WAM model (WAMDI Group, 1988). These models describe the evolution of the wave energy spectrum under the combined action of several physical processes that generate, transfer or dissipate energy. Based on feedback on the use of these models and field measurement campaigns, some limitations have been pointed out by several research teams. The modeling of some physical processes raises some questions, and especially the non-linear wave-wave energy transfers within the wave spectrum. In deep water, these energy transfers mainly occur due to resonant interactions between quadruplets of spectral wave components.

A more accurate modeling of nonlinear wave-wave interactions is necessary to improve sea state models. For this term, a theoretical model has been available since the works by Hasselmann (1962) and Zakharov (1999), and many studies have already shown the major role of these interactions in the wave spectrum evolution. However, the complexity of the nonlinear transfer term makes its numerical computation very time consuming, so that its exact calculation is only conducted in a few research models. The DIA method ('Discrete Interaction Approximation') of Hasselmann et al. (1985) is the most currently used technique in operational models of wave forecasting, but it is a crude approximation of the nonlinear transfer rate and it exhibits many deficiencies (e.g. Benoit, 2005).

Based on a method introduced by Lavrenov (2001), we developed and optimized a quasi-exact method for computing the non-linear four-wave interactions in deep water. This method, called GQM ('Gaussian Quadrature Method'), uses Gaussian quadrature formulas for the different integrations and provides very accurate estimates of the nonlinear transfer term with acceptable CPU times.

In the present study, we first consider the temporal evolution of a homogeneous wave field when there is no energy input from the wind or dissipation. The spectrum only evolves under the effect of nonlinear interactions and reaches an equilibrium shape with a  $f^{-4}$  high frequency tail. Our results reproduce the self-similar evolution of the spectrum (Badulin et al., 2005), which is consistent with the theory of weak turbulence. Detailed analysis of the directional spectrum shows a complex structure, bimodal (two main directions of propagation) for frequencies above and below the peak frequency. This structure is confirmed, at least partially, by recent high-resolution field measurements (Hwang et al., 2000a,b).

In a second step, the wind input (Snyder et al., 1981; Yan, 1987; Janssen, 1991) and

whitecapping dissipation (Komen et al., 1984, 1994; Van der Westhuysen et al., 2007) are also taken into account. Results show the influence of the forcing terms on the evolution of the wave spectrum, and in particular on the shape of the high frequency tail of the spectrum and its directional distribution.

In the next step, we consider two more realistic situations with a simple geometry, including wave propagation, namely the fetch-limited case (constant and homogeneous wind, blowing perpendicular to a long and straight coastline) and the slanting fetch case (wind blowing obliquely).

Results of the simulation of the fetch-limited case, in a wide range of wind speeds from 5 to 30 m s<sup>-1</sup>, are first analyzed within a ‘traditional’ approach, based on wind speed scaling of the representative parameters of the sea state (energy, peak frequency) (Kitaigorodskii, 1962). This study shows strong dispersion of the non-dimensional parameters, depending on the wind speed and on the wind input formulation. Results are then analyzed within an alternative approach that uses results of the weak turbulence theory (Zakharov, 2005; Badulin et al., 2007). This approach highlights features of wave development that do not depend on particular choice of external forcing functions and makes apparent different stages of wind-wave development.

Results of slanting fetch simulations show that wind direction relative to the coastline strongly influences the wave parameters. At short fetches, the wave height increases and the peak frequency decreases as the wind obliquity increases. Low frequency waves are steered by the coastline, they tend to propagate in alongshore direction, while the high frequency waves behave similarly to locally generated wind waves. Simulations are compared with some field measurements of the SHOWEX campaign (Ardhuin et al., 2007).

The work presented in this thesis confirms the need to accurately model the nonlinear wave-wave interactions in spectral wave models and shows that these improvements are now feasible (in particular in terms of computing time), thanks to the GQM method and the algorithm developed in this thesis.

# Table des matières

<b>Remerciements</b>	i
<b>Résumé</b>	iii
<b>Abstract</b>	v
<b>Notations</b>	xi
<b>Introduction</b>	1
<b>1 Eléments sur la modélisation spectrale des états de mer</b>	7
1.1 Définitions, terminologie . . . . .	7
1.1.1 Spectres directionnels de l'état de mer . . . . .	8
1.1.2 Paramètres intégraux . . . . .	11
1.1.3 Quelques situations idéalisées . . . . .	12
1.1.4 Paramètres adimensionnels . . . . .	13
1.1.5 Formes spectrales classiques . . . . .	14
1.2 Equation de transport de la densité d'action des vagues . . . . .	16
1.2.1 Génération des vagues par le vent $S_{in}$ . . . . .	17
1.2.2 Dissipation par moutonnement $S_{diss}$ . . . . .	21
1.2.3 Transferts non-linéaires $S_{nl}$ . . . . .	22
1.3 Les modèles spectraux d'état de mer . . . . .	23
1.3.1 Modèles de 1ère et 2ème génération . . . . .	23
1.3.2 Modèles de 3ème génération . . . . .	24

---

1.3.3	Le modèle TOMAWAC . . . . .	25
1.4	Aspects numériques . . . . .	25
1.4.1	Discrétisation . . . . .	26
1.4.2	Méthodes numériques . . . . .	26
<b>2</b>	<b>The nonlinear four-wave interactions</b>	<b>31</b>
2.1	Introduction . . . . .	31
2.2	Different methods for computing the $S_{nl}$ term . . . . .	32
2.2.1	The exact methods . . . . .	32
2.2.2	The approximate methods . . . . .	33
2.2.3	A solution for a high precision and a reduced CPU time : the ‘quasi-exact’ methods . . . . .	35
2.3	The GQM method . . . . .	36
2.3.1	Transformation of the non-linear transfer term into a suitable form for numerical integration . . . . .	36
2.3.2	The various steps of integration : use of Gaussian quadrature formulas	41
2.3.3	Optimization of the method . . . . .	49
2.3.4	Comparison of the GQM method with more commonly used methods	54
2.3.5	Estimation of the CPU time . . . . .	56
2.4	Conclusions . . . . .	57
<b>3</b>	<b>Ocean wave spectrum properties</b>	<b>59</b>
3.1	Introduction . . . . .	60
3.2	Equations and numerical methods . . . . .	62
3.2.1	The nonlinear four-wave interactions $S_{nl}$ . . . . .	62
3.2.2	The GQM method . . . . .	63
3.2.3	Numerical aspects . . . . .	65
3.3	Results for the conservative equation (no wind input nor dissipation) . . . . .	66
3.3.1	Model equation and initial conditions . . . . .	66
3.3.2	Concept of self-similarity . . . . .	67
3.3.3	Evolution of representative sea state parameters . . . . .	68
3.3.4	Evolution of the frequency spectrum . . . . .	71

---

3.3.5	The angular spreading of wave energy . . . . .	73
3.4	Influence of wind input and dissipation . . . . .	76
3.4.1	Model equation and initial conditions . . . . .	76
3.4.2	Evolution of representative sea state parameters . . . . .	78
3.4.3	Evolution of the frequency spectrum . . . . .	82
3.4.4	The angular spreading of wave energy . . . . .	86
3.4.5	Comparison with measured wave directional distributions . . . . .	89
3.4.6	Discussion about the low frequency bimodality . . . . .	92
3.5	Conclusions and perspectives . . . . .	95
<b>4</b>	<b>On weakly turbulent scaling of wind sea</b>	<b>97</b>
4.1	Introduction . . . . .	98
4.2	Numerical model of fetch-limited growth . . . . .	101
4.2.1	Conditions and parameters of simulation . . . . .	102
4.2.2	Wave input : local quasi-linear linear Cherenkov-like forcing . . . . .	104
4.2.3	Wave dissipation : whitecapping by Hasselmann (1974) . . . . .	107
4.2.4	Nonlinear transfer term $S_{nl}$ : problems and solutions . . . . .	108
4.2.5	Computer resources and choice of method for $S_{nl}$ . . . . .	110
4.3	Physical scaling of wind-wave growth . . . . .	111
4.3.1	Split balance model vs the Kitaigorodskii (1962) wind speed scaling	111
4.3.2	Reference cases of wind-wave growth . . . . .	114
4.3.3	‘Cleanest’ dependencies of wind-wave growth . . . . .	117
4.4	Fetch-limited wind-wave growth in simulations . . . . .	119
4.4.1	Wind speed scaling : reactive understanding of wave growth . . . . .	119
4.4.2	Key points of weakly turbulent scaling . . . . .	123
4.4.3	Energy-flux diagrams and self-similarity parameter of growing wind waves . . . . .	128
4.4.4	Stages of wind-wave growth . . . . .	132
4.5	Discussion and Conclusions . . . . .	135

<b>5 Modeling wave growth</b>	<b>139</b>
5.1 Introduction . . . . .	139
5.2 Description of the set of simulations . . . . .	140
5.2.1 General layout of the cases . . . . .	140
5.2.2 Modeling of the source and transfer terms . . . . .	140
5.2.3 Numerical aspects . . . . .	141
5.2.4 Initial conditions . . . . .	141
5.3 Results on fetch-limited growth . . . . .	142
5.3.1 Growth curves . . . . .	142
5.3.2 Shape of the frequency spectrum . . . . .	145
5.3.3 Directional distribution of the spectrum . . . . .	147
5.4 Slanting fetch conditions . . . . .	152
5.4.1 The SHOWEX campaign . . . . .	153
5.4.2 Influence of the wind obliquity on the growth curves . . . . .	153
5.4.3 Frequency spectra and frequency dependent wave parameters . . . . .	155
5.4.4 Directional wave spectrum and nonlinear interactions . . . . .	162
5.4.5 Directional distribution of the spectrum . . . . .	165
5.5 Conclusions . . . . .	168
<b>Conclusion générale - Perspectives</b>	<b>171</b>
<b>Annexe A : Supplement to chapter 5</b>	<b>179</b>
<b>Annexe B : Valorisation et publications issues des travaux de thèse</b>	<b>191</b>
<b>Bibliographie</b>	<b>202</b>

# Notations

$a$	amplitude des vagues / de la houle	(m)
$a_n$	coefficients de Fourier dans la décomposition en série de Fourier de $D(f, \theta)$	
$b_n$	coefficients de Fourier dans la décomposition en série de Fourier de $D(f, \theta)$	
$C_{ph}$	vitesse de phase des vagues	(m s <sup>-1</sup> )
$C_D$	coefficient de trainée	
$C_{ph}/U_{10}$	âge des vagues	
$C_g$	vitesse de groupe intrinsèque (ou relative) des vagues	(m s <sup>-1</sup> )
$C_p$	vitesse de phase au pic	(m s <sup>-1</sup> )
$D(f, \theta)$	fonction de répartition angulaire	(rad <sup>-1</sup> )
$d$	profondeur d'eau	(m)
$E$	énergie totale déterminée à partir du spectre de variance	(m <sup>2</sup> )
$\tilde{E}$	énergie totale adimensionnelle	
$\mathcal{E}(f, \theta)$	densité spectro-angulaire d'énergie (spectre directionnel d'énergie)	(kg s <sup>-2</sup> Hz <sup>-1</sup> rad <sup>-1</sup> )
$\mathcal{E}_{tot}$	énergie totale des vagues par unité de surface	(kg s <sup>-2</sup> )
$F(f, \theta)$	densité spectro-angulaire de variance (spectre directionnel de variance)	(m <sup>2</sup> Hz <sup>-1</sup> rad <sup>-1</sup> )
$E(f)$	densité spectrale de variance (spectre fréquentiel de variance)	(m <sup>2</sup> Hz <sup>-1</sup> )
$f$	fréquence des vagues	(Hz)
$f_1$	première fréquence de discréétisation	(Hz)
$f_{max}$	dernière fréquence de discréétisation	(Hz)
$f_p$	fréquence de pic des vagues	(Hz)
$f_{PM}$	fréquence de pic de Pierson-Moskowitz	(Hz)
$f_{PM}^*$	fréquence de pic de Pierson-Moskowitz adimensionnelle	
$\tilde{f}_p$	fréquence pic adimensionnelle	
$g$	accélération de la pesanteur ( $g \approx 9.81$ )	(m s <sup>-2</sup> )
$H_{m0}$	hauteur significative spectrale	(m)
$k$	nombre d'onde des vagues	(rad m <sup>-1</sup> )

$m_n$	moment du spectre de variance d'ordre $n$	$(\text{m}^2 \text{ Hz}^n)$
$N(f, \theta)$	densité spectro-angulaire d'action (spectre directionnel d'action)	$(\text{m}^2 \text{ Hz}^{-2} \text{ rad}^{-1})$
$S_{der}(f, \theta)$	terme source dérivé (par rapport à $F$ )	$(\text{Hz})$
$S_{diss}(f, \theta)$	terme de dissipation d'énergie par moutonnement	$(\text{m}^2 \text{ rad}^{-1})$
$S_i(f, \theta)$	terme source	$(\text{m}^2 \text{ rad}^{-1})$
$S_{in}(f, \theta)$	terme de génération des vagues par le vent	$(\text{m}^2 \text{ rad}^{-1})$
$S_{nl}(f, \theta)$	terme de transfert non-linéaire vague-vague	$(\text{m}^2 \text{ rad}^{-1})$
$S_{tot}(f, \theta)$	terme source total	$(\text{m}^2 \text{ rad}^{-1})$
$T$	période des vagues	$(\text{s})$
$T_{m01}$	période et fréquence moyenne calculées à partir des moments d'ordre 0 et 1	$(\text{s})$
$T_{m02}$	période et fréquence moyenne calculées à partir des moments d'ordre 0 et 2	$(\text{s})$
$T_p$	période de pic des vagues	$(\text{s})$
$U_{10}$	vitesse du vent à 10 mètres	$(\text{m s}^{-1})$
$\mathbf{U}_c$	vitesse du courant	$(\text{m s}^{-1})$
$u_*$	vitesse de frottement	$(\text{m s}^{-1})$
$X$	fetch	$(\text{m})$

## Lettres grecques

$\alpha(f, \theta)$	terme de croissance linéaire	$(\text{m}^2 \text{ rad}^{-1})$
$\alpha_P$	la constante de Phillips	
$\beta$	taux de croissance adimensionnel	
$\Delta t$	pas de temps	$(\text{s})$
$\Delta x$	discrétisation spatiale	$(\text{m})$
$\varepsilon$	cambrure	
$\eta$	élévation de la surface libre	$(\text{m})$
$\gamma$	facteur d'amplification du pic pour un spectre de type JONSWAP	
$\theta$	direction de propagation des vagues	$(\text{rad})$
$\theta_m$	direction moyenne des vagues	$(\text{rad})$
$\theta_u$	direction du vent	$(\text{rad})$
$\lambda$	longueur d'onde des vagues	$(\text{m})$
$\rho_a$	masse volumique de l'air	$(\text{kg m}^{-3})$
$\rho_w$	masse volumique de l'eau	$(\text{kg m}^{-3})$
$\sigma$	étalement angulaire	$(\text{rad})$
$\tau$	durée adimensionnelle	
$\varphi$	phase des vagues	$(\text{rad})$
$\chi$	fetch adimensionnel	
$\omega$	pulsation intrinsèque (relative) des vagues	$(\text{rad s}^{-1})$

$\omega_p$	pulsation au pic	(rad s <sup>-1</sup> )
$\tilde{\omega}_p$	pulsation au pic adimensionnelle	

## Acronymes

CREST	Coupled Rays with Eulerian Source Terms
DIA	Discrete Interaction Approximation
GQM	Gaussian Quadrature Method
JONSWAP	Joint North Sea Wave Project
MDIA	Multiple DIA
SWAMP	Sea WAve Modeling Project
SWAN	Simulating WAves in the Nearshore
TOMAWAC	TELEMAC-based Operational Model Addressing Wave Action Computation
WAM	WAve Modeling
WAMDI Group	WAve Model Development and Implementation Group



# Introduction

Les vagues jouent un rôle fondamental pour de nombreuses problématiques en océanographie physique et disciplines connexes : gestion des zones côtières et des opérations en mer, conception et dimensionnement de structures marines et portuaires telles qu'une digue ou une plateforme pétrolière, étude de la morphodynamique côtière et de l'évolution du littoral, récupération de l'énergie des vagues, etc. De plus, par leurs effets sur les flux entre l'océan et l'atmosphère, les vagues ont aussi des effets directs ou indirects sur les dynamiques de circulation océaniques et atmosphériques. La connaissance précise et la prévision de la climatologie des états de mer (valeurs moyennes et extrêmes) représentent donc des enjeux importants pour de nombreuses applications.

Depuis les travaux de Sverdrup & Munk (1947) et les premiers modèles de prévision des vagues dans les années 1950 et 1960 (Gelci et al., 1957), de nombreuses études théoriques et observations ont permis le développement de modèles de description et de prévision des états de mer de plus en plus sophistiqués. Les modèles spectraux permettent de représenter l'évolution spatio-temporelle du spectre directionnel d'énergie (ou d'action) des vagues sous l'effet de forçages météorologiques instationnaires, éventuellement dans des conditions hydrodynamiques (niveau moyen de mer et courants ambients) instationnaires. Le spectre directionnel d'énergie fournit une information détaillée sur la répartition de l'énergie des vagues, à la fois en fréquences et en directions. On peut aussi en déduire des paramètres intégrés caractéristiques de l'état de mer, comme la hauteur significative spectrale, les périodes moyennes ou de pic, la direction moyenne de propagation, l'étalement angulaire moyen, etc.

Les modèles d'état de mer actuels, WAM (WAMDI Group, 1988; Komen et al., 1994), WAVEWATCH III (Tolman, 1991, 2002), SWAN (Booij et al., 1999), TOMAWAC (Benoit et al., 1996a), CREST (Ardhuin et al., 2001), dits de troisième génération, ont été développés dans les 20 dernières années depuis la mise au point du modèle WAM par le WAMDI Group (1988) qui a représenté une avancée majeure. Ils résolvent l'équation d'évolution du spectre d'énergie (ou d'action) de l'état de mer sous l'effet combiné de plusieurs processus physiques, qui créent, dissipent ou transfèrent l'énergie au sein du spectre. Les modèles de troisième génération ne font pas d'hypothèse *a priori* sur la répartition directionnelle ou fréquentielle de l'énergie de l'état de mer (hormis dans certains cas pour la partie hautes-fréquences, au-delà d'un certaine fréquence dite diagnostique). Le spectre est discréteisé suivant une grille en fréquences et directions, et chaque composante du spectre évolue « librement » sous l'action combinée des différents processus physiques pris en compte.

En grande profondeur d'eau, trois processus physiques dominants régissent l'évolution des vagues : la génération des vagues par le vent, la dissipation d'énergie par moutonnement (dissipation en eau profonde) et les transferts non-linéaires vague-vague (interactions entre quadruplets de fréquences). Ces termes, souvent appelés « termes sources », sont notés respectivement  $S_{in}$ ,  $S_{diss}$  et  $S_{nl}$ .

Sur la base de retours d'expérience issus de leur utilisation, certaines limitations des modèles de troisième génération ont pu être établies par plusieurs équipes de recherche, à l'occasion de campagnes de mesures *in situ*. La modélisation de certains processus physiques pose question. En réalité, deux problématiques très différentes relatives aux termes responsables de l'évolution du spectre d'état de mer peuvent être distinguées. En ce qui concerne les transferts non-linéaires d'énergie au sein du spectre, un modèle théorique permettant de calculer ces interactions est connu depuis les travaux de Hasselmann (1962) et Zakharov (1968). Dans ce cas, la difficulté réside en un calcul numérique le plus exact possible d'un terme très complexe et très lourd en temps de calcul. Concernant les termes de génération par le vent et de dissipation d'énergie, le problème est tout autre. Les modèles utilisés reposent sur des paramétrisations plus ou moins empiriques et leurs fondements physiques peuvent parfois poser question.

Une meilleure prise en compte des transferts non-linéaires d'énergie au sein du spectre d'énergie des vagues (terme  $S_{nl}$ ) est un objectif essentiel à l'amélioration des modèles numériques d'état de mer. En effet, il est aujourd'hui établi que ces mécanismes de transferts non-linéaires jouent un rôle déterminant dans l'évolution spatio-temporelle du spectre d'énergie des vagues (Young & Van Vledder, 1993; Badulin et al., 2005), puisqu'ils ont notamment la capacité de stabiliser la forme du spectre autour de morphologies connues par la mesure expérimentale. Cependant, le calcul numérique précis de ce terme demande des temps CPU très importants et son évaluation exacte n'est actuellement réalisée que dans certains modèles de recherche. La méthode DIA (« Discrete Interaction Approximation ») de Hasselmann et al. (1985), utilisée dans presque tous les codes de troisième génération depuis WAM pour évaluer le terme  $S_{nl}$ , paraît à présent trop simplifiée et approximative, en particulier lorsqu'on s'intéresse au spectre complet de l'état de mer, et non simplement aux paramètres intégrés cités précédemment. Le développement de méthodes de calcul quasi-exactes, permettant d'allier une estimation très précise du terme de transfert non-linéaire à des temps de calculs acceptables, et dans un futur proche, d'envisager des applications opérationnelles, est ainsi apparu nécessaire.

Les termes de génération par le vent  $S_{in}$  et de dissipation d'énergie par moutonnement  $S_{diss}$  s'appuient sur des formulations empiriques ajustées pour que les modèles reproduisent les observations de croissance des vagues sous l'effet du vent, habituellement formulées en termes de hauteur significative spectrale et de fréquence de pic. Or, ces observations donnent des résultats dispersés pour plusieurs raisons. Tout d'abord, les conditions météorologiques sont rarement identiques entre les différentes campagnes de mesures, les effets d'instabilité atmosphérique peuvent jouer un grand rôle sur la croissance des vagues, l'instationnarité de la vitesse du vent ou de sa direction (fluctuations turbulentes, effets de rafales, etc.) peut aussi avoir des effets prononcés, ainsi que la géométrie de la côte. De plus, les formulations sont généralement basées sur des mesures dans des conditions de vent et de hauteurs de vagues assez restreintes (vent et hauteurs de vagues relativement

faibles). Les paramétrisations sont alors étendues à un domaine plus large sans certitude de l'applicabilité de la formule à ces domaines. Enfin, la difficulté pour obtenir des mesures précises de la distribution directionnelle du spectre, et notamment dans les hautes fréquences, rend délicate la formulation de fonctions directionnelles précises pour  $S_{in}$  et  $S_{diss}$ . Mais même avec des observations parfaites, la difficulté serait encore présente ! En effet, il n'est pas évident de distinguer les différents processus physiques responsables de la génération des vagues ou de la dissipation et de quantifier expérimentalement les transferts non-linéaires  $S_{nl}$  qui co-existent avec  $S_{in}$  et  $S_{diss}$ . Ainsi, bien que des efforts importants aient été accomplis ces dernières années pour obtenir des paramétrisations acceptables, un consensus n'est pas aujourd'hui établi. Les différentes formulations de  $S_{in}$  (Snyder et al., 1981; Yan, 1987; Janssen, 1991, etc.) donnent des résultats dispersés pour les fortes vitesses de vent. Le terme  $S_{wc}$  est sûrement celui dont la connaissance physique est la plus limitée. Néanmoins les récents travaux de Alves & Banner (2003); Van der Westhuysen et al. (2007); Zakharov et al. (2007); Korotkevich et al. (2008); Ardhuijn et al. (2008, 2009) permettent d'envisager de nettes améliorations.

L'intitulé de la thèse « Amélioration de la modélisation spectrale des états de mer par un calcul quasi-exact des interactions non-linéaires vagues-vagues » se trouve ainsi clarifié après ces explications. Il exprime notre objectif principal : améliorer les modèles spectraux d'état de mer en s'appuyant sur une méthode précise pour calculer les transferts non-linéaires d'énergie au sein du spectre des vagues, qui sont, comme nous l'avons dit, un des mécanismes principaux régissant l'évolution du spectre d'énergie d'un état de mer. Bien entendu, les vagues ne peuvent être créées et amplifiées sans source d'énergie ; et sans dissipation, leur hauteur augmenterait indéfiniment. Cette amélioration nécessite donc de garder une préoccupation constante pour les autres termes sources et puits régissant l'évolution des vagues.

Dans le cadre de cette thèse, nous nous plaçons en grande profondeur d'eau et considérons un milieu sans courant ambiant, les trois mécanismes dominants étant alors ceux décrits précédemment. Notre cible concrète est ainsi le développement et la validation d'une méthode de calcul quasi-exacte des interactions non-linéaires entre quadruplets de fréquences en grande profondeur d'eau possédant un coût de calcul raisonnable et permettant d'envisager des simulations à grande échelle. Ce travail s'inscrit notamment dans une optique d'amélioration du logiciel TOMAWAC d'EDF R&D (Benoit et al., 1996a).

Pour cela, nous utilisons une approche de calcul originale, nommée GQM (Gaussian Quadrature Method), basée sur une intégration numérique à l'aide de quadratures de Gauss, suivant une idée proposée par Lavrenov (2001), et qui avait déjà commencé à être testée avant le début de la thèse sur un certain nombre de spectres académiques avec de bons résultats (Benoit, 2005). Dans le cadre de la thèse, cette méthode est validée sur plusieurs cas de complexité variable et croissante (évolution sous l'effet unique des termes non-linéaires, cas de durée limitée, fetch limité, fetch oblique), en combinaison avec différents termes pour la génération des vagues par le vent et la dissipation par moutonnement. L'évolution du spectre sous l'effet de ces différents processus est analysée à l'aide de plusieurs approches, et, dans certains cas, comparée à des mesures *in situ*. Nous avons choisi d'examiner les paramètres intégrés décrivant l'état de mer, tels la hauteur significative spectrale  $H_{mo}$

et la fréquence de pic  $f_p$ , habituellement considérés, mais aussi de porter une attention toute particulière aux spectres directionnels complets, comprenant la répartition énergétique spectrale et les aspects directionnels.

La thèse s'articule autour de cinq chapitres, et se termine par l'exposé des conclusions et diverses perspectives pour ce travail. Les chapitres 3 et 4 sont rédigés en langue anglaise sous forme d'articles scientifiques : le chapitre 3 a été soumis à la revue Journal of Geophysical Research - Oceans en juillet 2009 et le chapitre 4 à la revue Journal of Fluid Mechanics en septembre 2009. Les chapitres 2 et 5 sont également écrits en Anglais en vue d'une probable soumission future. De plus, le chapitre 5 s'appuie en partie sur un article publié dans les actes de la conférence International Conference on Coastal Engineering 2008 (Gagnaire-Renou et al., 2008).

- Le premier chapitre expose brièvement les concepts nécessaires à la compréhension du sujet. Les termes principaux sont définis, la notion de spectre de l'état de mer en particulier, et des éléments sur la modélisation des vagues sont rappelés. Après avoir explicité les équations de propagation de la densité spectro-angulaire d'énergie et d'action des vagues, à la base de tous les modèles spectraux d'état de mer, nous apportons quelques éléments sur les principaux processus physiques intervenant : expression du terme de transfert non-linéaire, formulation des termes de génération par le vent et de dissipation employés dans la suite du travail. Pour finir, une description générale des aspects numériques dans le modèle utilisé est proposée.
- Le deuxième chapitre traite spécifiquement du terme d'interactions non-linéaires entre quadruplets de fréquences. Les différentes méthodes de calcul du terme de transfert non-linéaire sont succinctement décrites, les méthodes « exactes » ou quasi-exactes, et les méthodes approchées. Un éclairage particulier est apporté sur la méthode DIA puisque cet algorithme est largement utilisé dans les chapitres suivants. La méthode GQM est ensuite plus spécifiquement détaillée. Nous présentons les différentes étapes de la transformation de l'intégrale, puis l'utilisation de quadratures de Gauss pour les diverses intégrations. Pour finir, quelques éléments sont donnés sur l'optimisation de la méthode, sa résolution, le filtrage de configurations, etc. Des premiers tests et comparaisons avec les méthodes DIA et MDIA (« Multiple Discrete Interaction Approximation ») en termes de résultats, mais aussi de temps de calcul, sont proposés.
- Dans le troisième chapitre, les résultats de notre modèle sont examinés dans des conditions idéalisées. Nous nous plaçons tout d'abord dans le cas d'un état de mer homogène et observons l'évolution du spectre d'énergie des vagues sous l'action unique des interactions non-linéaires, en partant de diverses conditions initiales, plus ou moins réalistes physiquement. L'objectif de ce travail est d'analyser l'influence du terme de transfert non-linéaire sur le spectre de l'état de mer et en particulier l'effet de stabilisation de la forme du spectre par ces interactions. Le concept d'auto-similarité du spectre d'état de mer est alors introduit et vérifié pour la dynamique d'évolution du spectre. Dans un deuxième temps, le cas de croissance de l'état de mer en conditions de durée limitée est modélisé en utilisant plusieurs combinaisons de termes de génération par le vent et

de dissipation. L'évolution des paramètres représentatifs de l'état de mer est examinée dans ces deux situations. Nous prêtions également une attention toute particulière à la distribution fréquentielle et directionnelle du spectre et à son évolution sous l'action des transferts non-linéaires (modélisés en utilisant les méthodes DIA et GQM), mais aussi des différents termes sources et puits.

- Le chapitre 4 relève d'une démarche plus singulière. Le cas considéré, nommé « fetch limité », nous permet d'analyser la propagation des vagues à distance plus ou moins grande d'une côte rectiligne, pour une large gamme de vitesses de vents soufflant perpendiculairement à la côte. Dans ce travail, seuls les paramètres intégrés (énergie, fréquence de pic) sont examinés, mais à partir de deux approches tout à fait différentes. La première approche, très classique, est utilisée habituellement pour comparer les courbes de croissance de l'énergie et de la fréquence de pic des vagues, obtenues dans différentes conditions de vent, avec les observations de campagnes de mesures. Elle utilise un adimensionnement des paramètres décrivant l'état de mer (énergie, fréquence de pic) par la vitesse du vent (Kitaigorodskii, 1962). La deuxième approche, plus originale, se place dans le cadre de la théorie de la turbulence faible, dont les bases théoriques ont été données par Zakharov (1966) (voir aussi Zakharov & Zaslavsky, 1982b,a, 1983a,b). Cette approche, développée récemment par Badulin et al. (2005); Zakharov (2005); Badulin et al. (2007), repose sur un modèle nommé « split balance », qui fait ressortir certaines caractéristiques du développement des vagues ne dépendant pas du choix particulier des modèles de génération par le vent et de dissipation. Elle s'appuie sur le rôle central du terme de transfert non-linéaire, supposé prépondérant par rapport aux autres processus physiques ( $S_{in}$  et  $S_{diss}$ ) pour un certain stade de croissance des vagues (nommé aussi « stade de développement auto-similaire »). Les résultats obtenus à partir de différentes méthodes pour modéliser les termes de génération par le vent  $S_{in}$  et les transferts non-linéaires  $S_{nl}$  donnent ainsi un nouvelle justification numérique à ce modèle de « split balance ». Les travaux décrits dans ce chapitre ont été réalisés en collaboration avec Sergei I. Badulin, chercheur à l'Institut P. P. Shirshov d'Oceanologie (Moscou). Ils ont été initiés au cours d'un séjour de trois semaines dans son laboratoire (Février-Mars 2009) et poursuivis par la suite.
- Le cinquième chapitre présente l'étude des cas de fetch limité et de fetch oblique, dans lequel le vent souffle avec une incidence oblique par rapport à la côte. Le rôle des interactions non-linéaires sur la structure du spectre directionnel est examiné attentivement. Les effets de la distance par rapport au rivage et des termes de vent et de dissipation sur cette structure sont identifiés. Le cas de fetch oblique nous permet de travailler sur une situation proche de conditions réelles, pouvant malgré tout être modélisée par un modèle à une dimension d'espace. A partir d'un continuum de directions de vent allant de 0 à 90° par rapport à la côte, nous analysons en détail l'influence de l'incidence du vent sur le spectre directionnel. Les résultats sont comparés à des mesures de la campagne SHOWEX (Ardhuin et al., 2007) pour un cas de vent oblique soufflant avec une incidence d'environ 20° par rapport à la normale à la côte.

Pour terminer, nous présentons une synthèse des différents résultats de la thèse. Nous exposons des conclusions générales et proposons des ouvertures sur les développements à venir et perspectives de recherche à plus ou moins long terme.



# Chapitre 1

## Eléments sur la modélisation spectrale des états de mer

Dans ce chapitre, les grandeurs nécessaires à la compréhension du sujet sont introduites.

### 1.1 Définitions, terminologie

On appelle « vagues » les ondes de gravité qui se propagent à la surface des mers et océans et sont directement ou indirectement générées par le vent. Ce sont des oscillations généralement irrégulières, et dont la période est typiquement comprise entre 2.5 et 25 s.

Le terme « houle » (ou houle océanique) désigne un système de vagues observé en un point éloigné de la zone de génération par le vent, lorsque les vagues se sont propagées sur de longues distances.

Le terme « état de mer » désigne l'agitation locale de la mer observée sur une certaine durée. L'état de mer peut recouvrir des formes diverses selon que la mer est calme ou peu agitée ou bien en phase de tempête, selon que les vagues sont en phase de formation (on parle alors de « mer de vent » ou de « clapot ») ou au contraire arrivent de l'océan après s'être propagées sur plusieurs milliers de kilomètres (on parle alors de « houle océanique »). Il peut être composé de plusieurs systèmes de vagues ayant des origines différentes.

Dans la suite, nous utiliserons les termes « vague » et « état de mer » de manière indifférente.

Le terme « fetch » désigne la distance sur laquelle souffle le vent, i.e. la longueur de la zone de génération des vagues.

Les vagues qui composent un état de mer sont toutes différentes, mais on ne s'intéresse pas au détail de leurs propriétés, on considère leurs caractéristiques globales. On pourra donc caractériser un état de mer par des valeurs moyennes telles que la hauteur significative  $H_{m0}$ , la période moyenne ou période de pic, mais aussi par son spectre d'énergie.

Le spectre d'énergie des vagues est la répartition de l'énergie des vagues sur un ensemble de fréquences et de directions. Alors que les vagues sont irrégulières, le spectre est relativement régulier, il varie assez lentement en espace et en temps. Cette régularité se prête à la modélisation numérique. On note que, en ne conservant que l'énergie des vagues et sa répartition spectrale, on perd une partie de l'information sur un état de mer réel et on ne pourra pas reconstituer de façon unique un champ de surface libre à partir du spectre.

Pour des précisions sur ces définitions et l'établissement des équations fondamentales, on pourra se référer aux livres généraux de Komen et al. (1994), Young (1999) ou Holthuijsen (2007).

### 1.1.1 Spectres directionnels de l'état de mer

Le déplacement de la surface libre associé à une vague sinusoïdale simple, onde monochromatique (une seule période ou fréquence) et monodirectionnelle (une seule direction de propagation), s'écrit de la façon suivante :

$$\eta(x, y, t) = a \cos(k(x \cos \theta + y \sin \theta) - \omega t + \varphi) \quad (1.1)$$

Le principe de la décomposition spectrale d'un état de mer consiste à faire l'hypothèse que le champ d'élévation de surface libre de la mer  $\eta(x, y, t)$  résulte de la superposition d'un grand nombre de composantes sinusoïdales élémentaires (i.e. monochromatiques et monodirectionnelles) indépendantes les unes des autres. Ces composantes sont superposées linéairement (hypothèse de linéarité de l'état de mer). On peut écrire cela sous forme discrète :

$$\eta(x, y, t) = \sum_{i=1}^N \eta_i(x, y, t) = \sum_{i=1}^N a_i \cos(k_i(x \cos \theta_i + y \sin \theta_i) - \omega_i t + \varphi_i) \quad (1.2)$$

où  $a_i$ ,  $\omega_i$ ,  $k_i$ ,  $\varphi_i$  sont l'amplitude, la pulsation, le nombre d'onde et la phase du i-ème composant de la somme et  $\theta_i$  est l'angle entre l'axe des x et la direction de propagation du i-ème composant de la somme.

On représente l'état de mer comme une réalisation d'un processus aléatoire tel que les phases  $\varphi_i$  de chaque composante sont aléatoirement distribuées sur  $[0, 2\pi]$  suivant une loi uniforme. Ce mode de représentation de l'état de mer est parfois appelé « stochastique ». De cette manière, l'énergie par unité de surface d'un état de mer aléatoire multidirectionnel est donnée par :

$$\mathcal{E}_{tot} = \sum_{i=1}^N \frac{1}{2} \rho_w g a_i^2 \quad (1.3)$$

Cependant il convient de souligner que cette relation n'est valable que dans l'hypothèse de

linéarité de l'état de mer.

$\mathcal{E}_{tot}$ , appelé par la suite énergie totale, peut aussi s'écrire :

$$\mathcal{E}_{tot} = \int_0^\infty \int_0^{2\pi} \mathcal{E}(f, \theta) df d\theta \quad (1.4)$$

On a donc la correspondance entre le cas discret et le spectre d'énergie  $\mathcal{E}(f, \theta)$  (appelé aussi densité spectro-angulaire d'énergie) par la relation suivante (cf. Holthuijsen, 2007) :

$$\sum_f \sum_\theta \frac{1}{2} \rho_w g a_i^2 = \mathcal{E}(f, \theta) df d\theta \quad (1.5)$$

La variable utilisée préférentiellement pour la représentation et la modélisation des états de mer est le spectre directionnel de variance (ou densité spectro-angulaire de variance) des vagues, noté  $F(f, \theta)$ , qui vérifie :

$$F(f, \theta) = \mathcal{E}(f, \theta) / (\rho_w g) \quad (1.6)$$

Enfin, dans le cas général de vagues se propageant dans un milieu non-homogène et non-permanent (en présence de courants ou de marées), les grandeurs  $\mathcal{E}$  et  $F$  n'étant plus conservées, il est nécessaire d'introduire une nouvelle quantité, le spectre directionnel d'action (ou densité spectro-angulaire d'action) de l'état de mer, noté  $N(f, \theta)$ , et vérifiant (cf. Komen et al., 1994) :

$$N(f, \theta) = F(f, \theta) / \omega \quad (1.7)$$

où  $\omega$  est la pulsation intrinsèque ou relative, donnée par la relation de dispersion des vagues de gravité :

$$\omega^2 = gk \tanh(kd) \quad (1.8)$$

où  $d$  est la profondeur d'eau.

En profondeur d'eau supposée infinie (situation que nous considérons ici), cette relation s'écrit simplement :

$$\omega^2 = gk \quad (1.9)$$

Précisons au passage que la pulsation relative des vagues correspond à la pulsation observée dans un repère se déplaçant à la vitesse du courant, et diffère de la pulsation absolue  $\Omega$  observée dans un repère fixe. Ces deux pulsations sont liées par la relation  $\Omega = \omega + \mathbf{k} \cdot \mathbf{U}_c$ . Dans tout ce travail, nous nous placerons uniquement dans des cas de courant nul ; les deux pulsations sont donc égales et peuvent être utilisées indifféremment.

Les densités spectrales ci-dessus peuvent aussi s'exprimer en fonction des couples de variables  $(\omega, \theta)$ ,  $(k_x, k_y) = (k \sin \theta, k \cos \theta) = \mathbf{k}$  ou  $(k, \theta)$ . Suivant la méthode de mesure ou le modèle numérique, certaines variables peuvent être plus faciles à manipuler. Les relations de correspondance permettant de passer entre les différentes coordonnées spectrales sont les suivantes :

$$F(f, \theta) df d\theta = F(k, \theta) dk d\theta \quad (1.10)$$

ce qui donne

$$F(f, \theta) = \frac{\partial k}{\partial f} F(k, \theta) = \frac{2\pi}{C_g} F(k, \theta) \quad (1.11)$$

où  $C_g$  est la vitesse de groupe (vitesse de propagation de l'énergie), définie par  $C_g = \partial \omega / \partial k$ . En grande profondeur d'eau, cette relation se réduit à :  $C_g = g/(2\omega)$ . De même, on trouve<sup>1</sup> :

$$F(f, \theta) = 2\pi F(\omega, \theta) \quad (1.12)$$

$$F(f, \theta) = \frac{2\pi k}{C_g} F(k_x, k_y) = \frac{2\pi k}{C_g} F(\mathbf{k}) \quad (1.13)$$

Le spectre directionnel de variance se décompose généralement de la façon suivante :

$$F(f, \theta) = E(f) D(f, \theta) \quad (1.14)$$

où  $E(f)$ , appelé spectre fréquentiel de variance (ou spectre 1D), s'obtient en intégrant le spectre directionnel de variance sur toutes les directions de l'état de mer :

$$E(f) = \int_0^{2\pi} F(f, \theta) d\theta \quad (1.15)$$

et  $D(f, \theta)$  est appelé fonction de répartition angulaire (ou distribution directionnelle) des vagues et traduit la façon dont l'énergie (ou la variance) est répartie angulairement pour chaque fréquence  $f$ . Cette fonction, positive et périodique sur  $[0, 2\pi]$ , vérifie la propriété :

$$\int_0^{2\pi} D(f, \theta) d\theta = 1 \quad (1.16)$$

---

1. Pour les fonctions de deux variables, le changement de variable permettant de passer de  $F(x_1, x_2)$  à  $\tilde{F}(y_1, y_2)$  sous la condition de conservation de l'intégrale s'obtient par la relation  $F(x_1, x_2) = J \tilde{F}(y_1, y_2)$

où  $J$  est le Jacobien  $\begin{vmatrix} \frac{\partial y_1}{\partial x_1} & \frac{\partial y_1}{\partial x_2} \\ \frac{\partial y_2}{\partial x_1} & \frac{\partial y_2}{\partial x_2} \end{vmatrix}$ .

### 1.1.2 Paramètres intégraux

A partir du spectre de variance (ou d'énergie) de l'état de mer, un certain nombre de paramètres caractéristiques de l'état de mer peuvent être calculés en utilisant les moments du spectre  $m_n$ , définis par :

$$m_n = \int_0^\infty f^n E(f) df \quad (1.17)$$

En particulier, la hauteur significative spectrale  $H_{m0}$  s'obtient à partir du moment d'ordre zéro :

$$H_{m0} = 4\sqrt{m_0} \quad (1.18)$$

Le moment d'ordre zéro est égal à la variance de l'élévation de la surface libre, appelée aussi énergie totale déterminée à partir du spectre de variance  $E$  :

$$m_0 = \int_0^\infty E(f) df = E \quad (1.19)$$

Les périodes moyennes  $T_{m01}$  et  $T_{m02}$  (appelée période zero up-crossing) sont calculées de la façon suivante :

$$T_{m01} = \frac{m_0}{m_1} \quad (1.20)$$

$$T_{m02} = \sqrt{\frac{m_0}{m_2}} \quad (1.21)$$

On définit aussi la période de pic  $T_p$ , ainsi que la fréquence de pic  $f_p = 1/T_p$ , qui correspond à la fréquence en laquelle le spectre  $E(f)$  atteint son maximum. Plusieurs méthodes permettent de la calculer (Young, 1995). On citera la méthode dite de Delft (ou moyenne barycentrique), et la méthode de Read, que nous utiliserons préférentiellement :

$$T_{p_n} = \frac{\int_0^\infty (E(f))^n df}{\int_0^\infty f(E(f))^n df} \quad (1.22)$$

où  $n$  est un exposant, habituellement égal à 4, 5 ou 8.

La fonction de répartition angulaire  $D(f, \theta)$ , périodique de période  $2\pi$ , définie précédemment, se décompose en série de Fourier :

$$D(f, \theta) = \frac{1}{2\pi} + \frac{1}{\pi} \sum_{n=1}^{\infty} (a_n(f) \cos(n\theta) + b_n(f) \sin(n\theta)) \quad (1.23)$$

où les  $a_n$  et  $b_n$  sont les coefficients de Fourier, définis par :

$$a_n(f) = \int_0^{2\pi} D(f, \theta) \cos(n\theta) d\theta \quad (1.24)$$

$$b_n(f) = \int_0^{2\pi} D(f, \theta) \sin(n\theta) d\theta \quad (1.25)$$

A partir des coefficients de Fourier  $a_1$  et  $b_1$  :

$$a_1(f) = \int_0^{2\pi} D(f, \theta) \cos(\theta) d\theta \quad (1.26)$$

$$b_1(f) = \int_0^{2\pi} D(f, \theta) \sin(\theta) d\theta \quad (1.27)$$

on peut définir l'étalement angulaire (ou étalement directionnel)  $\sigma(f)$  :

$$\sigma(f) = \sqrt{2 \left( 1 - \sqrt{a_1^2(f) + b_1^2(f)} \right)} \quad (1.28)$$

l'étalement angulaire moyen  $\sigma$  :

$$\sigma = \frac{\int_f \sigma(f) E(f) df}{\int_f E(f) df} \quad (1.29)$$

et la direction moyenne des vagues  $\theta_m(f)$  :

$$\theta_m(f) = \arctan \left( \frac{b_1(f)}{a_1(f)} \right) \quad (1.30)$$

### 1.1.3 Quelques situations idéalisées

De nombreux facteurs peuvent influencer l'évolution d'un état de mer, le vent bien entendu, mais aussi la position et la géométrie de la côte, la profondeur d'eau, etc., donnant lieu à des situations plus ou moins complexes et difficiles à modéliser. Deux situations idéalisées sont couramment examinées (Young, 1999) :

- un cas nommé « durée limitée » (ou limitation par le temps), qui correspond au développement des vagues à partir d'un état de mer initial calme, en grande profondeur d'eau. Le vent souffle de façon constante et uniforme et il n'y a pas de côte à proximité. On a donc une homogénéité spatiale (pas de propagation des vagues) et l'état de mer n'est fonction que du temps pendant lequel le vent a soufflé.

- un cas appelé « fetch limité » (ou limitation par le fetch), qui correspond à un vent constant soufflant perpendiculairement à une côte longue et droite. On se place en eau profonde et le vent souffle depuis suffisamment longtemps pour qu'un état d'équilibre soit atteint. Cette fois, les paramètres représentant l'état de mer ne sont fonction que du fetch, noté  $X$ .

De nombreuses campagnes de mesures ont permis d'obtenir des estimations du spectre d'état de mer dans des situations proches du cas de fetch limité. On citera, parmi les plus connues, les premières tentatives de Sverdrup & Munk (1947) ou Bretschneider (1952), le projet JONSWAP (Joint North Sea Wave Project) (Hasselmann et al., 1973) qui a donné lieu à une campagne de mesures majeure dont les résultats sont encore aujourd'hui largement utilisés, les campagnes menées par Kahma (1981); Kahma & Calkoen (1992) ou Donelan et al. (1985, 1992), etc.

Le cas idéal de durée limitée se produit assez rarement dans la nature et est difficile à observer. On pourra se référer à Young (1999) ou Hwang & Wang (2004) pour une description plus détaillée.

Un dernier cas, nommé « fetch oblique », a donné lieu à des études récentes (p.ex. Ardhuin et al., 2007) s'appuyant sur les mesures de la campagne SHOWEX (SHOaling Waves EXperiment). Ce cas correspond à une situation très proche du cas de fetch limité, mais le vent souffle de manière oblique par rapport à la côte.

Ces trois cas seront envisagés dans les diverses simulations proposées dans les chapitres suivants.

#### 1.1.4 Paramètres adimensionnels

L'étude des états de mer utilise la plupart du temps des paramètres adimensionnels, supposés représentatifs de ces cas idéalisés, et ne dépendant pas de l'intensité du vent (Kitaigorodskii, 1962, 1983).

Quatre paramètres adimensionnels principaux peuvent être définis :

- l'énergie adimensionnelle, notée  $\tilde{E}$

$$\tilde{E} = Eg^2/U_a^4 \quad (1.31)$$

où  $U_a$  représente la vitesse du vent et  $E$  est l'énergie totale déterminée à partir du spectre de variance

$$E = \int_0^\infty \int_0^{2\pi} F(f, \theta) df d\theta = \frac{H_{m0}^2}{16} \quad (1.32)$$

- la fréquence de pic adimensionnelle, notée  $\tilde{f}_p$

$$\tilde{f}_p = f_p U_a / g \quad (1.33)$$

- le fetch adimensionnel, notée  $\chi$

$$\chi = Xg/U_a^2 \quad (1.34)$$

- la durée adimensionnelle, notée  $\tau$

$$\tau = tg/U_a \quad (1.35)$$

Le choix de  $U_a$ , souvent discuté (Komen et al., 1984), se porte généralement sur  $U_{10}$ , la vitesse du vent à 10 mètres ou  $u_*$ , la vitesse de frottement.

Ceci nous amène à définir un dernier paramètre adimensionnel, nommé âge des vagues  $C_p/U_a$ , où  $C_p = \omega_p/k_p$  est la vitesse de phase au pic, qui permet de décrire l'état de développement des vagues.

A partir de ces paramètres adimensionnels, on peut formuler les lois de croissance de l'énergie et de la fréquence de pic pour les cas de durée et de fetch limité, de la façon suivante :

$$\tilde{f}_p = f_0 \chi^{-q}; \quad \tilde{f}_p = f'_0 \tau^{-q'} \quad (1.36)$$

$$\tilde{E} = E_0 \chi^p; \quad \tilde{E} = E'_0 \tau^{p'} \quad (1.37)$$

Cet adimensionnement par le vent est aujourd'hui remis en question par certains chercheurs (Badulin et al., 2007), comme nous le verrons au chapitre 4.

### 1.1.5 Formes spectrales classiques

Les campagnes de mesures successives ont permis d'établir des formes analytiques pour le spectre fréquentiel  $E(f)$ . En particulier, deux estimations du spectre fréquentiel dans les hautes fréquences ont été proposées par Phillips (1958) :  $E(f) \propto f^{-5}$ , puis Toba (1973a,b) :  $E(f) \propto f^{-4}$ .

A partir de l'expression de Phillips (1958), la campagne de mesures JONSWAP (Hasselmann et al., 1973) a permis d'établir la forme suivante, pour un spectre fréquentiel dans des conditions de fetch limité :

$$E(f) = \alpha_P g^2 (2\pi)^{-4} f^{-5} \exp\left(-\frac{5}{4} \left(\frac{f}{f_p}\right)^{-4}\right) \gamma^{\exp\left(-\frac{(f-f_p)^2}{2\sigma^2 f_p^2}\right)} \quad (1.38)$$

où  $\alpha_P$  est la constante de Phillips (1958),  $\gamma$  est le facteur d'amplification du pic (on prendra généralement  $\gamma = 3.3$ ),  $\sigma$  correspond à la largeur du pic et prend fréquemment les valeurs suivantes :  $\sigma_A = 0.07$  pour  $f \leq f_p$  et  $\sigma_B = 0.09$  pour  $f > f_p$ .

En prenant  $\gamma = 1$  dans (1.38), on obtient la formulation du spectre dit de Pierson & Moskowitz (1964), qui correspond à un état de mer pleinement développé.

De nombreuses mesures en nature (Kahma, 1981; Kitaigorodskii, 1983; Donelan et al., 1985) ont ensuite appuyé la forme spectrale proposée par Toba (1973a,b). Après ré-analyse des mesures JONSWAP, il a été confirmé qu'une forme en  $f^{-4}$  était mieux adaptée. Donelan et al. (1985) ont alors proposé la formulation suivante :

$$E(f) = \beta g^2 (2\pi)^{-4} f_p^{-1} f^{-4} \exp\left(-\left(\frac{f}{f_p}\right)^{-4}\right) \gamma_d^{\exp\left(-\frac{(f-f_p)^2}{2\sigma^2 f_p^2}\right)} \quad (1.39)$$

En ce qui concerne la distribution directionnelle du spectre  $D(f, \theta)$ , les expressions de Mitsuyasu et al. (1975) ou Hasselmann et al. (1980), couramment utilisées, se basent sur la forme proposée par Longuet-Higgins et al. (1963) :

$$D(f, \theta) = Q(s) \cos^{2s} \left( \frac{\theta - \theta_m(f)}{2} \right) \quad (1.40)$$

$s$  a été paramétrisé par Mitsuyasu et al. (1975) :

$$\begin{cases} s = s_p \left( \frac{f}{f_p} \right)^5 & \text{pour } f < f_p \\ s = s_p \left( \frac{f}{f_p} \right)^{-2.5} & \text{pour } f \geq f_p \end{cases} \quad (1.41)$$

$s_p$  est la valeur de  $s$  à la fréquence de pic :

$$s_p = 11.5 \left( \frac{U_{10}}{C_p} \right)^{-2.5} \quad (1.42)$$

Hasselmann et al. (1980) ont proposé une paramétrisation différente de  $s$  :

$$\begin{cases} s = 6.97 \left( \frac{f}{f_p} \right)^{4.06} & \text{pour } f < 1.05 f_p \\ s = 9.77 \left( \frac{f}{f_p} \right)^\mu & \text{pour } f \geq 1.05 f_p \end{cases} \quad (1.43)$$

où  $\mu$  dépend de l'âge des vagues :

$$\mu = -2.33 - 1.45 \left( \frac{U_{10}}{C_p} - 1.17 \right) \quad (1.44)$$

On peut aussi mentionner l'expression de Donelan et al. (1985) en  $\operatorname{sech}^2 \theta$  et les formulations de Elfouhaily et al. (1997) ou Kudryavtsev et al. (1999).

## 1.2 Equation de transport de la densité d'action des vagues

L'évolution de la densité d'action d'un champ de vagues est donnée par l'équation de conservation suivante dans le cas général, appelée aussi équation cinétique (Gelci et al., 1957; Whitham, 1974) :

$$\frac{\partial N(\mathbf{k})}{\partial t} + \nabla_{x,y} \cdot ((\mathbf{C}_g + \mathbf{U}_c)N(\mathbf{k})) + \frac{\partial C_\theta N(\mathbf{k})}{\partial \theta} + \frac{\partial C_\omega N(\mathbf{k})}{\partial \omega} = \sum_i \frac{S_i(\mathbf{k})}{\omega} \quad (1.45)$$

Cette équation exprime que dans le cas général de vagues se propageant dans un milieu non-homogène et non-permanent, la densité spectrale d'action de l'état de mer est conservée aux termes sources et puits près (représentés par les  $S_i$ ).  $\mathbf{C}_g$  est le vecteur vitesse de groupe  $\mathbf{C}_g = (C_{gx}, C_{gy}) = (C_g \cos(\theta), C_g \sin(\theta))$ ,  $\mathbf{U}_c = (U_{cx}, U_{cy})$  désigne la vitesse du courant,  $C_\theta$  représente le changement de direction de propagation des vagues sous l'effet de la réfraction (due au courant ou à des variations de la profondeur) et  $C_\omega$  les changements de fréquence dus à des variations spatiales et temporelles du niveau marin ou à des variations spatiales du courant.

L'équation d'évolution de la densité d'action d'onde (1.45) peut décrire l'évolution des vagues dans différents domaines :

- le domaine océanique : caractérisé par une grande profondeur d'eau (profondeur relative  $d/\lambda$  supérieure à 0.5 ou  $kd > \pi$ ). Les processus physiques dominants sont alors la génération par le vent, la dissipation par moutonnement et les interactions non-linéaires entre quadruplets de fréquences.
- les mers continentales ou les profondeurs intermédiaires : caractérisées par une profondeur relative  $d/\lambda$  variant entre 0.05 et 0.5 ( $\pi/10 < kd < \pi$ ). En plus des phénomènes précédents, il est nécessaire de prendre en compte le frottement sur le fond, le shoaling (gonflement des vagues avec la remontée des fonds) et les effets de réfraction par la bathymétrie et/ou les courants marins.
- le domaine côtier : qui comprend les zones de faible profondeur ou proches de la côte (profondeur relative  $d/\lambda$  inférieure à 0.05 ou  $kd < \pi/10$ ). Pour ces zones de faible profondeur, il est nécessaire d'inclure les processus physiques de déferlement bathymétrique, interactions non-linéaires entre triplets de fréquences, frottement sur le fond, percolation, interaction avec les végétaux, etc. Par ailleurs, il peut s'avérer utile de prendre en compte les effets liés aux instationnarités du niveau marin et des courants (dues à la marée et/ou aux surcotes-décotes météorologiques).

Dans les cas que nous considérerons par la suite, de simulations en grande profondeur d'eau (domaine océanique), où courant et marée sont supposés négligeables, les grandeurs  $\mathbf{U}_c$ ,  $C_\theta$  et  $C_\omega$  s'annulent. De plus, en eau profonde, les vitesses de propagation  $C_{gx}$  et  $C_{gy}$  sont indépendantes de x et y, et peuvent être sorties des dérivées. L'équation (1.45) se réduit ainsi à :

$$\frac{\partial N(\mathbf{k})}{\partial t} + C_{gx} \frac{\partial N(\mathbf{k})}{\partial x} + C_{gy} \frac{\partial N(\mathbf{k})}{\partial y} = \sum_i \frac{S_i(\mathbf{k})}{\omega} \quad (1.46)$$

que l'on peut exprimer en fonction de  $F(f, \theta)$  :

$$\frac{\partial F(f, \theta)}{\partial t} + C_{gx} \frac{\partial F(f, \theta)}{\partial x} + C_{gy} \frac{\partial F(f, \theta)}{\partial y} = \sum_i S_i(f, \theta) \quad (1.47)$$

qui peut être notée aussi :

$$\frac{dF(f, \theta)}{dt} = \sum_i S_i(f, \theta) = S_{tot} \quad (1.48)$$

où  $S_{tot}$  est le terme source total.

Cette équation est une équation de transport, qui décrit le transport de chaque composante à la vitesse de groupe  $C_g$ , vitesse à laquelle l'énergie des vagues est transportée. Les  $S_i$  sont les termes sources ou puits. Ils représentent les différents processus physiques qui interagissent avec l'état de mer et transforment le spectre des vagues en temps et en espace.

En grande profondeur d'eau, ces processus se réduisent à un système de trois fonctions  $S_{in}$ ,  $S_{diss}$  et  $S_{nl}$  qui génèrent, dissipent et redistribuent l'énergie des vagues au sein du spectre :

$$\sum_i S_i(f, \theta) = S_{in}(f, \theta) + S_{diss}(f, \theta) + S_{nl}(f, \theta) \quad (1.49)$$

où  $S_{in}$  représente la génération des vagues par le vent,  $S_{diss}$  la dissipation d'énergie par moutonnement et  $S_{nl}$  les interactions non-linéaires entre quadruplets de fréquences.

Notons au passage que les variables  $E$ ,  $F$  et  $N$  ainsi que les termes sources  $S_i$  dépendent également de  $x$ ,  $y$  et  $t$ , mais, pour des raisons pratiques et conventionnelles, ces variables sont omises dans nos notations. Ainsi, par exemple, au lieu de  $F(f, \theta, x, y, t)$  on écrit  $F(f, \theta)$ .

Les modèles spectraux d'état de mer (par exemple WAM, WAVEWATCH III, SWAN, TOMAWAC, CREST) résolvent l'équation d'évolution en espace et en temps de la densité d'action (1.45) (ou de variance) de l'état de mer sous une des formes proposées ci-dessus. Les termes de forçage ou d'interaction et leurs formulations utilisées dans les modèles vont maintenant être détaillés.

### 1.2.1 Génération des vagues par le vent $S_{in}$

L'action du vent sur la surface et les apports d'énergie qu'elle constitue sont observables par tout un chacun. Les transferts d'énergie et de quantité de mouvement de l'air à l'eau s'effectuent au travers de forces de pression et de tensions de cisaillement qui contraignent la surface de l'océan. Ces mécanismes sont assez complexes et beaucoup d'incertitudes persistent quand à la quantification des processus qui permettent le transfert d'énergie entre le vent et les vagues. Ainsi, malgré les efforts de la communauté scientifique pour

obtenir des modèles assez fiables, le terme de vent  $S_{in}$  reste encore assez mal connu. Il est basé sur des formulations empiriques qui dépendent beaucoup des conditions de mesure et d'observation et les modèles proposés donnent des résultats assez dispersés.

Deux types de mécanismes peuvent être distingués pour décrire ces transferts d'énergie. Le premier, introduit par Phillips (1957, 1958), est basé sur une croissance linéaire des vagues au cours du temps. Dans ce modèle, le champ de pression atmosphérique turbulent à l'interface air-mer induit une résonance avec les ondes de surface. Ce mécanisme est particulièrement adapté à la description des premiers stades de génération de l'onde de surface, mais il ne peut expliquer la phase principale de croissance des vagues.

Le second mécanisme, mis en évidence par Miles (1957), tient compte des processus de rétroaction entre la croissance des vagues dans l'eau et la couche limite atmosphérique. En présence de vagues, l'écoulement et la pression de l'air sont modifiés et la vitesse du vent près de la surface peut être diminuée ou augmentée. Ce modèle donne une croissance exponentielle des vagues en temps. La théorie de Miles (1957) a été notamment étendue par Janssen (1989, 1991) et est aujourd'hui connue sous le nom de théorie quasi-linéaire de génération des vagues.

Ainsi, la croissance des vagues due aux apports du vent est souvent décrite par la somme d'un terme de croissance linéaire et exponentiel :

$$S_{in}(f, \theta) = \alpha(f, \theta) + \omega\beta(f, \theta)F(f, \theta) \quad (1.50)$$

Le terme de croissance linéaire domine initialement, puis le terme exponentiel devient rapidement prépondérant à son tour. Dans les modèles opérationnels, le mécanisme de croissance linéaire de Phillips (1957, 1958) est bien souvent ignoré, ou seulement utilisé pour initier la croissance des vagues.

Pour une description plus complète des processus de génération de vagues par le vent, on pourra se référer aux livres de Komen et al. (1994), Young (1999) ou Holthuijsen (2007).

Nous nous appuierons dans cette thèse sur les paramétrisations de Snyder et al. (1981), Yan (1987) et Janssen (1989, 1991). Ces trois expressions sont basées sur une formulation linéaire ou quasi-linéaire en fonction du spectre directionnel de variance :

$$S_{in}(f, \theta) = \omega\beta(f, \theta)F(f, \theta) \quad (1.51)$$

Le terme de croissance linéaire de Phillips (1957) sera parfois omis, il est alors nécessaire de donner une condition initiale non nulle à l'état de mer. Dans d'autres cas, nous utiliserons le terme de croissance linéaire de Cavaleri & Malanotte-Rizzoli (1981), proposé par Tolman (1992) sous la forme :

$$\alpha(f, \theta) = 1.5 \cdot 10^{-3} g^{-2} \{u_* \max[0, \cos(\theta - \theta_u)]\}^4 \exp\left[-\left(\frac{f}{f_{PM}}\right)^{-4}\right] \quad (1.52)$$

où  $f_{PM}$  est une fréquence de pic de type Pierson-Moskowitz (Pierson & Moskowitz, 1964), définie par :

$$f_{PM} = \frac{1}{2\pi} \frac{g}{28u_*} \quad (1.53)$$

Le modèle de Snyder et al. (1981) a été modifié par Komen et al. (1984) pour prendre en compte la vitesse de frottement  $u_*$  au lieu de la vitesse du vent à 5 mètres. Cette expression est couramment employée dans les modèles spectraux d'état de mer et correspond à la formulation de  $S_{in}$  préconisée dans la version 3 du code WAM (WAMDI Group, 1988). Dans ce modèle, le taux de croissance  $\beta(f)$  est une fonction linéaire du ratio de la vitesse de frottement  $u_*$  sur la vitesse de phase  $C_{ph} = \omega/k$  :

$$\beta(f, \theta) = \max \left[ 0; 0.25 \frac{\rho_a}{\rho_w} \right] \left( 28 \frac{u_*}{C_{ph}} \cos(\theta - \theta_u) - 1 \right) \quad (1.54)$$

où  $\rho_a$  et  $\rho_w$  sont les masses volumiques de l'air et de l'eau,  $\theta_u$  est la direction locale du vent. La vitesse de frottement est liée à la vitesse du vent à 10 mètres  $U_{10}$  par la relation :

$$u_* = \sqrt{C_D} U_{10} \quad (1.55)$$

où le coefficient de trainée  $C_D$  est considéré comme étant une fonction linéaire de la vitesse du vent (WAMDI Group, 1988) :

$$C_D = \begin{cases} 6.5 \cdot 10^{-5} U_{10} + 8 \cdot 10^{-4} & \text{si } U_{10} > 7.5 \text{ m} \cdot \text{s}^{-1} \\ 1.2875 \cdot 10^{-3} & \text{si } U_{10} < 7.5 \text{ m} \cdot \text{s}^{-1} \end{cases} \quad (1.56)$$

Cette expression a été proposée sur la base des mesures de Snyder et al. (1981), qui ont été confirmées par les résultats expérimentaux de Hasselmann & Bösenberg (1991), mais ne couvrent néanmoins que des vents et des hauteurs de vagues assez faibles et ne sont valables que pour des vagues de fréquence proche du pic spectral. En terme d'âge des vagues inverse, ce modèle s'applique dans l'intervalle  $1 < U_{10}/C_{ph} < 3$ , qui correspond à des forçages assez faibles.

Dans le cas de forçages plus importants, une dépendance de  $S_{in}$  en  $(u_*/C_{ph})^2$  a été proposée à la suite d'expériences en laboratoire et de mesures en nature (e.g. Plant, 1982; Hsiao & Shemdin, 1983). Le modèle de Yan (1987) est une combinaison de termes en  $u_*/C_{ph}$  et en  $(u_*/C_{ph})^2$ , il est valable dans un domaine de fréquences et de valeurs du vent plus étendu :

$$\beta(f, \theta) = D \left( \frac{u_*}{C_{ph}} \right)^2 \cos(\theta - \theta_u) + H \frac{u_*}{C_{ph}} \cos(\theta - \theta_u) + K \cos(\theta - \theta_u) + L \quad (1.57)$$

Nous utiliserons les coefficients proposés par Van der Westhuysen et al. (2007) :  $D = 4.0 \cdot 10^{-2}$ ,  $H = 5.52 \cdot 10^{-3}$ ,  $K = 5.2 \cdot 10^{-5}$  et  $L = -3.02 \cdot 10^{-4}$ . L'expression de Yan (1987) pouvant prendre des valeurs négatives pour des vagues allant plus vite que le vent, nous avons choisi de poser dans ce cas  $\beta(f, \theta) = 0$  pour éviter d'avoir une croissance négative.

La paramétrisation de Janssen (1989, 1991) est celle du code WAM-Cycle 4. C'est une formulation plus complexe qui utilise un certain nombre de paramètres pour représenter l'interaction entre les vagues et la couche limite atmosphérique :

$$\beta(f, \theta) = \Gamma \frac{\rho_a}{\rho_w} \left\{ \left[ \frac{u_*}{C_{ph}} + z_\alpha \right] \max [\cos(\theta - \theta_u); 0] \right\}^2 \quad (1.58)$$

où

$$\Gamma = \frac{\Gamma_m}{\kappa^2} \mu \ln^4 \mu$$

$z_\alpha$ ,  $\Gamma_m$  sont des constantes :  $z_\alpha = 0.011$  (WAM-Cycle-4),  $\Gamma_m = 1.2$ , fixé par Janssen (1991),  $\kappa = 0.41$  est la constante de Von Karman et  $z_0$  la longueur de rugosité.

La hauteur critique adimensionnelle  $\mu$  est déterminée par :

$$\mu = \min \left[ \frac{g z_0}{C_{ph}^2} \exp \left( \frac{\kappa}{[u_*/C_{ph} + z_\alpha] \cos(\theta - \theta_u)} \right); 1 \right]$$

La spécificité du modèle de Janssen (1989, 1991) réside dans la méthode utilisée pour calculer la vitesse de frottement  $u_*$  et la longueur de rugosité  $z_0$ , en résolvant le système d'équations suivant à l'aide d'une méthode itérative de Newton-Raphson :

$$U_{10} = \frac{u_*}{\kappa} \ln \left( \frac{10 + z_0 + \tilde{z}_0}{z_0} \right) \approx \frac{u_*}{\kappa} \ln \left( \frac{10}{z_0} \right) \quad (1.59a)$$

$$z_0 = \frac{\tilde{z}_0}{\sqrt{1 - \tau_w/\tau_s}} \quad (1.59b)$$

$$\tilde{z}_0 = \alpha \frac{u_*^2}{g} \quad (1.59c)$$

$$u_* = \sqrt{\tau_s/\rho_a} \quad (1.59d)$$

où  $\alpha$  est la constante de Charnock (valeur par défaut  $\alpha = 0.01$ ),  $\tau_s$  la contrainte de surface et  $\tau_w$  la contrainte des vagues, obtenue par la relation :

$$\tau_w = \left| \int \int \rho_w \omega S_{in}(f, \theta) (\cos \theta, \sin \theta) df d\theta \right| \quad (1.60)$$

La valeur initiale de la vitesse de frottement utilisée dans l'algorithme itératif est obtenue en considérant un coefficient de trainée constant dans (1.55) :

$$C_D = 1.2875 \cdot 10^{-3}$$

### 1.2.2 Dissipation par moutonnement $S_{diss}$

Le terme de dissipation  $S_{diss}$ , appelé dissipation par moutonnement ou « whitecapping », correspond aux pertes d'énergie lorsque les vagues déferlent en grande profondeur d'eau. Ce phénomène est peut-être le moins bien compris des mécanismes présents en eau profonde ; les différentes expressions proposées pour le modéliser reposent sur des formulations empiriques.

La plupart des paramétrisations de  $S_{diss}$  utilisées dans les modèles d'état de mer sont basées sur la formulation quasi-linéaire du mécanisme de moutonnement de Hasselmann (1974), implémentée dans un grand nombre de modèles sous la forme proposée par Komen et al. (1984) :

$$S_{diss}(f, \theta) = -\frac{C_{diss}}{g^p} \bar{\omega}^{2p+1} m_0^{p/2} \left[ (1 - \delta) \left( \frac{\omega}{\bar{\omega}} \right)^2 + \delta \left( \frac{\omega}{\bar{\omega}} \right)^4 \right] F(f, \theta) \quad (1.61)$$

où  $\bar{\omega}$  est la pulsation intrinsèque moyenne définie par :

$$\bar{\omega} = m_0 \left( \int_0^{+\infty} \int_{-\pi}^{\pi} \omega^{-1} F(f, \theta) df d\theta \right)^{-1}$$

L'exposant  $p = 4$  est généralement utilisé dans (1.61) (WAM-cycle 3 et 4). Les valeurs des paramètres  $C_{diss}$  et  $\delta$  que nous emploierons sont les suivantes :

- $C_{diss} = 2.6$  et  $\delta = 0$  : WAM-Cycle 3 (WAMDI Group, 1988)
- $C_{diss} = 4.5$  et  $\delta = 0.5$  : WAM-Cycle 4 (Günther et al., 1992; Komen et al., 1994)

$S_{diss}$  dépend de la cambrure moyenne des vagues  $\bar{\omega}\sqrt{m_0}/g$  à la puissance  $p$ . Des études récentes (Zakharov et al., 2007; Korotkevich et al., 2008) ont proposé des valeurs plus importantes pour  $p (> 10)$ . Selon Zakharov et al. (2007), les modèles WAM-Cycle 3 et WAM-Cycle 4 surestiment le terme de dissipation  $S_{diss}$  ; ils suggèrent en conséquence d'utiliser les paramètres suivants :  $C_{diss} = 0.11$ ,  $\delta = 0$  et  $p = 12$ .

D'autres formulations du terme de dissipation par moutonnement ont été proposées par Alves (2000); Alves & Banner (2003) et plus récemment Van der Westhuysen et al. (2007); Ardhuin et al. (2008, 2009). Ces modèles, appelés « saturation-based models », proposent des formes de  $S_{diss}$  dans lesquelles la probabilité de déferlement dépend d'un seuil de saturation, noté  $B_r$ .

Le modèle de Van der Westhuysen et al. (2007) s'écrit :

$$S_{diss}(f, \theta) = -C'_{diss} \left( \frac{B(k)}{B_r} \right)^{p_0/2} g^{1/2} k^{1/2} F(f, \theta) \quad (1.62)$$

où

$$B(k) = \frac{1}{2\pi} \int_0^{2\pi} C_g k^3 F(f, \theta) d\theta = C_g k^3 \frac{E(f)}{2\pi}$$

et

$$p_0(u_*/C) = 3 + \tanh \left[ w \left( \frac{u_*}{C} - 0.1 \right) \right]$$

La valeur  $w = 25$  est utilisée ici.

$C'_{diss} = 5.0 \cdot 10^{-5}$ ,  $B_r = 1.75 \cdot 10^{-3}$  sont des paramètres calibrés par Van der Westhuysen et al. (2007) pour des simulations dans un cas de fetch limité utilisant la méthode DIA pour le calcul des interactions non-linéaires (cf. chapitre 2).

Nous avons choisi d'implémenter ce modèle sous la forme proposée par Van der Westhuysen (2008), qui combine les termes de Komen et al. (1984) (noté ici  $S^K_{diss}$ ) avec les paramètres  $C_{diss} = 3.29$  et  $\delta = 0$  et de Van der Westhuysen et al. (2007) (noté  $S^W_{diss}$ ) de la façon suivante :

$$S_{diss}(f, \theta) = f_{br}(f) S^W_{diss} + (1 - f_{br}(f)) S^K_{diss} \quad (1.63)$$

avec

$$f_{br} = \frac{1}{2} + \frac{1}{2} \tanh \left\{ 10 \left[ \left( \frac{B(k)}{B_r} \right)^{1/2} - 1 \right] \right\}$$

Pour une description des problématiques liées à la modélisation de la dissipation en eau profonde et des récents progrès dans ce domaine, se référer à l'article du groupe WISE (Cavaleri et al., 2007).

### 1.2.3 Transferts non-linéaires $S_{nl}$

En eau profonde, les quadruplets de vagues interagissent par résonance. Ces interactions vague-vague redistribuent l'énergie sur le spectre. Cette redistribution est dite « conservatrice » : l'énergie peut être ajoutée ou ôtée à des composants, mais il n'y a pas de perte ni de gain d'énergie sur la totalité du spectre. Nous verrons par la suite que dans le cas d'un domaine fréquentiel fini, les interactions non-linéaires peuvent transférer de l'énergie en dehors du domaine considéré. On constate alors une diminution de l'énergie totale (sur le domaine fréquentiel considéré) (Pushkarev & Zakharov, 2000).

L'expression exacte du terme de transfert non-linéaire  $S_{nl}$  a été établie indépendamment par Hasselmann (1962) et Zakharov (1968). Ils ont montré qu'en grande et moyenne profondeur d'eau les interactions dominantes sont du troisième ordre et résonantes. Elles s'effectuent entre quadruplets de composantes spectrales. Le modèle théorique décrivant ces processus d'interactions entre quadruplets de composantes spectrales s'écrit :

$$\begin{aligned} S_{nl} [N_{\mathbf{k}}] = & \int_{\mathbf{k}_1} \int_{\mathbf{k}_2} \int_{\mathbf{k}_3} G(\mathbf{k}, \mathbf{k}_1, \mathbf{k}_2, \mathbf{k}_3) \{ N_2 N_3 (N + N_1) - N N_1 (N_2 + N_3) \} \\ & \times \delta(\mathbf{k} + \mathbf{k}_1 - \mathbf{k}_2 - \mathbf{k}_3) \delta(\omega + \omega_1 - \omega_2 - \omega_3) d\mathbf{k}_1 d\mathbf{k}_2 d\mathbf{k}_3 \end{aligned} \quad (1.64)$$

On a utilisé la notation  $N_j = N(\mathbf{k}_j)$  pour  $j = 1 \text{ à } 3$ .  $G(\mathbf{k}, \mathbf{k}_1, \mathbf{k}_2, \mathbf{k}_3)$  est un coefficient de couplage très complexe, dont les premières formulations dans le cas de grande profondeur d'eau ont été proposées par (Hasselmann, 1962; Webb, 1978). Herterich & Hasselmann (1980) ont développé une expression de ce coefficient dans le cas de la profondeur finie. Comme l'indiquent les fonctions de Dirac dans (1.64), les transferts s'effectuent au sein de quadruplets de composantes satisfaisant les deux conditions de résonance suivantes :

$$\mathbf{k} + \mathbf{k}_1 = \mathbf{k}_2 + \mathbf{k}_3 \quad (1.65a)$$

$$\omega + \omega_1 = \omega_2 + \omega_3 \quad (1.65b)$$

La prise en compte de ces mécanismes de transferts non-linéaires est déterminante pour simuler correctement l'évolution des spectres d'état de mer en conditions réelles, en particulier dans les cas complexes d'états de mer multiples (superposition de houle et de mer de vent) ou de conditions de forçage instationnaires (Young & Van Vledder, 1993). Une des propriétés remarquables des interactions non-linéaires entre quadruplets de fréquences est leur capacité à stabiliser la forme du spectre, et à lui donner une pente en  $f^{-4}$  dans les hautes fréquences, comme nous le verrons dans les simulations des prochains chapitres.

Le calcul exact du terme de transfert  $S_{nl}$  est très complexe et demande des ressources informatiques considérables en terme de temps CPU, de sorte que les modèles numériques d'état de mer actuels (WAM, WAVEWATCH III, SWAN, TOMAWAC, CREST) utilisent tous des approximations ou des versions simplifiées du modèle complet (1.64). Les différentes méthodes permettant de calculer le terme de transfert non-linéaire seront décrites dans le chapitre 2.

## 1.3 Les modèles spectraux d'état de mer

Les modèles spectraux d'état de mer, qui résolvent l'équation d'évolution du spectre d'énergie des vagues (1.45), sont couramment utilisés pour la prédiction des états de mer car ils permettent de s'affranchir des détails du mouvement des vagues. Trois générations de modèles de vagues se sont succédées, s'appuyant sur des connaissances physiques de plus en plus importantes et sur l'accroissement des capacités informatiques.

### 1.3.1 Modèles de 1ère et 2ème génération

Les premiers modèles spectraux d'état de mer ont été élaborés dans les années 1950 - 1960 (Gelci et al., 1957). Ils s'appuient sur les théories de Miles (1957) et Phillips (1957) pour la génération des vagues par le vent et sur le concept de saturation universelle de Pierson & Moskowitz (1964). Les interactions non-linéaires sont traitées comme un phénomène secondaire et négligées ou paramétrisées très sommairement. Ces modèles sont appelés « modèles de 1ère génération » (1G) (cf. SWAMP Group, 1985).

Dans les années 1970, des mesures plus précises, avec notamment le projet JONSWAP (Hasselmann et al., 1973), ont permis une meilleure connaissance de la physique des vagues et ont montré l'importance des transferts non-linéaires dans la modélisation des états de mer. Les modèles de 2ème génération (2G) apparaissent alors, prenant en compte les premières paramétrisations des interactions non-linéaires vague-vague (e.g. Barnett, 1968; Ewing, 1971; Hasselmann et al., 1976) et comprenant un couplage entre les différentes composantes spectrales. Ces paramétrisations souffrent de certaines limitations ; en particulier elle sont conçues pour des cas idéalisés et ne permettent pas de reproduire les observations dans des situations complexes.

On pourra se référer au SWAMP Group (1985) pour une description des caractéristiques et une classification des modèles de 1ère et 2ème génération.

### 1.3.2 Modèles de 3ème génération

Le développement de la méthode de calcul des interactions non-linéaires DIA (Hasselmann et al., 1985) a marqué le début des modèles de 3ème génération. Dans ces modèles, chaque composante spectro-angulaire du spectre de variance évolue « librement » sous l'action combinée des différents processus physiques pris en compte. Le terme de transfert non-linéaire  $S_{nl}$  n'est plus paramétrisé, mais calculé à partir de l'expression (1.64) de manière plus ou moins approchée (i.e. en considérant un nombre plus ou moins important de configurations vérifiant (1.65)). La méthode DIA permet aux modèles de résoudre l'équation d'évolution (1.45) pour des applications opérationnelles à des coûts de calculs raisonnables, sans imposer de restriction sur la forme du spectre.

Le premier modèle de 3ème génération (3G) est le modèle WAM (WAMDI Group, 1988; Komen et al., 1994), qui a été implémenté pour des applications dans le domaine océanique ou les mers continentales. A la suite de WAM, d'autres modèles comme WAVEWATCH III (Tolman, 1991, 2002), SWAN (Booij et al., 1999) ou TOMAWAC (Benoit et al., 1996a), puis plus récemment le modèle CREST (Ardhuin et al., 2001) ont été développés. Le modèle SWAN (Ris, 1997; Booij et al., 1999) est le premier modèle de 3ème génération conçu spécialement pour les applications côtières, incluant les effets de déferlement bathymétrique et les interactions non-linéaires entre triplets de fréquences. Des développements apportés à la version WAM-Cycle 4 du modèle WAM ont permis d'améliorer son fonctionnement en eau peu profonde (Monbaliu et al., 1999, 2000).

Certains modèles de recherche incluent aujourd'hui des méthodes de calcul quasi-exactes du terme  $S_{nl}$ , comme la méthode WRT (Webb-Resio-Tracy) (Webb, 1978; Resio & Perrie, 1991), ou la méthode GQM (Gaussian Quadrature Method) (Lavrenov, 2001) (voir description dans le chapitre 2). Les temps de calcul de ces méthodes sont encore trop importants pour des applications pratiques à grande échelle. Néanmoins, grâce aux améliorations de ces méthodes et aux outils informatiques de plus en plus puissants, on peut espérer un calcul quasi-exact des interactions non-linéaires dans un avenir proche.

### 1.3.3 Le modèle TOMAWAC

Le logiciel TOMAWAC (acronyme de TELEMAC-based Operational Model Addressing Wave Action Computation) d'EDF R&D, intégré au sein du système TELEMAC, a été développé au Laboratoire National d'hydraulique et Environnement (LNHE) par Michel Benoit et Frédéric Marcos en 1995-1996 (Benoit et al., 1996a,b).

Entre 1996 et 1998, les fonctionnalités de TOMAWAC ont été étendues au domaine côtier, principalement dans le cadre de la thèse de Françoise Becq-Girard (Becq, 1998). La modélisation des processus physiques d'interactions non-linéaires entre triplets de fréquences (« triad interactions ») et de déferlement est alors ajoutée.

TOMAWAC est aujourd'hui un outil utilisé au sein d'EDF pour plusieurs projets, mais également hors EDF par plusieurs universités et bureaux d'études. Récemment, il a permis de construire un Atlas Numérique d'états de mer (Benoit & Lafon, 2004), par simulation rétrospective des 25 dernières années à partir des champs de vent ré-analysés de la base ERA-40 du Centre Européen de Prévision Météorologique (ECMWF).

L'originalité du code TOMAWAC réside dans l'utilisation de maillages non-structurés de type « éléments finis » pour mailler le domaine maritime et côtier, allié à un schéma de propagation basé sur la méthode des caractéristiques (i.e. non-soumis à des conditions de stabilité sur le nombre de Courant).

## 1.4 Aspects numériques

Les simulations entreprises dans le cadre de cette thèse sont réalisées avec un modèle d'état de mer basé sur le code TOMAWAC, simplifié sous certains aspects :

- on se place en grande profondeur d'eau car la méthode de calcul quasi-exacte des interactions non-linéaires que nous utilisons n'est pas étendue au cas de la profondeur finie ;
- on utilise un maillage spatial simplifié pour effectuer :
  1. des simulations en 0 dimension (0D), i.e. comprenant un seul point en espace (homogénéité spatiale) : reproduction de l'évolution temporelle d'un spectre d'état de mer soumis aux termes sources en fonction de la durée d'action du vent, cas de durée limitée par exemple.
  2. des simulations à une dimension d'espace (1D), c'est à dire comprenant  $N$  points selon l'axe des  $x$ , et homogènes selon l'axe des  $y$  : cas de fetch limité ou oblique.

En revanche, plusieurs options ont été ajoutées, et devront être incorporées dans une nouvelle version du modèle d'état de mer TOMAWAC (ce qui sera fait après la thèse) :

- nous avons implémenté de nouvelles méthodes pour la modélisation des termes de génération par le vent, de dissipation et de transfert non-linéaire en eau profonde ;
- la possibilité d'utiliser un pas de temps dynamique pour l'intégration en temps des termes sources est proposée ;
- une nouvelle option a été ajoutée pour le calcul du limiteur de croissance ;

- enfin, il est possible de ne pas imposer de queue diagnostique dans les hautes fréquences du spectre.

### 1.4.1 Discréétisation

La densité spectrale de variance  $F$  est une fonction de 5 variables ( $f, \theta, x, y, t$ ). La discréétisation concerne donc les deux variables spectro-angulaires, mais aussi les variables d'espace et de temps. En ce qui concerne la discréétisation temporelle, nous verrons qu'elle peut s'effectuer à l'aide de pas de temps fixes ou dynamiques (variables au cours du temps) dans la partie suivante.

#### 1.4.1.1 Discréétisation spectro-angulaire

Le spectre directionnel de variance (ou d'action) de l'état de mer est décomposé en un nombre fini de fréquences ( $f$ ) et de directions de propagation des vagues ( $\theta$ ).

Le domaine fréquentiel  $[f_1, f_{max}]$  est discréétisé en considérant une suite de  $NF$  fréquences en progression géométrique :

$$f_n = f_1 q^{n-1} \quad \text{pour } n \text{ allant de 1 à } NF$$

où  $q$  est la raison de la suite géométrique. On a donc  $f_{max} = f_1 q^{NF-1}$ .

Les directions de propagation sont régulièrement réparties sur  $[0, 2\pi]$ , avec une résolution angulaire notée  $\Delta\theta$ . Dans les simulations exposées ci-après, on utilise généralement des résolutions angulaires de  $5^\circ$  à  $10^\circ$ .

#### 1.4.1.2 Discréétisation spatiale

Dans le modèle TOMAWAC, le domaine de calcul spatial (qui peut être cartésien ou sphérique) est discréétisé à l'aide d'un maillage d'éléments finis triangulaires. La taille de la maille peut ainsi être variable sur le domaine spatial, ce qui permet de raffiner le maillage dans certaines zones d'intérêt, en particulier à l'approche des côtes.

Les simulations réalisées dans cette thèse s'appuient sur un maillage simplifié, qui pourra être réduit à un point (0D) ou à  $N$  points selon l'axe des  $x$ , avec une résolution  $\Delta x$ .  $\Delta x$  pourra être choisi fixe ou en progression géométrique :

$$\Delta x_n = \Delta x_1 q^{n-1} \quad \text{pour } n \text{ allant de 1 à } N$$

### 1.4.2 Méthodes numériques

Le logiciel TOMAWAC résout l'équation d'évolution du spectre de variance de l'état de mer (1.47) en deux étapes successives et séparées : l'étape de convection, puis l'étape d'intégration des termes sources.

### 1.4.2.1 Etape de propagation

L'étape de propagation est résolue à l'aide de la méthode des caractéristiques. On résout l'équation sans terme source :

$$\frac{\partial F(f, \theta)}{\partial t} + \mathbf{C}_g \cdot \nabla F(f, \theta) = 0 \quad (1.66)$$

qui est discrétisée de la façon suivante, avec un pas de temps fixe  $\Delta t$  :

$$\frac{F^0 - F^{n-1}}{\Delta t} = (\mathbf{C}_g \cdot \nabla F)^{n-1} \quad (1.67)$$

où  $F^{n-1}$  est le spectre de variance à la date  $t = (n-1)\Delta t$  et  $F^0$  est le spectre obtenu après l'étape de propagation.

La méthode des caractéristiques possède des avantages en terme de temps de calcul. En effet, la remontée des caractéristiques peut n'être effectuée qu'une seule fois, en début de simulation. Il suffit ainsi de stocker les pieds des caractéristiques et de les rappeler à chaque appel de l'étape de convection. L'étape de propagation se limite alors à une opération d'interpolation à chaque pas de temps.

### 1.4.2.2 Etape d'intégration des termes sources

Après l'étape de propagation qui est traitée avec un pas de temps fixe  $\Delta t$ , on obtient un spectre noté  $F^0$ .

On passe alors à l'étape d'intégration des termes sources, dans laquelle on résout l'équation suivante :

$$\frac{\partial F(f, \theta)}{\partial t} = S_{tot} \quad (1.68)$$

à l'aide d'un schéma explicite ou semi-implicite (cf. WAMDI Group, 1988, eqs (4.1) à (4.10)).

Dans le cas d'un schéma explicite, l'équation discrétisée s'écrit :

$$\frac{F^n - F^0}{\Delta t} = S_{tot}^0 \quad (1.69)$$

où  $S_{tot}^0$  est le terme source correspondant au spectre  $F^0$  obtenu après l'étape de propagation.

Dans le cas d'un schéma semi-implicite, on a :

$$\frac{F^n - F^0}{\Delta t} = \frac{S_{tot}^n + S_{tot}^0}{2} \quad (1.70)$$

L'intérêt de l'intégration semi-implicite des termes sources est qu'elle permet d'utiliser des plus grands pas de temps.

L'étape d'intégration des termes sources est effectuée avec un certain nombre de sous-pas de temps  $\Delta t_d^j$ , pour  $j$  allant de 1 à  $m$ , tels que :

$$\sum_{j=1}^m \Delta t_d^j = \Delta t$$

Ces sous-pas de temps  $\Delta t_d^j$  peuvent être fixes ou dynamiques (Tolman, 1992).

Dans le cas de pas de temps dynamiques,  $\Delta t_d^j$  est calculé à chaque itération, de sorte que la variation relative du spectre de variance sous l'effet des termes sources (génération par le vent, dissipation, transferts non-linéaires) pendant un pas de temps reste en dessous d'un seuil  $\varepsilon$  (généralement de 5 à 10 %). Pour tout  $f, \theta$  :

$$\frac{|\Delta F^{j-1}(f, \theta)|}{F^j(f, \theta)} < \varepsilon \quad (1.71)$$

où  $\Delta F^{j-1}$  est la variation du spectre lors de l'intégration du sous-pas de temps  $\Delta t_d^j$  permettant de passer de  $F^{j-1}$  à  $F^j$ , et  $F^j$  est le spectre obtenu après la j-ème intégration.

Dans le cas d'un schéma d'intégration explicite, on écrit tout simplement :

$$\Delta t_d^j = \varepsilon \cdot \min_{f, \theta} \left( \frac{F^j(f, \theta)}{|S_{tot}^{j-1}(f, \theta)|} \right) \quad (1.72)$$

où  $S_{tot}^{j-1}$  est le terme source total :  $S_{tot}^{j-1} = S_{in}^{j-1} + S_{diss}^{j-1} + S_{nl}^{j-1}$  calculé à partir du spectre  $F^{j-1}$  au début du sous-pas de temps  $j$ .

Deux conditions sont ensuite ajoutées :

- le  $\Delta t_d^j$  ainsi calculé ne doit pas être supérieur à  $\Delta t$
- $\Delta t_d^j$  doit aussi vérifier  $\Delta t_d^j \leq 5 \cdot \Delta t_d^{j-1}$ .

Dans le cas où une des conditions ne serait pas respectée, on prend le minimum des trois termes  $\Delta t_d^j$ ,  $\Delta t$  et  $5 \cdot \Delta t_d^{j-1}$ .

L'intégration de  $F$  s'effectue alors, pour tout  $f, \theta$ , par :

$$F^j(f, \theta) = F^{j-1}(f, \theta) + \Delta F^{j-1}(f, \theta) = F^{j-1}(f, \theta) + \Delta t_d^j S_{tot}^{j-1}(f, \theta) \quad (1.73)$$

Dans le cas d'un schéma d'intégration semi-implicite, l'intégration des termes sources est plus complexe. On définit deux nouveaux termes : un terme source total noté  $S'_{tot}$  et un terme source dérivé par rapport à  $F$ , noté  $S'_{der}$  (WAMDI Group, 1988). On a alors :

$$\Delta t_d^j = \varepsilon \cdot \min_{f,\theta} \left( \frac{F^j(f,\theta)}{|S'^{j-1}_{tot}(f,\theta)|} \left( \frac{1}{1 + 0.5\varepsilon S'^{j-1}_{der}(f,\theta) \frac{F^j(f,\theta)}{|S'^{j-1}_{tot}(f,\theta)|}} \right) \right) \quad (1.74)$$

et

$$\begin{aligned} F^j(f,\theta) &= F^{j-1}(f,\theta) + \Delta F^{j-1}(f,\theta) \\ &= F^{j-1}(f,\theta) + \frac{\Delta t_d^j S'^{j-1}_{tot}(f,\theta)}{\max(1 - 0.5\Delta t_d^j S'^{j-1}_{der}(f,\theta), 1)} \end{aligned} \quad (1.75)$$

Pour une formulation précise de  $S'^{j-1}_{tot}$  et  $S'^{j-1}_{der}$ , on se référera au papier du WAMDI Group (1988) ou au livre de Komen et al. (1994) (WAM-Cycle 4).

Notons que si une queue diagnostique est imposée sur la partie hautes fréquences du spectre, le pas de temps dynamique n'est calculé que sur  $[0, f_d]$ .

A la fin de l'étape d'intégration des termes sources, on obtient un spectre  $F^n$ , qui va alors être à nouveau propagé.

#### 1.4.2.3 Limiteur de croissance

Le limiteur de croissance a été introduit dans WAM pour assurer la stabilité numérique du modèle. En particulier, lorsqu'on utilise un pas de temps constant assez grand, il évite une croissance trop rapide de la partie hautes fréquences du spectre, surtout en début de simulation. La variation du spectre de variance doit rester inférieure en valeur absolue à une fraction d'un spectre d'équilibre  $|\Delta F|_{max}$ .

Dans TOMAWAC, le limiteur de croissance implémenté est l'expression de WAM-Cycle 4 (Komen et al., 1994) :

$$|\Delta F|_{max} = 6.4 \cdot 10^{-7} g^2 f^{-5} \frac{\Delta t}{\tau} \quad (1.76)$$

avec  $\tau = 1200$  s.

Dans ces simulations, lorsqu'un limiteur de croissance est nécessaire, on utilisera l'expression proposée par Hersbach & Janssen (1999) et conseillée par Benoit (2006) :

$$|\Delta F|_{max} = 3.0 \cdot 10^{-7} g \max(u_*, g f_{PM}^*/f) f^{-4} f_{51} \Delta t \quad (1.77)$$

où  $f_{PM}^*$  est la fréquence de Pierson-Moskowitz adimensionnelle :  $f_{PM}^* = 5.6 \cdot 10^{-3}$ .

Dans certains cas, le limiteur de croissance pourra être omis (simulations spatialement homogènes avec un pas de temps dynamique).

#### 1.4.2.4 Imposition d'une queue diagnostique

Dans les modèles d'état de mer (e.g. WAM, TOMAWAC), une queue diagnostique (ou paramétrique) en  $f^{-m}$  est généralement imposée sur la partie hautes fréquences du spectre. Cela signifie qu'au-delà d'une fréquence notée  $f_d$  (fréquence diagnostique), le spectre fréquentiel de variance  $E(f)$  est proportionnel à  $f^{-m}$ . La fréquence diagnostique  $f_d$  est définie par (WAMDI Group, 1988) :

$$f_d = \min[f_{max}, \max(4f_{PM}, 2.5\bar{f})] \quad (1.78)$$

où  $f_{PM}$  est la fréquence de Pierson-Moskowitz définie par (1.53), et la fréquence moyenne  $\bar{f}$  est donnée par :

$$\bar{f} = m_0 \left( \int_0^{+\infty} \int_{-\pi}^{\pi} f^{-1} F(f, \theta) df d\theta \right)^{-1} \quad (1.79)$$

Au-dessus de la fréquence  $f_d$ , on impose une distribution directionnelle égale à celle en  $f = f_d$ . Le spectre directionnel vérifie donc :

$$F(f, \theta) = F(f_d, \theta) \left( \frac{f}{f_d} \right)^{-m} \quad (1.80)$$

L'exposant  $m$  est nommé facteur de queue, sa valeur est généralement prise égale à  $m = 4$  (WAMDI Group, 1988) ou 5 (Komen et al., 1984).

Comme nous le verrons par la suite, les résultats des simulations sont très sensibles à l'imposition d'une paramétrisation de  $F(f, \theta)$  dans les hautes fréquences, et au choix du facteur  $m$ . Néanmoins, dans certains cas, il est nécessaire d'imposer un queue diagnostique pour compenser les défauts des modèles de génération par le vent  $S_{in}$  et de dissipation  $S_{diss}$  dans les hautes fréquences du spectre.

Lorsque la paramétrisation de  $F(f, \theta)$  au-dessus de  $f = f_d$  n'est pas indispensable, on impose alors uniquement  $E(f) \propto f^{-m}$  au-dessus de la dernière fréquence de discréétisation  $f_{max}$ , afin de prendre en compte les effets des interactions non-linéaires avec les fréquences situées au-delà du domaine de discréétisation. Ceci n'affecte que très peu les résultats, et ne joue que sur les quelques dernières fréquences du domaine de discréétisation, quelque soit le facteur  $m$  choisi.

## Chapitre 2

# The nonlinear four-wave interactions

### 2.1 Introduction

The theoretical formulation of nonlinear third order wave-wave interactions developed by Hasselmann (1962) and Zakharov (1968) has been available for more than 40 years and its physical background is well established, in contrast to the external forcing terms. The integral, also known as the Boltzmann integral for wind waves or the collision integral, is written :

$$S_{nl}[N_{\mathbf{k}}] = \int_{\mathbf{k}_1} \int_{\mathbf{k}_2} \int_{\mathbf{k}_3} G(\mathbf{k}, \mathbf{k}_1, \mathbf{k}_2, \mathbf{k}_3) \{N_2 N_3 (N + N_1) - N N_1 (N_2 + N_3)\} \times \delta(\mathbf{k} + \mathbf{k}_1 - \mathbf{k}_2 - \mathbf{k}_3) \delta(\omega + \omega_1 - \omega_2 - \omega_3) d\mathbf{k}_1 d\mathbf{k}_2 d\mathbf{k}_3 \quad (2.1)$$

This theoretical model shows that quadruplets of spectral components satisfying the resonance conditions

$$\mathbf{k} + \mathbf{k}_1 = \mathbf{k}_2 + \mathbf{k}_3 \quad (2.2a)$$

$$\omega + \omega_1 = \omega_2 + \omega_3 \quad (2.2b)$$

can transfer energy to each other. The expression (2.1) is a six-fold integral cubic in wave spectrum involving two Dirac- $\delta$  functions and a very complex coupling coefficient  $G$ , which makes its exact evaluation rather difficult and very time consuming. Therefore, the computation of a full solution of this equation is not feasible for many problems of wave spectra modeling, especially for real applications of wave forecasting (typically 1000 to 10000 sea points). Due to the algorithmic complexity and the required amount of CPU time, the methods computing exact solutions of the  $S_{nl}$  equation have been only operated on schematic or simplified cases, while operational wave prediction models use approximate methods.

The fundamental role of nonlinear wave-wave interactions in the evolution of the wave spectrum is now widely accepted (see for instance the review of Young & Van Vledder,

1993). As this role has become clear, large research efforts have been undertaken in order to improve the modeling of these nonlinear transfers and develop efficient algorithms. In the last years, considerable progress has been made in decreasing the computational time of exact (or quasi-exact) methods. Benoit (2005) compared several possible improvements or alternative techniques to obtain higher accuracy in the evaluation of the Boltzmann integral while keeping acceptable CPU time. A review of these methods can be also found in the state of the art of Cavaleri et al. (2007).

The structure of this study is as follows : Section 2.2 presents the different methods for computing the nonlinear transfer term. Section 2.3 describes in detail the GQM method.

## 2.2 Different methods for computing the $S_{nl}$ term

In this section, the different methods for computing the nonlinear wave-wave interactions are briefly reviewed. We first introduce exact methods (subsection 2.2.1), and then approximate methods currently used in 3G operational wave models (subsection 2.2.2). Finally, we show that another way to calculate the nonlinear wave-wave interactions with a high degree of precision is to use quasi-exact methods, also called Reduced Exact Methods (REM) (Benoit, 2005). We put these methods into a specific category (subsection 2.2.3) since they are derived from exact methods and their accuracy can be controlled.

### 2.2.1 The exact methods

Precise computational techniques which permit ‘exact’ evaluation of (2.1) have been proposed less than 20 years after this model was established. All the exact methods use a reduction of the six-fold integration to a three-fold one by removing the Dirac- $\delta$  functions in the integrand. This transformation and the numerical integration of the obtained three-dimensional integral can be performed using different techniques. For example, the pair of wave numbers considered at the highest level varies between the methods. A brief review of the main contributions allows to identify four main approaches :

- Hasselmann & Hasselmann (1981, 1985) developed the EXACT-NL code based on a symmetric integration technique using the property of detailed balance<sup>1</sup> to reduce computational time.
- Webb (1978) proposed an alternative way of solving (2.1) by introducing a line-integral along a locus. This technique was used and extended by Tracy & Resio (1982), further by Resio & Perrie (1991) and more recently by Van Vledder (2006). It is often referred as the WRT (Webb-Resio-Tracy) method.
- Masuda (1980) used a local analytical integration scheme to deal with singularities which arise during the manipulation of (2.1). This approach was further developed by Komatsu & Masuda (1996) (RIAM method) and recently extended to the finite water depth case by Hashimoto et al. (1998) or adapted by Polnikov (1997).

---

1. The property of detailed balance states that the absolute value of the rate of change of the action density is equal for all the wave numbers within a resonant quadruplet.

- Lavrenov (2001, 2003b) introduced an efficient numerical integration method able to deal with the singularities by using adapted Gaussian cubature techniques. This method is now referred as GQM (Gaussian Quadrature Method).

The manipulation of the six-dimensional integral (2.1) for the case of the GQM method is described in the next section.

As already mentioned, these methods are two computationally expensive to be directly applied to operational wave forecasting models, which must therefore rely on simplified or approximate methods.

## 2.2.2 The approximate methods

### 2.2.2.1 The DIA method

The most known simplified method is the Discrete Interaction Approximation (DIA) of Hasselmann et al. (1985). It is by far the most used technique and is implemented in all the spectral models of wind-wave forecasting. The DIA method is based on the idea of dramatically reducing the number of configurations of interacting quadruplets by only considering a particular combination of wave components and its mirror image. In this particular quadruplet configuration, two of the wave numbers are equal ( $\mathbf{k} = \mathbf{k}_1$ ), which leads immediately to  $\omega = \omega_1$ . The two other frequencies  $\omega_2$  and  $\omega_3$  are expressed as a function of  $\omega$  by introducing a parameter  $\lambda$  :

$$\begin{aligned}\omega_2 &= (1 + \lambda) \omega = \omega^+ \\ \omega_3 &= (1 - \lambda) \omega = \omega^-\end{aligned}$$

The value  $\lambda = 0.25$  (Hasselmann et al., 1985) is used in WAM (WAMDI Group, 1988; Komen et al., 1994). The other wave numbers  $\mathbf{k}_2$  and  $\mathbf{k}_3$  must also fulfill the resonance condition (2.2a).

Within this configuration, the contributions of the three (different) wave numbers to the nonlinear transfer of this quadruplet configuration ( $\delta S_{nl}$ ,  $\delta S_{nl}^+$ ,  $\delta S_{nl}^-$ ) are given by :

$$\begin{bmatrix} \delta S_{nl} \\ \delta S_{nl}^+ \\ \delta S_{nl}^- \end{bmatrix} = \begin{bmatrix} -2 \\ 1 \\ 1 \end{bmatrix} C_{DIA} g^{-4} f^{11} \left( F^2 \left( \frac{F^+}{(1+\lambda)^4} + \frac{F^-}{(1-\lambda)^4} \right) - 2F \frac{F^+ F^-}{(1-\lambda^2)^4} \right)$$

where  $C_{DIA}$  is a constant equal to  $3 \cdot 10^7$  and  $F$ ,  $F^+$ ,  $F^-$  are the energy densities at the interacting wave numbers.

It is possible to build two symmetrical resonant quadruplets with regard to the direction of  $\mathbf{k} = \mathbf{k}_1$ . The first configuration is called the ‘standard’ configuration and the second one is called ‘image’. Thus, in this method, each frequency interacts with only two quadruplets : the standard configuration and its image. The number of configurations considered is then equal to twice the number of points of the frequency-direction grid, which means that it is reduced by three orders of magnitude compared to the full solution.

Despite the drastic reduction of the number of configurations, DIA preserves some important characteristics of the exact solution (2.1) as the peak frequency downshift, the formation of a  $f^{-4}$  high frequency tail or the existence of self-similar solutions of the conservative<sup>2</sup> balance equation (see next chapter). Nevertheless, it suffers from a number of limitations (e.g. Van Vledder et al., 2000), especially when trying to model unsteady conditions or complex sea states. Moreover, deficiencies of DIA are often masked by the tuning of the other source terms.

The DIA method has been extended to finite water depth by Herterich & Hasselmann (1980).

There have been various attempts to improve the original DIA. A number of other approximate methods have been suggested to compute the collision integral with a higher accuracy than DIA, keeping an acceptable CPU time. Among the other simplified schemes which may be used in wave models, four main approaches can be distinguished (see Benoit, 2005, for a description of some of these methods).

### 2.2.2.2 The extensions of DIA

First, extensions of DIA (e.g. Van Vledder et al., 2000; Hashimoto & Kawaguchi, 2001) allow to overcome some of the shortcomings of DIA, but still remain very approximate evaluations of (2.1) (see Van Vledder, 2001, for a general description of such extensions). The principle of these extensions is to consider more quadruplets in order to have a more accurate estimate for  $S_{nl}$ . These techniques can work quite well in some cases but they are not applicable in a general way and their accuracy cannot be controlled since they are developed for particular sets of test spectra (Cavaleri et al., 2007).

Among these extensions, the Multiple Discrete Interaction Approximation (MDIA) proposed by Tolman (2004) is performed in recent versions of 3G wave models and is based on the superposition of 4 quadruplet configurations.

### 2.2.2.3 Diffusion-type methods

The second approach is based on the use of diffusion-type operators, as first introduced by Hasselmann et al. (1985) and more recently proposed by Zakharov & Pushkarev (1999), Jenkins & Phillips (2001), Polnikov & Farina (2002) and Pushkarev et al. (2004). The principle is to use a second-order diffusion operator applied to a function of the wave spectrum. This technique is computationally efficient and is able to reproduce the main features of (2.1). However, it does not appear as a suitable alternative since it does not give a very accurate representation of  $S_{nl}$  in the general case (Benoit, 2005).

---

2. ‘Conservative’ means that there is no input from wind or dissipation. The total source term  $S_{tot}$  only includes nonlinear transfers.

#### 2.2.2.4 Neural networks

The third approach, still in development, is based on neural networks (Tolman et al., 2005) (see also the recent paper of Wahle et al., 2009).

#### 2.2.2.5 The Two-Scale Approximation

Finally, a very recent approach, named two-scale approximation (TSA) and introduced by Resio & Perrie (2008), could also be promising, but further investigations are needed.

The TSA method is based on a decomposition of a given directional wave spectrum into a parametric spectrum  $\hat{n}_i$  (e.g. of JONSWAP type) and a residual (non-parametric) component  $n'_i$ . With this decomposition, the nonlinear interaction term results from the contribution of so-called ‘broad scale’ interactions (interactions among  $\hat{n}_i$  components), ‘local-scale’ interactions (interactions among  $n'_i$  components) and ‘cross-interactions’ (interactions between  $\hat{n}_i$  and  $n'_i$  components). Considering the relative importance of the components resulting from the decomposition of the spectrum, most of the terms representing either the local-scale interactions or the cross-interactions are discarded by Resio & Perrie (2008). The efficiency of the method relies of the fact that the broad-scale interaction term (interactions among  $\hat{n}_i$  components) only involves the parametric component of the spectrum and can therefore be computed in advance by using the quasi-exact WRT method and then stored in memory. This broad-scale contribution is evaluated from the set of parameters describing the parametric component of the spectrum. Thus the TSA technique provide precise evaluations of the non-linear interaction term when the wave spectrum is close to a parametric form (Resio & Perrie, 2008; Perrie & Resio, 2009). However the performance and capabilities of the method on real spectra remain to be confirmed, in particular for complex sea-states such as bi- and tri-modal spectra (with various relative importance of the peaks of the components), directional skewed spectra, and parametric spectral and directional shapes that depart significantly from the set of spectra considered for pre-computing the broad-scale interaction component.

### 2.2.3 A solution for a high precision and a reduced CPU time : the ‘quasi-exact’ methods

An optimal technique might be found by using so-called ‘quasi-exact’ methods. The principle of these methods is to start from a potentially ‘exact’ method (i.e. one method from section 2.2.1) and to optimize it using a coarser resolution and/or a reduced integration range and eliminating some configurations that have a small contribution to the integral.

Note that the methods called ‘exact’ in the above subsection are never totally exact since the numerical integration of (2.1) uses a discretized grid with a finite number of points. The term ‘exact’ means that the solution converges toward the ‘true’ value when the resolution is increased. In this sense, a ‘quasi-exact’ method is just an exact method with a smaller number of integration points.

All the exact methods mentioned above can thus be simplified in quasi-exact methods. The optimization of the WRT or GQM algorithm seems a promising direction to investigate (Benoit, 2005). Such a simplification was already suggested by Lin & Perrie (1998) who tried to simplify the ‘exact’ WRT method by reducing the number of configurations. Van Vledder (2006) describes some methods allowing to speed-up the WRT algorithm (optimization of the number of integration points, filtering, use of symmetry conditions, more efficient interpolation or integration method, etc.). Similarly, the GQM method (Lavrenov, 2001) can also be used with a lower number of points in the quadrature formula for integration, plus some filtering to discard configurations which have negligible or minor contributions to the integral.

In this work, we selected the integration technique proposed by Lavrenov (2001) as a starting point and try to improve its efficiency, since this method seems to be a good candidate for further optimizations and an eventual implementation in 3G wave models (Benoit, 2005).

## 2.3 The GQM method

The GQM method is based on the use of Gaussian quadratures to deal with the singularities that appears in the course of the manipulation of the Boltzmann integral. This is what fundamentally differentiates this method from other exact integration techniques.

In this section, we detail the various steps of the transformation and integration of (2.1). Some precisions about the optimization of the method and the chosen resolution are given along with some comparisons with other methods (efficiency, CPU time).

### 2.3.1 Transformation of the non-linear transfer term into a suitable form for numerical integration

In this subsection, the expression (2.1) is transformed into a form suitable for numerical integration. This transformation is performed in four successive steps, which are described below.

#### 2.3.1.1 Step 1 : elimination of the wave-number Dirac function

The first step is the elimination of the Dirac- $\delta$  function on the wave-number vectors and the corresponding integral over  $\mathbf{k}_3$ , by imposing from the resonance condition (2.2a) :

$$\mathbf{k}_3 = \mathbf{k} + \mathbf{k}_1 - \mathbf{k}_2 \quad (2.3)$$

The expression (2.1) is thus reduced to a four-fold integral including only one Dirac- $\delta$  function :

$$S_{nl}[N_{\mathbf{k}}] = \int_{\mathbf{k}_1} \int_{\mathbf{k}_2} G \{ N_2 N_3 (N + N_1) - N N_1 (N_2 + N_3) \} \delta(\omega + \omega_1 - \omega_2 - \omega_3) d\mathbf{k}_1 d\mathbf{k}_2 \quad (2.4)$$

It is important to recall that in the above expression (and the rest of this section)  $\mathbf{k}_3$  is given by (2.3) and the corresponding intrinsic frequency  $\omega_3$  results from :

$$\omega_3 = \omega(\mathbf{k}_3) = \omega(\mathbf{k} + \mathbf{k}_1 - \mathbf{k}_2) \quad (2.5)$$

### 2.3.1.2 Step 2 : change of variables for the wave spectrum

The second step consists in a change of variables from  $\mathbf{k}$  to  $(\omega, \theta)$ . Equation (2.4), expressed in terms of the action spectrum  $N_{\mathbf{k}}$ , is reformulated for the case of the variance spectrum  $F(\omega, \theta)$  using the following correspondences :

$$N(\mathbf{k}) d\mathbf{k} = \frac{F(\omega, \theta)}{\omega} d\omega d\theta \quad \text{and} \quad d\mathbf{k} = \frac{\mathbf{k}}{C_g} d\omega d\theta \quad (2.6)$$

In the present work, deep water conditions are considered. Under this assumption, the dispersion equation (1.9) can be applied and equation 2.6 simplifies to :

$$N(\mathbf{k}) d\mathbf{k} = \frac{g^2}{2\omega^4} F(\omega, \theta) \quad \text{and} \quad d\mathbf{k} = \frac{2\omega^3}{g^2} d\omega d\theta \quad (2.7)$$

Inserting these relationships into (2.4) results in :

$$S_{nl}[F] = \int_{\omega_1} \int_{\theta_1} \int_{\omega_2} \int_{\theta_2} \frac{G}{\omega_1 \omega_2 \omega_3^4} \{ F_2 F_3 (F \omega_1^4 + F_1 \omega^4) - F F_1 (F_2 \omega_3^4 + F_3 \omega_2^4) \} \times \delta(W) d\omega_1 d\theta_1 d\omega_2 d\theta_2 \quad (2.8)$$

where  $F_j$  stands for  $F(\omega_j, \theta_j)$  ( $j = 0$  to  $3$ ) and the argument of the frequency Dirac- $\delta$  function is noted  $W = \omega + \omega_1 - \omega_2 - \omega_3$ .

### 2.3.1.3 Step 3 : elimination of the frequency Dirac function

The third step is to integrate over the direction  $\theta_2$  and to eliminate the frequency Dirac- $\delta$  function. However, some complications arise due to the fact that the argument  $W$  of this

Dirac- $\delta$  function depends upon the variable  $\theta_2$  and this step needs special attention. The following notations are introduced :

$$\mathbf{k}_a = \mathbf{k} + \mathbf{k}_1 = \mathbf{k}_2 + \mathbf{k}_3 \quad (2.9a)$$

$$gk_a = g \|\mathbf{k} + \mathbf{k}_1\| = \sqrt{\omega^4 + \omega_1^4 + 2\omega^2\omega_1^2 \cos(\theta_1 - \theta)} = g \|\mathbf{k}_2 + \mathbf{k}_3\| \quad (2.9b)$$

$$\omega_a = \omega + \omega_1 = \omega_2 + \omega_3 \quad (2.9c)$$

It is worth noting that, in the general case,  $\omega_a \neq \omega(\mathbf{k}_a) = \sqrt{gk_a}$ . The non-dimensional parameter  $\varepsilon_a$ , defined hereafter, offers a quantitative measure of this difference :

$$\varepsilon_a = 2 \frac{gk_a}{\omega_a^2} = 2 \left( \frac{\omega(\mathbf{k}_a)}{\omega_a} \right)^2 = 2 \left( \frac{\omega(\mathbf{k} + \mathbf{k}_1)}{\omega + \omega_1} \right)^2 = 2 \left( \frac{\omega(\mathbf{k} + \mathbf{k}_1)}{\omega(\mathbf{k}) + \omega(\mathbf{k}_1)} \right)^2 \quad (2.10)$$

Due to the dispersion relationship, it is straightforward to show that  $0 < \varepsilon_a \leq 2$ . Direction  $\theta_a$  of vector  $\mathbf{k}_a$  is computed from its two components and uniquely defined by :

$$\theta_a = \arctan \left[ \frac{\omega^2 \sin \theta + \omega_1^2 \sin \theta_1}{\omega^2 \cos \theta + \omega_1^2 \cos \theta_1} \right] \quad (2.11)$$

With these notations, argument  $W$  of the frequency Dirac function is rewritten as :

$$W = \omega_a - \omega_2 - \omega_3 = \omega_a - \omega_2 - \sqrt{g \|\mathbf{k}_a - \mathbf{k}_2\|} \quad (2.12)$$

which leads to :

$$W = \omega_a - \omega_2 - \sqrt[4]{g^2(k_a^2 + k_2^2 - 2k_a k_2 \cos(\theta_a - \theta_2))} \quad (2.13)$$

We recall that the last term of this expression is the intrinsic frequency  $\omega_3$  from (2.5). The following property of the Dirac function is then used :

$$\int_x \delta[f(x)] dx = \left| \frac{\partial f}{\partial x} \right|_{f(x)=0}^{-1} \quad (2.14)$$

This property is applied to  $\delta(W)$  in (2.8) to remove the frequency Dirac- $\delta$  function by integrating over  $\theta_2$  :

$$S_{nl}[F] = \int_{\omega_1} \int_{\theta_1} \int_{\omega_2} \sum_{\theta_2} \frac{1}{S} \frac{G}{\omega_1 \omega_2 \omega_3^4} \{ F_2 F_3 (F \omega_1^4 + F_1 \omega^4) - F F_1 (F_2 \omega_3^4 + F_3 \omega_2^4) \} d\omega_1 d\theta_1 d\omega_2 \quad (2.15)$$

with :

$$S = \left| \frac{\partial W}{\partial \theta_2} \right|_{W(\theta_2)=0} = \frac{gk_a \omega_2^2}{2\omega_3^2} |\sin(\theta_a - \theta_2)| = \frac{gk_a \omega_2^2}{2\omega_3^2} \sqrt{1 - \cos^2(\theta_a - \theta_2)} \quad (2.16)$$

for the values of  $\theta_2$  satisfying  $W(\theta_2) = 0$  in (2.13).

The formula (2.15) consists of a three-fold integral without any Dirac- $\delta$  function, which seems to be simpler to solve. However, denominator  $S$  can be equal to zero, giving raise to singularities in the evaluation of the integral term. In (2.15), the integral on  $\omega_1$  runs from 0 to  $+\infty$  and the integral on  $\theta_1$  runs from 0 to  $2\pi$ . The integral on  $\omega_2$  also theoretically runs from 0 to  $+\infty$ . However, due to the resonance conditions (2.2), the actual range of integration is much shorter, as shown in §2.2.2.2.

#### 2.3.1.4 Step 4 : final expression of the non-linear transfer term

The fourth step is to express the variables  $(\omega_3, \theta_3)$  and  $\theta_2$  appearing in (2.15) and (2.16) in terms of the spectral components of interest  $(\omega, \theta)$  and the remaining variables used for integration  $(\omega_1, \theta_1)$  and  $\omega_2$ . We alternatively use the variables  $\omega_a$ ,  $k_a$ ,  $\varepsilon_a$  and  $\theta_a$  which are fully determined by the components  $(\omega, \theta)$  and  $(\omega_1, \theta_1)$ .

From (2.9c),  $\omega_3$  is easily obtained as  $\omega_3 = \omega_a - \omega_2$ .

The direction  $\theta_2$  is calculated from (2.9a), which is further manipulated to give :

$$k_3^2 = \|\mathbf{k}_2 - \mathbf{k}_a\|^2 \quad (2.17)$$

$$\omega_3^4 = (gk_a)^2 + \omega_2^4 - 2gk_a\omega_2^2 \cos(\theta_a - \theta_2) \quad (2.18)$$

For  $k_a > 0$  :

$$\cos(\theta_2 - \theta_a) = \frac{(gk_a)^2 + \omega_2^4 - (\omega_a - \omega_2)^4}{2gk_a\omega_2^2} \quad (2.19)$$

from which, we get :

$$\theta_2^\pm = \theta_a \pm \arccos \left[ \frac{(gk_a)^2 + \omega_2^4 - (\omega_a - \omega_2)^4}{2gk_a\omega_2^2} \right] \quad (2.20)$$

The sign  $\pm$  indicates that there exists two directions  $\theta_2$  satisfying the condition  $W(\theta_2) = 0$  (resonance condition) for a given value of the triplet  $(k_a, \omega_a, \omega_2)$  and that they are symmetric with respect to the direction  $\theta_a$ . The corresponding directions  $\theta_3$  can be calculated in the same manner, resulting in :

$$\theta_3^\pm = \theta_a \pm \arccos \left[ \frac{(gk_a)^2 + (\omega_a - \omega_2)^4 - \omega_2^4}{2gk_a(\omega_a - \omega_2)^2} \right] \quad (2.21)$$

or alternatively in :

$$\theta_3 = \arctan \left[ \frac{gk_a \sin \theta_a - \omega_2^2 \sin \theta_2}{gk_a \cos \theta_a - \omega_2^2 \cos \theta_2} \right] \quad (2.22)$$

Substitution of (2.19) in (2.16) and some algebraic manipulations yield the following expression of the  $S$  term :

$$S = \frac{1}{2\omega_3^3} \sqrt{\omega_a \left[ (gk_a + \omega_3^2)^2 - \omega_2^4 \right]} \sqrt{\omega_2 - \frac{\omega_a}{2} + \frac{gk_a}{\omega_a}} \sqrt{\left( \omega_2 - \frac{\omega_a}{2} \right)^2 - \left( \frac{gk_a}{2} - \frac{\omega_a^2}{4} \right)} \quad (2.23)$$

This expression is further transformed into a non-dimensional form, function of only two non-dimensional variables  $\varepsilon_a$  (see (2.10)) and  $w_2 = \omega_2/\omega_a$  :

$$\frac{\omega_3^3}{\omega_a^4} S = \sqrt{\tilde{B}_0(\varepsilon_a, w_2) \tilde{B}_1(\varepsilon_a, w_2) \tilde{B}_2(\varepsilon_a, w_2)} \quad (2.24a)$$

with :

$$\tilde{B}_0(\varepsilon_a, w_2) = \left[ \frac{1}{2} \left( 1 + \frac{\varepsilon_a}{2} \right) - w_2 \right] \left[ \left( w_2 - \frac{1}{2} \right)^2 + \frac{1}{4} (1 + \varepsilon_a) \right] \quad (2.24b)$$

$$\tilde{B}_1(\varepsilon_a, w_2) = w_2 - \frac{1}{2} \left( 1 - \frac{\varepsilon_a}{2} \right) \quad (2.24c)$$

$$\tilde{B}_2(\varepsilon_a, w_2) = \left[ \left( w_2 - \frac{1}{2} \right)^2 - \frac{1}{4} (\varepsilon_a - 1) \right] \quad (2.24d)$$

The behavior and properties of the terms composing the denominator  $S$  are discussed in the next section, in particular regarding the values of  $\omega_2$  which may cause singularities for  $S$ . Finally, symmetry conditions between wave components 2 and 3 are used to restrict the range of integration on  $\omega_2$  to  $\omega_2 \leq \omega_3$ , which corresponds to  $\omega_2 \leq \omega_a/2$ , or  $w_2 \leq 0.5$ . The non-linear term is thus multiplied by a factor 2 to compensate for this reduction in the integration space.

The final expression obtained for the non-linear transfer rate is written :

$$S_{nl}[F] = \sum_{\theta_2^\pm} \int_{\omega_1=0}^{+\infty} \int_{\theta_1=0}^{2\pi} \int_{\omega_2=0}^{\omega_a/2} 2 \frac{\omega_a^4 G}{\omega_1 \omega_2 \omega_3} \frac{F_2 F_3 (F \omega_1^4 + F_1 \omega^4) - F F_1 (F_2 \omega_3^4 + F_3 \omega_2^4)}{\sqrt{\tilde{B}_0(\varepsilon_a, w_2) \tilde{B}_1(\varepsilon_a, w_2) \tilde{B}_2(\varepsilon_a, w_2)}} d\omega_1 d\theta_1 d\omega_2 \quad (2.25)$$

In the above expression, the  $\sum$  symbol means that two values of the direction  $\theta_2$  need to be considered (see (2.20)).

### 2.3.2 The various steps of integration : use of Gaussian quadrature formulas

The denominator of (2.25) is a function of the two non-dimensional variables  $\varepsilon_a$  and  $w_2$  and can be equal to zero for values of  $\varepsilon_a$ ,  $w_2$ , which causes some difficulties to integrate numerically. The particularity of the GQM method, which makes it an optimal algorithm of integration, is the use of quadratures adapted to these singularities (Lavrenov, 2001).

#### 2.3.2.1 Gaussian quadrature formulas

A quadrature is an approximation of an integral as a weighted sum of the integrand at a number of specified points within the domain of integration :

$$\int_a^b W(x)f(x)dx \approx \sum_{i=0}^n w_i f(x_i) \quad (2.26)$$

where  $W$  is a weighting function. The location of the abscissas  $x_i$  at which the function is evaluated are not necessarily equally spaced.

The particularity of Gaussian quadrature formulas is that they provide an exact result for polynomial  $f(x)$  of order  $2n - 1$  or less by a suitable choice of the points  $x_i$  and weights  $w_i$  for  $i = 1$  to  $n$ . The weighting function  $W$  can be chosen to remove integrable singularities from the desired integral. This means that if an integrand can be written as a product of a polynomial and a known function  $W$ , it can be integrated numerically in an exact way.

Some of the most common Gaussian quadrature schemes are (see Press et al., 1992, for concise description of these formulas and associated algorithm of computation) :

- Gauss-Legendre quadrature :  $W(x) = 1$ , the integration range is  $[-1, 1]$ . The abscissas  $x_i$  are the roots of the Legendre polynomial  $P_n(x)$  of degree  $n$  and the weights  $w_i$  are given by :

$$w_i = \frac{2}{(1 - x_i^2) [P'_n(x_i)]^2} \quad (2.27)$$

- Gauss-Chebyshev quadrature :  $W(x) = 1/\sqrt{1-x^2}$ , the integration range is  $] -1, 1[$ . The  $x_i$  are the roots of the Chebyshev polynomial of degree  $n$ . The analytical values of abscissas and weights are :

$$x_i = \cos\left(\frac{\pi(i-1/2)}{n}\right) \quad \text{and} \quad w_i = \frac{\pi}{n} \quad (2.28)$$

- Other schemes include Gauss-Laguerre ( $W(x) = x^\alpha e^{-x}$ ), Gauss-Hermite ( $W(x) = e^{-x^2}$ ), or Gauss-Jacobi ( $W(x) = (1-x)^\alpha(1-x)^\beta$ ) quadrature formulas. The Gauss-Chebyshev quadrature is a particular case of the Gauss-Jacobi quadrature for  $\alpha = \beta = -1/2$ .

The particular choice of quadrature formula (Gauss-Legendre, Gauss-Chebyshev, etc.) depends on the form of the integrand and especially on the type of singularities.

The advantage of the use of Gaussian quadratures is that the integration can be very accurate with only a small number of integration points.

### 2.3.2.2 Analysis of denominator $S$ and determination of the integration range for the first integration over $\omega_2$

The first integration is performed over the non-dimensional variable  $w_2$ , using a simple change of variable from  $\omega_2$  to  $\omega_2/\omega_a$ . The first step is to determine the integration bounds, i.e. the possible values of  $w_2$  depending on the values of  $\varepsilon_a$ . The formulation of  $S$  in (2.16) shows that  $S$  is zero if  $\cos(\theta_2 - \theta_a) = \pm 1$ . Expression (2.19) can be put into non-dimensional form :

$$\cos(\theta_2 - \theta_a) = \frac{\frac{1}{4}\varepsilon_a^2 + w_2^4 - w_3^4}{\varepsilon_a w_2^2}$$

with  $w_3 = \omega_3/\omega_a$ . Condition (2.9c) leads to  $w_2 + w_3 = 1$ , and gives :

$$\cos(\theta_2 - \theta_a) = \frac{\frac{1}{4}\varepsilon_a^2 + w_2^4 - (1 - w_2)^4}{\varepsilon_a w_2^2} \quad (2.29)$$

This expression only depends on  $\varepsilon_a$  and  $w_2$  for  $k_a > 0$  ( $\varepsilon_a > 0$ ). Therefore, condition  $-1 \leq \cos(\theta_2 - \theta_a) \leq 1$  determines the possible values of  $w_2$  for a given  $\varepsilon_a$  :

- From  $\cos(\theta_2 - \theta_a) \geq -1$ , we get  $(w_2^2 + \frac{1}{2}\varepsilon_a)^2 \geq (1 - w_2)^4$ , which leads directly to  $w_2 \geq \frac{1}{2}(1 - \frac{\varepsilon_a}{2})$ . It gives us the minimum value of  $w_2$ , included in the range  $[0, 0.5]$ , and denoted :

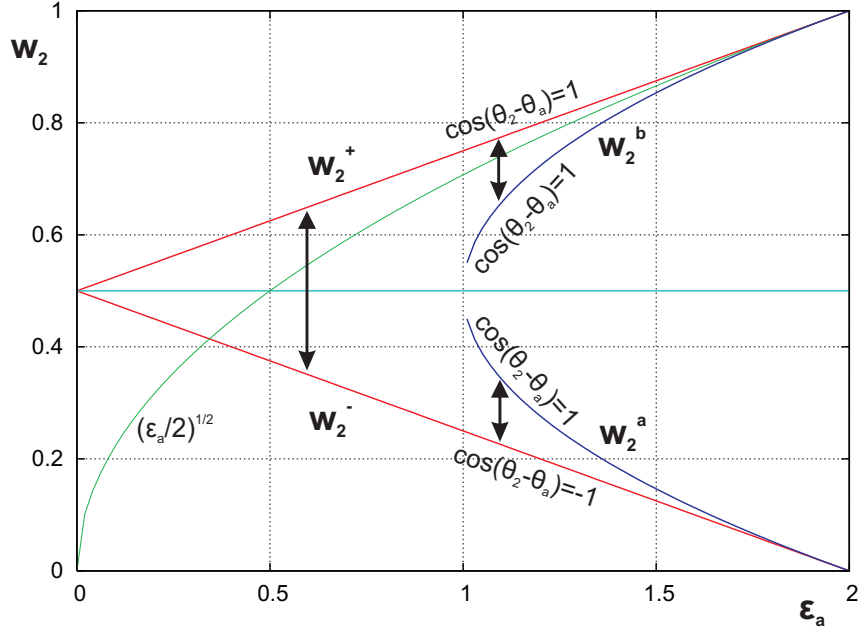
$$w_2^- = \frac{1}{2} \left(1 - \frac{\varepsilon_a}{2}\right) \quad (2.30)$$

- Condition  $\cos(\theta_2 - \theta_a) \leq 1$  gives  $(w_2^2 - \frac{1}{2}\varepsilon_a)^2 \leq (1 - w_2)^4$ . In this case the result is somewhat more tricky.
  - If  $w_2^2 - \frac{1}{2}\varepsilon_a \leq 0$  ( $\Leftrightarrow w_2 \leq \sqrt{\frac{\varepsilon_a}{2}}$ ), we obtain  $(w_2 - \frac{1}{2})^2 \leq \frac{1}{4}(\varepsilon_a - 1)$ . If  $\varepsilon_a \leq 1$ , this condition is always verified. If  $\varepsilon_a > 1$ , it gives  $|w_2 - \frac{1}{2}| \leq \frac{1}{2}\sqrt{\varepsilon_a - 1} \Leftrightarrow w_2 \leq \frac{1}{2}(1 - \sqrt{\varepsilon_a - 1})$  or  $w_2 \geq \frac{1}{2}(1 + \sqrt{\varepsilon_a - 1})$ . Two other limiting values are thus defined in the case  $\varepsilon_a > 1$  :

$$w_2^a = \frac{1}{2} \left(1 - \sqrt{\varepsilon_a - 1}\right) \quad (2.31)$$

$$w_2^b = \frac{1}{2} \left(1 + \sqrt{\varepsilon_a - 1}\right) \quad (2.32)$$

- If  $w_2^2 - \frac{1}{2}\varepsilon_a \geq 0$  ( $\Leftrightarrow w_2 \geq \sqrt{\frac{\varepsilon_a}{2}}$ ), we obtain  $w_2 \leq \frac{1}{2}(1 + \frac{\varepsilon_a}{2})$  and the maximum value of  $w_2$ , included in the interval  $[0.5, 1]$  (given that  $0 < \varepsilon_a \leq 2$ ), is :

FIGURE 2.1 – Integration bounds of  $w_2$  versus  $\varepsilon_a$ .

$$w_2^+ = \frac{1}{2} \left( 1 + \frac{\varepsilon_a}{2} \right) \quad (2.33)$$

Figure 2.1 represents the integration range of  $w_2$  as a function of  $\varepsilon_a$ . The last condition to be added is  $w_2 \leq 0.5$  (or  $\omega_2 \leq \omega_a/2$ ).

Term by term analysis of  $S$  shows :

- Term  $\tilde{B}_0$  cannot be equal to zero in the integration range  $w_2 \leq 0.5$ , unless  $k_a$  is zero.
- Term  $\tilde{B}_1$  is equal to zero for  $w_2 = w_2^- = \frac{1}{2} \left( 1 - \frac{\varepsilon_a}{2} \right)$ .
- If  $\varepsilon_a < 1$ ,  $\tilde{B}_2$  is strictly positive. If  $\varepsilon_a \geq 1$ ,  $\tilde{B}_2$  can be written

$$\tilde{B}_2 = (w_2 - \frac{1}{2} \left( 1 - \sqrt{\varepsilon_a - 1} \right))(w_2 - \frac{1}{2} \left( 1 + \sqrt{\varepsilon_a - 1} \right)) = (w_2 - w_2^a)(w_2 - w_2^b)$$

and vanishes only once in the domain  $w_2 \leq 0.5$  : at  $w_2 = w_2^a$ .

The shape of  $1/\sqrt{\tilde{B}_0(\varepsilon_a, w_2)\tilde{B}_1(\varepsilon_a, w_2)\tilde{B}_2(\varepsilon_a, w_2)}$  is illustrated in Figure 2.2 for the three cases  $\varepsilon_a < 1$ ,  $\varepsilon_a = 1$  and  $\varepsilon_a = 1$ .

To summarize, we have :

- In the case  $\varepsilon_a < 1$ , the integration range is :

$$w_2^- = \frac{1}{2} \left( 1 - \frac{\varepsilon_a}{2} \right) \leq w_2 \leq 0.5 \quad (2.34)$$

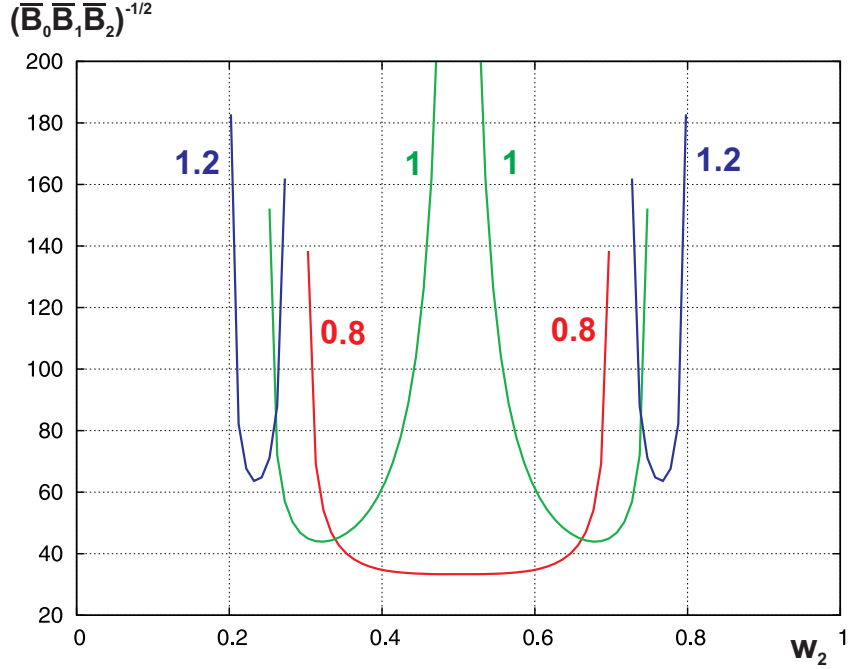


FIGURE 2.2 – Factor  $1/\sqrt{\tilde{B}_0(\varepsilon_a, w_2)\tilde{B}_1(\varepsilon_a, w_2)\tilde{B}_2(\varepsilon_a, w_2)}$  versus  $w_2 = \omega_2/\omega_a$  for three values of  $\varepsilon_a$  : 0.8, 1, 1.2.

and there is only one singularity at the lower bound  $w_2 = w_2^-$ .

- In the case  $\varepsilon_a \geq 1$ , the integration range is :

$$w_2^- = \frac{1}{2} \left( 1 - \frac{\varepsilon_a}{2} \right) \leq w_2 \leq w_2^a = \frac{1}{2} \left( 1 - \sqrt{\varepsilon_a - 1} \right) \quad (2.35)$$

and there are two singularities at  $w_2 = w_2^-$  and  $w_2 = w_2^a$ .

The integration over  $w_2$  is computed with Gauss-Legendre or Gauss-Chebyshev quadrature, depending on the value of  $\varepsilon_a$ , and thus on the number and type of singularities.

In the case  $\varepsilon_a < 1$ , there is one singularity in the integrand. The integral over  $w_2$  can be expressed under the form :

$$I_1(\omega_1, \theta_1) = \int_{w_2^-}^{1/2} \frac{f_1(w_2, \omega_1, \theta_1)}{\sqrt{\omega_2 - w_2^-}} dw_2 \quad (2.36)$$

where  $f_1$  has no singularity in the interval  $[w_2^-, 0.5]$ . Before applying the Gauss-Legendre quadrature formula, the integral needs to be transformed, eliminating the singularity in the integrand with the following change of variable :

$$z = \sqrt{w_2 - w_2^-} \quad \text{and} \quad dz = \frac{1}{2\sqrt{w_2 - w_2^-}} dw_2$$

which gives

$$I_1(\omega_1, \theta_1) = \int_0^{\sqrt{1/2 - w_2^-}} 2f_1(w_2^- + z^2, \omega_1, \theta_1) dz \quad (2.37)$$

Then, the integral (2.37) must be changed into an integral over  $[-1, 1]$ , using the change of variable :

$$z = \frac{\sqrt{1/2 - w_2^-}}{2} + \frac{\sqrt{1/2 - w_2^-}}{2} u \quad \text{and} \quad dz = \frac{\sqrt{1/2 - w_2^-}}{2} du$$

$$I_1(\omega_1, \theta_1) = \sqrt{1/2 - w_2^-} \int_{-1}^{+1} f_1 \left( w_2^- + \sqrt{1/2 - w_2^-} \left( \frac{1+u}{2} \right)^2, \omega_1, \theta_1 \right) du \quad (2.38)$$

The integral  $I_1$  can be evaluated by :

$$I_1(\omega_1, \theta_1) \approx \sqrt{1/2 - w_2^-} \sum_{i=1}^n W_i f_1 \left( w_2^- + \sqrt{1/2 - w_2^-} \left( \frac{1+x_i}{2} \right)^2, \omega_1, \theta_1 \right) \quad (2.39)$$

Weights  $W_i$  and abscissas  $x_i$  are given by the Gauss-Legendre quadrature formula (2.27).

In the case  $\varepsilon_a \geq 1$ , there are two singularities in the integrand for  $w_2 = w_2^-$  and  $w_2 = w_2^a$ . The integral over  $w_2$  can be expressed under the form :

$$I_2(\omega_1, \theta_1) = \int_{w_2^-}^{w_2^a} \frac{f_2(w_2, \omega_1, \theta_1)}{\sqrt{(w_2 - w_2^-)(w_2^a - w_2)}} dw_2 \quad (2.40)$$

where  $f_2$  has no singularity in the interval  $[w_2^-, w_2^a]$ . The integral  $I_2$  is transformed into an integral over  $[-1, 1]$ , using a similar change of variable :

$$w_2 = \frac{w_2^- + w_2^a}{2} + \frac{w_2^a - w_2^-}{2} u \quad \text{and} \quad dw_2 = \frac{w_2^a - w_2^-}{2} du$$

which gives

$$I_2(\omega_1, \theta_1) = \int_{-1}^{+1} \frac{f_2\left(\frac{\omega_2^- + w_2^a}{2} + \frac{w_2^a - \omega_2^-}{2}u, \omega_1, \theta_1\right)}{\sqrt{1-u^2}} du \quad (2.41)$$

The weighting function of the Gauss-Chebyshev quadrature formula is easy to identify, and the integral can be approximated by :

$$I_2(\omega_1, \theta_1) \approx \frac{\pi}{n} \sum_{i=1}^n f_2\left(\frac{\omega_2^- + w_2^a}{2} + \frac{w_2^a - \omega_2^-}{2} \cos\left(\frac{\pi(i-1/2)}{n}\right), \omega_1, \theta_1\right) \quad (2.42)$$

using the analytical expressions of  $W_i$  and  $x_i$  (2.28). The number of points  $n$  sufficient to obtain a good accuracy is determined in §2.3.3.1.

### 2.3.2.3 Integration over $\theta_1$

Function  $I(\omega_1, \theta_1)$  (equal to  $I_1(\omega_1, \theta_1)$ , eq. (2.39) or  $I_2(\omega_1, \theta_1)$ , eq. (2.42)) is then integrated over  $\theta_1$  :

$$J(\omega_1) = \int_{-\pi}^{\pi} I(\omega_1, \theta_1) d\theta_1 \quad (2.43)$$

Lavrenov (2001) notes that  $I(\omega_1, \theta_1)$  presents a singularity for  $\varepsilon_a = 1$  and proposes, this time again, to use a Gaussian quadrature formula to perform the integration. He suggests to transform the integral, multiplying and dividing the integrand by  $D = \sqrt{|\varepsilon_a^2 - 1|}$ .

Factor  $D$  can be developed using expressions (2.10) and  $k_a^2 = k^2 + k_1^2 + 2k + k_1 \cos(\theta - \theta_1)$  :

$$D = \sqrt{|\varepsilon_a^2 - 1|} = \frac{1}{\omega_a^2} \sqrt{|4g^2(k^2 + k_1^2 + 2k + k_1 \cos(\theta - \theta_1)) - \omega_a^4|} \quad (2.44)$$

which gives, using (2.9c) :

$$D = \frac{2\sqrt{2}\omega\omega_1}{\omega_a^2} \sqrt{\left|\cos(\theta - \theta_1) - \frac{(\omega + \omega_1)^4 - 4(\omega^4 + \omega_1^4)}{8\omega^2\omega_1^2}\right|} \quad (2.45)$$

We set :

$$A = \frac{(\omega + \omega_1)^4 - 4(\omega^4 + \omega_1^4)}{8\omega^2\omega_1^2} \quad (2.46)$$

Integral  $J(\omega_1)$  is then written :

$$\begin{aligned} J(\omega_1) &= \int_{-\pi}^{\pi} \left\{ I(\omega_1, \theta_1) \sqrt{|\varepsilon_a^2 - 1|} \right\} \frac{1}{\sqrt{|\varepsilon_a^2 - 1|}} d\theta_1 \\ &= \int_{-\pi}^{\pi} \frac{\tilde{I}(\omega_1, \theta_1)}{\sqrt{|\cos(\theta - \theta_1) - A|}} d\theta_1 \end{aligned} \quad (2.47)$$

where  $\tilde{I}(\omega_1, \theta_1) = I(\omega_1, \theta_1) \sqrt{|\cos(\theta - \theta_1) - A|}$ .

The change of variable :

$$x = \cos(\theta - \theta_1) \quad \text{and} \quad dx = \sin(\theta - \theta_1) d\theta_1$$

gives :

$$\begin{aligned} \text{If } \theta - \theta_1 \in [-\pi, 0], \quad \theta_1^+ &= \theta + \arccos(x) \quad \text{and} \quad d\theta_1 = \frac{1}{\sqrt{1-x^2}} dx \\ \text{If } \theta - \theta_1 \in [0, \pi], \quad \theta_1^- &= \theta - \arccos(x) \quad \text{and} \quad d\theta_1 = -\frac{1}{\sqrt{1-x^2}} dx \end{aligned}$$

Using the periodicity of function  $I$ , this leads to :

$$\begin{aligned} J(\omega_1) &= \int_{-1}^1 \frac{\tilde{I}(\omega_1, \theta_1^+)}{\sqrt{1-x^2} \sqrt{|x-A|}} dx + \int_1^{-1} -\frac{\tilde{I}(\omega_1, \theta_1^-)}{\sqrt{1-x^2} \sqrt{|x-A|}} dx \\ &= \sum_{\theta_1^\pm} \int_{-1}^1 \frac{\tilde{I}(\omega_1, \theta_1^\pm)}{\sqrt{1-x^2} \sqrt{|x-A|}} dx \end{aligned} \quad (2.48)$$

Function  $A(\omega, \omega_1)$  can be expressed as a function of a single variable  $u = \omega_1/\omega$  :

$$A(u) = \frac{(1+u)^4 - 4(1+u^4)}{8u^2} \quad (2.49)$$

and has the following properties :

- $\forall u, A(u) \leq 1$
- $A(u) = 1 \Leftrightarrow u = 1$
- $A(u) = -1 \Leftrightarrow u = 1/3$  or  $u = 3$
- $A$  has a bell shape, increasing up to  $u = 1$ , and then decreasing.

In the range  $\frac{1}{3} < \frac{\omega_1}{\omega} < 3$ , where  $A \in ]-1, 1[$ , the integrand has a singularity in  $A$ . The integration range can be divided into two parts :

$$\begin{aligned} J(\omega_1) &= \sum_{\theta_1^\pm} \int_{-1}^A \left[ \frac{\tilde{I}(\omega_1, \theta_1^\pm)}{\sqrt{1-x}} \right] \frac{1}{\sqrt{(1+x)(A-x)}} dx \\ &\quad + \int_A^1 \left[ \frac{\tilde{I}(\omega_1, \theta_1^\pm)}{\sqrt{1+x}} \right] \frac{1}{\sqrt{(1-x)(x-A)}} dx \end{aligned} \quad (2.50)$$

$$J(\omega_1) = \sum_{\theta_1^\pm} \{J_A(\omega_1) + J_B(\omega_1)\} \quad (2.51)$$

$J_A$  and  $J_B$  possess two singularities and can be integrated numerically using the Gauss-Chebyshev quadrature formula after a simple change of variable :

$$\begin{aligned} x &= \frac{A-1}{2} + \frac{A+1}{2}z \quad \text{for } J_A \\ x &= \frac{A+1}{2} + \frac{1-A}{2}z \quad \text{for } J_B \end{aligned}$$

In the domain  $\frac{\omega_1}{\omega} < \frac{1}{3}$  or  $\frac{\omega_1}{\omega} > 3$ ,  $A(u) \leq -1$  and the Gauss-Chebyshev quadrature formula can be used directly :

$$\begin{aligned} J(\omega_1) &= \int_{-1}^1 \frac{\tilde{I}(\omega_1, \theta \pm \arccos(x))}{\sqrt{x-A}} \frac{1}{\sqrt{1-x^2}} dx \\ &= \frac{\pi}{n} \sum_{i=1}^n \frac{\tilde{I}\left(\omega_1, \theta \pm \frac{\pi(i-1/2)}{n}\right)}{\sqrt{\cos\left(\frac{\pi(i-1/2)}{n}\right) - A}} \end{aligned} \quad (2.52)$$

Integration could also be performed with a simple rectangle method, which gives a very accurate estimate of the integral, but a larger number of points is then necessary to integrate precisely.

#### 2.3.2.4 Integration over $\omega_1$

The last integration is performed over the non-dimensional variable  $\omega_1/\omega$ . Function  $J(\omega_1)$  is rather smooth. According to Lavrenov (2001),  $J(\omega_1)$  can be approximated by :

- $J(\omega_1) \propto \omega_1^{-6}$  for large values of  $\omega_1$  ;
- $J(\omega_1) \propto \omega_1^{15-25}$  for small values of  $\omega_1$ .

Taking into account the behavior of  $J(\omega_1)$  in the high and low frequencies, a reduction of the integration range to  $\frac{1}{3} < \frac{\omega_1}{\omega} < 3$  is used to optimize the integration.

Two options have been considered for this integration :

- the use of the Gauss-Legendre quadrature formula,
- a simple trapezoidal method with selected values of  $\omega_1/\omega$ .

Comparisons show no advantage of using Gaussian quadratures for this integration (for a given number of points). At the end, we thus used trapezoidal integration with values of  $\omega_1/\omega$  carefully chosen to give the best evaluation of the nonlinear term in the more general case.

More details about resolution of the three integrations and errors are given in the next subsection.

### 2.3.3 Optimization of the method

#### 2.3.3.1 Different resolutions of the GQM method

We performed simulations with different resolutions of the method, i.e. different numbers of points for the numerical integration, to study the properties and the robustness of our algorithm. Many resolution were tested to see the influence of the number of points considered for each integration and three were selected after a series of numerical experiments (Benoit & Gagnaire-Renou, 2007) :

- a so-called ‘fine’ resolution with 26 points for the integration on  $\omega_1$  (noted  $NF_1$ ), 16 points for the integration on  $\theta_1$  (noted  $NT_1$ ) and 12 points on  $\omega_2$  (noted  $NF_2$ ) ;
- a ‘medium’ resolution with  $NF_1 = 14$  points,  $NT_1 = 8$  and  $NF_2 = 8$  ;
- a ‘rough’ resolution with  $NF_1 = 11$  points,  $NT_1 = 6$  and  $NF_2 = 6$ .

Integration on  $\omega_1$  is the less optimized, it is the one that requires the largest number of points in our calculations. It should be noticed that according to Lavrenov (2001) 6-8 points for the integration on  $\theta_1$ , and 7 points on  $\omega_2$  are sufficient to ‘obtain a good result with a relative error less than 1-2%’. Lavrenov (2001) does not suggest any value for  $NF_1$ .

As the integration domain is reduced to  $\omega_2 \leq \omega_3$ , the number of quadruplet configurations per point of the frequency-direction grid is  $2 \times NF_1 \times NF_2 \times NT_1$ , which gives for the three resolutions considered :

- Fine resolution : 9984 configurations ;
- Medium resolution : 1792 configurations ;
- Rough resolution : 792 configurations.

The GQM fine resolution is considered here as an ‘exact’ (reference) computation of the nonlinear transfer term. Compared to the fine resolution, a larger increase of the resolution does not induce any noticeable improvement of the results. The rough resolution of the GQM method is considered as representative of a quasi-exact method, with an interesting reduction of the CPU time and accurate results.

The choice of an optimum resolution for practical applications requires of course to take into account the CPU time. In this thesis, simulations are handled with the GQM method resolution medium for a high precision of the results, but for larger scale simulations the rough resolution can be completely satisfactory.

Figure 2.3 presents the  $S_{nl}$  term computed using the GQM method for the three resolutions, rough, medium and fine. Differences between fine and medium resolutions are small, and almost invisible near the main positive and negative lobes, which shows the good convergence of the method when increasing its resolution. Results obtained with the rough resolution underestimate the value of the main positive lobe, but they reproduce quite well

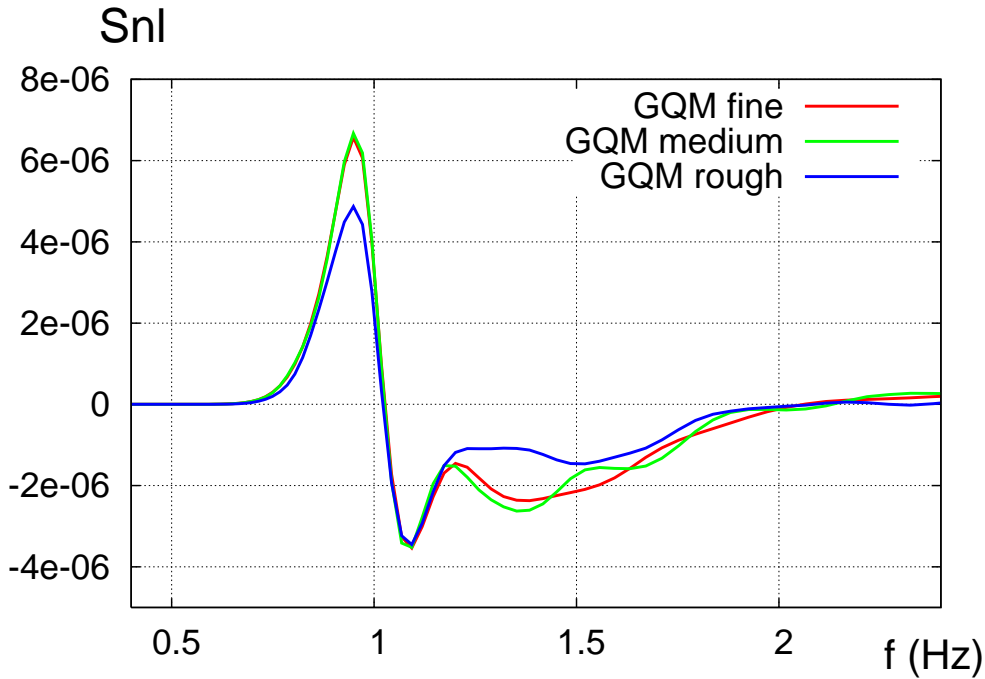


FIGURE 2.3 – Nonlinear transfer term  $S_{nl}$  computed using the GQM method (rough, medium and fine resolutions) and applied to a JONSWAP-type spectrum with usual features ( $f_p = 1$  Hz,  $\sigma = 0.07$  if  $f \leq f_p$ ,  $\sigma = 0.09$  if  $f > f_p$ ,  $\gamma = 3.0$ ) combined with a  $\cos^6(\theta/2)$  directional distribution.

the main characteristics of  $S_{nl}$ . The medium and rough resolutions show some deviations from the fine calculation at high-frequencies.

Influence of the method resolution on the evolution of a variance spectrum  $F(f, \theta)$  under the effect of nonlinear transfers only (called conservative equation) is observed in Figure 2.4. The simulation time is set to 128 physical hours ; initial condition is a step-like frequency spectrum combined with a half plane directional distribution. The discrete spectral grid is composed of 128 frequencies with geometric spacing and a constant angular spacing of  $10^\circ$ . Figure 2.4 shows  $E(f)$  at six different times for the three resolutions. The fine and medium resolutions give almost identical results, which confirms again the good convergence of the method. Results obtained with the rough resolution show slight differences, but they are all very similar after a few minutes.

Directional spectra at the final simulation time are presented in Figure 2.5. No difference can be seen between the spectrum obtained with GQM medium and fine. The rough resolution also seems to produce a very accurate estimation of  $F(f, \theta)$ .

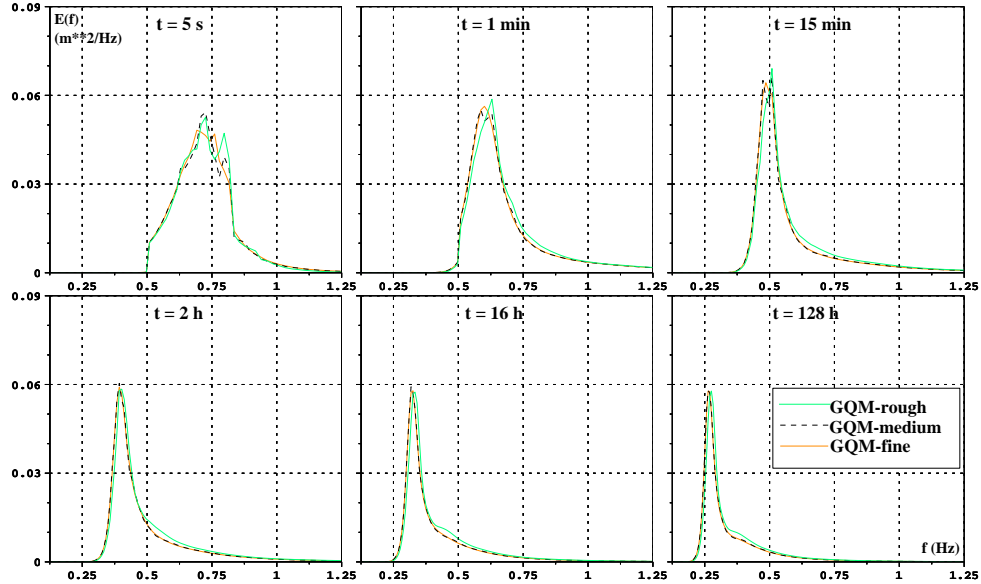


FIGURE 2.4 – Variance frequency spectrum  $E(f)$  at six times (5 s, 1 min, 15 min, 2 h, 16 h, 128 h) computed with the rough, medium and fine resolutions of the GQM method.

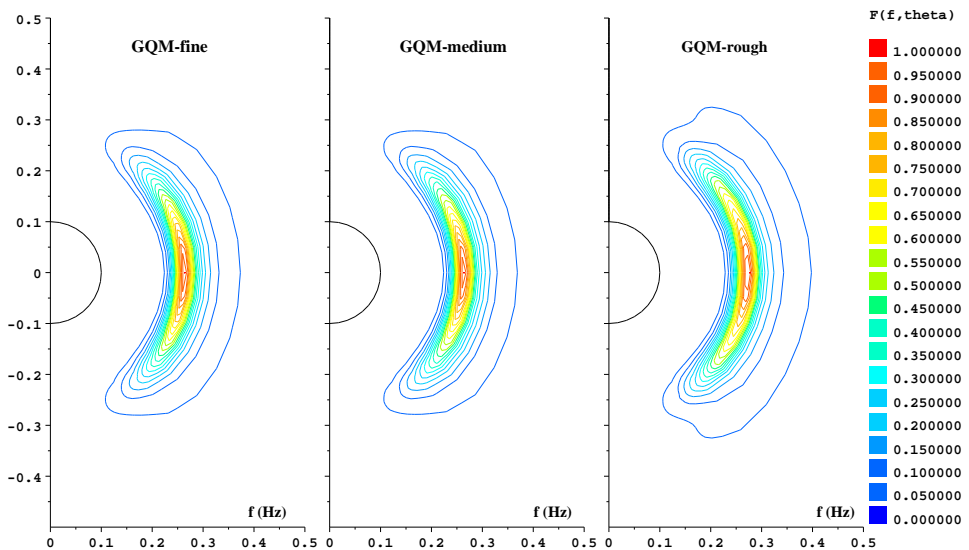


FIGURE 2.5 – Directional spectrum  $F(f, \theta)$  at  $t = 128 \text{ h}$  computed with the GQM method, resolution a) fine, b) medium, and c) rough.

### 2.3.3.2 Filtering : elimination of configurations

A further reduction in CPU time can be obtained by using filtering techniques. The principle is to filter out configurations that have a minor contribution in the global calculation of the  $S_{nl}$  term.

The integrand in expression (2.25) can be written as a function of four terms :

$$Scale \times Factor \times G \times (F_2 F_3 (F v_1^4 + F_1) - F F_1 (F_2 v_3^4 + F_3 v_2^4)) \quad (2.53)$$

where  $G$  (coupling coefficient) and  $Factor$  are function of  $v_i = \omega_i/\omega$  and only depend on the configuration.  $Scale$  only depends on  $\omega$ .

A simple way to filter minor contributions to the total  $S_{nl}$  term is to eliminate a configuration when  $G$  or  $Factor$  (or the product of  $G$  and  $Factor$ ) is smaller than a fixed threshold. The following condition is used in our algorithm :

If  $Factor \times G < Limit \times Maxim$  the configuration is eliminated.

Here  $Limit$  is a chosen threshold and  $Maxim$  is the maximum value of the product  $Factor \times G$  over all the configurations for a given value of  $v_1 = \omega_1/\omega$ . A good choice of  $Limit$  requires to take into account savings in computational time but also increasing of the error.

In the previous simulations, filtering was used for the three resolutions presented, and was chosen as follows :

- 21 % of the configurations are eliminated for the fine resolution,
- 34 % of the configurations for the medium resolution,
- 64 % of the configurations for the rough resolution,

which leads to a corresponding decrease of the CPU time needed to compute the nonlinear term.

Figure 2.6 shows  $S_{nl}$  computed with the rough, medium and fine resolutions of GQM (same initial case as in Figure 2.3) with and without filtering of configurations.

The rough calculation of  $S_{nl}$  is degraded by the use of filtering, which gives a larger underestimation of the positive peak, but reduction of CPU time is considerable and very interesting for operational applications. For cases medium and fine, the filtering results in very slight changes, almost not visible for the fine resolution.

The proportion of discarded configurations based on filtering used in the three above settings (rough, medium and fine) could certainly be further optimized. This would require additional tests on a set of different spectra.

### 2.3.3.3 Additional optimizations

In addition to optimization of the resolution and filtering of configurations, other optimizations of the algorithm for computing the GQM method were carried out.

- **Algorithm optimization :**

- The order of nested loops was optimized, using symmetry and scaling properties. Loops on  $\omega$  and  $\theta$  are the most inner ones.
- Factoring out and pre-computing all terms not depending on  $\omega$  and  $\theta$  (i.e. all terms except spectra products) also make significant saving in computational time.

- **Non-interpolating version of the algorithm :**

We also tested a non-interpolating version of the GQM algorithm. This is the version currently used. In this version, no interpolation is performed to calculate  $F(\omega_1, \theta_1)$ ,  $F(\omega_2, \theta_2)$  and  $F(\omega_3, \theta_3)$  but the closest mesh points are taken. This causes a slight deterioration of the results but reduces the computational time. In this case, it appeared necessary to use the detailed balance principle (Hasselmann & Hasselmann, 1981) to compute and store simultaneously  $S_{nl}(\omega_1, \theta_1)$ ,  $S_{nl}(\omega_2, \theta_2)$  and  $S_{nl}(\omega_3, \theta_3)$ , in addition to  $S_{nl}(\omega, \theta)$ , in order to keep the same overall level of accuracy.

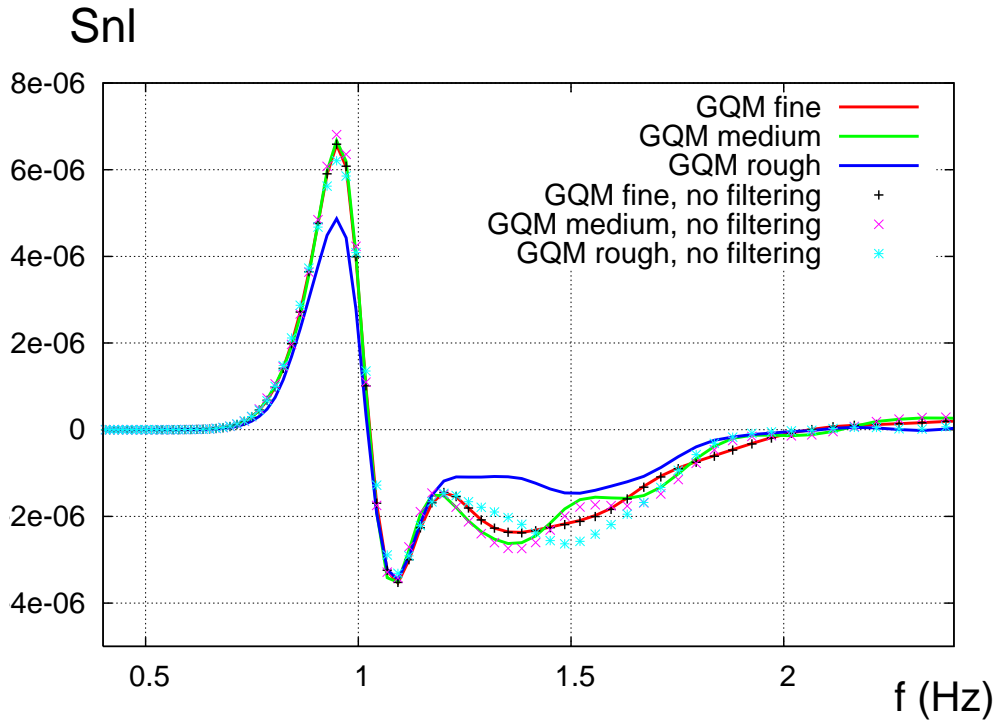


FIGURE 2.6 – Nonlinear transfer term  $S_{nl}$  computed with the GQM method (rough, medium and fine resolutions) with and without filtering.

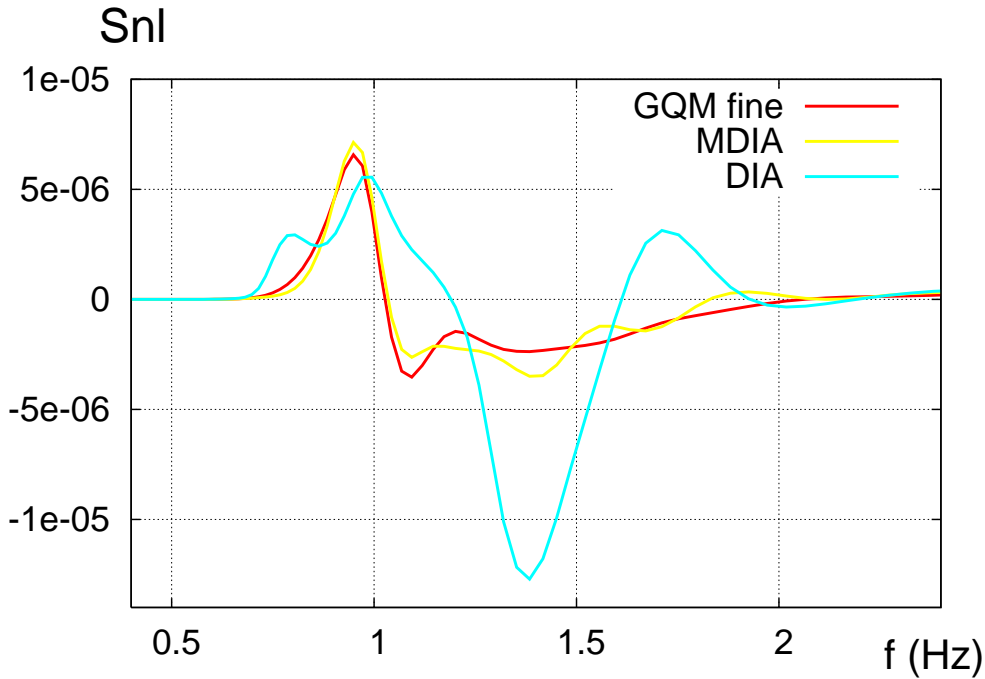


FIGURE 2.7 – Nonlinear transfer term  $S_{nl}$  computed using DIA, MDIA, and GQM (fine resolution) and applied to a JONSWAP-type spectrum with usual features ( $f_p = 1$  Hz,  $\sigma = 0.07$  if  $f \leq f_p$ ,  $\sigma = 0.09$  if  $f > f_p$ ,  $\gamma = 3.0$ ) combined with a  $\cos^6(\theta/2)$  directional distribution function.

### 2.3.4 Comparison of the GQM method with more commonly used methods

Some simple comparisons are offered here to give an overview of the accuracy of the GQM method. For further comparisons between the methods, please refer to Benoit (2005) or Cavalieri et al. (2007). Fig. 2.7 shows the  $S_{nl}$  terms given by DIA, Multiple DIA (MDIA) as proposed by Tolman (2004) and GQM method with fine resolution, considered as the reference for exact evaluation of nonlinear transfers. Note that results are not compared here to other exact methods (EXACT-NL code, WRT method), since this type of analysis was already performed by Benoit (2005), validating the implementation of the algorithm.

Differences between DIA and GQM-fine curves are very important. DIA gives several positive lobes; its negative lobe is shifted towards higher frequencies and several times higher than the one obtained with GQM-fine (see also Benoit, 2005; Cavalieri et al., 2007). The MDIA curve gives significantly improved results compared to the original DIA. At the first glance, it looks very attractive as it gives a better estimation of the positive lobe than the GQM method with rough resolution (Figure 2.3). However, as explained in §2.1.2, MDIA can give good results for particular spectral distributions such as an initial JONSWAP spectrum with a standard set of parameters, but its use is questionable in general case.

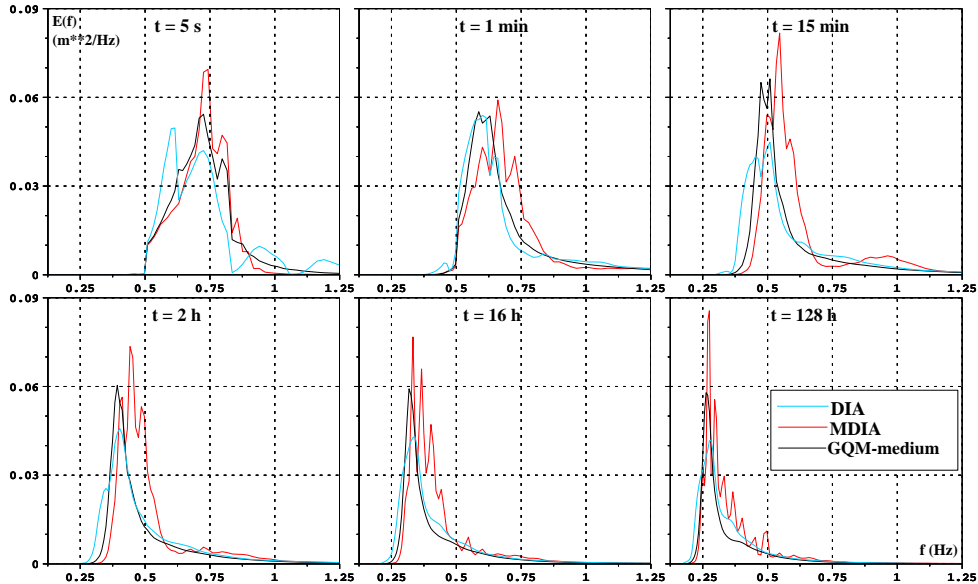


FIGURE 2.8 – Variance frequency spectrum  $E(f)$  at six times (5 s, 1 min, 15 min, 2 h, 16 h, 128 h) computed with the methods DIA, MDIA, and GQM (medium resolution).

As an illustration, Benoit (2006) showed that in case of abrupt changes of wind direction, results obtained from DIA, Multiple DIA (Tolman, 2004) and GQM methods can differ significantly.

128 hours simulations with identical parameters as in Figure 2.4 were also performed using DIA and MDIA. Variance frequency spectra  $E(f)$  at six different times are plotted in Figure 2.8. The resolution medium is used here for comparison, since it is the resolution used in the next chapters and obtained results are very close to the exact computation. Spectra computed with DIA clearly differ from spectra obtained with the GQM method resolution medium. At the beginning of the simulation ( $t < 1$  min), the DIA method produces a succession of peaks at high frequencies instead of a smooth  $f^{-4}$  tail. However, after about 1 min, the formation of the equilibrium  $f^{-4}$  shape is observed. The evolution of the peak frequency seems to be relatively well reproduced by DIA. Nevertheless, at the end of the simulation, the shape of the DIA spectrum is quite different from the GQM one : it is more spread in frequency and its peak is lower. MDIA spectra are not closer to the GQM medium computations than the DIA ones ; they are very irregular with many spurious peaks.

Figure 2.9 shows significant differences between the directional spectra obtained at  $t = 128$  h with the three methods. The directional spreading of the DIA spectrum is significantly larger than the GQM one. The MDIA spectrum has a very irregular shape.

Application of the GQM method to more realistic conditions, as duration-limited, fetch limited, or slanting fetch cases and comparisons with DIA simulations are performed in the next chapters.

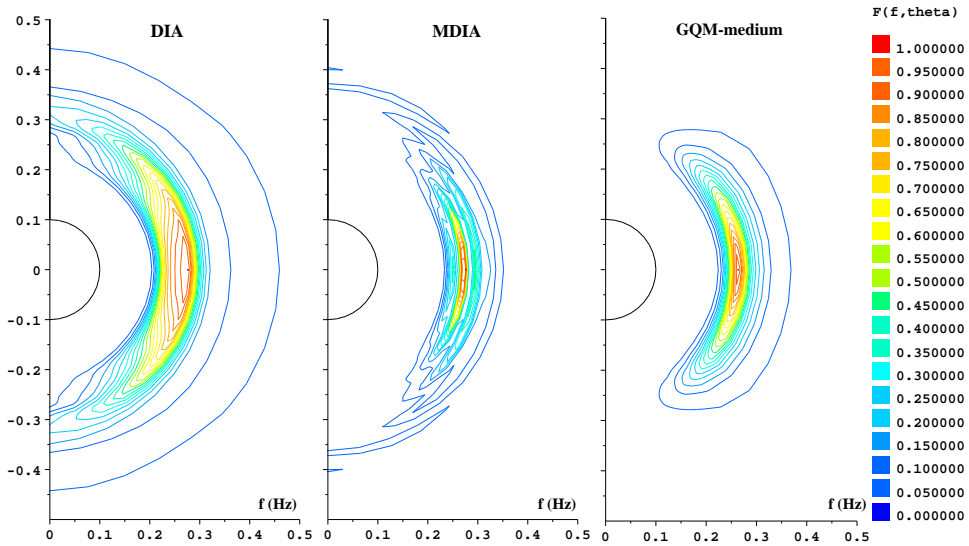


FIGURE 2.9 – Directional spectrum  $F(f, \theta)$  at  $t = 128$  h computed with the methods a) DIA, b) MDIA, and c) GQM (medium resolution).

### 2.3.5 Estimation of the CPU time

In this subsection, some estimations of CPU time of the  $S_{nl}$  calculation, which is the most time-consuming part of the simulation of the balance equation (1.45), are presented.

#### 2.3.5.1 Single-point runs

‘Exact’ methods like the EXACT-NL algorithm of Hasselmann & Hasselmann (1981, 1985), the WRT method of Webb (1978) or the GQM method with fine resolution provide very accurate estimation of the nonlinear transfer term, but their CPU time is prohibitive. For example, the EXACT-NL code need about 1000 times the computing time of DIA. Recent optimizations of the WRT method by Van Vledder (2006) result in an increase of CPU time of 300 compared to DIA.

The three resolutions, rough, medium and fine with filtering of configurations require the following CPU time compared to DIA :

- Fine resolution :  $\approx 2000$  times the DIA computation ;
- Medium resolution :  $\approx 350$  times DIA ;
- Rough resolution :  $\approx 100$  times DIA.

For information, for the simulation presented in subsection 2.3.4 (128 h of physical time with a dynamic time step), the DIA method requires 4.5 s of CPU time on a 2.33 GHz Intel Xeon processor with 2 GB RAM.

Without filtering, the CPU time increases to :

- Fine resolution :  $\approx 2500$  times the DIA computation ;
- Medium resolution :  $\approx 540$  times DIA ;
- Rough resolution :  $\approx 270$  times DIA.

Later in this work, simulations are always handled with filtering. As described in the previous subsections, medium and fine resolutions give very close results, even when using filtering techniques. Therefore, the gain in computing time convinced us to use the GQM medium method in the next simulations.

MDIA calculation of  $S_{nl}$  takes about four times the DIA computing time, which is very efficient, but results did not appear convincing. A MDIA algorithm with higher number of configurations is still a direction that could be investigated.

The GQM method with rough resolution needs about 100 times the DIA computational time. This is an interesting result although there is still a need to reduce computational effort for practical applications. It is interesting to notice that the ratio of CPU times of the GQM and DIA algorithms decreases in simulations with other source terms or including spatial propagation.

### 2.3.5.2 Single-point runs including forcing terms

The single-point version of our model including other source terms (e.g. duration-limited simulations) gives the following computational times :

- Fine resolution :  $\approx 1000$  times the DIA computation ;
- Medium resolution :  $\approx 150$  times DIA ;
- Rough resolution :  $\approx 50$  times DIA.

These estimations depend a little of the source term formulations considered, but order of magnitude are similar.

### 2.3.5.3 One-dimensional runs

The 1-D version of our model (e.g. fetch-limited or slanting fetch simulations) gives :

- Fine resolution :  $\approx 500$  times the DIA computation ;
- Medium resolution :  $\approx 80$  times DIA ;
- Rough resolution :  $\approx 25$  times DIA.

## 2.4 Conclusions

In this work, we briefly presented the different methods for the calculation of the  $S_{nl}$  term. We showed that an optimal technique might be the use of a quasi-exact method and we illustrated our purpose with a selected method : the Gaussian Quadrature Method (GQM).

After showing how the six dimensional equation (2.1) can be reduced to a three-dimensional one, we described the use of Gaussian quadrature formulas for the three different integrations.

Finally, we compared the results of the GQM method, with three different resolutions (rough, medium and fine), to DIA and MDIA results. We established that the GQM method is stable and accurate and presents good possibilities to make its CPU time acceptable. The rough resolution seems to be a valuable candidate for use in 3G models, as it shows promising efficiency : 25 times the DIA CPU time for one-dimensional simulations of the kinetic equation.

## Chapitre 3

# Ocean wave spectrum properties as derived from quasi-exact computations of nonlinear wave-wave interactions

by E. Gagnaire-Renou, M. Benoit, P. Forget

Journal of Geophysical Research - C (Oceans), doi :10.1029/2009JC005665, in press

## Abstract

The estimation of nonlinear wave-wave interactions is one of the central problems of the development of operational and research models for ocean wave prediction. In this paper, we present results obtained with a numerical model based on a quasi-exact computation of the nonlinear wave-wave interactions called GQM (Gaussian Quadrature Method) that gives both precise and computationally efficient calculations of the four-wave interactions. Two situations are presented : a purely nonlinear evolution of the spectrum, and a duration-limited case. Properties of the directional wave spectrum obtained using GQM and the Discrete Interaction Approximation (DIA) are compared. Different expressions for the wind input and dissipation terms are considered. Our results are consistent with theoretical predictions. In particular, they reproduce the self-similar evolution of the spectrum. The bimodality of the directional distribution of the spectrum at frequencies lower and greater than the peak frequency is shown to be a strong feature of the sea states, which

is consistent with high-resolution field measurements. Results show that nonlinear interactions constitute the key mechanism responsible for bimodality, but that forcing terms also have a quantitative effect on the directional distribution of the spectrum. The influence of wind and dissipation parameterizations on the high frequency shape of the spectrum is also highlighted. The imposition of a parametric high frequency tail has a significant effect on the high frequency shape of the spectrum, but also on the energy level and peak period and on the global directional distribution.

### 3.1 Introduction

Existing operational models for ocean wave modeling (either hindcasting or forecasting) are based on a transport equation for the wave action density. Since the pioneering model of Gelci et al. (1957), the understanding and modeling of surface waves dynamics has been constantly improving. The first models relied on parameterizations of the shape of the spectrum and/or of the physical processes (for a review, see e.g. Komen et al., 1994; Young, 1999; Cavalieri et al., 2007; Holthuijsen, 2007). About 20 years ago the first third generation (3G) model, called WAM, was proposed by the WAMDI Group (1988). Other 3G models have been developed in the recent years, for example WAVEWATCH (Tolman, 1991, 2002), SWAN (Booij et al., 1999) and TOMAWAC (Benoit et al., 1996a).

These 3G discrete spectral models compute the evolution of the wave action density  $N$ , defined as  $N(\mathbf{k}) = F(\mathbf{k})/\omega$ , where  $F(\mathbf{k})$  is the directional (two-dimensional) variance spectrum of ocean waves, expressed here as a function of the wave-number vector  $\mathbf{k} = (k_x, k_y)$ , and  $\omega$  is the intrinsic wave frequency. This evolution can be described by the action balance equation, called kinetic equation (KE), written for the general case of waves propagating in a medium with an ambiant current  $\mathbf{U}$  as (e.g. Phillips, 1977; Andrews & McIntyre, 1978; Komen et al., 1994) :

$$\frac{\partial N}{\partial t} + \frac{\partial(\dot{x}N)}{\partial x} + \frac{\partial(\dot{y}N)}{\partial y} + \frac{\partial(\dot{k}_x N)}{\partial k_x} + \frac{\partial(\dot{k}_y N)}{\partial k_y} = S(k_x, k_y, x, y, t) \quad (3.1)$$

with  $\dot{x} = \partial\Omega/\partial k_x$ ,  $\dot{y} = \partial\Omega/\partial k_y$ ,  $\dot{k}_x = -\partial\Omega/\partial x$ ,  $\dot{k}_y = -\partial\Omega/\partial y$  and  $\Omega = \omega + \mathbf{k} \cdot \mathbf{U}_c$ .

The term  $S$  on the right hand side of equation 3.1 gathers the various source, sink and transfer terms representing physical processes such as wind-wave interactions, wave-wave interactions, dissipation of energy due to breaking, bottom friction, etc. In the present work, we assume that there is no ambient current and we limit ourselves to deep water conditions and spatially homogeneous cases, i.e. we only consider the evolution in time. Equation 3.1 can then be simplified in the following way :

$$\frac{\partial N}{\partial t} = S_{in} + S_{diss} + S_{nl} \quad (3.2)$$

where  $S_{in}$  represents the energy input from the wind,  $S_{diss}$  the dissipation by whitecap-ping, and  $S_{nl}$  the nonlinear four-wave interactions. Several models have been proposed

during the last decades for  $S_{in}$  and  $S_{diss}$  (see for instance Cavaleri et al., 2007, for a recent review and discussion). As the physics of wind-wave interactions and dissipation is quite complex and still only partially understood, the formulations used in existing 3G models involve some level of parameterization of the processes, based on measurements and/or theoretical considerations. On the other hand a theoretical model exists for the  $S_{nl}$  term since the works by Hasselmann (1962) and Zakharov (1968) (see Section 2). Existence of third-order nonlinear wave-wave interactions was confirmed experimentally by e.g. McGoldrick et al. (1966). Recent efforts to validate and compare theories of Hasselmann (1962) and Zakharov (1968) have been undertaken by Tanaka (2001); Korotkevich et al. (2008). Many studies have already shown the importance of the  $S_{nl}$  term for a proper modeling of the spectrum evolution, e.g. Young & Van Vledder (1993). However, the complexity of  $S_{nl}$  makes its numerical computation time consuming, even using recent computers (Cavaleri et al., 2007; Janssen, 2004). In the mid 80s, Hasselmann et al. (1985) developed an approximate computational method which was fast enough to be implemented in 3G operational models, the Discrete Interaction Approximation (DIA). Improvements of DIA or alternative techniques have been developed thereafter, mainly the Multiple DIA (MDIA) method (Van Vledder et al., 2000; Tolman, 2004), or more exact techniques such as EXACT-NL (Hasselmann & Hasselmann, 1981), the Webb-Resio-Tracy method (WRT) (Webb, 1978; Resio & Perrie, 1991), the Reduced Interaction Approximation method RIAM (Masuda, 1980), Gaussian Quadrature Method (GQM) (Lavrenov, 2001). Comparison between some of these methods can be found in Benoit (2005) and Cavaleri et al. (2007). A very recent approach, named two-scale approximation (TSA) (Resio & Perrie, 2008), could also be promising but further investigations are needed.

This paper focuses on the effects of the nonlinear wave-wave interactions on the structure of the wave spectrum. Our primary concern is to study the effect of a precise computation of the nonlinear term  $S_{nl}$  on the wave spectrum estimation. To that end we used a numerical algorithm adapted from the Gaussian Quadrature Method (GQM) proposed by Lavrenov (2001). We addressed first the so-called “conservative” case, considering only the nonlinear transfer term in equation 3.2 ( $S_{in} = S_{diss} = 0$ ), and then the simultaneous effects of the three physical processes of equation 3.2 by using existing models for  $S_{in}$  and  $S_{diss}$ . The temporal evolution of the spectrum and the structure of the directional distribution are analyzed.

For the study of the dynamics of the wave spectrum evolution, we followed a similar approach as Badulin et al. (2005) who considered both the conservative case and the effects of wind input and dissipation. For a homogeneous and deep ocean, they showed that the conservative KE leads to self-similar solutions for the frequency spectrum (e.g. Badulin et al., 2005; Pushkarev et al., 2003). These solutions are consistent with the theory of weak turbulence, leading to spectra of Kolmogorov type (Zakharov & Filonenko, 1966; Zakharov & Zaslavsky, 1982b). The shape and evolution of the directional spectrum was also simulated by Lavrenov (2003a). The wind input and dissipation were taken into account for example by Banner & Young (1994). The non-stationary and non-homogeneous equation was recently simulated by Ardhuin et al. (2007) using the WRT method. Finite depth case was investigated by Polnikov (1997) and Resio et al. (2001).

We are particularly interested in the bimodality of the angular distribution of the wave

spectrum (two peaks of the angular distribution at a given frequency) that is now known to occur at frequencies higher than the peak frequency and also in the low frequency part of the spectrum. Indeed, until recently, the directional distribution of the ocean waves had most often been considered as unimodal. For instance Mitsuyasu et al. (1975), Hasselmann et al. (1980), Donelan et al. (1985), Elfouhaily et al. (1997) and Kudryavtsev et al. (1999) provided unimodal parameterizations of the directional distribution. Remote sensing measurements carried out with airborne radars or lidars, aerial stereo-photography techniques, HF radars, etc., evidenced bimodality in the directional spectrum of surface gravity waves (see Hwang et al., 2000b, for a review). Bimodal directional distributions were also measured by directional buoys or arrays of wave gauges (Young, 1994; Young et al., 1995; Ewans, 1998; Wang & Hwang, 2001; Long & Resio, 2007). These data all show the bimodal structure of the angular distribution at frequencies higher than the spectral peak. These observations suggest that bimodality could be a fundamental feature of the wind wave spectrum for very different water depth and wind conditions, which supports the idea that the nonlinear wave-wave interactions play an important role in the mechanism that creates and maintains bimodality (Banner & Young, 1994). It should be noticed that bimodality associated with another mechanism (Phillips resonance mechanism of wind-wave generation) was observed using HF radars by Trizna et al. (1980).

The organization of the paper is as follows. Section 2 introduces the basic equations and numerical methods for computing  $S_{nl}$ . Section 3 presents the simulation results of the conservative KE (model equation and initial conditions are given in subsection 3.1, the concept of self-similarity is discussed in subsection 3.2, the evolution of representative sea state parameters, frequency spectrum and directional distribution are analyzed in subsections 3.3, 3.4 and 3.5-3.6, respectively). Section 4 describes the effects of wind input and dissipation by whitecapping. Section 5 gives our conclusions and perspectives for this work.

## 3.2 Equations and numerical methods

### 3.2.1 The nonlinear four-wave interactions $S_{nl}$

3G spectral models aim at representing each physical process in a source term as reliably as possible. This is rather difficult, either because the physics is poorly understood, which is the case for the dissipation by whitecapping, or because the computational method is too time-consuming, which is the case for the nonlinear four-wave interactions. Several models and parameterizations have been implemented for wind input and whitecapping dissipation. Regarding the term  $S_{nl}$ , a theoretical model has been available since Hasselmann (1962) and Zakharov (1968), who independently formulated its expression as a Boltzmann-type integral :

$$S_{nl} [N_{\mathbf{k}}] = \int_{\mathbf{k}_1} \int_{\mathbf{k}_2} \int_{\mathbf{k}_3} G(\mathbf{k}, \mathbf{k}_1, \mathbf{k}_2, \mathbf{k}_3) \{ N_2 N_3 (N + N_1) - N N_1 (N_2 + N_3) \} \times \delta(\mathbf{k} + \mathbf{k}_1 - \mathbf{k}_2 - \mathbf{k}_3) \delta(\omega + \omega_1 - \omega_2 - \omega_3) d\mathbf{k}_1 d\mathbf{k}_2 d\mathbf{k}_3 \quad (3.3)$$

In the above expression,  $N_j$  stands for  $N(\mathbf{k}_j)$  and  $\omega_j$  is the frequency corresponding to the wave-number  $k_j$  through the dispersion relationship ( $\omega^2 = gk$ ).  $G(\mathbf{k}, \mathbf{k}_1, \mathbf{k}_2, \mathbf{k}_3)$  is the coupling coefficient, whose expression may be found in Webb (1978) for instance. As indicated by the two Dirac- $\delta$  functions, the interactions occur between quadruplets of spectral components that fulfill the two resonance conditions :

$$\begin{cases} \mathbf{k} + \mathbf{k}_1 = \mathbf{k}_2 + \mathbf{k}_3 \\ \omega + \omega_1 = \omega_2 + \omega_3 \end{cases} \quad (3.4)$$

The computation of this complicated nonlinear six-fold integral is a tricky problem. The exact evaluation of equation 3.3 requires specific algorithms together with a large computational time, so that in operational wave models this nonlinear term is most often evaluated by approximate and simplified methods. The most commonly used technique is DIA (Hasselmann et al., 1985), which only considers a particular arrangement of wave components. In spite of its wide use, DIA suffers from a number of limitations (Van Vledder et al., 2000). Benoit (2005) compared several methods to evaluate the nonlinear interactions in deep water conditions and highlighted significant differences between them. Only quasi-exact methods, such as those proposed by Webb (1978) or Lavrenov (2001) allow an accurate evaluation of this term.

Therefore, our concern is to work on a method that can be suitable for use in operational models but with a higher precision than DIA. In this perspective, we have developed an efficient numerical algorithm to compute the Boltzmann integral, called GQM method (Gaussian Quadrature Method), and based on the work of Lavrenov (2001).

### 3.2.2 The GQM method

The GQM method is based on the use of Gaussian quadratures for the various numerical integrations in equation 3.3. The six-dimensional integral can be reduced to a three-dimensional integral over  $\omega_1$ ,  $\theta_1$ , and  $\omega_2$  when suppressing the two Dirac (resonance conditions). Indeed, the term  $\delta(\mathbf{k} + \mathbf{k}_1 - \mathbf{k}_2 - \mathbf{k}_3)$  involves  $\mathbf{k}_3 = \mathbf{k} + \mathbf{k}_1 - \mathbf{k}_2$ , which permits to eliminate two dimensions of integration. We chose to work with the spectrum  $F(\omega, \theta)$ . The change of variable from  $\mathbf{k}$  to  $(\omega, \theta)$  thus leads to an integral over  $\omega_1$ ,  $\theta_1$ ,  $\omega_2$ , and  $\theta_2$ . Then integration over  $\theta_2$  eliminates the second Dirac. Rewriting the equation in term of the variance spectrum  $F$  (instead of the action density  $N$ ), we obtain the following expression :

$$\frac{\partial F}{\partial t} = \int_{\omega_1=0}^{+\infty} \int_{\theta_1=0}^{2\pi} \int_{\omega_2=0}^{\omega_a/2} 2 \frac{\omega_a^4 G}{\omega_1 \omega_2 \omega_3} \frac{F_2 F_3 (F \omega_1^4 + F_1 \omega^4) - FF_1 (F_2 \omega_3^4 + F_3 \omega_2^4)}{\sqrt{\tilde{B}_0(\varepsilon_a, w_2) \tilde{B}_1(\varepsilon_a, w_2) \tilde{B}_2(\varepsilon_a, w_2)}} d\omega_1 d\theta_1 d\omega_2 \quad (3.5)$$

where  $\omega_a = \omega + \omega_1 = \omega_2 + \omega_3$ ,  $\varepsilon_a = 2gk_a/\omega_a^2$  with  $\mathbf{k}_a = \mathbf{k} + \mathbf{k}_1 = \mathbf{k}_2 + \mathbf{k}_3$ ,  $w_2 = \omega_2/\omega_a$  and  $\tilde{B}_0$ ,  $\tilde{B}_1$ ,  $\tilde{B}_2$  are three non-dimensional functions.

The integration over  $\theta_2$  introduces singularities since the denominator of equation 3.5 can be equal to zero. The specificity of the GQM method, which makes it an optimal algorithm of integration, is the use of quadratures adapted to these singularities. Integration over  $\omega_2$  is divided into two intervals, and computed with Gauss-Legendre and Gauss-Chebyshev quadratures. Integration over  $\theta_1$  uses Gauss-Chebyshev quadrature and the last integration (over  $\omega_1$ ) is performed with a simple trapezoidal method.

The GQM method can be used with a reduced number of integration points in the quadrature formulas, plus some filtering to discard configurations which have negligible or minor contributions to the overall integral. Thus, the computing time can be reduced, while the method still produces results with high accuracy.

To study the properties and the robustness of our algorithm, we performed simulations with different resolutions of the method, i.e. different numbers of points for the numerical integration. Three resolutions were tested in Benoit & Gagnaire-Renou (2007), a so-called “fine” resolution (26 points for the integration on  $\omega_1$ , 16 points for the integration on  $\theta_1$ , and 12 points on  $\omega_2$ ), a “medium” resolution (14, 8, 8) and a “rough” resolution (11, 6, 6). In order to illustrate the performance of the GQM method we present in figure 3.1 the (angular integrated) nonlinear transfer terms  $S_{nl}$  as obtained with various methods. The nonlinear terms are computed for a directional wave spectrum corresponding to the case number 3 of Hasselmann et al. (1973) which combines a JONSWAP frequency spectrum  $E(f)$  with Phillips constant  $\alpha = 0.01$ , peak frequency  $f_p = 0.3$  Hz, peak enhancement factor  $\gamma = 3.3$ ,  $\sigma = 0.07$  if  $f \leq f_p$  and  $\sigma = 0.09$  if  $f > f_p$ , and a frequency-independent angular spreading function  $D(\theta) = \Delta \cos^4(\theta)$  over  $[-\pi/2, \pi/2]$ . It can be seen from figure 3.1 that the  $S_{nl}$  term computed with the GQM-fine method is very close to the term computed by the EXACT-NL code from Hasselmann & Hasselmann (1981) although this latter term exhibit some spurious oscillations. Results obtained with the GQM-rough method are a bit more irregular than the GQM-fine term but lies in very good overall agreement with it. In comparison it is seen that the  $S_{nl}$  term computed with the DIA method is clearly different, both in magnitude and shape of the lobes of the nonlinear transfer term. The fine and medium resolutions give almost identical results (not shown in figure 3.1 because the curves are very close). Comparison of results thus confirmed the good convergence of the method when increasing its resolution.

The choice of the optimum setting for practical applications requires to take into account the computing time. For simulation of the conservative KE, the medium resolution requires 3-4 times more CPU time than the rough resolution, and the fine calculation 25 times more CPU time than the rough one. In comparison with DIA, the rough resolution is 80 to 100 times slower. This can be compared with the CPU times of the EXACT-NL code (approximately 1000 times DIA) and the WRT method (approximately 300 times DIA). Therefore, the method appears suitable for implementation in 3G models. In the remainder of this paper, simulations are handled using the GQM method with medium resolution. Results obtained using the GQM (medium) and the DIA methods are compared throughout the paper.

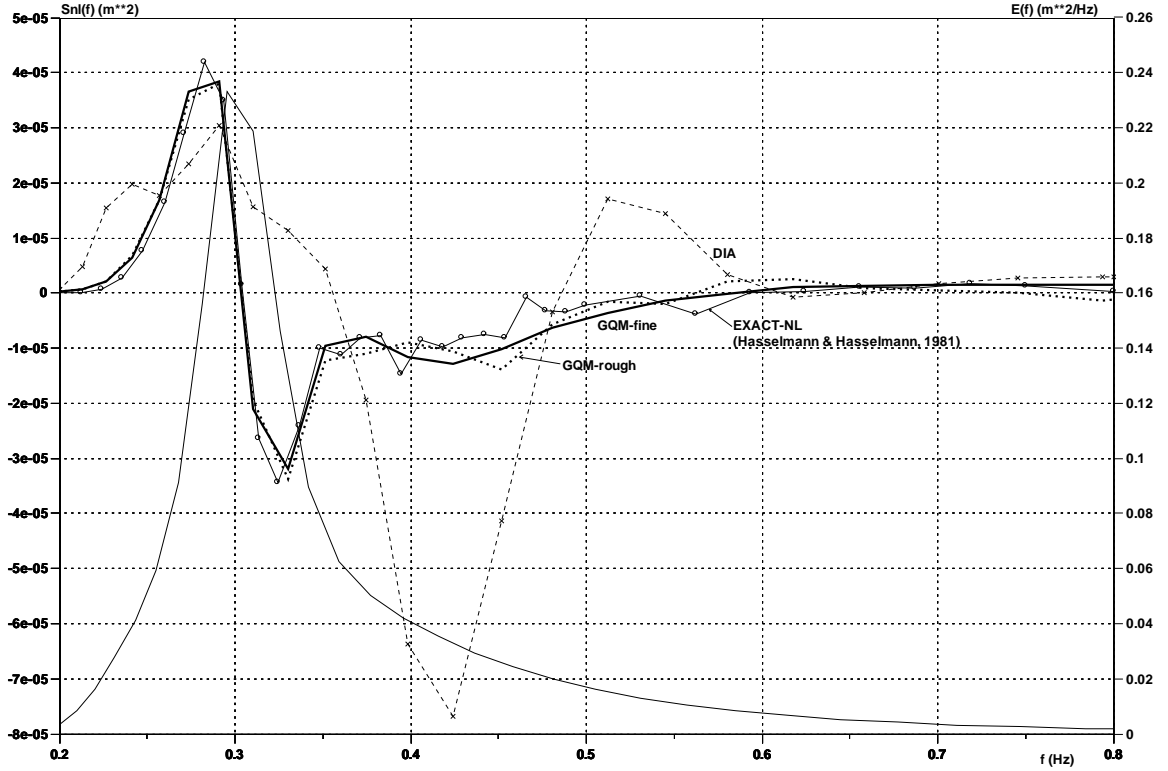


FIGURE 3.1 – Angular integrated nonlinear transfer terms  $S_{nl}(f)$  computed with various methods : EXACT-NL, DIA, GQM-fine, GQM-rough for the spectrum of case 3 of Hasselmann & Hasselmann (1981). The frequency spectrum  $E(f)$  is superimposed.

### 3.2.3 Numerical aspects

It should be first recalled that numerical settings (e.g. spectral resolution and range, time step, diagnostic tail, growth limiter) cannot be dissociated from the parameterizations of the physical processes themselves (e.g. Tolman, 1992). Here the time integration of the source terms in equation 3.2 is performed using a semi-implicit scheme with a dynamic time step. This time step is calculated at each iteration so that the relative variation of the variance spectrum as the result of the input, dissipation and transfer terms during a time step remains below a threshold  $\varepsilon$  (generally 5 to 10 %). No wave growth limiter is used in these simulations.

For some calculations (set III-it in section 4), a diagnostic tail (or constrained tail) is applied to the spectrum above  $f_d = \min[f_{max}; \max(4f_{PM}, 2.5f_{mean})]$ , where  $f_{max}$  is the last discrete frequency,  $f_{PM}$  is the Pierson-Moskovitz frequency and  $f_{mean}$  is the mean frequency. It means that the high frequency range of the spectrum is constrained to decrease as  $f^{-m}$  with  $m$  a fixed parameter called “tail factor”, set to  $m = 4$  in our simulations.

In the following, the high frequency shape of the spectrum is often called HF tail. The implications of imposing a  $f^{-4}$  HF tail is discussed later in the paper.

No diagnostic tail is applied for the simulations of sections 3 and 4 (sets I, II and III-ft). However, above the last discrete frequency  $f_{max}$ , the spectrum is assumed to have a  $f^{-4}$  shape.

### 3.3 Results for the conservative equation (no wind input nor dissipation)

#### 3.3.1 Model equation and initial conditions

We first address the particular case of evolution of ocean waves when there is no energy input from the wind nor dissipation. In this case, equation 3.2, written in term of the variance spectrum  $F$ , reduces to :

$$\frac{\partial F}{\partial t} = S_{nl} \quad (3.6)$$

We performed several runs in order to investigate the effect of the initial energy and wave steepness, and of the initial shape of the spectrum on the evolution of  $F$ . This latter is written as  $F(f, \theta) = E(f)D(f, \theta)$ , with  $\theta$  the wave direction,  $F$  the frequency (one-dimensional) variance spectrum and  $D$  the directional spreading function satisfying  $\int_\theta D(f, \theta) = 1$ .

The wave (total) energy is  $E_{tot} = \rho g \int_f E(f)df$ , with  $g$  the gravitational acceleration and  $\rho$  the sea water density. The spectral significant wave height is defined as  $H_{m0} = 4\sqrt{m_0}$  with  $m_0$  the zero-th order moment of  $E(f)$ . The spectral peak frequency,  $f_p$ , is another important parameter. The wave steepness is defined here as  $\varepsilon = k_p H_{m0}/2$ , with  $k_p = (2\pi f_p)^2/g$ .

The initial peak frequency  $f_{p0}$  was always fixed to 1 Hz. Eight cases were considered corresponding to four initial shapes of  $F$  (labeled C1 to C4), combined with two values of initial  $H_{m0}$  (labeled a and b) : 0.05 m and 0.10 m (the corresponding steepnesses are 0.10 and 0.20, respectively).

The parameters defining the initial spectra are given in Table 3.1. The different shapes for  $E(f)$  and  $D(\theta)$  are illustrated in figure 3.2. Our cases C1 and C2 were chosen to examine how the model responds when a non-realistic spectrum is imposed at the beginning of the run.

The discrete grid is composed of 128 frequencies, with geometric spacing ( $f_{i+1}/f_i = 1.024$ ) from  $f_{p0}/5$  (0.2 Hz) to  $4f_{p0}$  (4 Hz) and 72 directions with a constant spacing of 5 degrees. The simulations were run during 128 hours of physical time.

Simulations are computed using the GQM method. In order to compare with the DIA method, we repeated the same simulations by simply replacing GQM by DIA in equation 3.6 , parameters and computing options being identical for both methods.

Initial case	$F(f, \theta) = E(f)D(\theta)$	$H_{m0} = 0.05 \text{ m}$ <b>a</b>	$H_{m0} = 0.10 \text{ m}$ <b>b</b>
<b>C1</b>	$E(f)$ : step, $D(\theta)$ : half-plane $E(f) = A$ ( $0.8 \leq f \leq 1.2 \text{ Hz}$ ), $E(f) = 0$ (otherwise) $D(\theta) = 1/\pi$ ( $90^\circ \leq \theta \leq 270^\circ$ ), $D(\theta) = 0$ (otherwise)	$A = 3.91 \cdot 10^{-4}$	$A = 1.56 \cdot 10^{-3}$
<b>C2</b>	$E(f)$ : Gaussian, $D(\theta)$ : half-plane $E(f) = A \exp\left(-\frac{(f-f_p)^2}{2\sigma^2}\right)$ , $f_p = 1 \text{ Hz}$ , $\sigma = 0.1$	$A = 6.23 \cdot 10^{-4}$	$A = 2.49 \cdot 10^{-3}$
<b>C3</b>	$E(f)$ : Jonswap, $D(\theta)$ : broad cardioid $E(f) = Ag^2(2\pi)^{-4}f^{-5}\exp\left(-\frac{5}{4}\left(\frac{f}{f_p}\right)^{-4}\right)\gamma^{\exp\left(-\frac{(f-f_p)^2}{2\sigma^2f_p^2}\right)}$ $f_p = 1 \text{ Hz}$ , $\sigma = 0.07$ if $f \leq f_p$ , $\sigma = 0.09$ if $f > f_p$ , $\gamma = 3.0$ $D(\theta) = 0.51 \cos^6\left(\frac{1}{2}(\theta - \theta_0)\right)$ , $\theta_0 = 180^\circ$	$A = 8.62 \cdot 10^{-3}$	$A = 3.45 \cdot 10^{-2}$
<b>C4</b>	$E(f)$ : Jonswap, $D(\theta)$ : narrow cardioid $D(\theta) = 1.27 \cos^{40}\left(\frac{1}{2}(\theta - \theta_0)\right)$ , $\theta_0 = 180^\circ$	$A = 8.62 \cdot 10^{-3}$	$A = 3.45 \cdot 10^{-2}$

TABLE 3.1 – Description of the initial spectra : cases C1 to C4

### 3.3.2 Concept of self-similarity

The self-similar solutions of the conservative homogeneous KE (equation 3.6), called “purely nonlinear” KE, can be written as (Pushkarev et al., 2003; Badulin et al., 2005) :

$$N(\mathbf{k}, t) = at^\alpha U_\beta(\xi), \quad \xi = b\mathbf{k}t^\beta \quad (3.7)$$

where  $U_\beta$  is a shape function and  $a$ ,  $\alpha$ ,  $b$  and  $\beta$  are constants. Values of  $\alpha$  and  $\beta$  are  $4/11$  and  $2/11$ , respectively.

The variance spectrum writes as :

$$F(\omega, \theta, t) = a't^\alpha \omega^4 U_\beta(y, \theta), \quad y = b'\omega^2 t^\beta \quad (3.8)$$

with  $a'$  and  $b'$  constants.

Spectra that are solution of equation 3.6 have a strong tendency to self-similar behavior. This means that the shape function  $U_\beta$  becomes time-independent after a short time of simulation.

One can deduce from these solutions that the total energy  $E_{tot}$  decreases as  $t^{-1/11}$  (Pushkarev et al., 2003; Badulin et al., 2005), which leads to  $H_{m0} \propto t^{-1/22}$ . The self-similar

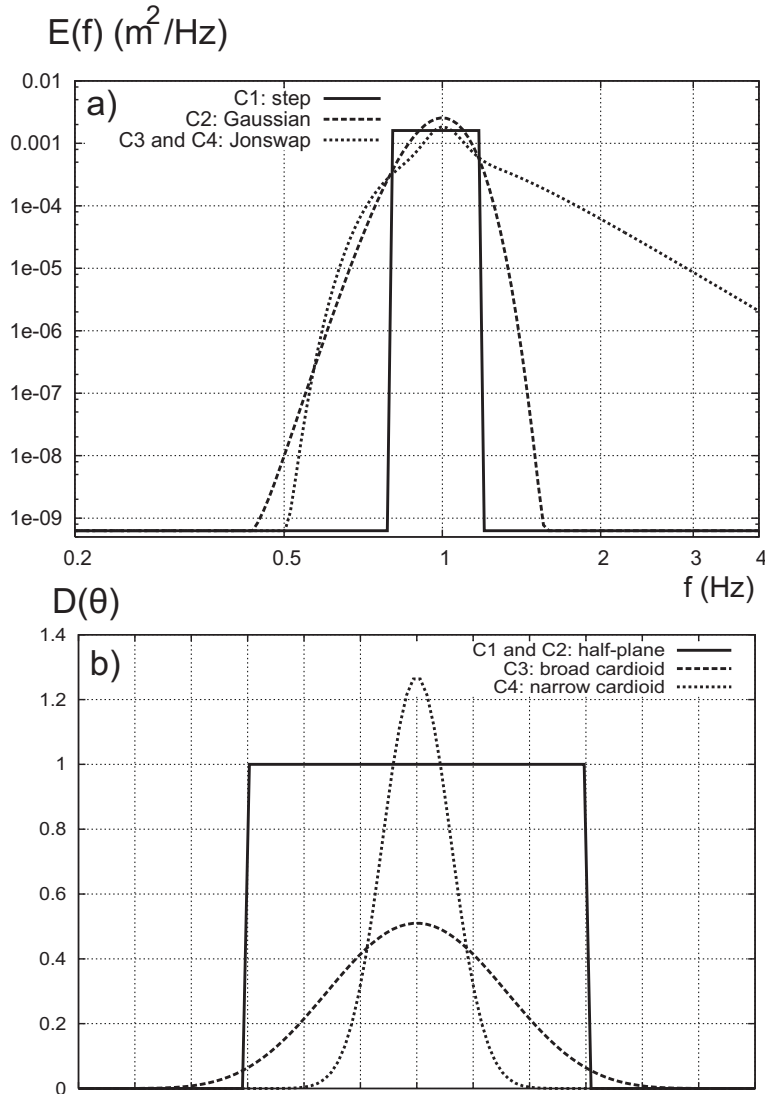


FIGURE 3.2 – Initial conditions : a) three different frequency spectra : step, Gaussian and Jonswap combined with b) three different distribution  $D(\theta)$  : half-plane, broad and narrow cardioids.

solutions also describe the downshift of the spectral peak frequency  $f_p$ , varying as  $t^{-1/11}$ . These results are assessed in the following.

### 3.3.3 Evolution of representative sea state parameters

Figure 3.3 shows the time evolution of  $H_{m0}/H_{m0,\text{init}} = H_{m0}/H_{m0}(t = 0)$  using the GQM algorithm. This evolution is compared with  $t^{-1/22}$  and with the  $H_{m0}/H_{m0,\text{init}}$  curve obtained with the DIA method for C3.b.

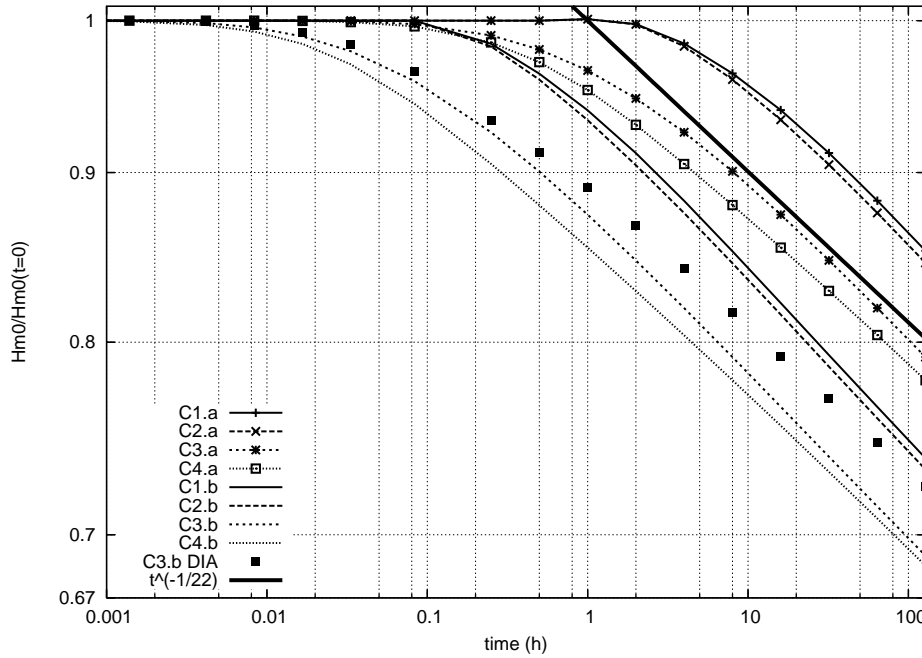


FIGURE 3.3 – Time evolution of  $H_{m0}/H_{m0,\text{init}}$ . GQM method : eight test-cases. DIA : Case C3.b. Comparison to the law in  $t^{-1/22}$  (Badulin et al., 2005).

$H_{m0}$  is monotonically decreasing, which means that the energy is not conserved. There is a loss of energy with time because the integration of the KE is performed over a limited frequency domain (0.2-4 Hz) and the nonlinear wave interactions carry part of the energy out of this range. After a certain time,  $H_{m0}$  evolves like  $t^{-1/22}$ . As energy is proportional to  $H_{m0}^2$ , we verify the behavior of  $E_{\text{tot}}$  in  $t^{-1/11}$  described by e.g. Badulin et al. (2005). This confirms the known theoretical result that the wave energy is only formally conserved (Pushkarev & Zakharov, 2000; Pushkarev et al., 2003).

We note that  $H_{m0}$  begins to behave like  $t^{-1/22}$  more rapidly for C3 and C4 than for C1 and C2. Indeed, with the initial step-like or Gaussian spectra (C1 and C2),  $H_{m0}$  is conserved over the modeled frequency range until the HF part of the spectrum reaches the upper frequency  $f_{\max}$ . Then energy starts leaking toward higher frequencies. As pointed out by Young & Van Vledder (1993) and Young (1999), even if the nonlinear interactions can involve components of the whole wavenumber space, they are much more effective for neighbouring than for distant components. Thus, losses of energy at high frequencies are small when the high frequency energy level is low, as in cases C1 and C2 where a small amount of energy is sent outside the discretization domain at the beginning of the simulation. The initial Jonswap-type spectra (C3 and C4) start leaking toward higher frequencies from the beginning of the simulation because of their initial  $f^{-5}$  high frequency shape. Furthermore,  $H_{m0}$  evolution for the step-like and Gaussian cases (C1 and C2) is very similar, which shows that, apart from the effect of the HF shape, the initial shape of  $E(f)$  has a small influence. The initial angular distribution  $D(\theta)$  does not affect the

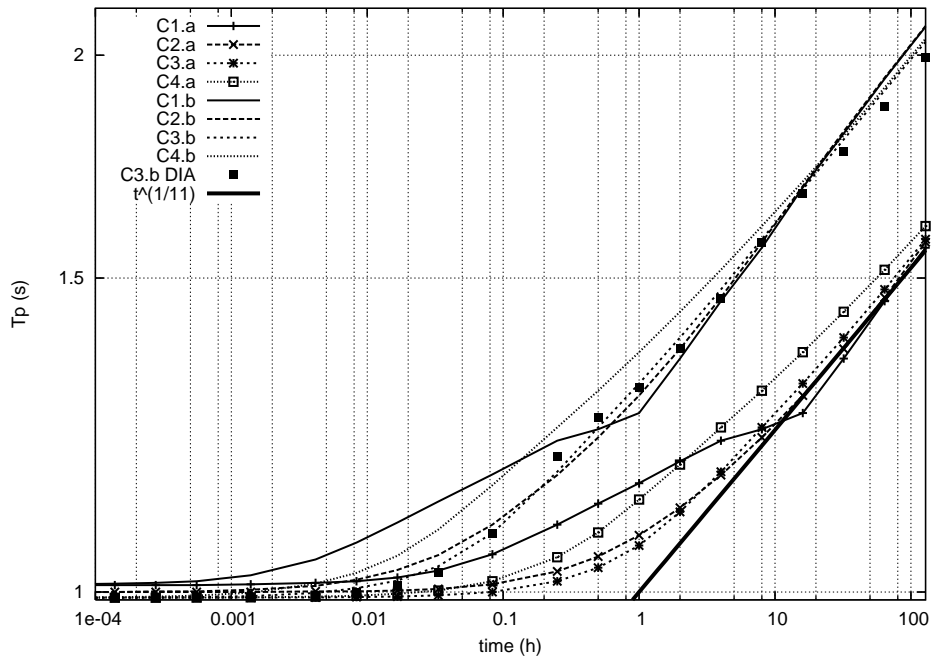


FIGURE 3.4 – Time evolution of the peak period of the wave spectrum  $T_p$ . GQM method : eight test-cases. DIA : Case C3.b. Comparison to the law in  $t^{1/11}$  (Badulin et al., 2005).

evolution of  $H_{m0}$  since C3 and C4 curves are very similar.

The time evolution of  $H_{m0}/H_{m0,\text{init}}$  depends on the initial value of  $H_{m0}$  or the corresponding initial steepness  $\varepsilon$ . It is as faster as  $\varepsilon_{\text{init}}$  is larger. This is due to more intense nonlinear energy transfers as the steepness of the sea state increases. In case a ( $\varepsilon_{\text{init}} = 0.10$ ),  $H_{m0}$  is reduced by 15 to 20% at the end of the simulation. In case b ( $\varepsilon_{\text{init}} = 0.20$ ), the decrease is larger, about 25 to 30%.

The DIA curve shows a smaller decrease than the GQM curve for the same case (C3.b), which may be related to the slower formation of the HF tail when using DIA (see subsection 3.4 below).

Another important parameter to look at is the peak period  $T_p$  (Figure 3.4). Results obtained with the same initial steepness are quite close to each others, suggesting that the influence of the initial shape of the directional spectrum is weak. The peak period stabilizes quite rapidly when a peak is formed in the spectrum. By contrast, the influence of the initial steepness is more significant.  $T_p$  varies more rapidly for a larger  $\varepsilon_{\text{init}}$  and increases to a much higher value. This reflects that the spectrum migrates faster toward low frequencies. Furthermore, it can be noticed that after a certain time,  $T_p$  tends to vary in  $t^{1/11}$ . This reproduces the downshift of the spectral peak according to the self-similarity theory (Pushkarev et al., 2003; Badulin et al., 2005). Comparisons with DIA results show small differences.

Finally we examine the mean angular width defined by :

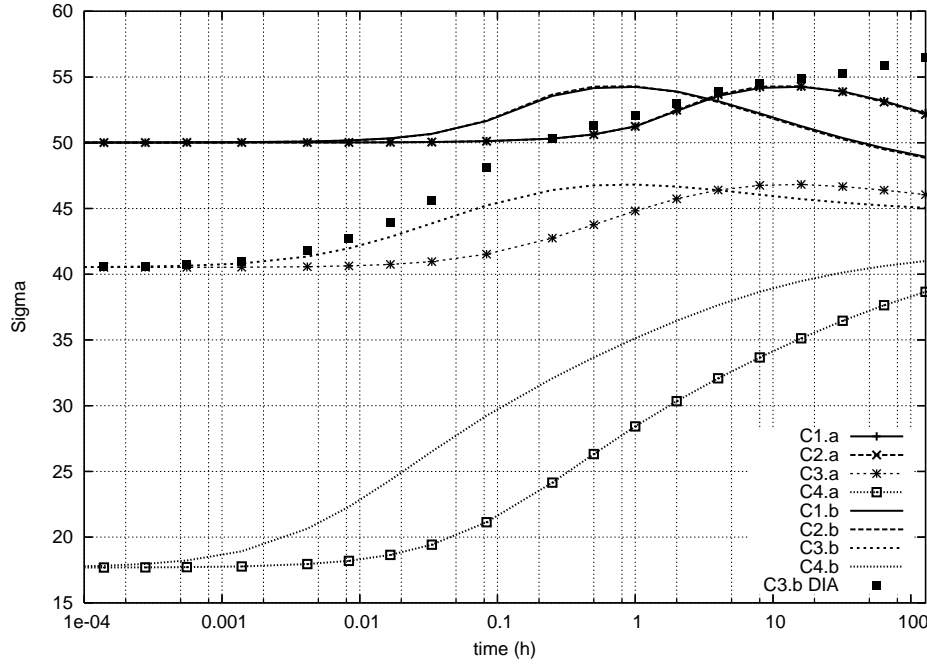


FIGURE 3.5 – Time evolution of the wave spectrum mean angular width  $\sigma$ . GQM method : eight test-cases. DIA : Case C3.b.

$$\sigma = \frac{\int_f \sigma(f) E(f) df}{\int_f E(f) df}$$

with  $\sigma(f) = \sqrt{2(1 - m_1)}$  and  $m_1 = \int_0^{2\pi} D(f, \theta) \cos(\theta - \theta_0) d\theta$ , where  $\theta_0(f)$  is the mean direction of the wave field (Figure 3.5).  $\sigma$  converges to a value in the range 40-50 degrees whichever the initial conditions are. Time evolution of  $\sigma$  for cases C1 and C2 (same initial angular half-plane distribution) is identical. The two other cases (cardioids) evolve in a quite different way. The initial value of  $\sigma$  for C4 ( $\cos^{40}(\theta/2)$  initial angular distribution) is smaller than the other ones. Thus  $\sigma$  monotonically increases during the simulation. For cases C1 to C3,  $\sigma$  starts increasing at the beginning of the simulation and then decreases. Differences between cases Ci.a and Ci.b can be noticed : the mean angular width appears to be changing much more quickly in case b (higher initial steepness). DIA simulations give a much higher  $\sigma$ , increasing with time.

### 3.3.4 Evolution of the frequency spectrum

Results using GQM (Figures 3.6 and 3.7) and DIA (Figures 3.8 and 3.9) algorithms for evaluating  $S_{nl}$  are consecutively presented. Figure 3.6 reports the temporal evolution of  $E(f)$  for case C1.b. A short term scale from 0 to 15 min (Figure 3.6-a) and long term scale from 30 min to 128 h (Figure 3.6-b) are considered. The beginning of the simulation

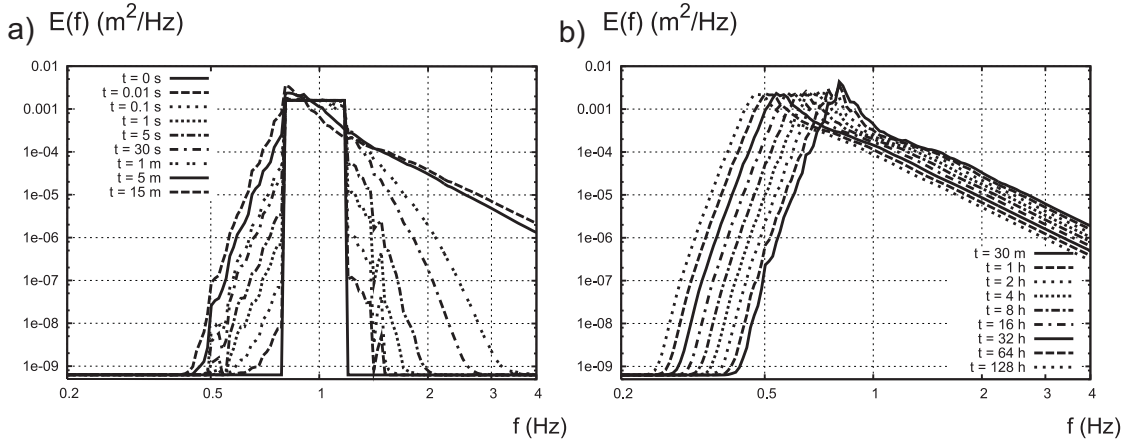


FIGURE 3.6 – Evolution of the frequency spectrum  $E(f)$  (from 0 to 128 h), using the GQM method. Initial case C1.b. a) Short term evolution (from 0 to 15 min). b) Long term evolution (from 30 min to 128 h).

is a period of intense wave-wave energy transfers. During this phase, the spectrum, which presents a shape very different from the quasi-equilibrium final shape, evolves very rapidly. A main peak appears after about 15 min and then migrates towards lower frequencies. The high frequency (often referred as HF) part of the spectrum takes a typical shape in  $f^{-m}$  with  $m \approx 4.1$  after a short time period ( $t \geq 15$  min).

The spectra of the eight cases considered (not shown here) evolve similarly with time. The shape of  $E(f)$  reached at the end of the simulations slightly depends on the initial shape. Time evolution of  $E(f)$  is faster for larger (cases Ci.b) than for smaller (cases Ci.a)  $\varepsilon_{init}$ .

In order to verify the self-similar evolution of the spectrum (subsection 3.2), Figure 3.7 shows the shape function  $U_\beta$  for a wave direction corresponding to the main direction of propagation ( $\theta_0 = 180$  degrees) superimposed at 7 times, spanning the interval 2-128 h (case C3.b). The variations of  $U_\beta$  during this interval are very small (less than a few percent), which confirms a self-similar evolution. Cases C1.b, C2.b and C4.b also lead to self-similarity after a few hours (not shown here).

On the whole, the self-similarity depends little on the initial spectrum. The time necessary to reach self-similarity depends on the initial steepness. Indeed, in the cases Ci.a, the spectrum needs more time (about 16 to 32 h) to reach its typical self-similar shape.

These results show that the dynamical evolution of the spectrum is described in an almost perfect way by the self-similarity equations 3.7 or 3.8. Moreover, they confirm the ability of our algorithm to reproduce the expected theoretical evolution.

The DIA spectra obtained in the same conditions (Figure 3.8) are quite different from the GQM spectra, especially at the beginning of the simulation ( $t < 5$  min) for frequencies greater than the peak frequency. Instead of a  $f^{-4}$  tail, the DIA method produces a succession of peaks in the HF range. However, after some time (about 5 min), we also

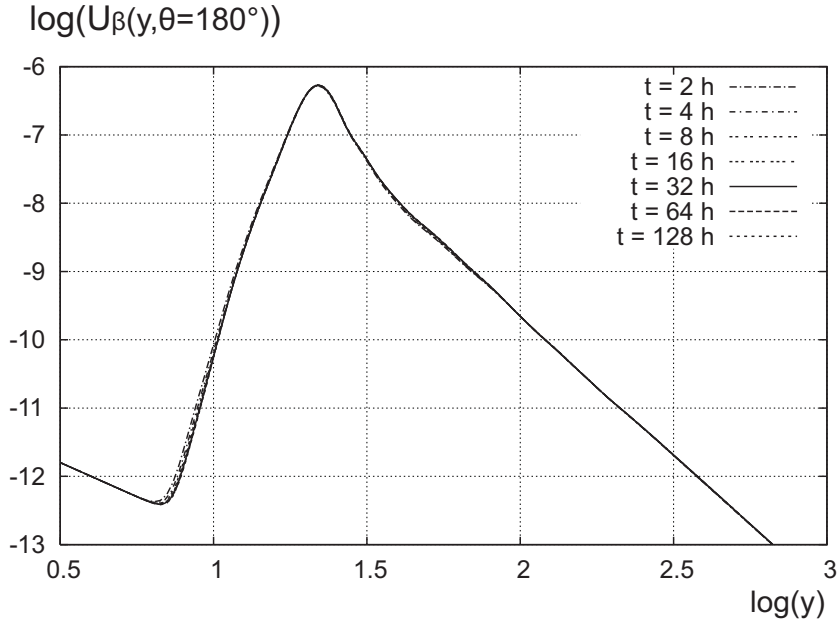


FIGURE 3.7 – Variation of the shape function  $U_\beta(y, \theta = 180^\circ)$  with  $y$  (equation 3.8), as computed using the GQM method between  $t = 2$  h and  $t = 128$  h. Initial spectrum C3.b.

observe with DIA the formation of the  $f^{-4}$  HF tail. At the end of the simulation, the DIA spectrum has a larger bandwidth than the GQM spectrum, and its peak value is lower. The self-similarity of DIA frequency spectra is shown in Figure 3.9 (case C3.b). As for the GQM simulations, the self-similarity of  $E(f)$  is observed after a few hours (depending on the initial case). This is not surprising because the collision integral  $S_{nl}$  (equation 1.64) obeys homogeneity properties (Badulin et al., 2005) for both methods of calculation of the nonlinear interactions. Self-similar solutions can thus be derived in both cases.

### 3.3.5 The angular spreading of wave energy

Here we aim at analyzing the detailed angular distribution of energy. To that end we computed the normalized directional spreading function under the form  $\tilde{D}(f/f_p, \theta) = D(f/f_p, \theta)/D_{max}(f/f_p)$  where  $D_{max}(f/f_p)$  is the maximum value of  $D(f/f_p, \theta)$  over  $\theta$  at each frequency  $f/f_p$ .

$\tilde{D}(f/f_p, \theta)$  is represented for GQM in Figure 3.10-a at  $t = 128$  h for case C2.b. This representation allows us to get a better idea of the structure of the directional distribution, although the normalized values at each frequency can give some false impressions. In particular, we should remember that at high frequencies the absolute values of the spectrum are low and that the HF bimodality is somewhat amplified by this normalization. The GQM method clearly exhibits the bimodal structure of the angular distribution for frequencies above and below the peak frequency. The side lobes are symmetrically placed around the mean direction  $\theta_0 = 180$  degrees. The directional distribution is unimodal and very narrow

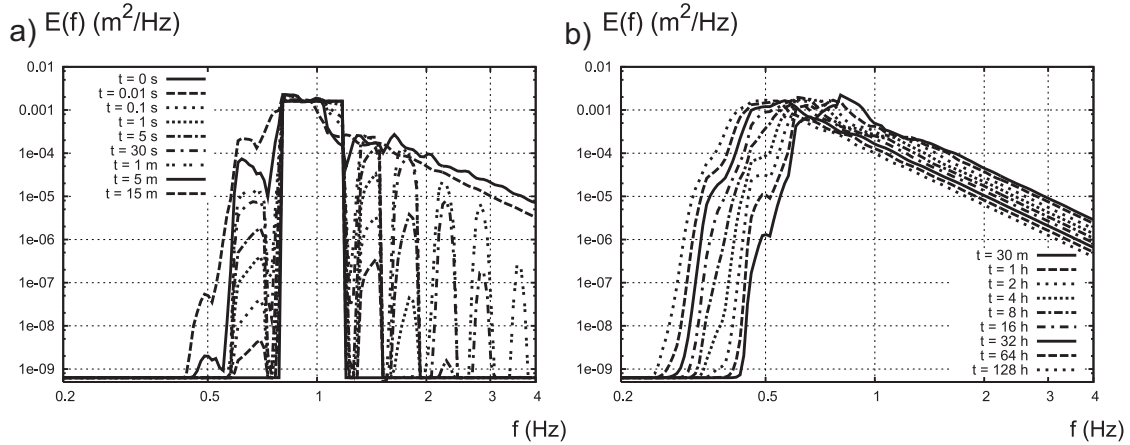


FIGURE 3.8 – Time evolution of the frequency spectrum, using the DIA method. Initial case C1.b. a) Short term evolution (from 0 to 15 min). b) Long term evolution (from 30 min to 128 h).

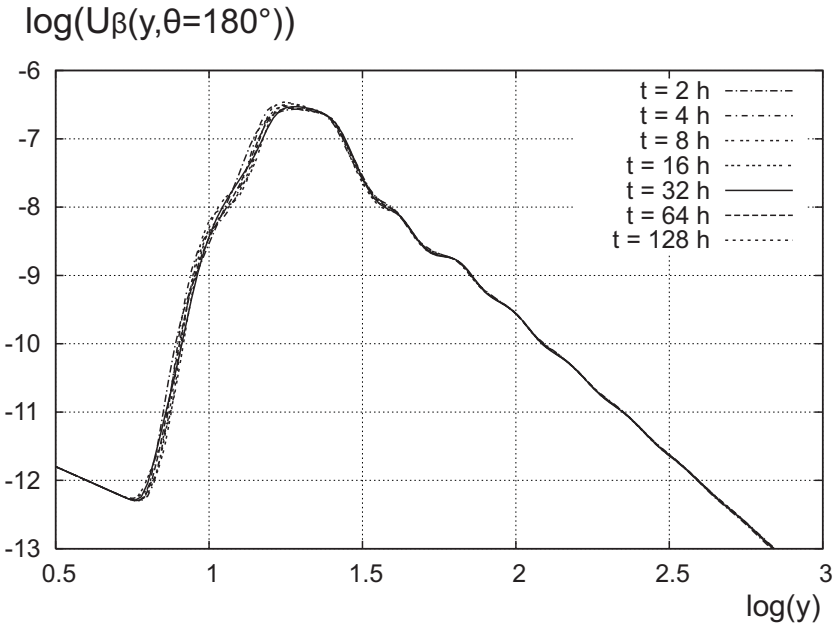


FIGURE 3.9 – Variation of the shape function  $U_\beta(y, \theta = 180^\circ)$  with  $y$  (equation 3.8), as computed using DIA between  $t = 2$  h and  $t = 128$  h. Initial spectrum C3.b.

near the peak frequency. For  $f/f_p \geq 4$ , the directional spectrum becomes unimodal again but is much more isotropic. This structure is due to nonlinear interactions which redistribute energy to large angles from the mean wave direction and contribute to the broadening of the spectrum (Young & Van Vledder, 1993). Figure 3.11 illustrates these redistributions of energy rather well. It shows that  $S_{nl}$  sends energy in oblique directions, not only at

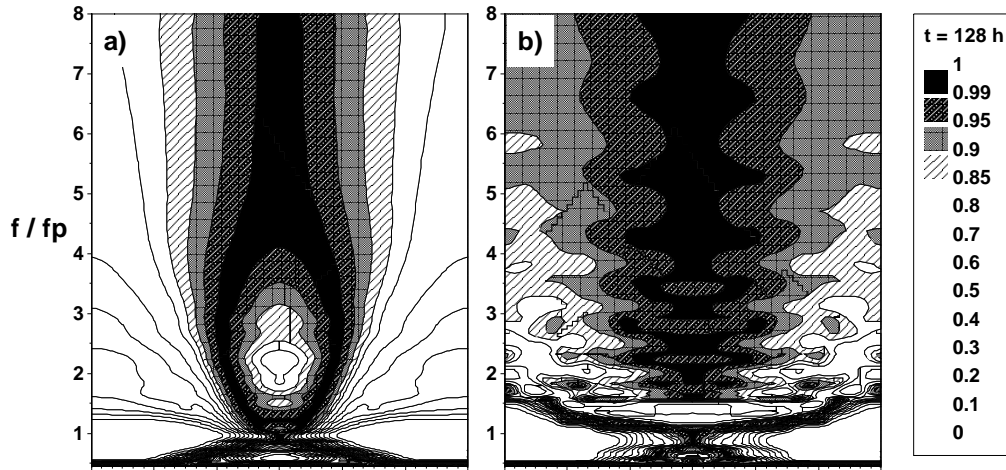


FIGURE 3.10 – Normalized directional spreading function  $\tilde{D}(f/f_p, \theta)$  at  $t = 128 \text{ h}$ . Case C2.b. a) GQM method. b) DIA method.

frequencies above the peak, but also at low frequencies (Figure 3.11-b), and induces the relatively narrow distribution of the spectrum around the peak. The unimodality of the directional distribution for frequencies above  $4f_p$  could be explained by the weakness of the  $S_{nl}$  term at these frequencies at the end of the simulation, that is too small to redistribute energy to oblique directions.

The variation of the angle between the two (symmetric) lobes,  $2\theta_l$  (where  $\theta_l$  is the angle between each lobe and the main direction), with  $f/f_p$  is shown in Figure 3.12. For frequencies greater than  $f_p$ ,  $2\theta_l$  increases to a maximum varying in the range 110-140 degrees. This maximum is reached for frequencies between  $2f_p$  to  $3f_p$ . Then  $2\theta_l$  decreases and the directional spectrum becomes unimodal for frequencies between 3.8 and  $6f_p$ .

Figure 3.10-b represents  $\tilde{D}(f/f_p, \theta)$  obtained using DIA, again at  $t = 128 \text{ h}$  for case C2.b. The results are dramatically different. The directional distribution is very irregular. Nevertheless we can note that the two distributions are unimodal and narrow near the peak frequency and seem to be bimodal below  $f_p$ .

Figure 3.13 compares sections of  $D(f, \theta)$  at different frequencies for GQM and DIA simulations (initial case C3.b). The shape of the directional distribution obtained using GQM is rather similar for the 8 cases (not shown here), although some differences were noted. In particular, the HF bimodality is more pronounced in the case C4, and especially C4.a, than in the other ones. DIA gives a much more spread directional distribution at  $f > f_p$ , and no clear bimodality. The low frequency (sometimes referred as LF) bimodality is more pronounced when using an exact method for  $S_{nl}$ , as already described by Hisaki (2007).

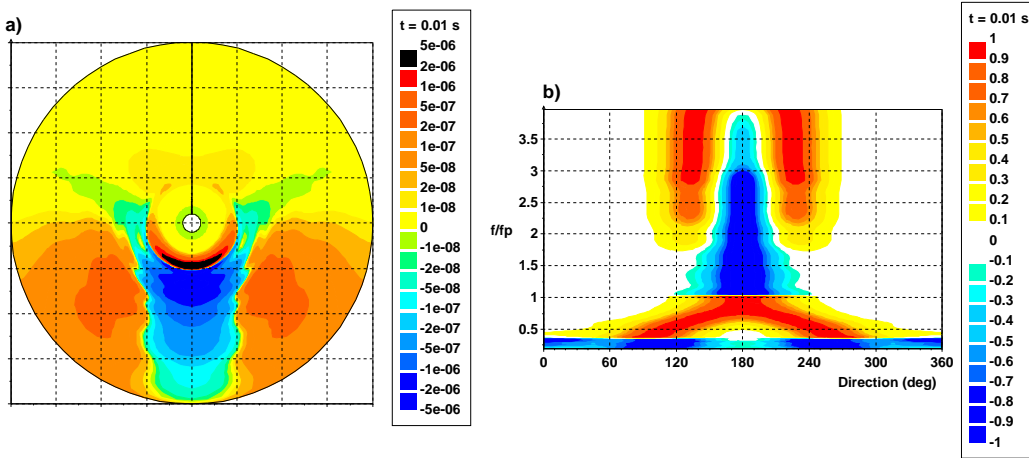


FIGURE 3.11 – Nonlinear transfer term  $S_{nl}$  calculated by the GQM method at  $t = 0.01$  s (first time step) for case C3.b. a)  $S_{nl}(f, \theta)$  in polar coordinates, b)  $S_{nl}(f/f_p, \theta) / |Q_{nl4,max}(f/f_p)|$  in Cartesian coordinates.

## 3.4 Influence of wind input and dissipation

### 3.4.1 Model equation and initial conditions

In this section, we examine the influence of wind input and dissipation in addition to wave-wave nonlinear transfers, on the evolution of the wind wave spectrum. This is typical of a duration-limited wave growth case (e.g. Young, 1999). This case was chosen as a first step in our work for faster simulation times (“point model” version of our code). Extension to 1D situations (e.g. fetch limited cases) is now under consideration and will be reported in a separate paper. A constant wind of  $10\text{ m.s}^{-1}$  is considered. We test three combinations (termed set I, II and III) of the wind input ( $S_{in}$ ) and dissipation ( $S_{diss}$ ) terms (see Table 3.2). Set I corresponds to WAM-Cycle 3 with the wind parameterization of Snyder et al. (1981) and the whitecapping dissipation of Hasselmann (1974) as formulated by Komen et al. (1984). Set II consists of the expression of Yan (1987) for  $S_{in}$  with the parameters values of Van der Westhuysen et al. (2007), combined with the whitecapping model of Van der Westhuysen et al. (2007) and Van der Westhuysen (2008). Set III corresponds to WAM-Cycle 4 with the Janssen (1989, 1991) wind input model and the  $S_{diss}$  model of Komen et al. (1984) with the coefficients values proposed in WAM-Cycle 4 (Günther et al., 1992). Set III is run with two options : no parametric tail (free tail : ft) ;  $f^{-4}$  HF tail imposed over the frequency range  $[f_d, f_{max}]$  (imposed tail : it) as implemented in WAM-Cycle 4. Note that among the parameterizations used here, the sets I and III-it are the only ones that have been tested in a wide range of sea states.

We chose to use some traditional parameterizations (sets I and III) and a more recent one

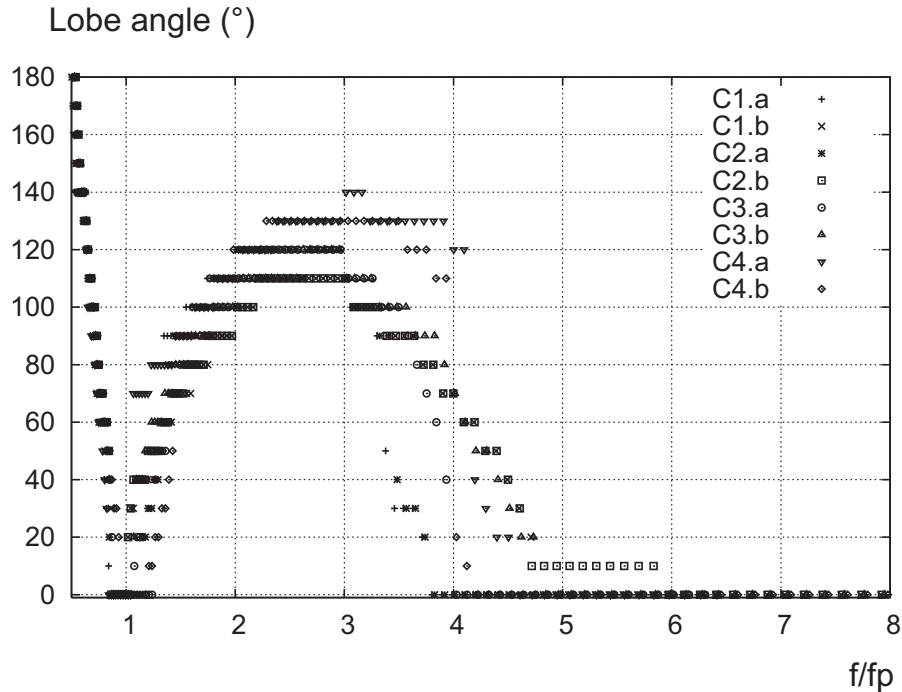


FIGURE 3.12 – Angle between the lobes of the wave directional distribution,  $2\theta_l$ , versus  $f/f_p$  at  $t = 128$  h for the eight simulated cases. GQM method.

for the dissipation (set II). This is of course a restricted choice but it allows to highlight some interesting differences in the evolution of the spectrum. Moreover, we may note that some questions have been raised on the validity of set II at large scales (Ardhuin & Boyer, 2006). For completeness the reader should refer, for instance, to the recent work of Babanin et al. (2007b,a); Ardhuin et al. (2008, 2009). The parameterizations of Tolman & Chalikov (1996) or Bidlot et al. (2005) could also be interesting candidates.

As previously, all the simulations are run using the GQM and DIA methods for comparison. The parameters of the source and sink terms were not retuned when changing the method for calculating the  $S_{nl}$  term. For instance the model of Van der Westhuyzen et al. (2007) for  $S_{diss}$  was computed with the coefficients  $C_{ds} = 5.0 \cdot 10^{-5}$  and  $B_r = 1.75 \cdot 10^{-3}$ , calibrated for DIA simulations.

Simulations were run from the initial cases Ci.a described in Section 3. As the evolution of the spectrum is strongly influenced by the amount of energy brought by the wind, we estimated that it was not useful to test two different values of  $H_{m0,init}$ .

In the simulations the discrete frequency-direction grid is composed of 128 frequencies, with geometric spacing ( $f_{i+1}/f_i = 1.031$ ) from  $f_{p0}/25$  (0.04 Hz) to  $2f_{p0}$  (2 Hz) and 72 directions with a constant spacing of 5 degrees. The simulations were run during 96 hours of physical time.

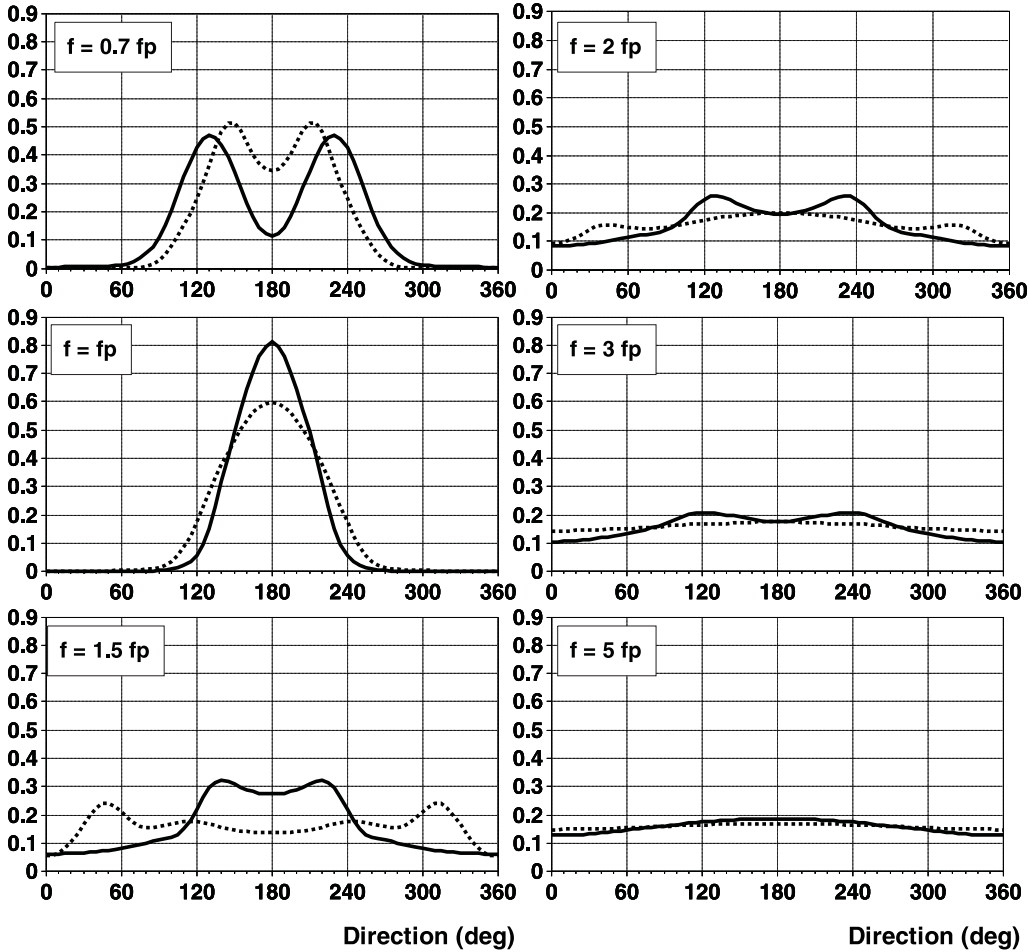


FIGURE 3.13 – Sections of the directional spreading function  $D(f, \theta)$  at  $t = 128$  h, at six frequencies ( $f = 0.7f_p$ ,  $f = f_p$ ,  $f = 1.5f_p$ ,  $f = 2f_p$ ,  $f = 3f_p$  and  $f = 5f_p$ ) for case C3.b. GQM (solid lines) and DIA (dashed lines) methods.

### 3.4.2 Evolution of representative sea state parameters

Time evolutions of  $H_{m0}$ ,  $T_p$  and  $\sigma$  are plotted in Figure 3.14 for set II.  $H_{m0}$  and  $T_p$  are increasing and become quasi-steady after 48 h of simulation when using GQM, close to the end of the simulation for DIA. At first sight, there is almost no difference between the curves obtained from the 4 initial cases Ci.a. Plots in logarithmic scale show little differences at the initial stage (first few minutes) for  $H_{m0}$  and  $T_p$ . These differences are more pronounced for  $\sigma$ , due to differences in the initial value of  $\sigma$ . However, after about 10 min, simulations converge to the same value. The figure enables to compare DIA and GQM. We recall that the parameters in  $S_{in}$  and  $S_{diss}$  are the same for both simulations and that they were calibrated for DIA simulations. This results in differences between  $H_{m0}$  and  $T_p$  growth curves. DIA curves are higher for both  $H_{m0}$  and  $T_p$ , but recalibration of some coefficients could lead to similar results when using GQM. Nevertheless, we emphasize that

Set	$S_{in}$	$S_{diss}$	Tail option
<b>I</b> WAM-Cycle 3	Snyder et al. (1981)	Komen et al. (1984)	free tail
<b>II</b>	Yan (1987)	Van der Westhuysen et al. (2007) Van der Westhuysen (2008)	free tail
<b>III-ft</b>	Janssen (1989, 1991)	Komen et al. (1984) Günther et al. (1992)	free tail
<b>III-it</b> WAM-Cycle 4	Janssen (1989, 1991)	Komen et al. (1984) Günther et al. (1992)	imposed $f^{-4}$ tail

TABLE 3.2 – Description of the sets (I, II, III) and options (free tail or imposed tail).

under unsteady and turning wind conditions, differences can be much more important (e.g. Benoit, 2006). Unsteady cases are more sensitive to the choice of the method for  $S_{nl}$  and DIA was shown to react more slowly to changing conditions. Beside this, DIA gives a larger directional spreading, which is a classical problem of the DIA method.

Figure 3.15 shows the differences arising from the use of the four sets. As initial conditions have almost no influence, we choose to consider only C3.a results. At first, significant trends can be noticed : results obtained with set III without parametric tail gives much higher  $H_{m0}$  and  $T_p$  values. They stabilize more slowly and do not really reach the quasi-steady state before the end of the simulation. We analyze precisely the reasons for this much important growth in subsection 4.3. The three other curves (sets I, II and III-it) are closer to each other, but still with some differences. The growth curves for  $H_{m0}$  and  $T_p$  obtained using DIA are slightly over those obtained using GQM. Differences are very small when using sets I and III-ft. Although the objective of this work is not to calibrate or validate the parameterizations, it should be noticed that the final values of  $H_{m0}$  and  $T_p$  for sets I, II and III-it are quite underestimated compared to the fully developed Pierson-Moskowitz asymptotic limits as reanalyzed by Alves et al. (2003), showing some deficiencies of the presently used source terms or need to calibrate them.

For the mean directional width  $\sigma$ , DIA gives once again a larger directional spreading, whichever the parameterization used to model the source terms. Set I gives a much larger directional spreading than the other sets whenever DIA or GQM is used for  $S_{nl}$ . This is related to the directional structure and magnitude of the sum  $S_{in} + S_{diss}$ . For instance, the  $S_{in}$  model has a  $\cos \theta$  directional dependence for sets I and II and a narrower distribution in  $\cos^2 \theta$  for set III.  $S_{in}$  therefore plays a role in the spreading of the angular spectrum, but the relative magnitude and structure of  $S_{in}$  and  $S_{diss}$  is also determinant. The influence of  $S_{in}$  and  $S_{diss}$  on the directional structure of the spectrum is analyzed in subsection 4.4.

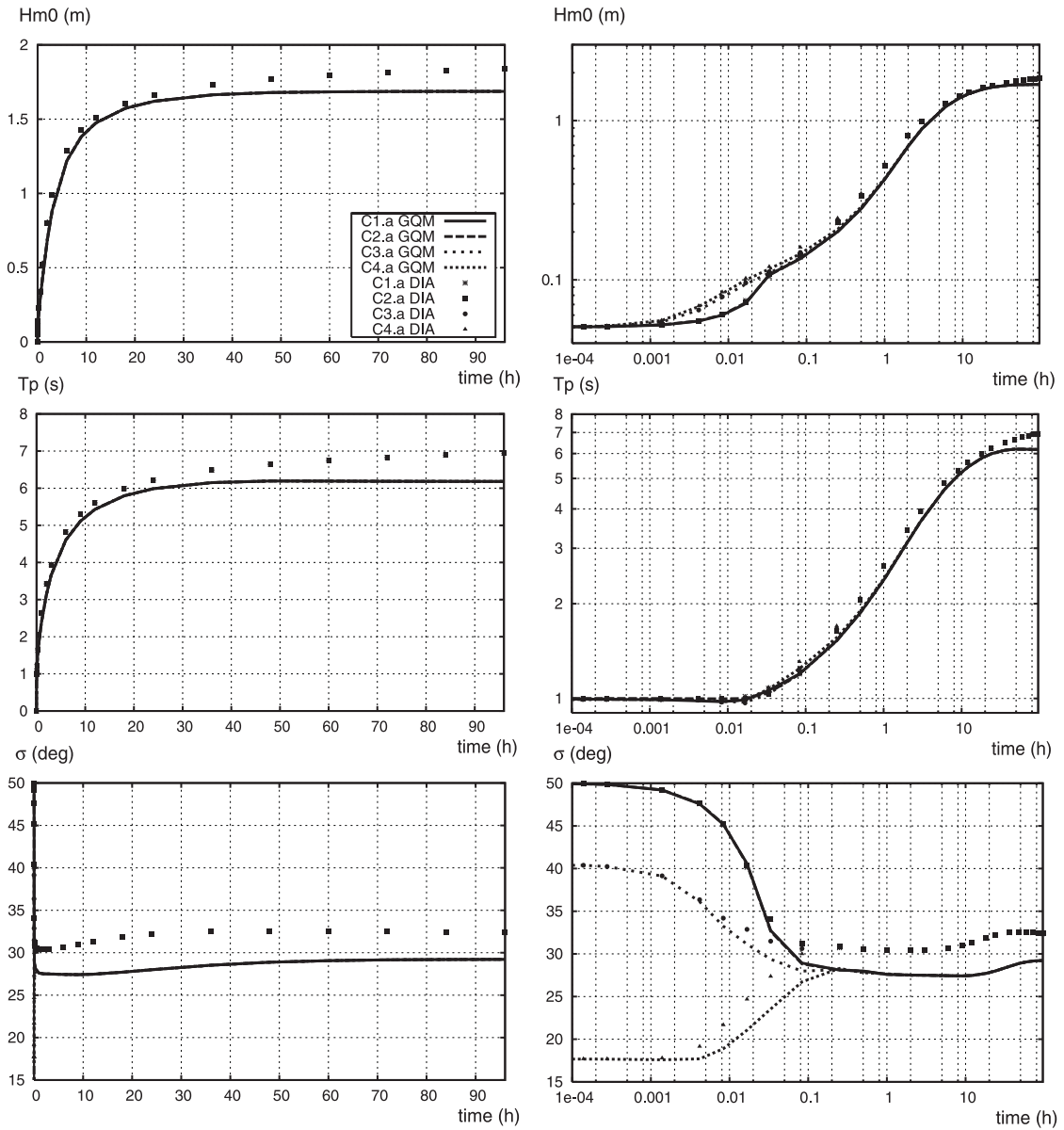


FIGURE 3.14 – Time evolution of the wave height  $H_{m0}$ , the peak period  $T_p$  and the mean angular width  $\sigma$  for the 4 initial cases. Set II, GQM and DIA methods, linear scale (left column), logarithmic scale (right column).

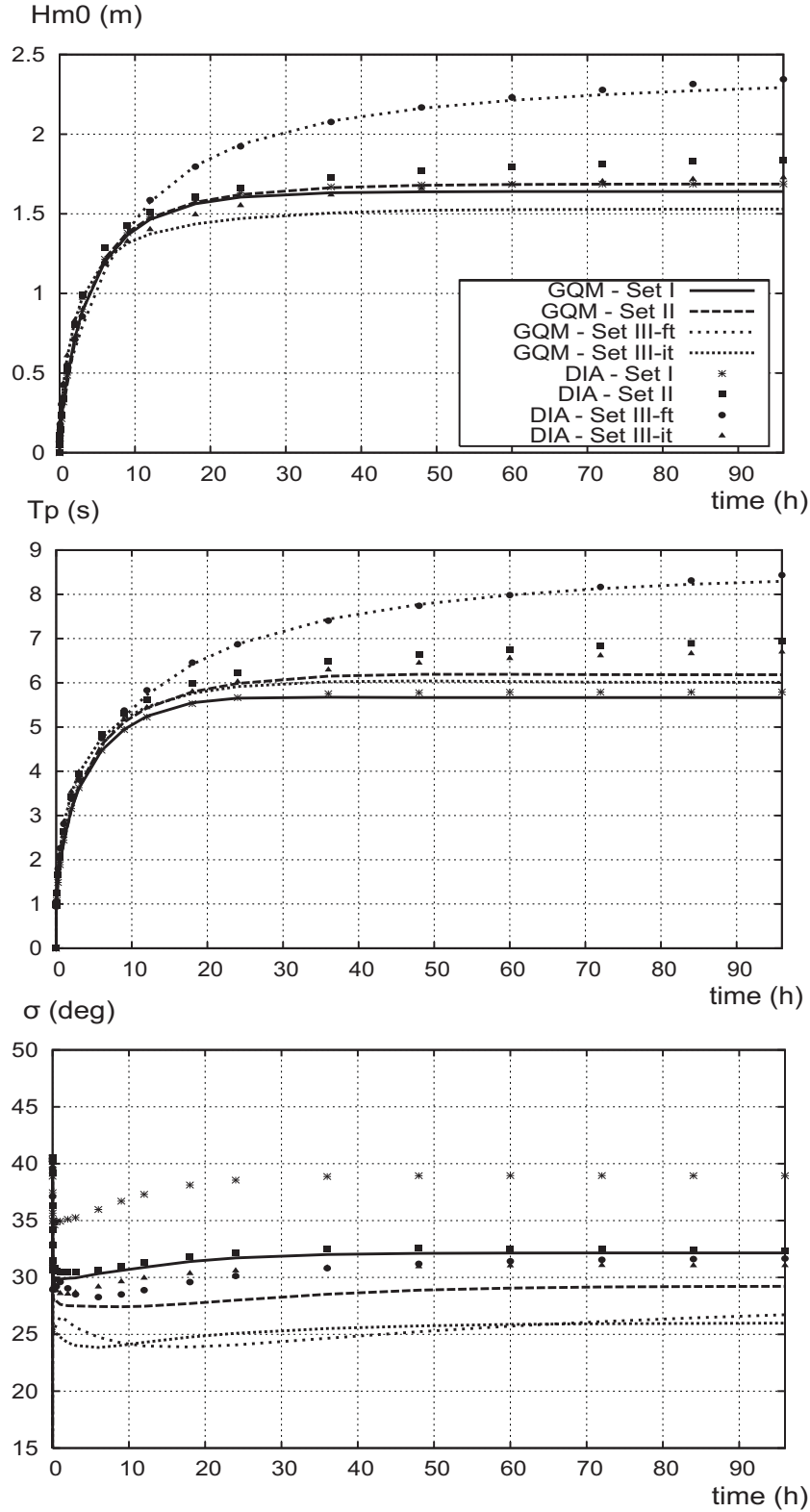


FIGURE 3.15 – Time evolution of the wave height  $H_{m0}$ , the peak period  $T_p$  and the mean angular width  $\sigma$ . Initial case C3.a, GQM and DIA methods. Comparison of sets I, II, III-ft and III-it.

### 3.4.3 Evolution of the frequency spectrum

Figure 3.16 reports the evolution of the frequency spectrum  $E(f)$  (initial condition C1.a) using sets I to III. For all sets, the evolution of  $E(f)$  shows similar trends.  $E(f)$  evolves rapidly during the first few minutes. The spectral peak appears after about 5 minutes, then it begins to migrate towards low frequencies, gaining energy due to wind input. Then the increase slows down and  $E(f)$  stabilizes. It is noted that the three other initial conditions produce the same spectra after a few minutes (figures not reported here).

The final shape (at  $t = 96$  h) is a little different from the purely nonlinear shape obtained in Section 3. It is less peaked and the HF  $f^{-4}$  tail is not observed in every case. For example, the  $f^{-4}$  HF tail can be only observed over a very limited range for set III-ft (without constrained tail). At higher frequencies,  $E(f)$  decreases much more steeply than observed spectra (Banner et al., 1989; Young & Babanin, 2006; Long & Resio, 2007) due to dissipation. Differences between DIA and GQM spectra are observed for all the source terms used. At the beginning of the simulation, DIA produces a succession of peaks around the initial step, instead of the smooth and regular shape obtained with GQM. The final shape of the DIA spectrum is more spread in frequency.

One can notice that the evolution of the spectra is influenced by the parameterizations chosen for the source/sink terms. Set III-ft gives spectra that have a much higher maximum value and a smaller peak frequency. Moreover, the evolution of the spectrum is not totally stabilized at the end of the simulation. Similar observations were made in subsection 4.2 for  $H_{m0}$  and  $T_p$ .

#### 3.4.3.1 The HF tail : influence of the models and of the constrained tail

In every studied case, the spectrum is assumed to have a  $f^{-4}$  shape above the last discrete frequency. As observed by Banner & Young (1994) and verified in our calculations, this only influences the last upper frequencies.

In contrast, applying a constrained tail over  $[f_d; f_{max}]$  can influence the results over the entire frequency domain. In the simulations, at the end of the run ( $t = 96$  h), the diagnostic tail is imposed from  $f_d = 3.3f_p$  when using GQM method, and  $f_d = 3f_p$  with DIA.

For sets I, II and III-ft, no diagnostic tail is imposed over the frequency domain. Results obtained using sets I and II show similar evolution, with a HF tail close to  $f^{-4} : f^{-3.97}$  and  $f^{-3.85}$  for set I with GQM and DIA, respectively, and  $f^{-4.18}$  for set II with both DIA and GQM. Note that Van der Westhuysen et al. (2007) found a  $f^{-4.1}$  decay with forcing terms corresponding to set II when modeling a fetch-limited case. Results from set III-ft show a much steeper HF tail with a slope increasing sharply with frequency and decaying much faster than the Banner et al. (1989)  $f^{-5}$  equivalent in terms of k-spectrum. Such a behavior is not supported by theoretical analyses nor observations. This much steeper tail is due to the strong dissipation at high frequencies of the implementation in WAM-Cycle 4 of the Komen et al. (1984) model.

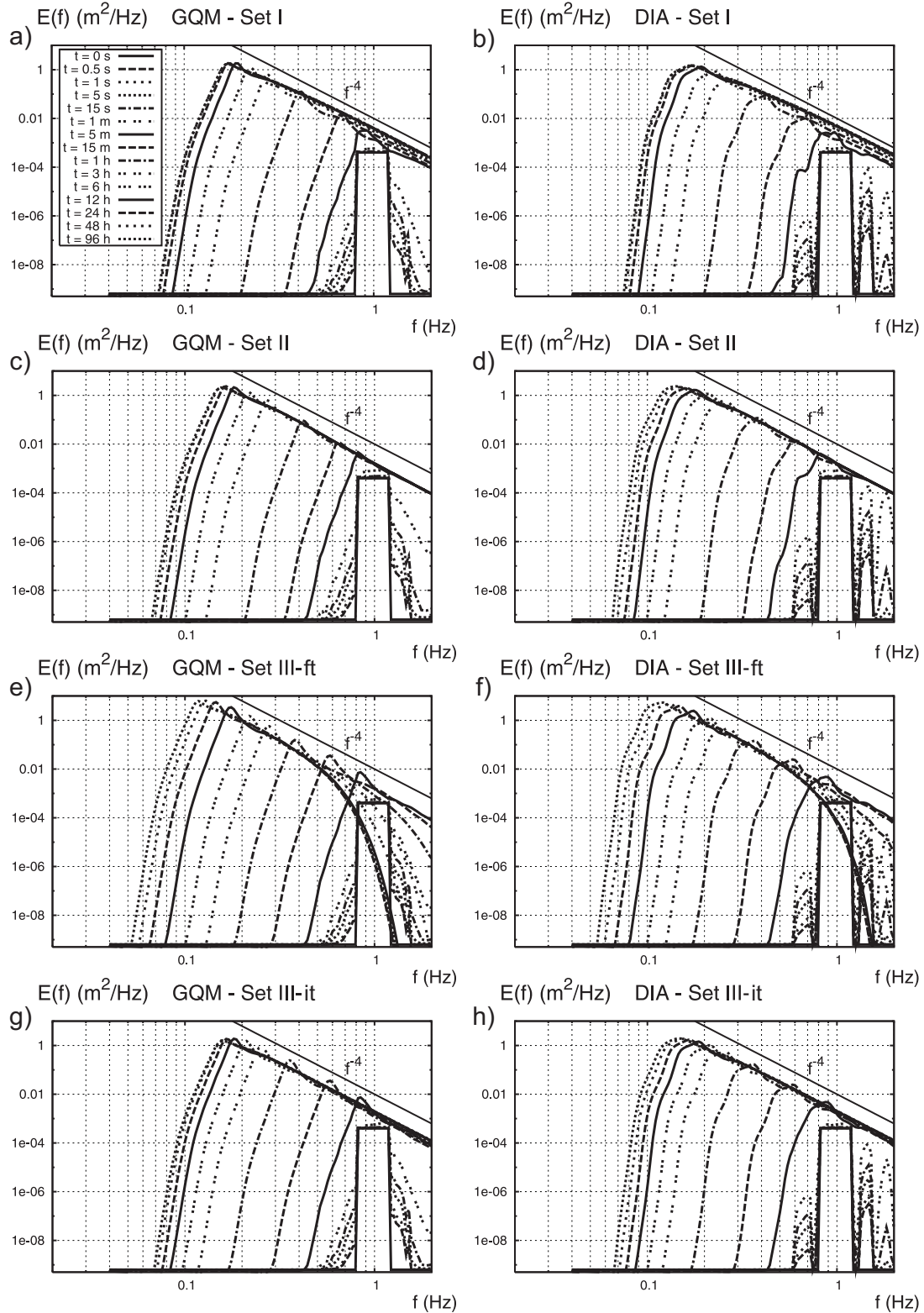


FIGURE 3.16 – Evolution of the frequency spectrum  $E(f)$  (from 0 to 96 h). Initial case C1.a), c), e), g) : GQM method with sets I, II, III-ft and III-it, respectively. b), d), f), h) : DIA method with sets I, II, III-ft and III-it, respectively.

Set III-it (imposed  $f^{-4}$  tail) gives results that are in better agreement with theory and observations than set III-ft. Adding such a parametric tail is not very physical, it just compensates the deficiencies of the parameterizations of set III (WAM 4).

The influence of an imposed HF tail on the computed spectrum was examined by Banner & Young (1994), who showed, as we also found, the importance of an accurate modeling of the HF part of the spectrum and the significant influence of a constrained tail on the development of the entire spectrum. On the other hand, according to Komen et al. (1984) and the WAMDI Group (1988), the precise form of the diagnostic tail has no influence on the results.

We also made some tests using set I and a constrained tail  $f^{-4}$  to see what happens when the modeled tail is very close to the imposed one. As expected, GQM simulations with or without  $f^{-4}$  give nearly the same results.

The main reason why the high frequency range of the spectrum can affect significantly all its evolution, while such low levels of energy are involved, is related to the influence of the HF part of the spectrum on the terms  $S_{in}$  and  $S_{diss}$ . When the energy is increased at high frequencies, the dissipation term of Komen et al. (1984) is increased and the wind input of Janssen (1991) is reduced, which leads to a slowdown in the growth of the spectrum. Figure 3.17 shows the impact of imposing a  $f^{-4}$  HF tail on the calculated source and transfer terms : it results in an increase of  $S_{diss}$  over the whole frequency domain and in a decrease of  $S_{in}$  at the spectral peak. This is due to the presence of integrated parameters (like  $m_0$  and the mean frequency) in the  $S_{diss}$  formula and to a pronounced feedback via the friction velocity  $u_*$  and the wave-induced stress in the Janssen (1991)  $S_{in}$  formula. Thus, the sum  $S_{in} + S_{diss}$  is strongly reduced around the spectral peak frequency. At the same time, the  $S_{nl}$  term is not significantly impacted near  $f_p$ . The sum of the three terms has been plotted in the range 0.04-0.5 Hz for more visibility. Observation of the positive and negative peaks show that the total source term has been reduced by the imposition of the  $f^{-4}$  tail. This therefore explains the artificial increase of wind-wave energy in the absence of a diagnostic tail (III-ft).

Banner & Young (1994) proposed an alternative explanation. According to these authors, a smaller level of energy at high frequencies results in an increase of the  $S_{nl}$  term and thus leads to a larger growth of the spectrum. This explanation was not retained here. As seen in Figure 3.17, the imposition of a HF  $f^{-4}$  tail has a small impact on the global nonlinear energy transfers. The effects on  $S_{nl}$  at high frequencies are important, as seen in the curve representing the relative nonlinear transfer term  $S_{nl}/E(f)$  (e), but the impact on the overall evolution of the spectrum is not significant as compared with the pronounced effect of  $S_{in}$  and  $S_{diss}$ .

### 3.4.3.2 Analysis of source terms balance in the high frequency range

The slope of the HF tail can be explained by the balance of the source terms.

It was shown in section 3 that without any forcing term, the HF tail is close to  $f^{-4.1}$ . The quadruplet interactions tend to maintain a shape close to  $f^{-4}$  at high frequencies,

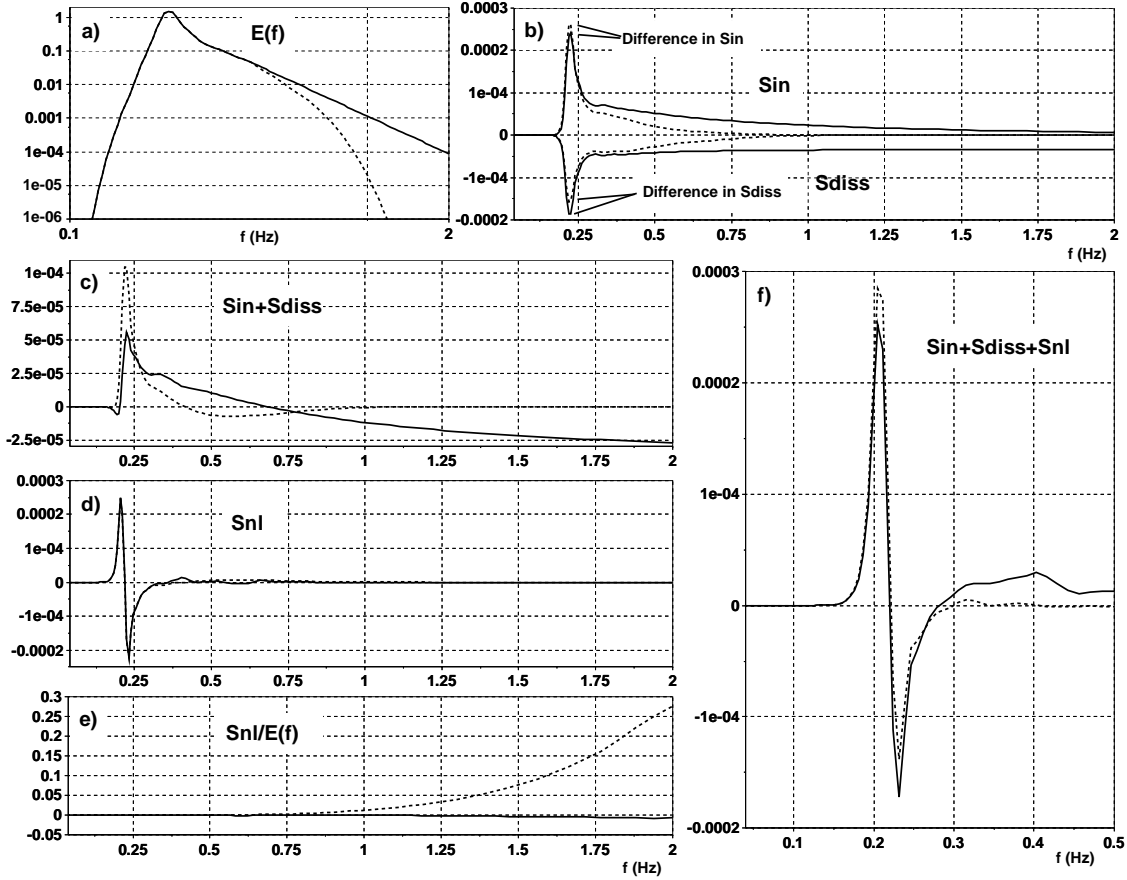


FIGURE 3.17 – Influence of the HF tail on the evolution of the spectrum : effect of the dissipation term  $S_{diss}$ . a) The frequency spectrum  $E(f)$  simulated with set III-ft and GQM at  $t = 6$  h is considered (dotted line). A  $f^{-4}$  tail is applied to this spectrum (solid line). b)  $S_{in}$  (Janssen, 1989, 1991) and  $S_{diss}$  (Komen et al., 1984; Günther et al., 1992) are calculated from both spectra. c)  $S_{in} + S_{diss}$ . d)  $S_{nl}$  (GQM method). e) Relative nonlinear transfer term  $S_{nl}/E(f)$ . f) Total source term  $S_{in} + S_{diss} + S_{nl}$

as observed/shown by Zakharov & Filonenko (1966), Toba (1973b), Kahma (1981), Kitai-gorodskii (1983), Phillips (1985) and Resio et al. (2001). To obtain the same slope when input and dissipation are also present, it is necessary that the dissipation and source terms scale similarly with frequency in the HF range (Resio et al., 2004).

We point that there is quite a strong experimental support of the  $f^{-4}$  HF tail for the frequency spectrum in deep water conditions. The extensive analyses carried out by Young & Babanin (2006) on Lake George data reveal that the mean value of the exponent  $n$  of  $f^{-n}$  in the frequency range  $5f_p < f < 10f_p$  lies close to 4 (3.9 actually). Considering the range of values of  $f_p$  of this data set, Young & Babanin (2006) noted that the spectral components in this frequency range were always in deep water conditions.

On the other hand, some observations in real sea conditions indicate that a  $f^{-4}$  high frequency shape applies up to few times  $f_p$  and then the decays is somewhat faster with frequency. For instance spectra presented in Long & Resio (2007) for particular conditions with short fetches and proximity of coastlines in Currituck Sound reveal a decay closer to  $f^{-5}$  when  $f >$  two or three times  $f_p$ .

In the HF range, the wind input terms vary as  $f^2 E(f)$ ,  $f^3 E(f)$  and  $f^3 E(f)$  for sets I, II and III, respectively. Yan (1987) parameterization (set II) is a combination of the Janssen (1991) (set III) and Snyder et al. (1981) (set I) terms, and scales like Janssen's one in the HF range. The dissipation terms for sets I, II and III vary as  $f^2 E(f)$ ,  $f^{11} E(f)^3$  and  $f^4 E(f)$ , respectively. When considering the combined effect of  $S_{in}$  and  $S_{diss}$  on can notice that :

- For set I,  $S_{in}$  and  $S_{diss}$  scale similarly at high frequencies (as  $f^2 E(f)$ ). When  $E(f) \propto f^{-4}$  in the HF range, they behave like  $f^{-2}$ .
- For set II, when  $E(f) \propto f^{-4}$  in the HF range,  $S_{in}$  and  $S_{diss}$  also scale similarly at high frequencies and both tend to  $f^{-1}$ .
- For test III, in contrast,  $S_{in}$  and  $S_{diss}$  scale differently. If we again assume that  $E(f) \propto f^{-4}$  in the HF range,  $S_{in} \propto f^{-1}$  and  $S_{diss} \propto 1$ . This raises questions about the validity of the dissipation term : the  $f^{-4}$  or even  $f^{-5}$  shape of the spectrum could not be maintained with this source balance and with such a strong high frequency dissipation. This is the reason why we observe with set III-ft a very steep HF tail. This in turn could also justify the motivation of using an imposed parametric tail : it can help in improving the prediction of parameters such as  $H_{m0}$  and  $T_p$ , and eventually of the frequency spectrum. However, it also modifies the whole directional structure of the spectrum (see subsection 4.4).

### 3.4.4 The angular spreading of wave energy

Figure 3.18 reports the normalized directional spreading function  $\tilde{D}(f/f_p, \theta)$  at  $t = 96$  h obtained from the initial spectrum C2.a (but results are almost the same for the 4 cases) using the different source terms.

GQM simulations give here again a bimodal structure of the directional spectra at frequencies lower and higher than  $f_p$ . The low frequency structure of the spectrum is very close to the one observed in section 3. Nonlinear interactions are responsible for the two directional lobes. However, the structure also depends on the parameterizations of the source terms.

As in section 3, the directional distribution has a very marked bimodal structure at  $f < f_p$ , slim down around the peak frequency and is bimodal above  $f_p$ . Transition to unimodality above  $5f_p$  is observed for sets I and II. Set I gives a more spread directional distribution than sets II and III for frequencies above  $f_p$ . In all cases, the directional distribution obtained when forcing terms are present is narrower at frequencies above the peak than the one of section 3. This shows the influence of the source/sink terms on the wave directional distribution. In section 3, the calculated mean directional width  $\sigma$  was around 40-50 degrees. When adding wind input and dissipation,  $\sigma$  is reduced to 26-33 degrees for the GQM runs (see also Figure 3.15).

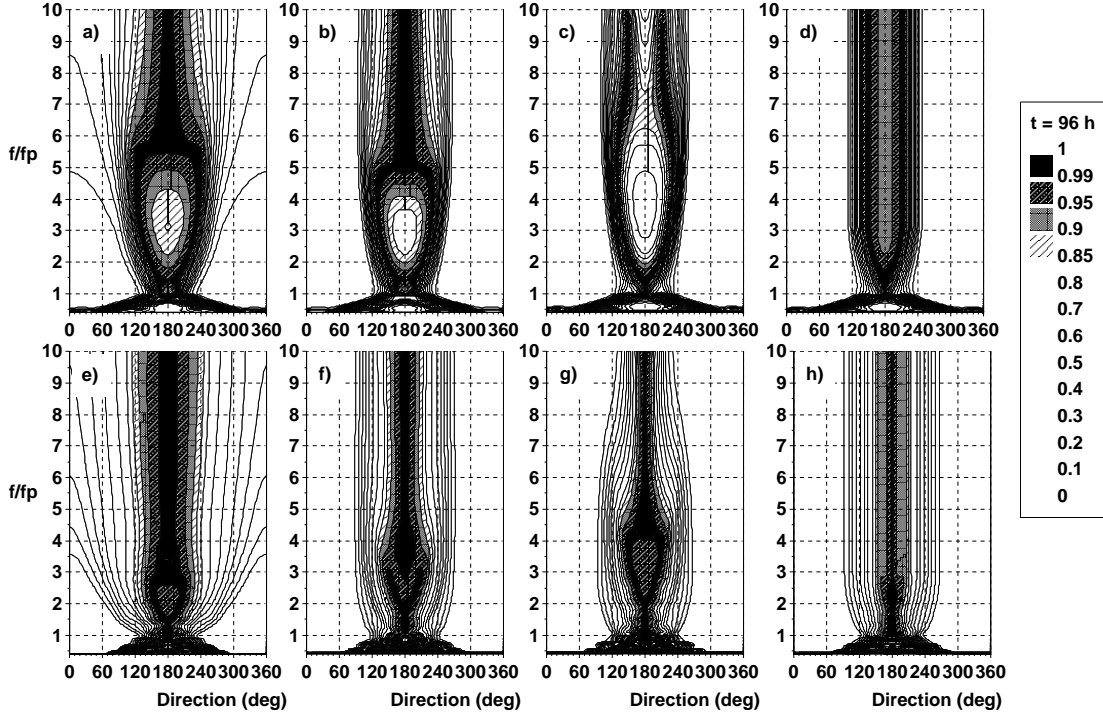


FIGURE 3.18 – Normalized directional spreading function  $\tilde{D}(f/f_p, \theta)$  at  $t = 96$  h. Initial case C2.a, b, c, d) : GQM method with source terms I, II, III-ft and III-it, respectively. e), f), g), h) : DIA method with source terms I, II, III-ft and III-it, respectively.

It is not straightforward to analyze the combined effects of  $S_{in}$ ,  $S_{diss}$  and  $S_{nl}$  on the directional distribution of the spectrum. The  $S_{nl}$  term plays a major role in determining the directional spreading of the spectrum (Young & Van Vledder, 1993), redistributing energy in directions oblique to the wind, as shown in subsection 3.5. But whichever the terms  $S_{in}$  and  $S_{diss}$  are, the spectrum always evolves to an equilibrium shape (Banner & Young, 1994). This means that  $S_{nl}$  always acts to balance the sum  $S_{in} + S_{diss}$  (Young & Van Vledder, 1993), and shows the importance of the sum  $S_{in} + S_{diss}$ , as confirmed by our simulations.

The angular distribution of  $S_{in}$  is determined by the product of  $\cos \theta$  (or  $\cos^2 \theta$ ) and  $F(f, \theta)$ , while that of  $S_{diss}$  is only determined by  $F(f, \theta)$  for the parameterizations chosen here. Therefore,  $S_{in}$  decreases faster than  $S_{diss}$  with  $\theta$ . From some angle value, the sum  $S_{in} + S_{diss}$  thus becomes negative. As  $S_{nl}$  acts to compensate the sum  $S_{in} + S_{diss}$  when the directional stability is achieved, it is clear that this angle influences the directional spreading of the spectrum. A narrower directional distribution of the input term or a stronger dissipation then influences the directional spreading function. For example, the  $S_{in}$  model of set III has a narrow  $\cos^2 \theta$  distribution. Thus, the sum  $S_{in} + S_{diss}$  starts being negative at angles

smaller than for a  $\cos \theta$  distribution (sets I and II). This could explain why the directional spreading is smaller with the parameterizations of set III. But the relative magnitudes of  $S_{in}$  and  $S_{diss}$  also have an influence. Keeping the same input term, a stronger dissipation (as for WAM 4, set III) leads to a smaller directional spreading. Set I has the smallest dissipation and gives the more spread distribution.

A slight bimodality at  $f_p$  starts being visible after 9 h of simulation for set II and 12 h for set I, whereas the distributions obtained with set III are unimodal from  $0.95f_p$  to  $1.4f_p$  (see also Figure 3.21). Bimodality at the peak was also recently obtained from simulations by Korotkevich et al. (2008) who used a modified version of the WRT method (Webb, 1978; Resio & Perrie, 1991) for calculation of the nonlinear interactions and three different models for the  $S_{diss}$  term. Their Figures 27 and 28 show spectra with a strong bimodality at the spectral peak.

For sets III-ft and III-it, results show directional distributions that are not unimodal at  $f \geq 5f_p$ . When the parametric tail is not imposed (set III-ft), the HF bimodality is more pronounced than for sets I and II. The angle between the lobes,  $2\theta_l$ , increases to a maximum around 100 degrees at  $f \approx 4f_p$ . Then  $2\theta_l$  decreases to a value around 60 degrees and remains constant.

Differences in the structure of  $\tilde{D}$  for  $f \geq 5fp$  (unimodality or bimodality) are related to the source terms balance. The unimodality of the directional distribution at these high frequencies is associated to low values of  $S_{nl}$ . For set III-ft, the input and dissipation terms are not scaling similarly with frequency at high frequencies (see §4.3.2). Thus, the  $S_{nl}$  term has to compensate for the difference between  $S_{in}$  and  $S_{diss}$ , and does not take low values in comparison with  $F(f, \theta)$ , as seen in figure 3.17-e) : the relative term  $S_{nl}/E(f)$  is much more important at high frequencies when the HF tail is steeper. This explains the process that maintains bimodality at higher frequencies in case III-ft. For sets I and II, the proper balance of the source/sink terms at high frequencies leads to smaller values of  $S_{nl}$  in comparison with  $F(f, \theta)$ . As in section 3, we thus observe a transition to unimodality for  $f \geq 5 - 6f_p$ . This simulation result needs to be validate against sufficiently accurate measurements and analyses at these high frequencies.

Regarding the results of set III-it, for frequencies above  $f_d$  (here  $f_d \approx 3.3f_p$ ), the directional distribution is forced to be equal to the one obtained at  $f = f_d$ . Thus the directional distribution cannot be consistent with observations, at least at frequencies  $f > f_d$ . Furthermore, the bimodality above  $f_p$  is less pronounced. Thus we see that the HF tail has an influence, not only on the energy level and spectral peak (subsection 4.2) and on the high frequency shape (subsection 4.3), but also on the overall directional distribution.

Panels e), f), g), h) of Figure 3.18 show the same simulations carried out using DIA. The directional distributions are narrow near the spectral peak. The spectra obtained with sets I, II and III-ft show some broadening at  $f > f_p$ , and a very slight bimodality can even be noticed. As for GQM simulations, set I produces a more spread spectrum. The distribution obtained using set III-it does not show any HF bimodality. In all cases, at low frequencies, some bimodality exists but the results are quite noisy compared to GQM results. Comparison of these results with the DIA distribution obtained in section 3 shows several differences. The DIA distribution without any forcing term is much more spread

and noisy for frequencies above  $f_p$ . Directional distributions of section 3 and 4 are quite similar at low frequencies.

Similar simulations of the homogeneous KE were recently performed by Hisaki (2007), using the WAM-Cycle 3 parameterizations of  $S_{in}$  and  $S_{diss}$  and two methods to calculate  $S_{nl}$ : DIA and an other exact method, called RIAM (Komatsu & Masuda, 1996). Directional distributions are also bimodal below  $f_p$ . The distribution calculated with the exact method shows high frequency bimodality.

### 3.4.5 Comparison with measured wave directional distributions

#### 3.4.5.1 Comparison with the expressions of Mitsuyasu et al. (1975) and Hasselmann et al. (1980)

The structure of  $D(f, \theta)$  obtained from GQM simulations at the final simulation time ( $t = 96$  h) is compared to the widely used parametric expressions of the form  $\cos^{2s}((\theta - \theta_0)/2)$  (cardioid model), where  $s$  is a parameter that was determined by the pioneering works of Mitsuyasu et al. (1975) and Hasselmann et al. (1980). These parameterizations were proposed on the basis of temporal measurements recorded by directional buoys. Results show that most of the energy is propagating in the wind direction, decays with increasing angle to the wind direction and that the directional spreading is narrowest near the spectral peak and broadens towards both higher and lower frequencies. Note that the models of Mitsuyasu et al. (1975) and Hasselmann et al. (1980) were designed in the  $f/f_p$  intervals 0.3-3 and 0.3-4, respectively. If one assumes that  $D$  can be fitted to the given parametrical unimodal expression  $A \cos^{2s}((\theta - \theta_0)/2)$ , we can calculate the corresponding parameter  $s$ , using the method of Longuet-Higgins et al. (1963). In our case,  $\theta_0 = 180$  degrees.  $s$  is given in Figure 3.19 for the directional distributions obtained with sets I and II and III. The curves of Mitsuyasu et al. (1975) and Hasselmann et al. (1980) are superimposed (the value  $U_{10}/C_p = 1.03$  is taken, corresponding to set II). Results show the narrowing of the directional distribution near the spectral peak ( $s$  is maximum around 1 to  $1.3f/f_p$ , depending on the source terms) and the increasing of the directional spreading toward low and high frequencies. For frequencies greater than  $1 - 1.3f_p$ ,  $s$  decreases quite slowly and then stabilizes for sets II and III, while the results of Mitsuyasu et al. (1975) or Hasselmann et al. (1980) do not suggest such a tendency to stabilization. Note that the  $s$  value of set III-it (with constrained tail) is constant after  $f = f_d$ . The  $s$  parameter obtained with set I does not stop decreasing, but with a smaller slope than the Mitsuyasu et al. (1975) and Hasselmann et al. (1980) curves. We conclude that the  $\cos^{2s}((\theta - \theta_0)/2)$  relationship allows to represent some major features of the directional distribution but gives a very incomplete representation of  $\bar{D}$  (Figure 3.20-b).

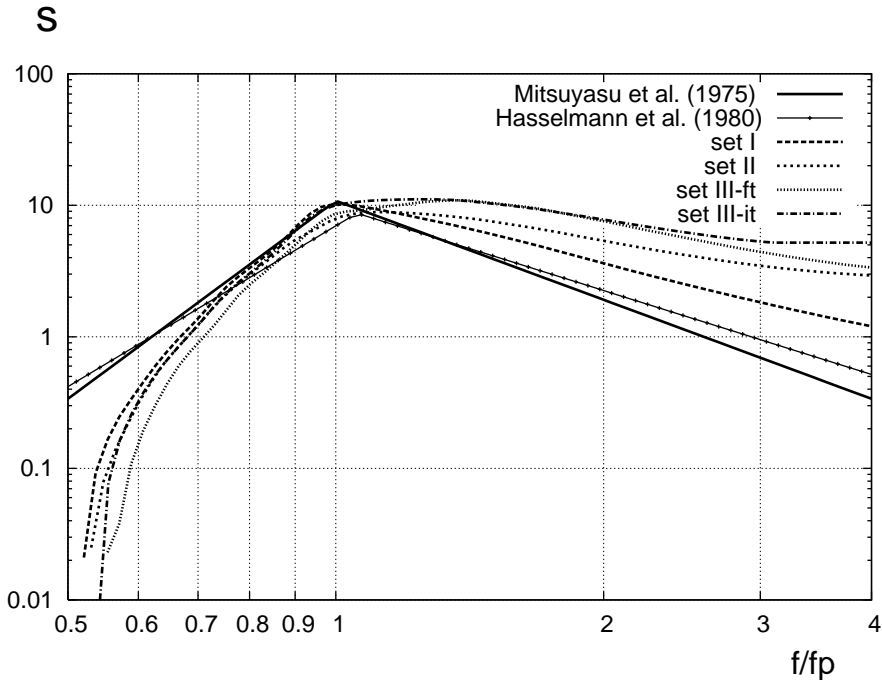


FIGURE 3.19 – The parameter  $s$  of the cardioid model for the directional distribution as a function of  $f/f_p$  at  $t = 96$  h. GQM method, sets I, II and III-ft and III-it, initial case C2.a. Comparison with Mitsuyasu et al. (1975) and Hasselmann et al. (1980)

### 3.4.5.2 Comparison with bimodal distributions : measurements and parameterizations

Bimodal directional distributions had been observed since the 90s from buoy or wave gauge data, but large uncertainties were remaining. Since the 2000s, thanks to new means of measurements (e.g. Hwang et al., 2000a,b), the accuracy of the data was increased and new evidence showed that the structure of the directional spectrum can be bimodal. Bimodal parametric relationships were suggested by Ewans (1998) and Hwang et al. (2000b). Ewans (1998) proposed a double Gaussian parameterization, Hwang et al. (2000b) presented a Fourier decomposition of their measured directional distribution. These parametric relationships both show the bimodality of the directional spectrum at frequencies above  $f_p$ , and are unimodal below  $f_p$ . The LF bimodality is observed by Wang & Hwang (2001) and by Hwang et al. (2000b) who propose parameterizations of the lobe angle that are bimodal at low frequencies. Ewans (1998) also notice bimodal distributions at  $f < f_p$ .

Figure 3.20-c shows the results from Ewans (1998). There is an interesting agreement with our results at high frequencies but some differences can be observed. The angle between the lobes is zero below  $f = 2.4f_p$  and then grows without stabilizing, while  $\theta_l$  obtained using GQM starts growing around 0.95 to  $1.4f_p$  depending on the models employed, and then stabilizes or becomes again equal to zero. We emphasize that the parameterization of Ewans (1998) was designed on the basis of heave-pitch-roll buoy measurements, delivering

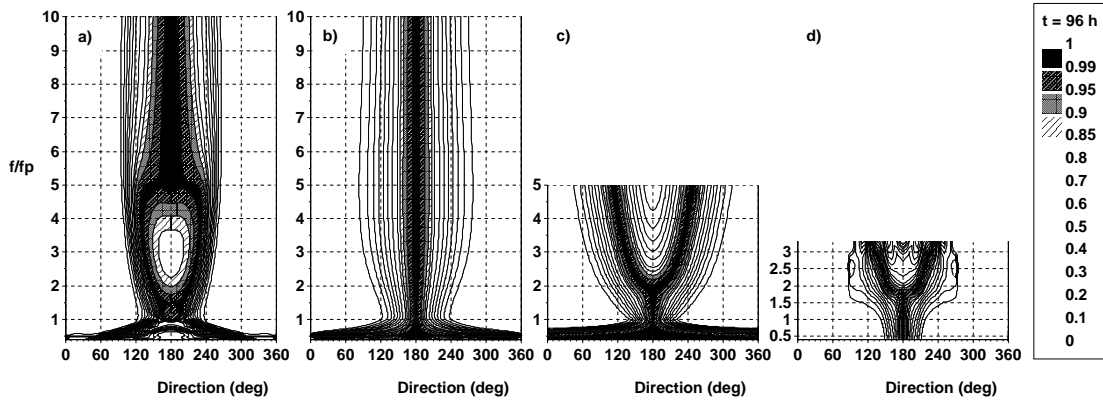


FIGURE 3.20 – Normalized directional spreading function  $\tilde{D}(f/f_p, \theta)$  at  $t = 96$  h. a) GQM method, source terms II, initial case C2.a. b)  $A \cos^{2s}((\theta - \theta_0)/2)$ . c) Ewans (1998) model. d) Hwang et al. (2000b) (FFT, 9 terms).

a limited number of independent parameters to estimate the angular distribution at each frequency and whose precision might be questionable for high frequencies.

Our results are also quite close to the Fourier decomposition of Hwang et al. (2000b) (Figure 3.20-d) for  $1.8 \leq f_p \leq 3.3$ .  $\theta_l$  given by Hwang et al. (2000b) is zero up to  $f = 1.8f_p$ .

The lobe ratio, noted  $r_{lobe}$ , is defined as the ratio of the maximum value of  $D(f, \theta)$  to its value at the dominant wave direction ( $\theta_0 = 180$  degrees). Figure 3.21 compares our modeling results for  $\theta_l$  and  $r_{lobe}$  with the experimental results of Ewans (1998) and Hwang et al. (2000a,b). We restrict our comparisons to  $0.6 \leq f/f_p \leq 3.3$ . The Hwang et al. (2000a,b) measurements correspond to a spatially homogeneous and quasi-steady wave field with a mean wind speed of  $9.5 \text{ m.s}^{-1}$  and an inverse wave age  $U_{10}/C_p \approx 0.98$ . The inverse wave age for sets I, II and III-it at  $t = 96$  h ( $U_{10}/C_p \approx 1.1, 1.03$  and  $1.06$ , respectively) is slightly larger than the one given by measurements. For set III-ft,  $U_{10}/C_p$  is much smaller ( $\approx 0.77$ ).

All the models, simulations and measurements give lobe angles that agree well above  $f/f_p = 2$ , except set III-it, which gives a slightly lower angle. The transition to bimodality at  $f > f_p$  depends on the models used for  $S_{in}$  and  $S_{diss}$ , which is consistent with the simulation results of Alves & Banner (2003). Results from set III-ft are the closest to the data of Hwang et al. (2000a,b). Set I and II show a slight bimodality around the peak, which is not in agreement with the results of Hwang et al. (2000b) or Ewans (1998). For  $f \leq f_p$ , the measured  $\theta_l$  is 2 to 3 times smaller than our calculated angles, but in both cases the existence of the LF bimodality is clear. The Fourier decomposition of Hwang et al. (2000b) and the parameterization of Ewans (1998) are also very close to our results

above  $1.8f_p$  and  $1.9f_p$ , respectively, but are unimodal below.

Our results underestimate  $r_{lobe}$  at  $f > f_p$  compared to the measurements of Hwang et al. (2000a,b), which means that the high frequency bimodality is more pronounced than it appears in our simulations. Ewans (1998) gives a lobe ratio smaller than ours up to  $2.3 - 2.8f_p$ , but it then increases rapidly. Set III-ft gives higher  $r_{lobe}$  values than the other sets, which is related to the balance of the source/ sink terms and the strong high frequency dissipation (see subsection 4.4). Set III-it gives the smallest  $r_{lobe}$  values. At  $f < f_p$ , our simulations give a higher  $r_{lobe}$ , but measurements also show bimodality.

The lobe ratio is also calculated from GQM simulations of section 3 (purely nonlinear case) for comparison.  $r_{lobe}$  is again globally smaller than observations at  $f > f_p$  (figure not reported here). It increases to a maximum value of 1.33 at  $f = 2.2f_p$  (quite close to observations) and then decreases. This suggests the influence of wind input and dissipation on the  $r_{lobe}$  magnitude at  $f > f_p$ .

Alves & Banner (2003) compared simulations using several parameterizations of  $S_{in}$  and  $S_{diss}$  to the data of Hwang et al. (2000b) for a constant inverse wave age  $U_{10}/C_p = 0.98$ . They found a lobe angle close to Hwang et al. (2000b) at  $f > 2f_p$  and a generally smaller lobe ratio. Their results point out the influence of  $S_{in}$  and  $S_{diss}$  on  $r_{lobe}$  values.

We observed that higher values of  $r_{lobe}$  were obtained at earlier times, suggesting a dependence on wave age (Figure 3.22). Our analysis indicates that the highest lobe ratios are most of the time observed when the nonlinear transfers are maximum and the redistribution of energy to oblique angles is the largest. Curves representing set II, III-ft and III-it have a bell shape.  $r_{lobe}$  increases with the inverse wave age up to a maximum value and then decreases. Set III curve increases with  $U_{10}/C_p$ . Hwang et al. (2000b) measurements at  $f = 2.5f_p$  are given with an error bar, and seem closer to results of set III-ft. Our results also indicates a small dependence of the lobe angle on  $U_{10}/C_p$ , in agreement with the observations of Ewans (1998) and Long & Resio (2007). This analysis might deserve additional studies or investigations.

### 3.4.6 Discussion about the low frequency bimodality

Our simulations showed that a fundamental feature of the spectrum is the low frequency bimodality, which is present whenever using GQM or DIA, with or without forcing terms. Young et al. (1995) also observed LF bimodality on their simulated spectra, but argued that a “strong bimodal spreading for  $f/f_p < 1$ ” was “in contrast to the measured results which are broad and unimodal in this region” and discussed possible causes of this feature. This raises the question whether the LF bimodality comes from the numerical models or is a real feature of ocean waves. According to Young et al. (1995), there is always a small atmospheric input at frequencies below  $f_p$ , which is enough to dominate the nonlinear term and make the directional distribution unimodal. They stated that, as there is no atmospheric input in the models at frequencies below the peak, the directional distribution is only controlled by nonlinear terms, and becomes bimodal.

In our simulations, there is a small but positive input at frequencies lower than the peak.

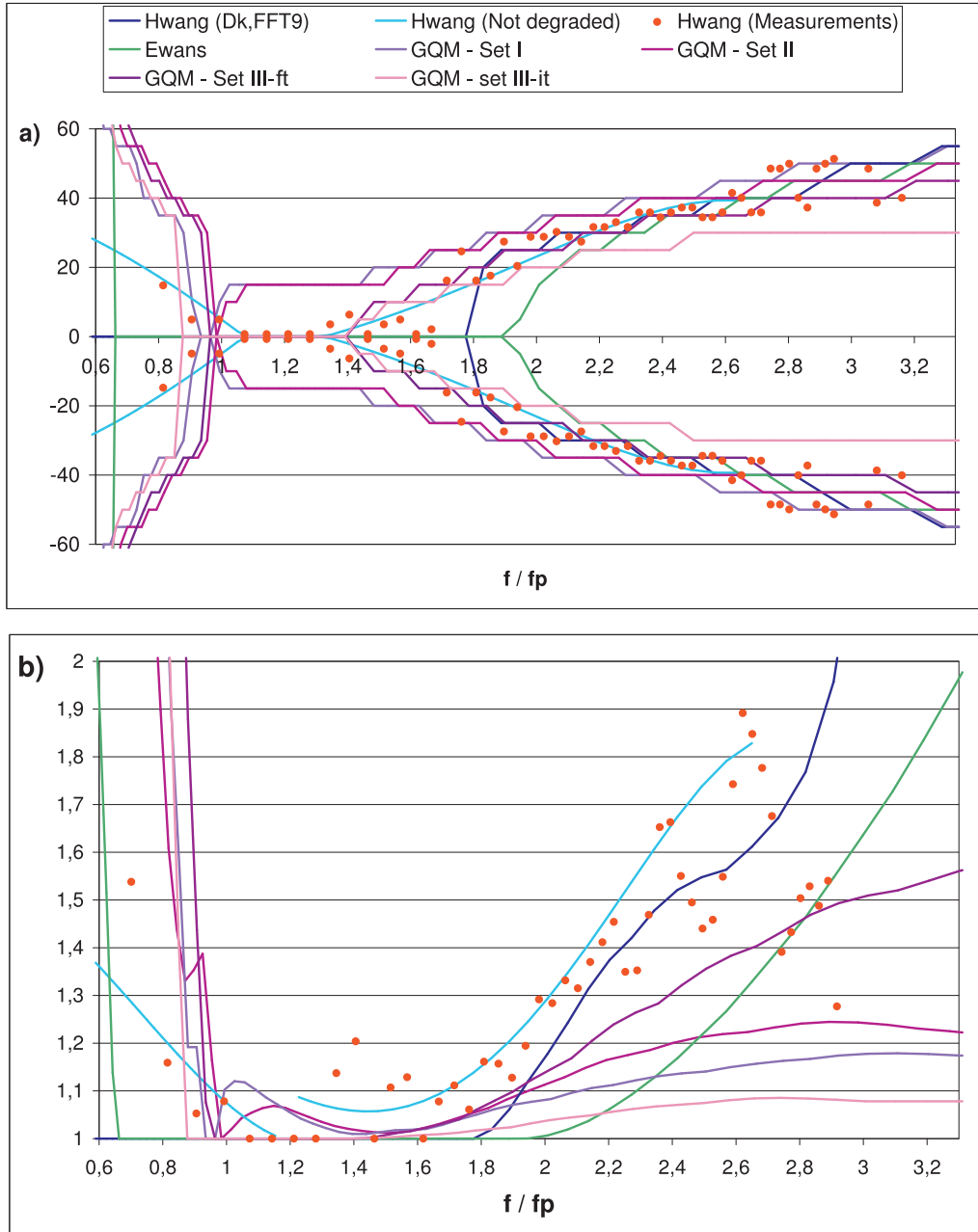


FIGURE 3.21 – a) Angle between the lobes and the main direction  $-\theta_l, \theta_l$ , b) Lobe ratio  $r_{lobe}$  versus  $f/f_p$  at  $t = 96$  h. Initial case C2.a, GQM method, source terms I, I and III-ft and III-it. Comparison with Hwang et al. (2000a,b) (measurements with an airborne scanning lidar system, Fourier decomposition with 9 components  $D_{k,FFT9}$  and polynomial fitting not degraded (see Fig.10 and Table 2 of their paper)) and the Ewans (1998) parameterization.

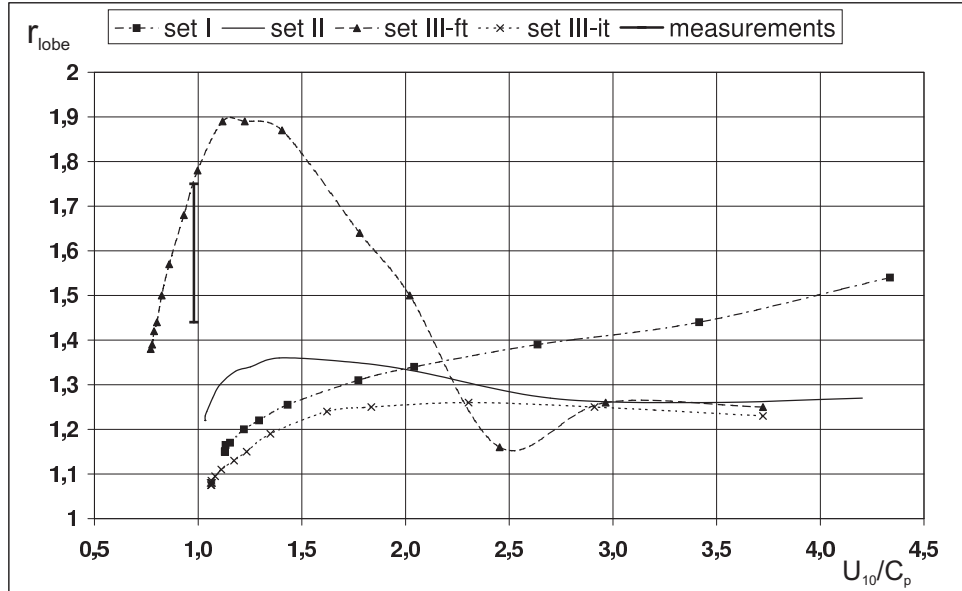


FIGURE 3.22 – Lobe ratio  $r_{lobe}$  versus inverse wave age  $U_{10}/C_p$  for  $f = 2.5f_p$ . Initial case C2.a, GQM method, source terms I, II and III-ft and III-it.

The initial spectrum is non-zero over the whole frequency domain. Therefore, the atmospheric input is equal to zero only if the growth rate  $\beta$  (defined as  $\beta(f, \theta) = S_{in}(f, \theta)/(\omega F(f, \theta))$ ) is equal to zero.

For each of the parameterizations used here, there is a cutoff frequency below which  $S_{in} = 0$ . This cutoff frequency is smaller than the peak frequency for all the sets when using GQM, even at the end of the simulation where the peak frequency is small. For the model of Snyder et al. (1981) (set I), the cutoff frequency is  $f \approx 0.15$  Hz in our simulations, which corresponds approximately to  $U_{10}/C = 1$ , where  $C$  is the wave phase velocity. Below this limit, there is not input from the wind since waves go faster than the wind. The  $S_{in}$  model of Yan (1987) with the coefficients given by Van der Westhuysen et al. (2007) can take negative values for waves going faster than wind. In set II, we chose to cut the value of  $\beta$  to  $\beta = 0$  to avoid negative growth. The cutoff frequency is then again close to 0.15 Hz. The Janssen (1991) input term (set III) also has a cutoff frequency, which depends on several parameters, and takes values between 0.095 Hz and 0.11 Hz in the two options (1 and 2) considered here. Thus, in our simulations, the small input does not modify the structure of the LF directional distribution, which is still controlled by the nonlinear term. It seems that a small low frequency input does not stop the nonlinear terms from creating bimodal lobes.

It is very difficult to obtain precise measurements of directional spectra at frequencies with low levels of energy. This is the case at low frequencies, where observations are showing the broadening of the spectrum. The interpretation of such a broadening in term of spectral isotropisation is questionable. Furthermore, some high resolution field measurement campaigns, as the one of Hwang et al. (2000a,b) and the buoy data of Wang & Hwang (2001)

clearly show LF bimodality. Inspection of figure 7 of Wang & Hwang (2001), in particular the panels (d), (e), (i) and (j) corresponding to energetic sea states ( $H_{m0}$  between 3 and 5.2 m), reveal directional spectra with a LF bimodality consistent with our simulations, at least qualitatively. Observations of Ewans (1998) also report bimodality at frequencies lower than  $f_p$ , although he suggested that it could eventually come from a swell component in some of the spectra.

All this make us think that the low frequency bimodality is a real feature of natural sea states, and is not associated with a limitation of the numerical models.

### 3.5 Conclusions and perspectives

In this study, we investigate the properties of the directional wave spectrum as derived using a quasi-exact computation (GQM method, Lavrenov (2001)) of the nonlinear wave-wave interactions. Two methods for computing the  $S_{nl}$  term and different expressions for  $S_{in}$  and  $S_{diss}$  are considered. Purely nonlinear and duration-limited cases are both simulated. This enables us to point out the importance of the nonlinear wave-wave interactions and of the accuracy of their computing. Influence of the input and dissipation terms on the results is discussed.

The purely nonlinear case gives us the opportunity to check some theoretical results on the evolution of the significant wave height  $H_{m0}$  and the peak period  $T_p$  and on the self-similarity of the spectrum (e.g. Badulin et al., 2005). The GQM algorithm reproduces quite well the theoretical evolutions. The influence of the initial directional spectrum is studied in detail. In the purely nonlinear case, the choice of the initial wave spectrum has a moderate influence on the evolution and final values of  $H_{m0}$ ,  $T_p$  and the mean angular width  $\sigma$ . However, the shape of the spectrum no longer depends on the initial condition after some minutes. When wind input and dissipation are included in the wave model, the effect of the initial spectrum is very small and almost no difference is seen after a few minutes of simulation.

Analysis of the directional distribution shows that bimodality is a robust feature of the wave spectrum, except near the spectral peak, and at frequencies greater than  $\approx 4 - 5f_p$  where unimodality may apply. The angle between the two symmetric lobes varies with frequency. Whichever the parameterization used for the wind input and the dissipation terms, the global structure of the spectrum is close to the one observed without any source/sink term up to  $4f_p$ . This demonstrates that nonlinear interactions constitute the key mechanism responsible for bimodality. However, we established that the parameterizations of  $S_{in}$  and  $S_{diss}$  have a quantitative effect on the directional distribution of the spectrum. They can enhance or reduce the magnitude of the bimodal lobes, and play a role in maintaining bimodality at frequencies greater than  $5f_p$ . The transition to bimodality at frequencies higher than  $f_p$  also depends on the parameterizations of  $S_{in}$  and  $S_{diss}$ . Our GQM simulation results are globally consistent with the measurements of Hwang et al. (2000a,b), even if we found a smaller lobe ratio at frequencies  $f > f_p$  and a more pronounced low frequency bimodality.

The DIA method, when compared to GQM, gives acceptable results concerning the evaluation of  $H_{m0}$  and  $T_p$ , but does not give a good prediction of the directional distribution of the spectrum, particularly at frequencies above  $f_p$ .

The influence of the parameterizations of  $S_{in}$  and  $S_{diss}$  on the high frequency shape of  $E(f)$  is highlighted. When  $S_{in}$  and  $S_{diss}$  scale similarly at high frequencies, we obtain a fairly good prediction of the HF tail of the spectrum. When the dissipation is too strong at high frequencies, the frequency spectrum has a very sharp HF tail that is not in agreement with theoretical and experimental results. The inclusion of a constrained tail is then required to obtain coherent results. The effects of imposing a parametric tail are significant, not only on the high frequency part of the spectrum but also on the energy level and peak period and on the global directional distribution. The influence of the HF tail on the whole spectrum is explained by the pronounced effects on the input and dissipation terms near the spectral peak frequency and is essentially caused by the lower mean wavenumber parameter which gives an artificially lower dissipation rate.

Investigations are in progress for the simulation of the heterogeneous KE (i.e. including propagation in space of the directional spectrum) with an accurate evaluation of the non-linear four-wave interactions. More “realistic” cases (fetch-limited growth, slanting fetch, combination of swell and wind-sea) are already being simulated using the GQM method. Despite a need to further optimize the CPU time (about 80-100 times the CPU time of DIA), results obtained using the GQM method are really encouraging and we plan to implement the method in operational sea wave models, as TOMAWAC (Benoit et al., 1996a). Extension of the GQM method to finite depth is not straightforward but should be worked out, as done for other exact methods (e.g. Hashimoto et al., 1998; Van Vledder, 2006).

## Acknowledgments

We acknowledge Dr. Paul Hwang for providing us with 2D spectrum data measured by an airborne scanning lidar system and for his helpful advices.

## Chapitre 4

# On weakly turbulent scaling of wind sea in simulations of fetch-limited growth

by E. Gagnaire-Renou, M. Benoit and S. I. Badulin

Submitted to Journal of Fluid Mechanics, in revision

### Abstract

Extensive numerical simulations of fetch-limited growth of wind-driven waves are analyzed within two approaches : a ‘traditional’ wind speed scaling proposed by Kitaigorodskii (1962) in early sixties and an alternative weakly turbulent approach developed recently by Badulin et al. (2007). The latter one uses spectral fluxes of wave energy, momentum and action as physical scales of the problem and allows for advanced qualitative and quantitative analysis of wind-wave growth and features of air-sea interaction. In contrast, the traditional approach is shown to be descriptive rather than proactive.

Numerical simulations are conducted within the Hasselmann kinetic equation for deep water waves in a wide range of wind speeds from 5 to 30 m s<sup>-1</sup> and for two different wave input functions  $S_{in}$ . Two methods of calculation of the nonlinear transfer term  $S_{nl}$  are used : a quasi-exact method based on the Gaussian Quadrature Method (GQM) and the Discrete Interaction Approximation (DIA) widely used in modern spectral wind-wave forecasting models.

Weakly turbulent approach allows to identify three stages of wind wave development corresponding to qualitatively different balance of source terms  $S_{in}$ ,  $S_{diss}$ ,  $S_{nl}$  : initial growth,

growing sea and fully developed sea.

Validity of the asymptotic weakly turbulent approach for the stage of growing wind sea is determined by dominance of nonlinear transfer that results in rigid link between spectral fluxes and wave energy. Total net wave input  $\langle S_{in} + S_{diss} \rangle$  provides physically relevant scaling at this stage while details of wave input and dissipation  $S_{in}$ ,  $S_{diss}$  become of minor importance. DIA shows rather good accuracy at this asymptotic stage due to homogeneity property of  $S_{nl}$  and resulting self-similarity of wind-wave spectra. The stage of self-similar growth is investigated in details and presented as a consequence of sub-stages of qualitatively different coupling of air flow and growing wind waves. The key self-similarity parameter of the asymptotic theory is estimated to be  $\alpha_{ss} = 0.68 \pm 0.1$ .

Further prospects of wind-wave modeling in the context of the presented weakly turbulent scaling are discussed.

## 4.1 Introduction

The Hasselmann equation is the basic theoretical model for statistical description of surface gravity waves. First derived by Hasselmann (1962) in early sixties for evolution of weakly nonlinear free waves (with no wind input nor dissipation), it was further generalized to the case of wind waves and became a core of all the modern spectral forecasting models of wind-driven seas (e.g. WAMDI Group, 1988). The extension to situations where many physical processes of wave generation and damping are interwoven was accompanied by serious technical and conceptual difficulties. Actually, the extension of the authentic Hasselmann equation (the kinetic equation for weakly nonlinear water waves) is written as follows

$$\frac{\partial N_{\mathbf{k}}}{\partial t} + \nabla_{\mathbf{k}} \omega_{\mathbf{k}} \nabla_{\mathbf{r}} N_{\mathbf{k}} = S_{in} [N_{\mathbf{k}}] + S_{diss} [N_{\mathbf{k}}] + S_{nl} [N_{\mathbf{k}}] \quad (4.1)$$

Here intrinsic frequency  $\omega$  satisfies linear dispersion equation for gravity water waves

$$\omega^2(\mathbf{k}) = g|\mathbf{k}| \tanh(|\mathbf{k}|d) \quad (4.2)$$

$d$  is the water depth and  $N_{\mathbf{k}}$  is the wave action spectral density that can be expressed in terms of  $F(\mathbf{k}) = \omega N(\mathbf{k})$ , the two-dimensional spectral density of wave variance.  $N(\mathbf{k})$ ,  $F(\mathbf{k})$  are usually treated in the sense of the theory of linear water waves as squares of the corresponding Fourier coefficients. Strictly speaking, functions  $N(\mathbf{k})$ ,  $F(\mathbf{k})$  for weakly nonlinear waves are related to their ‘linear’ counterparts by a quadratic transformation (see Krasitskii, 1994; Zakharov, 1999; Badulin et al., 2005) and equivalence of the ‘linear’ and ‘weakly nonlinear’ functions can be accepted as an approximation which is valid for deep water waves only.

The right-hand side of (4.1) requires more remarks on hypotheses and approximations that underly the modeling of wind wave spectra. First of all, weak nonlinearity (smallness of the collision integral  $S_{nl}$ ) implies slow evolution of wave field at times and distances

of order of  $\varepsilon^{-4}$ , where steepness  $\varepsilon = a_* k_* \ll 1$  is expressed in terms of characteristic wave amplitude  $a_*$  and wavenumber  $k_*$  (see Hasselmann, 1962, 1963b,a; Zakharov, 1999). Secondly, terms of wave input  $S_{in}$  and wave dissipation  $S_{diss}$  should be small as well to satisfy the weakly nonlinear scaling and, thus, to be consistent with the extension of the authentic conservative Hasselmann equation to the ‘full’ kinetic equation (4.1).

The problem of scaling  $S_{in}$ ,  $S_{diss}$  is not trivial because so far there are no physically consistent and reliable models for these terms. Our knowledge is based on empirical parameterizations of these terms that are, in some ways, controversial : ocean field experiments give no direct way to discriminate different physical processes responsible for wave generation or dissipation and to quantify experimentally nonlinear transfer term  $S_{nl}$  which is co-existing with  $S_{in}$ ,  $S_{diss}$  (Plant, 1982). To resolve this problem, heuristical models for  $S_{in}$ ,  $S_{diss}$  have been proposed (e.g. whitcapping mechanism by Hasselmann, 1974) as work-pieces for further parameterizing the observed wave input and dissipation. All the experimental studies of  $S_{in}$ ,  $S_{diss}$  have been carried out within these heuristical models for quite narrow range of physical conditions (low winds, narrow range of wave scales *etc.*) and their physical relevance is generally not clear. In the wave forecasting models, e.g. WAM (WAMDI Group, 1988), WAVEWATCH-III (Tolman, 1991, 2002), SWAN (Booij et al., 1999), TOMAWAC (Benoit et al., 1996a), this difficulty is tackled by introducing a number of parametric formulas for  $S_{in}$ ,  $S_{diss}$  as options (e.g. Stewart, 1974; Snyder et al., 1981; Plant, 1982; Hsiao & Shemdin, 1983; Donelan & Pierson-jr., 1987; Janssen, 1989, 1991). The validity of each option is a question of preferences of a particular user. These preferences can be based on the models verification and calibration or, in many cases, just on habits. So far, no physical or practical criteria exist for a unique undoubted choice of functions  $S_{in}$ ,  $S_{diss}$ .

In contrast to the terms of external forcing the collision integral  $S_{nl}$  is known ‘from first principles’ and, hence, there is no problem of its physical background. This good luck is however compensated by mathematical problems : the extremely time-consuming computations of exact  $S_{nl}$  is unacceptable for many problems of spectral wave modeling, and especially for wave forecasting models with their tight time restrictions. The use of approximate methods is unavoidable in that case. The most known one is DIA – Discrete Interaction Approximation (Hasselmann et al., 1985). This method or its extension MDIA (Multiple Discrete Interaction Approximation) are implemented in all the spectral models for wind-wave forecasting. In fact, the term *approximation* is not correct for DIA or MDIA : a continuum of resonant wave quadruplets for every wave harmonic is replaced by one (for DIA) or few (for MDIA) quadruplet configurations. The accuracy of such approach cannot be estimated *a priori* for an arbitrary spectral distribution and can be quite low (see figure 7 in Cavalieri et al., 2007, for illustration). It would be better to refer to DIA and MDIA as *substitutes for the true nonlinear transfer term  $S_{nl}$*  in (4.1). These substitutes can work perfectly well or lead to a complete fiasco as in the case of suddenly changing wind (Young et al., 1987; Benoit, 2006) or mixed sea conditions (Pettersson, 2004; Young, 2006).

The first exact method for  $S_{nl}$ , proposed by Webb (1978) and now referred as WRT-method (Tracy & Resio, 1982; Van Vledder, 2006), is based on elimination of the Dirac  $\delta$ -functions and integration along resonant sub-spaces called locii. The EXACT-NL algorithm by Hasselmann & Hasselmann (1981, 1985), the RIAM method proposed by Masuda (1980,

1986) and developed by Komatsu & Masuda (1996) and the GQM (Gaussian Quadrature Method) introduced by Lavrenov (2001, 2003b) all use a reduction of six-fold integration to a three-fold one by removing the  $\delta$ -functions in the integrand (see equation 4.14) and rely on different integration techniques to deal with singularities arising from manipulation of the collision integral  $S_{nl}$ . Theoretically, all the listed numerical approaches could be recasted to approximate or ‘reduced exact’ methods for  $S_{nl}$  with reasonable time and acceptable (and, additionally, controlled) accuracy of calculations. Of course, this work should be done. But it cannot be done with no reference to problems of introducing terms  $S_{in}$ ,  $S_{diss}$  into the Hasselmann equation. Results of our struggle for high accuracy of  $S_{nl}$  can be nullified by uncertainty of our knowledge of  $S_{in}$ ,  $S_{diss}$ . Experimental verification or transparent physical criteria for the wind-wave models are required to balance our computational efforts and our scanty knowledge of air-sea interaction physics.

When modeling wind-driven seas the air-sea interaction is traditionally scaled by wind speed  $U_h$  at a reference height  $h$  ( $h = 10$  m is generally used) or by friction velocity  $u_*$ . This scaling comes from the Kitaigorodskii (1962, 1983) similarity approach and implies a direct link of the only wind parameter  $U_h$  (or  $u^*$ ) to wave characteristics :  $E = \int F(\mathbf{k})d\mathbf{k} = \langle \eta^2 \rangle$  the total wave energy, and  $\omega_*$  a characteristic wave frequency (mean or spectral peak frequency). Such scaling ignores all the details of wind-wave interaction and can be successful if and only if the wind speed is the only physical parameter of this interaction. Complexity of wind effect on waves, such as gustiness, effect of air flow stratification *etc.* hampers the use of wind speed scaling as a proactive tool of wind-wave modeling.

Evidently, not the wind speed itself but momentum and energy transferred to waves are real physical quantities that are responsible for the wind-wave interaction. Recent studies by Badulin et al. (2005, 2007) showed that wave growth is determined, first of all, by integral quantities of fluxes of energy, momentum and wave action coming to waves. The ‘details’ of how these fluxes are delivered to waves (what are the scales of waves acquiring these fluxes) appeared to be of secondary importance. This ‘flux scaling’ is based on a solid background of the theory of weak turbulence and closely related to classic Kolmogorov-Zakharov stationary solutions for the Hasselmann equation (4.1) (Zakharov & Filonenko, 1966; Zakharov & Zaslavsky, 1982b). The extension of the stationary solutions to non-stationary and spatially inhomogeneous cases makes the theory a useful tool of analysis of wind-wave growth.

The goal of this paper is to show advantages of the weakly turbulent approach as a proactive tool for developing wind-wave models. The extensive simulation of fetch-limited growth in the spirit of testbeds for wind-wave forecasting models (e.g. SWAMP Group, 1985; Komen et al., 1994) has been carried out for different wave input functions (Snyder et al., 1981; Janssen, 1989, 1991) and for different numerical methods for the nonlinear transfer term  $S_{nl}$  (DIA and GQM methods). Analysis of the numerical results within the weakly turbulent approach and within the ‘traditional’ wind-speed scaling allows one to identify qualitatively different stages of wave development and to delimit these stages quantitatively.

In § 4.2 we present the setup of our numerical experiments. Conditions and parameters of the simulations are reported. The chosen functions for the wind input and the whitecap-dissipation are basically described, as well as the numerical methods for computing

the nonlinear wave-wave interactions. Accuracy and associated computing times of the simulations are briefly given.

§ 4.3 introduces conventional wind speed scaling based on similarity analysis by Kitai-gorodskii (1962). An alternative approach uses results of the theory of weak turbulence (Zakharov et al., 1992). An asymptotic weakly turbulent model – the so-called *split balance model* can be formulated based on the hypothesis that nonlinear transfer dominates as compared with external wave forcing. The validity of the asymptotic theory has been demonstrated recently both numerically and by analysing experimental data on wind-wave growth for a wide range of physical conditions (Badulin et al., 2007). The theory provides a family of self-similar solutions for particular cases of duration- or fetch-limited growth of wind waves at different rates. In time-(fetch-) independent form all these non-stationary or non-homogeneous solutions give rigid link of spectral fluxes to wave energy quite similarly to the classic stationary Kolmogorov-Zakharov solutions of the theory of weak turbulence (Zakharov & Filonenko, 1966; Zakharov & Zaslavsky, 1982b).

Three reference cases are of special interest : they correspond to constant fluxes of wave momentum, energy or wave action to waves. These cases were derived long time ago (Toba, 1972; Hasselmann et al., 1976; Zakharov & Zaslavsky, 1983b) from very different theoretical and experimental perspectives. The unified weakly turbulent approach allows to associate these reference cases with qualitatively different stages of wave growth.

In § 4.4 results of simulation are described both in terms of wind speed scaling and in terms of spectral flux weakly turbulent scaling. Different stages of wave development from initial growth to the fully developed (mature) sea are delimited qualitatively and quantitatively. The stage of growing wind sea described by asymptotic weakly turbulent theory is detailed as a consequence of qualitatively different sub-stages of air-sea coupling based on the reference cases (Toba, 1972; Hasselmann et al., 1976; Zakharov & Zaslavsky, 1983b) mentioned above.

§ 4.5 closes the paper with discussions and conclusions.

## 4.2 Numerical model of fetch-limited growth

In this section we describe the setup of our numerical studies of fetch-limited growth. Generally, we follow similar works on wind-wave spectra modeling (Komen et al., 1984, 1994) drawing attention to the effects of particular mechanisms involved in wind-wave evolution. Moreover, we use different approaches for the wave input function  $S_{in}$  and for the nonlinear transfer term  $S_{nl}$  in order to specify possible coupling of these constituents. The goal of the wide-front attack is underlying essentially nonlinear physics : benefits and disadvantages of these approaches cannot be assessed for each of the terms independently. Interdependency of wave input, dissipation and nonlinear transfer requires a certain coordination of the approaches to insure basic features of wind-wave physics.

We start with models of wave input function  $S_{in}$  and dissipation function  $S_{diss}$  to fix an important point which is usually ignored in wind-wave modeling : the net total wave input

(integral in wave scales) is a key quantity of wind-wave growth. We used two parameterizations of  $S_{in}$  by Snyder et al. (1981) and by Janssen (1989, 1991) to show that wave growth is determined by this basic quantity of air-sea interaction rather than by particular dependence of wave input on wave frequency.

Then we discuss two methods for the nonlinear transfer function  $S_{nl}$ : the well-known DIA method widely used in wind-wave forecasting models and the exact method proposed by Lavrenov (2001) and developed recently by Benoit (2005). The latter exact method with coarser resolution appears to be acceptable for extensive simulations and its accuracy can be estimated easily for questionable cases. We show that irrespective of the well-known deficiency of DIA that, in particular, corrupts dramatically spectral angular distributions (e.g. Gagnaire-Renou et al., in press), both approaches reflect basic features of the nonlinear transfer adequately.

The physical model of wave dissipation, in our opinion, is the most questionable. We use the whitecapping parameterization of Hasselmann (1974) for the dissipation term  $S_{diss}$  without alternative approaches. New alternatives for the dissipation function  $S_{diss}$  are coming soon (e.g. Zakharov et al., 2007; Korotkevich et al., 2008; Arduin et al., 2008, 2009) while other are already implemented in third generation models (e.g. Alves & Banner, 2003; Van der Westhuysen et al., 2007). We plan their study in the nearest future.

#### 4.2.1 Conditions and parameters of simulation

The idea of numerical setup is to reproduce wave spectra evolution at some standard conditions. We let wind blow offshore normally to the coast ( $\Theta = 0$ ). The wind speeds range from 5 to 30 m s<sup>-1</sup> (we considered four standard values  $U_{10} = 5, 10, 20, 30$  m s<sup>-1</sup>). The wave field is assumed homogeneous in the along-shore direction.

The Hasselmann equation is solved both in space and time to guarantee physically relevant stationary solutions developing in offshore direction. The simulation parameters were selected so as to maintain the same dimensionless parameters (non-dimensional fetch  $\chi = Xg/U_{10}^2$ , non-dimensional frequency  $\tilde{f} = fU_{10}/g$  and non-dimensional time  $\tau = gt/U_{10}$ ) in each simulation.

The spatial grid is logarithmic in  $\Delta X$  ( $\Delta X_{n+1}/\Delta X_n = 1.068$ ) and includes 121 points ( $\Delta X_1 = 6.25$  m for  $U_{10} = 5$  m s<sup>-1</sup>, while for  $U_{10} = 30$  m s<sup>-1</sup>  $\Delta X_1 = 225$  m). The maximal fetch  $X_{max}$  (corresponding to non-dimensional fetch  $\chi_{max} = 10^5$  in each simulation) was chosen to be sufficiently long to reach a sort of a mature sea state. The existence itself of this state is a big issue (see Komen et al., 1984) that we discuss below.

The discrete frequency-direction grid is composed of 51 frequencies with logarithmic distribution ( $f_{n+1}/f_n = 1.071$ ) and 36 directions with a constant spacing of 10° ( $\theta_{m+1} - \theta_m = 10^\circ$ ). For wind speeds  $U_{10} = 5, 10, 20, 30$  m s<sup>-1</sup>, the corresponding lowest and highest frequencies are  $f_1 = 0.16, 0.08, 0.04, 0.027$  Hz and  $f_{51} = 5, 2.5, 1.25, 0.83$  Hz, respectively. The resolution is adequate for the problem discussed as it has been shown by Komatsu & Masuda (1996). Additional tests have been carried out within our approach with higher frequency and directional resolutions (from 51 to 128 frequencies and up to 72 directions,

respectively). Results are only marginally affected by the higher resolutions, while the CPU time increases dramatically.

The initial wave spectrum (at  $t = 0$ ) is set to be plain zero. A small linear growth term  $S_{lin}$  has been added to the source function so that the waves start to grow from the initial state. We used the form of Cavalieri & Malanotte-Rizzoli (1981), as proposed by Tolman (1992)

$$S_{lin} = 1.5 \times 10^{-3} g^{-2} \{u_* \max [0, \cos(\theta - \theta_u)]\}^4 \exp \left[ - \left( \frac{f}{f_{PM}} \right)^{-4} \right] \quad (4.3)$$

where  $f_{PM}$  is the Pierson-Moskowitz frequency

$$f_{PM} = \frac{1}{2\pi} \frac{g}{28u_*}$$

Time integration of the source terms is performed with a semi-implicit scheme (WAMDI Group, 1988) with a constant time-step ( $\Delta t = 5, 10, 20, 30$  s for the corresponding wind speeds  $U_{10} = 5, 10, 20, 30$  m s $^{-1}$ ). Results are given at non-dimensional time  $\tau_f = gt/U_{10} \approx 6.36 \times 10^4$  (corresponding to 9, 18, 36, and 54 hours of physical time, respectively) as corresponding to quasi-stationary state and, thus, to fetch-limited growth.

In these simulations, we used the wave growth limiter corresponding to the modified WAM-Cycle 4 expression of Hersbach & Janssen (1999) :

$$|\Delta F|_{max} = 3.0 \times 10^{-7} g \max(u_*, gf_{PM}^*/f) f^{-4} f_{51} \Delta t \quad (4.4)$$

where  $f_{PM}^* = 5.6 \times 10^{-3}$  is the non-dimensional Pierson-Moskowitz frequency. Benoit (2006) analyzed the influence of different wave growth limiters on spectral shape and recommended the use of (4.4) when such a limiter is necessary (for instance when using a large static time step).

In the wave model, the high-frequency range of the spectrum (above a given frequency  $f_d$ ) is introduced in a standard way as power-like extrapolation  $F(f, \theta) \propto f^{-m}$ , with  $m = 4$ . The diagnostic frequency  $f_d$  is set as follows

$$f_d = \min[f_{51}; \max(4f_{PM}, 2.5\bar{f})] \quad (4.5)$$

where the mean frequency  $\bar{f}$  is given by

$$\bar{f} = m_0 \left( \int_0^{+\infty} \int_{-\pi}^{\pi} f^{-1} F(f, \theta) df d\theta \right)^{-1} \quad (4.6)$$

with

$$m_0 = \int_0^{+\infty} \int_{-\pi}^{\pi} F(f, \theta) df d\theta$$

Such a diagnostic high-frequency tail is usually used in simulations of spectral evolution to compensate the lack of physics of  $S_{in}$  and  $S_{diss}$  in the high-frequency part of the spectrum or to reduce computational time. The inclusion of a high-frequency diagnostic tail and the particular choice of exponent  $m$  and frequency  $f_d$  affect the whole evolution of the spectrum (e.g. Banner & Young, 1994; Gagnaire-Renou et al., in press). In our simulations, the strong dissipation in the high-frequency range would give a very sharp high-frequency tail that justifies the use of a constrained tail. Note that we follow standard setup of the modeling of wind-wave spectra when introducing the diagnostic tail (e.g. WAMDI Group, 1988).

It should be emphasized that the high-frequency diagnostic tail influences the wave input and dissipation terms (Gagnaire-Renou et al., in press) as soon as conventional quasi-linear parameterizations of  $S_{in}$  and  $S_{diss}$  depend on wave spectrum. Thus, a special care should be taken to discriminate the wave input and dissipation terms themselves and artifacts due to choice of the diagnostic tail.

#### 4.2.2 Wave input : local quasi-linear linear Cherenkov-like forcing

A great number of parameterizations has been proposed for modeling the wind input term  $S_{in}$  (e.g. Stewart, 1974; Snyder et al., 1981; Plant, 1982; Hsiao & Shemdin, 1983; Donelan & Pierson-jr., 1987; Janssen, 1989, 1991). In fact, all these parameterizations can be treated in terms of Cherenkov mechanism of wind-wave interaction as follows

$$S_{in}^{(F)} = \omega \beta(u_*/C_{ph}, \theta, u_1, \dots) F(f, \theta) \quad (4.7)$$

The key argument of the non-dimensional increment  $\beta$  is the ratio of friction velocity  $u_*$  (or a reference wind speed  $U_{10}$ ) to wave phase velocity  $C_{ph}$ . The inverse ratio  $C_{ph}/u_*$  is usually referred as age of particular wave harmonic. Additional arguments  $u_i$  are introduced to describe variety of physical effects of wind-wave coupling. The Cherenkov mechanism assumes that the wave harmonic can be generated if ratio  $C_{ph}/u_*$  is below certain threshold. Only waves propagating slower than this threshold (say, slower than wind speed at height  $U_{10}$ ) can be generated within the Cherenkov mechanism. The waves propagating faster than this threshold speed, the so-called old waves, are not affected by wind, or, even are damped by the wind.

Note that  $S_{in}$  was defined in (4.1) in terms of wave action  $N(\mathbf{k})$ . In (4.7), wave input is introduced in terms of the variance spectrum  $F(\mathbf{k})$  as  $S_{in}^{(F)} = \omega S_{in}$ . For more convenience, we omit superscript for  $S_{in}$  below.

In our study we consider two input terms  $S_{in}$  which are usually implemented as options in the most recent third generation (3G) models (e.g. WAM, WAVEWATCH-III, SWAN, TOMAWAC). Model by Snyder et al. (1981) is used in the WAM-Cycle 3 version. The second one is the model by Janssen (1989, 1991), as it is given in WAM-Cycle 4.

The growth rate  $\beta(f, \theta)$  for the Snyder input term is determined by the ratio  $u_*/C_{ph}$  only :

$$\beta(f, \theta) = \max \left[ 0; 0.25 \frac{\rho_a}{\rho_w} \left( 28 \frac{u_*}{C_{ph}} \cos(\theta - \theta_u) - 1 \right) \right] \quad (4.8)$$

$\rho_a$ ,  $\rho_w$  are the air and water densities,  $\theta_u$  is the local direction of the wind. The friction velocity is related to the wind speed by the drag coefficient :

$$C_D = \left( \frac{u_*}{U_{10}} \right)^2 \quad (4.9)$$

which is assumed to be a linear function of wind speed in our study (WAMDI Group, 1988)

$$C_D = \begin{cases} 6.5 \times 10^{-5} U_{10} + 8 \times 10^{-4} & \text{if } U_{10} \geq 7.5 \text{ ms}^{-1} \\ 1.2875 \times 10^{-3} & \text{if } U_{10} < 7.5 \text{ ms}^{-1} \end{cases} \quad (4.10)$$

As it seen from (4.8) and (4.9) the threshold speed is close to wind speed  $U_{10}$  ( $U_{10} = 28u_*$  for  $U_{10} < 7.5 \text{ m s}^{-1}$ ).

Note that the Snyder expression is based on field measurements of weakly forced waves in a narrow range of observed inverse wave ages ( $1 < U_{10}/C_{ph} < 3$ ). Thus, the use of this input term (as well as other empirical parameterizations) is ‘based on extrapolation’ (Snyder et al., 1981, figure 26) that can lead, in some cases, to corruption of physics.

Dimensional wave increment ( $\omega\beta$ ) by Snyder is growing rapidly with frequency (as  $\omega^2$ ). Thus, the finite frequency domain used for the simulations can affect the total wave input significantly. The problem can be even more critical for other input parameterizations (e.g. Hsiao & Shemdin, 1983; Donelan & Pierson-jr., 1987) where wave increment grows faster with frequency (as  $\omega^3$ ). Hsiao & Shemdin (1983) introduce high-frequency cut-off explicitly at  $0.85 \times U_{10}/C_{ph} = 7.4$  i.e. at very high frequencies.

The model of wave input by Janssen (1989, 1991) uses more parameters of atmospheric boundary layer. In addition to Cherenkov-like dependence on ratio  $u_*/C_{ph}$  it introduces dependence on sea roughness parameters.

$$\beta(f, \theta) = \Gamma \frac{\rho_a}{\rho_w} \left\{ \left[ \frac{u_*}{C_{ph}} + z_\alpha \right] \max [\cos(\theta - \theta_u); 0] \right\}^2 \quad (4.11a)$$

where

$$\Gamma = \frac{\Gamma_m}{\kappa^2} \mu \ln^4 \mu \quad (4.11b)$$

$\Gamma_m = 1.2$  is fixed by Janssen (1991),  $\kappa = 0.41$  – von Karman constant for no-slip turbulent boundary layer,  $z_\alpha = 0.011$  is constant as in WAM-Cycle-4. Parameter  $\mu$  is determined by

$$\mu = \min \left[ \frac{gz_0}{C_{ph}^2} \exp \left( \frac{\kappa}{[u_*/C_{ph} + z_\alpha] \cos(\theta - \theta_u)} \right); 1 \right] \quad (4.11c)$$

where

$$z_0 = \frac{\tilde{z}_0}{\sqrt{1 - \tau_w/\tau_s}} \quad (4.11d)$$

depends on ratio of wind stress

$$\tau_s = \rho_a u_*^2 \quad (4.11e)$$

and wave-induced stress

$$\tau_w = \left| \int \int \rho_w \omega S_{in}(f, \theta) (\cos \theta, \sin \theta) df d\theta \right| \quad (4.11f)$$

Here

$$\tilde{z}_0 = \alpha u_*^2 / g \quad (4.11g)$$

with the Charnock constant default value  $\alpha = 0.01$ . Friction velocity  $u_*$ , roughness parameter  $z_0$  and  $\tau_s$  are derived from fixed wind velocity  $U_{10}$  in our simulations

$$U_{10} = \frac{u_*}{\kappa} \ln \left( \frac{10 + z_0 + \tilde{z}_0}{z_0} \right) \approx \frac{u_*}{\kappa} \ln \left( \frac{10}{z_0} \right) \quad (4.11h)$$

using the iterative method of Newton-Raphson for the equation set (4.11).

Note that the Janssen (1989, 1991) parameterization introduces an additional wind speed scale  $u_{z_0}$  and the corresponding non-dimensional argument  $u_1 = u_{z_0}/C_{ph}$  into general expression (4.7)

$$u_1 = \frac{u_{z_0}}{C_{ph}} = \frac{\sqrt{g z_0}}{C_{ph}} = \frac{\sqrt{\alpha}}{(1 - \tau_w/\tau_s)^{1/4}} \frac{u_*}{C_{ph}} \quad (4.12)$$

$u_{z_0}$  is the friction velocity modified by the feedback effect of wave-induced stress  $\tau_w$  (4.11f) on air flow and, generally, is small in comparison with  $u_*$ . Its effect becomes visible for short waves as it is illustrated by figure 4.1 where increments by Snyder et al. (1981) and by Janssen (1989, 1991) are plotted as functions of non-dimensional frequency (inverse wave age) at wind speed  $U_{10} = 10 \text{ m s}^{-1}$ . The most pronounced feature of Janssen (1989, 1991) formula is a decay of  $\beta$  at high frequencies. The Snyder parameterization for  $\beta$  shows simple linear dependence on frequency, i.e. on the only non-dimensional ratio of wind speed scale  $u_*$  to wave phase speed  $C_{ph}$ . This linear dependence looks logical for experimental results obtained in relatively narrow range of wave and wind parameters (see Snyder et al., 1981, for details).

The most striking feature of the comparison in figure 4.1 is that the growth rate  $\beta(f)$  by Janssen (1989, 1991) is substantially higher than the one by Snyder et al. (1981) that means, first of all, considerable difference in integral wave input. We see an important

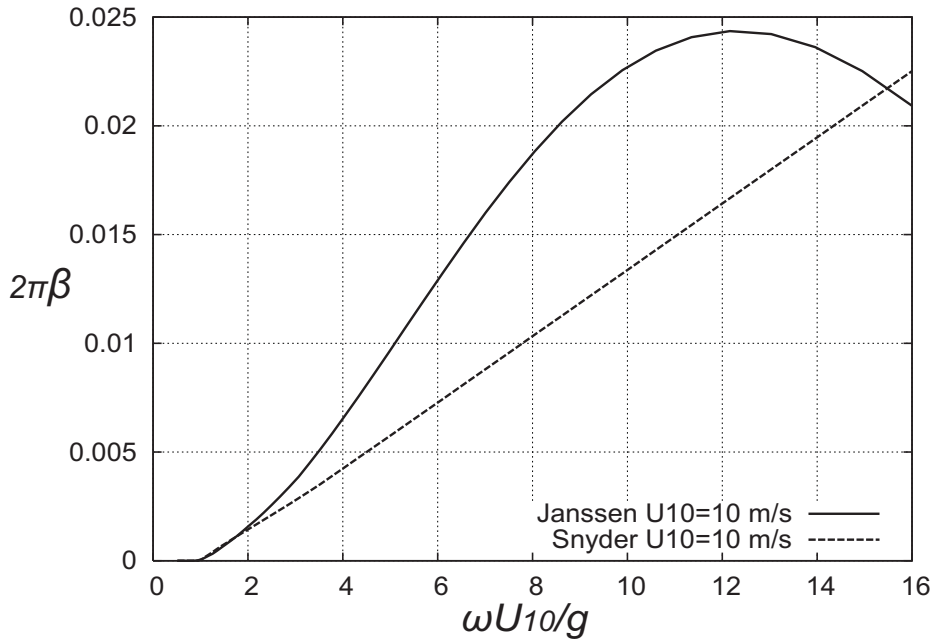


FIGURE 4.1 – Non-dimensional growth rate  $S_{in}(f)/(fE(f))$  as function of the inverse wave age  $\omega U_{10}/g$  for parameterizations of the input term  $S_{in}$  by Snyder et al. (1981) and Janssen (1989, 1991). Wind speed  $U_{10} = 10 \text{ m s}^{-1}$ .

physical problem in this difference : wave input parameterizations widely used in research and forecasting models are not ‘calibrated’ in bulk physical quantity of wind-sea interaction, namely total wave energy coming to waves.

#### 4.2.3 Wave dissipation : whitecapping by Hasselmann (1974)

Wave dissipation is the most poorly understood term in the kinetic equation (4.1). The quasi-linear parameterization of whitecapping mechanism by Hasselmann (1974) is still one of the main models implemented in most of the the wind-wave forecasting models. Alternative saturation-based whitecapping formulations have been proposed by Alves & Banner (2003) and Van der Westhuysen et al. (2007). Some other essentially nonlinear parameterizations of the term  $S_{diss}$  (e.g. Phillips, 1985; Donelan & Pierson-jr., 1987) are discussed predominantly in the context of research models.

Some problems of the original whitecapping parameterization were demonstrated by Komnen et al. (1984) for the balance of fully developed wind-driven sea. Nowadays, 3G spectral wind-wave models use this parameterization in the following form

$$S_{diss}(f, \theta) = -\frac{C_{diss}}{g^p} \bar{\omega}^{2p+1} m_0^{p/2} \left[ (1-\delta) \left( \frac{\omega}{\bar{\omega}} \right)^2 + \delta \left( \frac{\omega}{\bar{\omega}} \right)^4 \right] F(f, \theta) \quad (4.13)$$

where  $\bar{\omega}$  is defined by  $\bar{\omega} = 2\pi\bar{f}$  (see equation 4.6).  $C_{diss} = 4.5$  and  $\delta = 0.5$  are default values in the WAM-cycle 4 model (Günther et al., 1992; Komen et al., 1994). The exponent  $p = 4$  is usually used in (4.13). Recent studies (Zakharov et al., 2007; Korotkevich et al., 2008) rely on much sharper, threshold-like dependence of the dissipation on wave steepness  $\varepsilon = \bar{\omega}\sqrt{m_0}/g$ , with  $p > 10$ . According to Zakharov et al. (2007), the whitecapping dissipation is overestimated in the WAM-cycle 3 and WAM-cycle 4 models. They propose to use the dissipation term (4.13) with the following parameters :  $C_{diss} = 0.11$ ,  $\delta = 0$  and  $p = 12$ . The key message of such revision is high exponent  $p$  that models threshold-like dependence of dissipation on wave steepness  $\varepsilon$ .

In our study we follow WAM-cycle 4 formula for  $S_{diss}$  (4.13) with standard parameters given above. Effects of the parameters as well as alternative formulations for the dissipation term are a subject of further studies.

#### 4.2.4 Nonlinear transfer term $S_{nl}$ : problems and solutions

As it was noted at the very beginning of the paper, the Hasselmann equation (4.1) itself presupposes importance or, more, leading role of the nonlinear transfer term  $S_{nl}$ . This term is the only one in the Hasselmann equation derived in a physically consistent way. Additionally, the validity itself of (4.1) implies that nonlinearity, generation and dissipation compete at least on equal terms. The leading role of nonlinear transfer for wind-driven seas was illustrated both theoretically (Young & Van Vledder, 1993; Badulin et al., 2005) and experimentally (Pettersson, 2004; Young, 2006), and is in conceptual contradiction with models that consider wave generation and dissipation as major constituents of the wind-sea balance. In these models, input and dissipation terms determine shapes of wave spectra and their evolution in space and time (e.g. Phillips, 1985; Hara & Belcher, 2002).

The motive to simplify the nonlinear transfer term  $S_{nl}$  or, even, to remove it from consideration comes from mathematical difficulties of calculation of the six-fold integral

$$S_{nl}[N_{\mathbf{k}}] = \int_{\mathbf{k}_1} \int_{\mathbf{k}_2} \int_{\mathbf{k}_3} G(\mathbf{k}, \mathbf{k}_1, \mathbf{k}_2, \mathbf{k}_3) \{N_2 N_3 (N + N_1) - N N_1 (N_2 + N_3)\} \times \delta(\mathbf{k} + \mathbf{k}_1 - \mathbf{k}_2 - \mathbf{k}_3) \delta(\omega + \omega_1 - \omega_2 - \omega_3) d\mathbf{k}_1 d\mathbf{k}_2 d\mathbf{k}_3 \quad (4.14)$$

Functions  $N_{\mathbf{k}}$  are generally strongly localized in wavevector space, the kernel  $G(\mathbf{k}, \mathbf{k}_1, \mathbf{k}_2, \mathbf{k}_3)$  (see Badulin et al., 2005, for a collection of possible representations) grows rapidly with wavevector (as  $|\mathbf{k}|^6$ ) and  $\delta$ -functions contour the subspace of resonant quadruplets

$$\begin{cases} \mathbf{k} + \mathbf{k}_1 = \mathbf{k}_2 + \mathbf{k}_3 \\ \omega + \omega_1 = \omega_2 + \omega_3 \end{cases} \quad (4.15)$$

As said before, a number of algorithms for exact evaluation of collision integral  $S_{nl}$  has been proposed and used for wave spectra modeling starting with the Webb (1978) method,

referred as WRT (Tracy & Resio, 1982), which was further developed in a number of works (see Resio & Perrie, 1991; Pushkarev et al., 2003; Van Vledder, 2006). The EXACT-NL code by Hasselmann & Hasselmann (1981, 1985) was the first applied for burning questions of wind-sea physics (Komen et al., 1984). Methods by Masuda (1980, 1986) and then Hashimoto et al. (1998), by Polnikov (1990) and, finally, by Lavrenov (2001) can be considered as versions of the Hasselmann method with particular transformations of variables and different methods for processing singularities in the integrands.

An optimal integration technique was found by Lavrenov (2001). This method, the so-called GQM (Gaussian Quadrature Method), is based on the use of Gaussian quadratures adapted to the singularities that appear in the course of the manipulation of the kinetic integral (4.14), and has the advantage to be both precise and efficient.

Benoit (2005) reviewed and compared several possible improvements or alternative techniques to obtain higher accuracy in the evaluation of the (4.14) while keeping acceptable CPU time. It appeared that an optimal technique might be found by using so-called ‘Reduced Exact Methods’. The principle of these methods is to start from a potentially ‘exact’ method and to use a similar algorithm with either a coarser resolution and/or a reduced integration range. The GQM method (Lavrenov, 2001) was found to be the best to make its CPU time acceptable (see § 4.2.5). Based on this approach, Benoit (2005) improved and optimized the GQM method for use in a real 3G model.

The Reduced Exact Method approach differs dramatically from methods used in operational models for the nonlinear transfer term  $S_{nl}$ , as DIA (Hasselmann et al., 1985), or MDIA, realized in recent versions of 3G models. There is no regular mathematical procedure for estimating accuracy of these methods since they are tested for particular wave spectra. Benoit (2006) showed that results obtained from the DIA, Multiple DIA (Tolman, 2004) and GQM methods can differ significantly. In some situations (e.g. of abrupt changes of wind direction) the results can give qualitative differences that makes the use of DIA or MDIA questionable in general case.

As an illustration, figure 4.2 shows  $S_{nl}$  terms given by DIA, Multiple DIA (MDIA) as proposed by Tolman (2004) and by GQM method with three different resolutions, for a given JONSWAP-like spectrum. ‘Fine’ GQM resolution with 26, 16 and 12 points for the first, second and third components of integration (after suppressing the Dirac-functions in equation 4.14) is considered as ‘true’ nonlinear transfer term and is given by solid line in both panels in figure 4.2. The ‘medium’ (14,8,8) and the ‘rough’ (11,6,6) resolutions show some deviations from the ‘true’ curve of the fine resolution, especially in the high-frequency part of the wave spectra. Differences between the fine and medium resolutions are small, and almost invisible near the spectral peak, which confirms the good convergence of the method when increasing its resolution.

Pronounced difference between the DIA and the reference GQM-fine curves does not require detailed comments. One can note several positive lobes of DIA curve and very deep negative lobe shifted towards higher frequencies relative to the reference curve (see Benoit, 2005; Cavalieri et al., 2007, for further comparisons). The MDIA curve gives significantly improved results as compared to the original DIA. At the first glance, it looks even more attractive than the GQM rough curve near the  $S_{nl}$  peak. It should be noted that the comparison

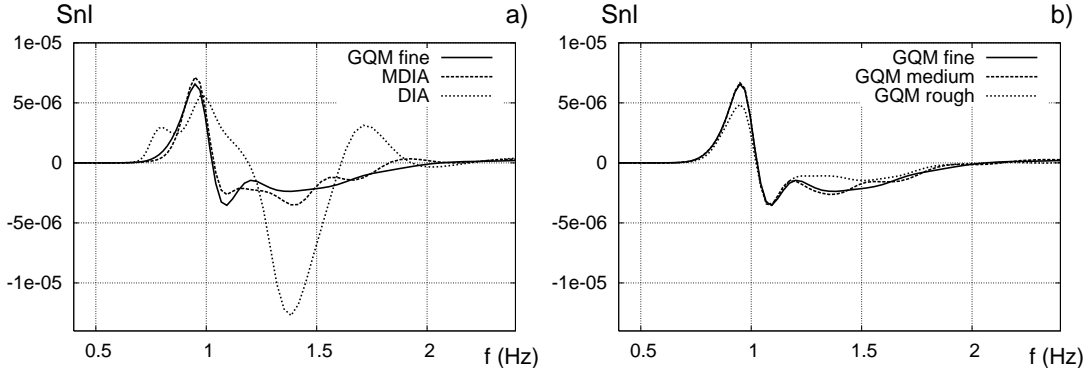


FIGURE 4.2 – Nonlinear transfer term  $S_{nl}$  computed with a) the method DIA, MDIA, and GQM (fine resolution), and b) the GQM method (rough, medium and fine resolutions)

is made for a particular spectral function (JONSWAP spectrum with a standard set of parameters) and angular-averaged  $S_{nl}$  terms are presented in figure 4.2. Deficiency of DIA (MDIA) approaches become more pronounced when looking at arbitrary spectral forms and angular distributions. This problem has been detailed recently by Benoit (2005) (see also Gagnaire-Renou et al., in press) : DIA (MDIA) gives large deviations for both the  $S_{nl}$  term and the resulting spectra compared to ‘true’ distributions.

The problem related to spectral shapes obtained with approximate methods of calculation of the nonlinear transfer term is two-fold. First, spectral shapes can differ significantly from ‘true’ ones, that is, evidently, not good thing if we need accurate spectra of wind sea. The second point seems more critical : corruption of spectral shape leads to corruption of wave input and dissipation terms that depend on spectral magnitude. This corruption affecting total wave input and dissipation, eventually, corrupts physics itself of wind-wave interaction.

There is an important basic property that reconciles both approaches for  $S_{nl}$ . The collision integral  $S_{nl}$  for deep water waves obeys homogeneity property

$$S_{nl} [\nu N(v\mathbf{k})] = \nu^3 v^{19/2} S_{nl} [N(\mathbf{k})] \quad (4.16)$$

for arbitrary positive coefficients  $v$  and  $\nu$ . This basic property should be satisfied both for exact methods (Badulin et al., 2005) and for their substitutes like DIA or MDIA irrespective of possible corruption of the resulting spectral shapes.

#### 4.2.5 Computer resources and choice of method for $S_{nl}$

Calculation of nonlinear transfer term is a very time-consuming part of simulation of wind-wave growth. The fastest (and the least accurate!) DIA takes about 25 – 30% of the total simulation time when computing the global Hasselmann equation (4.1) (with wind

input, dissipation and advection). The use of exact methods increases dramatically the time required to compute the  $S_{nl}$  term, making it completely unacceptable for operational models. For EXACT-NL of Hasselmann & Hasselmann (1981, 1985) and the method of Webb (1978) the CPU time of  $S_{nl}$  calculation is 1000 times larger than the DIA CPU time. Recent improvements of the WRT method by Van Vledder (Van Vledder, 2006; Bottema & Van Vledder, 2008) and Pushkarev et al. (2003) decreases this factor up to value 300.

The GQM algorithm with rough resolution needs about 100 time the DIA CPU time to compute the nonlinear wave-wave interactions. Moreover, for a simulation of the Hasselmann equation including wind input, dissipation and propagation, as in fetch-limited situations, the CPU time for GQM rough is only about 25 times the DIA simulation time. This shows that the GQM method is a valuable candidate for implementation in 3G wave models and could soon be used for practical applications.

In this work we are trying to reach a reasonable compromise between high accuracy and reasonable time of simulation. Calculations with resolution medium requires 2 to 4 times more CPU time than the rough simulations, and the fine calculations need 10 to 25 times more CPU time than the rough ones. Figure 4.2 shows rather small difference between  $S_{nl}$  terms calculated with medium and fine resolutions. The effect of resolution of the GQM method on spectral shapes has been investigated in details by Benoit & Gagnaire-Renou (2007). On the basis of these results, we accept the GQM method with medium resolution as a regular one for the present study. Fine resolution has been used in some cases only to control accuracy of simulations.

## 4.3 Physical scaling of wind-wave growth

### 4.3.1 Split balance model vs the Kitaigorodskii (1962) wind speed scaling

Having different models of wave input  $S_{in}$  and different approaches for nonlinear transfer term  $S_{nl}$  we are trying to construct a physically transparent scheme for coupling these constituents of wind-wave evolution in a wide range of physical conditions. It calls for an introduction of physical scaling where results for the different conditions could be presented in comparable form.

Conventional scaling of wind-wave data relies on wind speed as a physical scale (Kitaigorodskii, 1962). This approach is quite restrictive even for the simplified model presented here. First of all, this approach belittle implicitly the role of nonlinear transfer : the nonlinear resonant interactions are capable to reproduce inherent features of wind-wave evolution on their own without any wind (Badulin et al., 2005). Secondly, the wind speed  $U_{10}$  (or friction velocity  $u_*$ ) is just one of many physical parameters responsible for wave development. This is what we call *reactiveness of wind speed approach* : wind speed scaling reflects features of wind-wave growth partially only, a number of additional physical effects (atmospheric layer stability, feedback of waves on atmospheric boundary layer etc.) are completely ignored by

this approach. It explains high dispersion of wind-wave growth dependencies in terms of non-dimensional fetch (duration), energy and characteristic frequency.

Power-law dependencies of energy  $E = m_0$  (we follow ‘oceanographic definition’ of wave energy here) and spectral peak frequency  $\omega_p$  on non-dimensional fetch

$$\tilde{E} = E_0 \chi^{p_\chi}; \quad \tilde{\omega}_p = \omega_0 \chi^{-q_\chi} \quad (4.17a)$$

or non-dimensional duration

$$\tilde{E} = E_0 \tau^{p_\tau}; \quad \tilde{\omega}_p = \omega_0 \tau^{-q_\tau} \quad (4.17b)$$

play an important role in generalization of results of experimental studies.  $p_\chi$ ,  $p_\tau$  and  $q_\chi$ ,  $q_\tau$  are exponents of energy growth and frequency downshift for fetch-limited and duration-limited cases. Further we use Greek letters and tildes for ‘traditional’ non-dimensional values :  $\chi = Xg/U_{10}^2$  – non-dimensional fetch,  $\tau = tg/U_{10}$  – duration,  $\tilde{\omega} = \omega U_{10}/g$  – frequency and energy  $\tilde{E} = Eg^2/U_{10}^4$ .

As it has been shown by Badulin et al. (2005, 2007) a really proactive approach to analyze wind-wave evolution can be proposed when nonlinear transfer dominates over wave input and dissipation. This asymptotic physical model – the split balance model – ‘splits’ effects of nonlinear transfer and external forcing into two equations. In terms of wave action spectral density  $N(\mathbf{k})$  it is written as follows (Badulin et al., 2007)

$$dN_{\mathbf{k}}/dt = S_{nl}[N_{\mathbf{k}}] \quad (4.18a)$$

$$\langle dN_{\mathbf{k}}/dt \rangle = \langle S_{in} + S_{diss} \rangle \quad (4.18b)$$

Here angle brackets  $\langle \cdot \rangle$  mean integration over the whole wavenumber space  $\mathbf{k} = (k_x, k_y)$ . Strictly speaking, the system (4.18) should be supplemented by equations for external forcing  $\langle S_{in} + S_{diss} \rangle$ , i.e. by description of air-sea interaction. The asymptotic model shows that some general features of the wave forcing are sufficient to determine evolution of wave spectra. In a sense, it separates the tricky air-sea model from the wave model. The success of such approach is determined by the fact that the model (4.18) possesses self-similar solutions for a family of power-law dependencies of wave forcing  $\langle S_{in} + S_{diss} \rangle$  on fetch or duration (Badulin et al., 2005, 2007). The non-dimensional parameters for these solutions should be made of dimensional parameters of (4.18) only : total flux  $\langle S_{in} + S_{diss} \rangle$  (4.18b) and scales of nonlinear transfer term  $S_{nl}$  (4.18a) with no reference to wind speed and specific mechanisms of air-sea coupling. Homogeneity property of the collision integral  $S_{nl}$  (4.16) allows for existence of these self-similar solutions and possibility to scale the nonlinear transfer term  $S_{nl}$  by two parameters only : characteristic frequency and magnitude of wave spectrum. It gives a really proactive tool of wind-wave studies – the weakly turbulent law of wave growth that links total energy  $E$ , spectral peak frequency  $\omega_p$  and total wave flux  $\langle S_{in} + S_{diss} \rangle$

$$\frac{E\omega_p^4}{g^2} = \alpha_{ss} \left( \frac{\omega_p^3}{g^2} \langle S_{in} + S_{diss} \rangle \right)^{1/3} = \alpha_{ss} \left( \frac{\omega_p^3}{g^2} \frac{dE}{dt} \right)^{1/3} \quad (4.19)$$

Here  $\alpha_{ss}$  – parameter of self-similarity depends slightly on exponents of spatial or temporal growth  $p_\chi, p_\tau$  in (4.17) (Badulin et al., 2007)

$$\alpha_{ss}^{(f)} \sim p_\chi^{-1/3}; \quad \alpha_{ss}^{(d)} \sim p_\tau^{-1/3} \quad (4.20)$$

Superscripts (*d*) and (*f*) for duration and fetch-limited cases respectively are omitted in the following.

We should stress once more a conceptual difference between the weakly turbulent scaling and traditional wind speed scaling by Kitaigorodskii (1962). The latter links wind characteristics directly with parameters of waves. Additionally, it relies (somewhat implicitly) upon an idea of universality of wind speed as a characteristic of air flow that governs wave evolution. In fact, discrepancies of experimental results themselves in the form of dependencies (4.17) with 4 free parameters ( $\omega_0, E_0, p_{\chi(\tau)}, q_{\chi(\tau)}$ ) contradict such idea of universality, as outlined by Donelan et al. (1992) :

‘Perhaps it is time to abandon the idea that a universal power law for non-dimensional fetch-limited growth rate is anything more than an idealization.’

On the contrary, the weakly turbulent scaling separates the air flow dynamics from inherent wave dynamics assuming the hypothesis of dominant nonlinear transfer. The hypothesis makes total wave forcing a key physical scale and gives quantitative link of integral parameters of wave spectra. Parameters  $\omega_0, E_0, p_{\chi(\tau)}, q_{\chi(\tau)}$  in (4.17) cease to be free anymore but obey two relationships resulting from the split balance model (see for details § 2.1, 2.2 in Badulin et al., 2007).

In (4.19) we give two alternative formulations in order to show possible advantages of the weakly turbulent approach for the problem of wind-wave growth. First, instantaneous parameters of wave field, energy and peak frequency, give us information on net wave energy input. Secondly, one can estimate wave period or self-similarity parameter  $\alpha_{ss}$  from temporal (spatial) history of wave energy (energy  $E$  itself and its derivative  $dE/dt$ ). The latter feature has been used by Badulin et al. (2007, 2008a) in order to validate the asymptotic split balance model (4.18) and to estimate self-similarity parameter  $\alpha_{ss}$  numerically for particular case of duration-limited growth.

For the fetch-limited growth, the law (4.19) in the form

$$\frac{E\omega_p^4}{g^2} = \alpha_{ss} \left( \frac{\omega_p^2}{2g} \frac{\partial E}{\partial x} \right)^{1/3} \quad (4.21)$$

has been checked for a collection of experimental power-law parameterizations of wind-wave

growth covering a wide range of energy growth exponents

$$0.7 < p_\chi < 1.1 \quad (4.22)$$

After thorough analysis of consistency of the experimental conditions with basic assumptions of statistical description of wave field, the self-similarity parameter  $\alpha_{ss}$  has been estimated as

$$\alpha_{ss} = 0.55 \pm 0.25 \quad (4.23)$$

Analysing results of our simulations, we are trying to use both advantages of weakly turbulent scaling in the sense of the law (4.19).

### 4.3.2 Reference cases of wind-wave growth

The weakly turbulent law (4.19) can be introduced in different forms : for energy (see 4.19), wave momentum  $M$

$$\frac{M\omega_p^3}{g^2} = \alpha_{ss}^{(M)} \left( \frac{\omega_p^2}{g^2} \frac{dM}{dt} \right)^{1/3} \quad (4.24)$$

or wave action  $N$

$$\frac{N\omega_p^5}{g^2} = \alpha_{ss}^{(N)} \left( \frac{\omega_p^4}{g^2} \frac{dN}{dt} \right)^{1/3} \quad (4.25)$$

where the self-similarity parameters  $\alpha_{ss}^{(M)}$ ,  $\alpha_{ss}^{(N)}$  are counterparts of  $\alpha_{ss}$  in (4.19). It makes possible to fix reference cases of interaction of wind and waves corresponding to different regimes of wave production at different stages of wave growth. These cases correspond to constant fluxes of energy, wave momentum and wave action and give simple single-parameter dependencies of energy on peak frequency (period). The theoretical and experimental aspects will be presented in details in a separate paper. Here we discuss these reference cases in brief as a background for analysis of results of simulations.

All the cases are known for a long time but so far their relevance with weak turbulence theory was not demonstrated properly.

#### 4.3.2.1 The Toba 3/2 law as a regime of constant energy flux to waves

The relevance of empirical Toba's 3/2 law as a basic regime of wave growth was shown by Badulin et al. (2007). Take the Toba law in the original form (Toba, 1997) for significant wave height  $H_s$  and period  $T_s$

$$H_s = B(gu_*)^{1/2} T_s^{3/2} \quad (4.26)$$

Conversion to conventional total energy  $E = H_s^2/16$  and peak frequency  $\omega_p = 2\pi/T_s$  gives

$$\frac{E\omega_p^4}{g^2} = \left( \frac{\pi^9 B^6 u_*^3}{8g} \frac{\omega_p^3}{g^2} \right)^{1/3} \quad (4.27)$$

Comparing (4.27) and (4.19), we see that the Toba law corresponds to constant in time total flux of energy  $dE/dt$ . This flux or net total input can be easily estimated (attention to misprint in equation 5.1 of Badulin et al., 2007)

$$\frac{dE}{dt} = \frac{\pi^9 B^6 u_*^3}{8\alpha_{ss}^3 g} = 0.16 \frac{\rho_a}{\rho_w} \frac{u_*^3}{\alpha_{ss}^3 g} \quad (4.28)$$

when  $B = 0.062$  (Toba, 1972). The estimate of wave energy looks reasonable. In terms of explicit dependence on fetch this case gives exponents  $p_\chi = 3/4$ ;  $q_\chi = 1/4$  in (4.17). The spatial growth rate is lower than linear because of effect of downshift – longer waves at longer fetches are traveling faster.

#### 4.3.2.2 The Hasselmann et al. (1976) 5/3 law of constant momentum flux to waves

Hasselmann et al. (1976) considered a special case that gives one-parametric 5/3 law linking significant wave height and peak period. In terms of non-dimensional energy, it writes

$$\tilde{E} = C_0 \left( \frac{\tilde{\omega}_p}{2\pi} \right)^{-10/3}; \quad C_0 = 5.1 \times 10^{-6} \quad (4.29)$$

The term ‘law’ seems to be quite relevant : this case corresponds to constant flux of momentum to waves, i.e.  $dM/dt = \text{const}$  in (4.24). It is interesting to remind attempts by Toba (1978) to identify this case with his own law as soon as experimental data are close to both 3/2 (see 4.26) and 5/3 (see 4.29) dependencies. From the ‘weakly turbulent viewpoint’ the difference between these two laws is fundamental : Toba’s law works for constant energy flux while the 5/3 law is valid for constant flux of wave momentum. From (4.19) one has immediately the following estimate of energy growth rate

$$\frac{dE}{dt} = 7.7 \times 10^{-3} \frac{\rho_a}{\rho_w} \frac{C_p u_*^2}{\alpha_{ss}^3 g} \quad (4.30)$$

Here we used dependence of reference wind speed  $U_{10}$  and friction velocity  $u_*$  in the simplest form

$$U_{10} = 28u_* \quad (4.31)$$

For growing wind sea the spectral peak phase speed  $C_p$  is growing. Thus, the energy production grows along the trajectory. This growth is compensated by the spectra downshift that gives linear growth of energy with fetch ( $p_\chi = 1$ ) and frequency downshift ( $q_\chi = 3/10$ ) faster than in the previous case.

#### 4.3.2.3 The Zakharov and Zaslavsky (1983) 4/3 law of constant action flux to waves

The last reference case of wave growth has been found by Zakharov & Zaslavsky (1983b). In their series of papers, Zakharov & Zaslavsky (1982b,a, 1983a,b) first applied weakly turbulent theory for analysis of wind-driven seas when they associated the wave growth with a mechanism of inverse cascading of wave action. They started with the classic stationary solution for the kinetic equation that corresponds to constant in time flux of wave action from infinitely small to infinitely large wave scales. Extending this mechanism to non-stationary case they proposed an explanation of experimental data available at the beginning of the eighties. The theory gave exponents of energy growth and frequency downshift while experimental data were used to find the corresponding pre-exponents. The one-parametric relationship energy-to-frequency in this case was found from available experimental data (Hasselmann et al., 1980)

$$\tilde{E} = 1.5 \times 10^{-3} \tilde{\omega}_p^{-8/3} \quad (4.32)$$

for theoretical exponents

$$p_\chi = 4/7; \quad q_\chi = 3/14$$

Similarly to previous cases and with (4.31), one has for energy input

$$\frac{dE}{dt} = 1.6 \frac{\rho_a}{\rho_w} \frac{C_p^{-1} u_*^4}{\alpha_{ss}^3 g} \quad (4.33)$$

The energy input at constant friction velocity  $u_*$  decreases with time as peak frequency.

In our overview of reference cases of self-similar wave spectra growth we related these cases with constant fluxes of key physical quantities : wave energy (Toba, 1972), momentum (Hasselmann et al., 1976) and wave action (Zakharov & Zaslavsky, 1983b). The 4/3 law of wave growth (Zakharov & Zaslavsky, 1983b) corresponds to the slowest growth of wind sea with the smallest exponent of wave energy growth with fetch  $p_\chi = 4/7 \approx 0.57$  that is close to minimal values  $p_\chi$  observed experimentally (see 4.22). The two other cases are represented by a number of sea experiments (Table 1,2 in Badulin et al., 2007). The Hasselmann et al. (1976) 5/3 law is likely associated with the growth of relatively young waves when energy flux is growing with time while wave momentum flux remains constant.

Case	$T = p_\chi/(2q_\chi)$	$\tilde{B}$	$p_\chi$	$q_\chi$	$\rho_w/\rho_a \times dE/dt$
$dM/dt = \text{const}$	5/3	$2.33 \times 10^{-3}$	1	3/10	$0.0077 \frac{C_p u_*^2}{\alpha_{ss}^3 g}$
Hasselmann et al. (1976)					
$dE/dt = \text{const}$	3/2	$2.13 \times 10^{-3}$	3/4	1/4	$0.16 \frac{u_*^3}{\alpha_{ss}^3 g}$
Toba (1972)					
$dN/dt = \text{const}$	4/3	$1.5 \times 10^{-3}$	4/7	3/14	$1.6 \frac{C_p^{-1} u_*^4}{\alpha_{ss}^3 g}$
Zakharov & Zaslavsky (1983b)					

TABLE 4.1 – Summary of reference regimes of wind wave growth. Exponents  $p_\chi$ ,  $q_\chi$  are given for explicit dependencies on fetch (4.17).  $\tilde{B}$  and  $T$  are parameters in energy-to-frequency relationship  $\tilde{E} = \tilde{B}\tilde{\omega}_p^{-2T}$ . Last column is parameterization of net wave forcing  $dE/dt$  in accordance with weakly turbulent relationship (4.19).

This case is of special interest as far as wave momentum can be related quite naturally with turbulent wind stress.

The most known 3/2 Toba's law is very close to majority of cases of wind-wave growth. Toba himself treats this law as a result of local balance of wind stress and nonlinearity of wind waves as a sort of ‘saturation’ of wave growth (Toba, 1997). In terms of our approach this saturation is dealing with independence of energy flux on wave properties, the total energy input depends on friction velocity  $u_*$  only. Following Toba one can treat 5/3 regime as ‘under-saturated’ one when energy input is growing with the wave growth, while the case 4/3, logically, can be called ‘over-saturated’ one when energy input is decaying.

We finalize this section by a summary given in Table 4.1. The listed reference cases give a background for comparison with numerical results. Such comparison can be two-fold : first, we can discuss evolution of key parameters of wave spectra – energy and frequency. Secondly, the reference cases treated in the spirit of weakly turbulent approach give information on external forcing behavior, i.e. on the terms of  $S_{in}$  and  $S_{diss}$  which are given by an additional model of wave input and dissipation. Thus, one can try to discriminate features of inherent wave physics and physics of air-sea interaction.

### 4.3.3 ‘Cleanest’ dependencies of wind-wave growth

In addition to the above reference cases we use experimental dependencies to analyze our numerical results. A great number of these experimental dependencies has been obtained during last 50 years of wind-wave studies but a small part only can be used for correct physical analysis of wind-wave growth. This important message has been formulated many times, first, when considering methodological aspects of measurements and data processing (Kahma & Calkoen, 1992), secondly, proposing physical approach for the data analysis. Following this message Badulin et al. (2007) analyzed more than 20 available dependencies

Case	$T = \frac{p_\chi}{2q_\chi}$	$\tilde{B}$	$p_\chi$	$q_\chi$	$T_{th} = \frac{5p_\chi}{2p_\chi + 1}$
Babanin & Soloviev (1998a)	1.62	$2.91 \times 10^{-3}$	0.89	0.275	1.60
Kahma & Calkoen (1992) unstable	1.68	$3.99 \times 10^{-3}$	0.94	0.28	1.63
Kahma & Calkoen (1992) stable	1.58	$2.43 \times 10^{-3}$	0.76	0.24	1.51

TABLE 4.2 – Summary of experimental cases of wind wave growth. Exponents  $p_\chi$ ,  $q_\chi$  are given for explicit dependencies on fetch (4.17).  $\tilde{B}$  and  $T$  are parameters in the corresponding energy-to-frequency relationship  $\tilde{E} = \tilde{B}\tilde{\omega}_p^{-2T}$ . Last column is the theoretical estimate of exponent  $T$  in the energy-to-frequency relationship (Badulin et al., 2007) for given value of  $p_\chi$ .

of wind-wave growth to fit them to certain physical criteria of measurements and processing wind-wave data.

First, wind wave tank data should be excluded from consideration because of perfectly different physics of almost unidirectional wind wave growth at very short fetches (100–200 wavelengths at the best).

Secondly, one-point measurements where variance of non-dimensional fetch is dealing with instantaneous wind speed scaling should be considered as irrelevant to the problem discussed as well.

Finally, the use of composite data sets where different cases of wind development are mixed together is also questionable for analysis within the weakly turbulent approach and relationship (4.19). For further discussion we shall refer to three experimental dependencies listed as ‘the cleanest’ cases (1.1, 1.3, 1.4 of Tables 2, 3 in Badulin et al., 2007). We do not take case 1.2 of the list (airborne data by Walsh et al., 1989) because of significant departure of the corresponding estimate of  $\alpha_{ss}$  from estimates for other cases. This ‘outlier’ can be explained by the methods of measurements and data processing. All the airborne measurements analyzed in Badulin et al. (2007), ‘the cleanest’ by Walsh et al. (1989) and ‘bad’ dependencies by Ross (1978) or Liu & Ross (1980), show lower values of  $\alpha_{ss}$  as compared with direct measurements of wave growth.

Table 4.2 presents exponents  $T$ ,  $p_\chi$ ,  $q_\chi$  as well as pre-exponents  $\tilde{B}$  for the selected dependencies. As soon as experimental exponents  $p_\chi$ ,  $q_\chi$  do not obey precisely the theoretical relationship (4.19) we give also a theoretical value of exponent  $T_{th} = 5p_\chi/(2p_\chi + 1)$  (see equation (2.38) of Badulin et al. (2007)), considering exponent of wave energy growth with fetch as ‘more reliable’ than exponent of frequency downshift  $q_\chi$ . Note that all the listed dependencies are quite close to reference cases of Table 4.1. The exponent  $T_{th}$  is well between the Toba 3/2 and the Hasselmann et al. (1976) 5/3. Within the weakly turbulent approach presented above it means energy flux growing with fetch in all the presented cases. Theoretical cases of Table 4.1 and experimental dependencies of Table 4.2 are used below for analysis of numerical results on wind-wave growth.

## 4.4 Fetch-limited wind-wave growth in simulations

In this section we present results of simulations within the setup of § 4.2. Within the ‘traditional’ wind speed scaling these simulations show nothing but necessity to tune model and give no hints to the most critical points of the modeling. In this sense, the traditional scaling can be characterized as ‘reactive’. Alternatively, the weakly turbulent scaling operates with physical parameters of the split balance model (4.18). Reference cases of this model presented in the previous section allow for tracing wind-wave balance in more definite and physically consistent way. Claiming ‘proactiveness’ of the weakly turbulent scaling we claim a potential of this approach to fix critical points of wind-wave modeling and propose effective solutions for more accurate and physically correct simulation of wave spectra.

### 4.4.1 Wind speed scaling : reactive understanding of wave growth

#### 4.4.1.1 Explicit dependencies of energy and frequency on fetch

The simulation results can be presented straightforwardly in terms of conventional non-dimensional variables (Kitaigorodskii, 1962, 1983) : non-dimensional fetch  $\chi = Xg/U_{10}^2$ , spectral peak frequency  $\tilde{\omega}_p = U_{10}/C_p$  (inverse wave age) and energy  $\tilde{E} = Eg^2/U_{10}^4$ . Figures 4.3 and 4.4 present wave energy growth and frequency downshift curves. Each value of wind speed is presented in a separate panel for two different functions of wave input, and two different methods for calculating  $S_{nl}$ . Straight lines show the experimental ‘cleanest’ dependencies of Table 4.2.

One can see a strong dispersion in both numerical and experimental dependencies. While experimental curves are fixed in all panels, their numerical counterparts drift with wind speed within almost one order of magnitude for non-dimensional energy (figure 4.3) and by several tens of percents for non-dimensional frequency (inverse wave age) (figure 4.4).

In all the panels of figures 4.3 and 4.4, we see first of all differences dealing with wave input functions. The non-dimensional energy  $\tilde{E}$  obtained with Janssen (1989, 1991) reaches two times higher magnitudes than the one using Snyder et al. (1981) input. The corresponding difference for  $\tilde{\omega}_p$  can reach 20% in these cases. Effect of method of calculation of nonlinear transfer term  $S_{nl}$  is incomparably weaker but is still visible for relatively young waves.

In figures 4.3 and 4.4 one can see that Snyder et al. (1981) and Janssen (1989, 1991) growth curves can increase faster or slower than the other one depending on the wind speed : for low winds ( $U_{10} = 5 \text{ m s}^{-1}$ ) waves grow faster for input by Snyder et al. (1981) while for high winds ( $U_{10} = 20 - 30 \text{ m s}^{-1}$ ) the input by Janssen (1989, 1991) leads to stronger growth. As compared with dependencies of Table 4.2 the curves show close tangents for low winds  $U_{10} = 5, 10 \text{ m s}^{-1}$ . For strong winds  $U_{10} = 20, 30 \text{ m s}^{-1}$  these tangents can be essentially steeper in some cases.

The white-capping dissipation is growing with fetch faster if compared with wave input. It can lead to a state where wave energy and peak frequency cease to evolve. As it is seen in

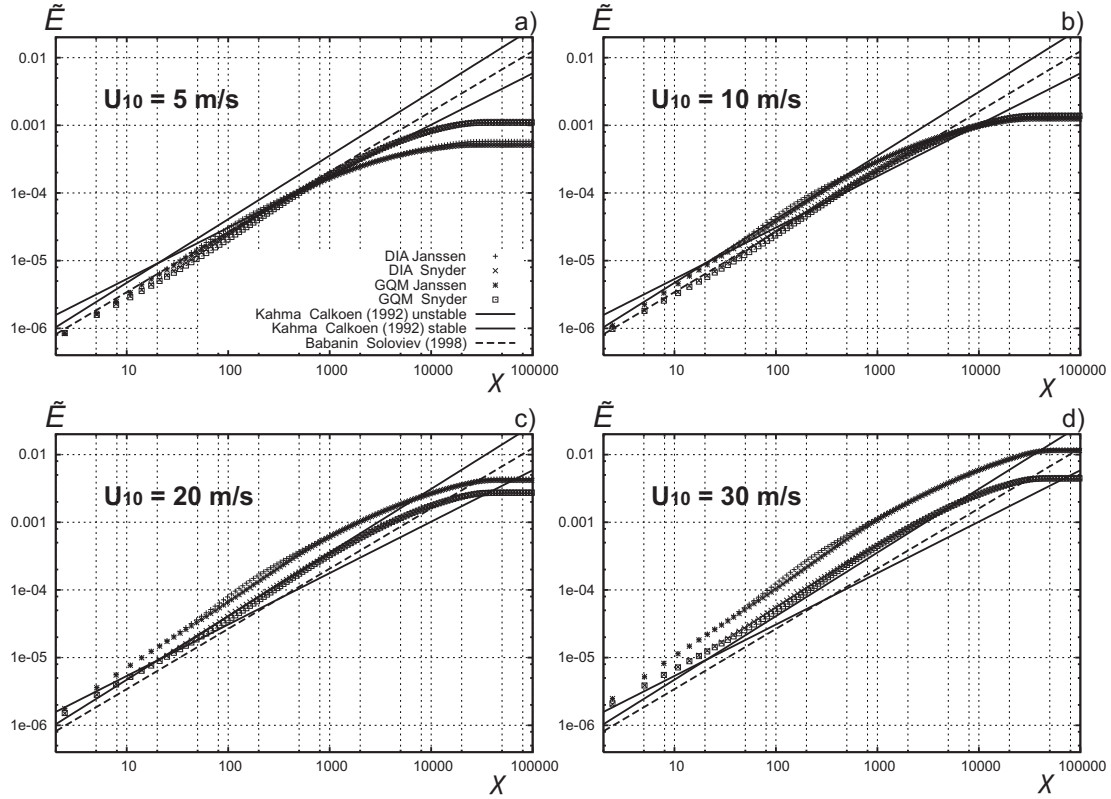


FIGURE 4.3 – Non-dimensional energy  $\tilde{E} = Eg^2/U_{10}^4$  as function of non-dimensional fetch  $\chi = Xg/U_{10}^2$ , for different wind speeds  $U_{10} = 5, 10, 20, 30 \text{ m s}^{-1}$ , parameterizations of wave input term  $S_{in}$  by Snyder et al. (1981) and Janssen (1989, 1991), DIA and GQM methods for calculating  $S_{nl}$  (shown in legends). ‘The cleanest’ experimental dependencies of Table 4.2 are given for comparison.

figures 4.3 and 4.4 the state of ‘mature’ sea is not universal in terms of non-dimensional wave energy and frequency. This is in contradiction with the classic Pierson & Moskowitz (1964) parameterization of the mature sea spectra where universal values of wave age and wave steepness are postulated.

In finer details of spectral distributions the existence of a stationary wind-driven sea where all the constituents of wave field are fully balanced is a big question which is far from definite answer (Komen et al., 1984). For mature sea state, GQM method and DIA give close results that might suggest that DIA is sufficient to describe evolution of integral characteristics. Nevertheless, the problem of existence and balance of mature sea requires a thorough analysis of the spectral distributions. It is very unlikely that this fundamental problem can be solved without exact (or quasi-exact) calculation of  $S_{nl}$  (e.g. Gagnaire-Renou et al., in press). Further in this paper we refer to the ‘mature’ sea state in terms of total energy and spectral peak frequency only.

Note that within the conventional scaling two qualitatively different stages of wave deve-

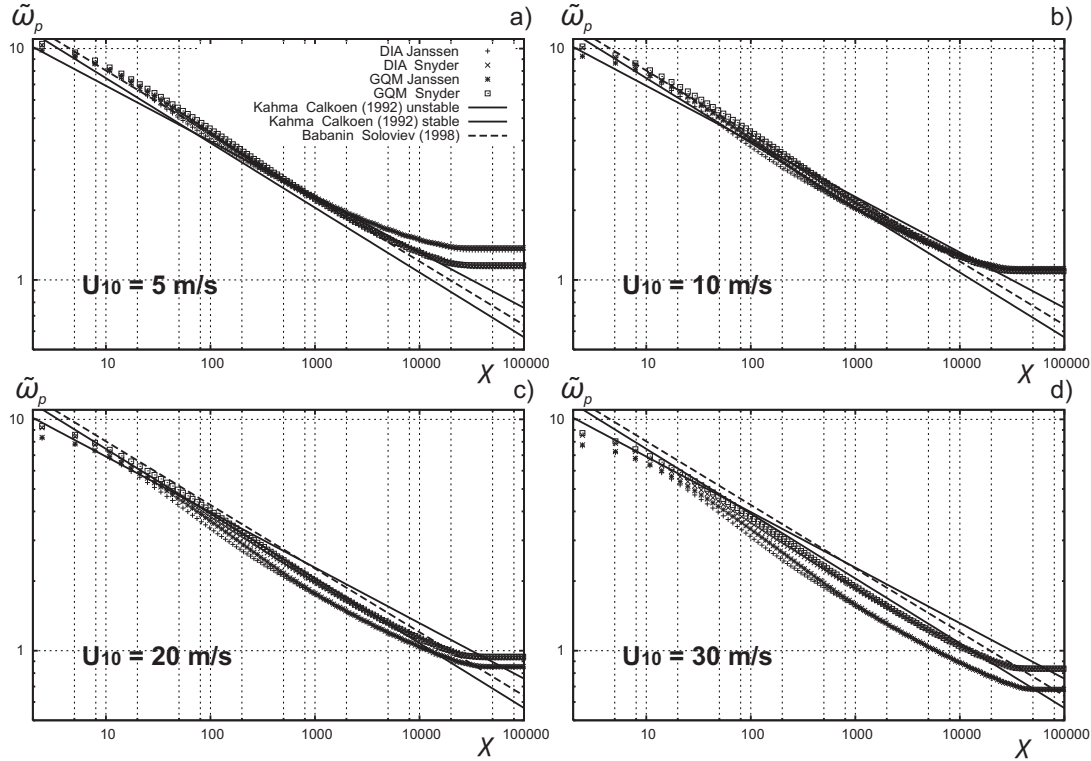


FIGURE 4.4 – Inverse wave age  $\tilde{\omega}_p = \omega_p U_{10} / g$  as function of non-dimensional fetch  $\chi = X g / U_{10}^2$ , for different wind speeds  $U_{10} = 5, 10, 20, 30 \text{ m s}^{-1}$ , parameterizations of wave input term  $S_{in}$  by Snyder et al. (1981) and Janssen (1989, 1991), DIA and GQM methods for calculating  $S_{nl}$  (see legends). ‘The cleanest’ experimental dependencies of Table 4.2 are given for comparison.

lopment can be identified only : the growing wind sea and the mature sea. No quantitative criterium can be proposed to distinguish these two regimes : the demarcation line can be put in an arbitrary way in a quite wide range of non-dimensional fetches (20000 – 40000 in our simulations). Curves in the ‘traditional’ wind speed scaling do not show any specific feature of initial wave growth. As it will be shown below, the growth of these young waves is of special interest and the special physics can be identified adequately within an alternative weakly turbulent scaling.

An explanation of the most pronounced features of energy growth (figure 4.3) looks trivial : the energy is higher when total input is higher (see figure 4.1). It allows us to explain qualitatively (not quantitatively) different energies of growing waves and different magnitudes of the mature seas at long fetches.

The trivial explanation does not work when considering evolution of spectral peak frequency (figure 4.4). The wave input affects frequency downshift indirectly, through spectral distribution and, hence, through nonlinear transfer. The latter is beyond the conventional approach to the wind wave growth as it was mentioned above. At the same time, a remar-

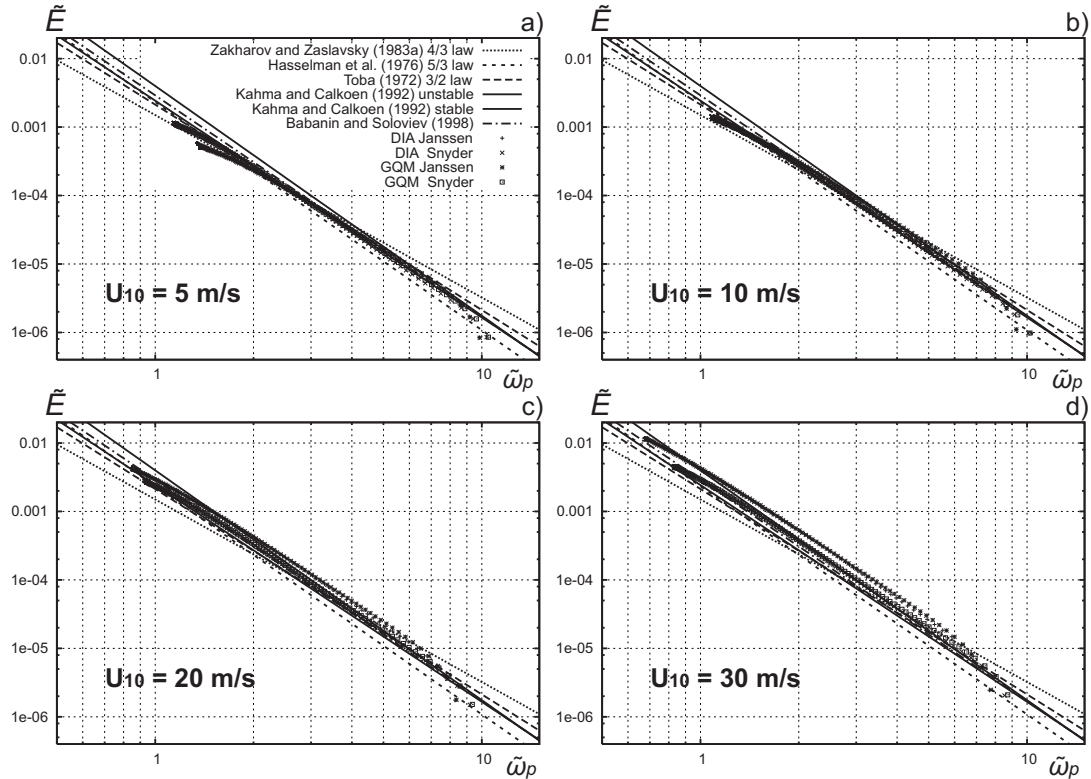


FIGURE 4.5 – Non-dimensional energy  $\tilde{E}$  vs non-dimensional peak frequency  $\tilde{\omega}_p$ . Straight lines – ‘the cleanest’ experimental dependencies, Toba’s 3/2 law for the reference case  $dE/dt = \text{const}$ , the Hasselmann et al. (1976) 5/3 law for  $\omega_p dE/dt = \text{const}$  and the Zakharov & Zaslavsky (1983b) 4/3 law for the case  $\omega_p^{-1} dE/dt = \text{const}$ .

kable correlation should be noted for energy and frequency curves : higher magnitudes of the mature sea amplitudes correspond to lower spectral peak frequencies (cf. figures 4.3 and 4.4).

#### 4.4.1.2 The single-parameter dependencies

The single-parameter representation of wind-wave growth, as called by Hasselmann et al. (1976) for the representation of energy  $\tilde{E}$  versus peak frequency  $\tilde{\omega}_p$ , has a long history and a solid physical background. We discussed briefly these dependencies in our overview of reference cases in § 4.3.2.

Toba (1972) formulated his 3/2 law (4.26) and then tried to treat all the available wind wave data in the spirit of this single-parametric dependence of energy on frequency. He extends the law validity for the whole range of wave development up to the state of mature sea.

Hasselmann et al. (1976) stressed that their 5/3 law is just a particular case of wave growth that is associated with particular balance of wind waves (hypothesis of dominating nonlinear transfer), self-similarity of this growth and a particular parameterization of wave forcing. Their coefficient  $C_0$  in (4.29) was found from parameters of wave prediction model and appeared to be quite close to experimental dependencies.

The single-parameter relationship (4.32) by Zakharov & Zaslavsky (1983b) is ensured by theoretical Kolmogorov-like link of wave parameters to total wave action flux. This flux was estimated based on field data of JONSWAP (Hasselmann et al., 1980). The quite questionable correspondence of the theory to experimental data available in the 80-ies can be illustrated by figures 5,6,8 in Zakharov & Zaslavsky (1983b) or by figure 9.5 in Zaslavsky (1984). It does not mean that the theory cannot obtain its experimental justification in future. In fact, such justification is extremely difficult to find as soon as this case correspond to a late stage of wave growth and low exponents  $p_\chi$ . In the list of observed fetch-limited dependencies given by Badulin et al. (2007) (Tables 1,2) the exponent  $p_\chi = 4/7 \approx 0.57$  is slightly below minimal values.

In figure 4.5, dependencies of non-dimensional energy on non-dimensional spectral peak frequency are given similarly to previous figures 4.3 and 4.4 for different wind speeds, parameterizations of wave forcing terms and methods of calculation for  $S_{nl}$ . In terms of this representation differences of all the results look unessential. Moreover, the mature sea state (upper left simulation points) and growing seas are difficult to discriminate in these plots because of fast convergence of total energy and peak frequency to limiting values.

All the dependencies listed in Tables 4.1, 4.2 give very close fit (at the first glance) to the results of simulations. The minor mismatches of different curves in figure 4.5, in fact, are of key importance. Within the weakly turbulent approach, the reference case by Toba (1972) gives constant wave energy flux acquired by waves and, hence, the single-parametric dependency (4.26) corresponds to constant non-dimensional flux of energy (4.28). Small deviation from the reference curve of Toba in figure 4.5 being converted into energy flux becomes a great value as soon as  $dE/dt \sim E^3$  (see equation 4.19). One can notice that slopes of the simulation curves are close to Hasselmann et al. (1980) law for relatively young waves, then they appear closer to Toba's curves and finally to Zakharov & Zaslavsky (1983b) plot at the end of growing wind sea stage.

The small drift of simulation curves for high winds relative to the reference cases being uninformative in terms of single-parametric dependencies, indicates dramatic changes of net wave input (total wave forcing  $\langle S_{in} + S_{diss} \rangle$ ) – a key parameter of weakly turbulent scaling.

#### 4.4.2 Key points of weakly turbulent scaling

The weakly turbulent scaling is based on total wave inputs (fluxes) of basic quantities (wave energy, wave momentum, wave action). In this paper we use mostly the scaling based on energy and flux of wave energy. In some cases, as it was demonstrated for reference cases in the previous section, alternative formulations for wave momentum or wave action can be

very useful. The approach itself, irrespective of its particular formulation, is based on a key hypothesis of the split balance model : the hypothesis of dominating nonlinear transfer.

#### 4.4.2.1 Total wave input as governing quantity of wind-wave evolution

Figure 4.6 illustrates the governing role of total wave input on evolution of wave parameters. Net wave input  $\langle S_{in} + S_{diss} \rangle$  for high winds is presented as function of dimensional fetch for different wave input parameterizations and DIA method for nonlinear transfer term (figure 4.6a). With  $S_{in}$  parameterization by Janssen (1989, 1991) the total wave forcing  $\langle S_{in} + S_{diss} \rangle$  appears to be 2 to 3 times higher than the one by Snyder et al. (1981) for the same wind speed  $U_{10} = 30 \text{ m s}^{-1}$ . The Janssen (1989, 1991) function at  $U_{10} = 26 \text{ m s}^{-1}$  is shown as one that is close to the Snyder et al. (1981) input at  $U_{10} = 30 \text{ m s}^{-1}$ .

Reference net wave inputs (wave energy fluxes) of § 4.3.2 are plotted for comparison. They appear five times to almost one order of magnitude below functions obtained in simulations. This dramatic difference can be related to high wind speeds that have been unlikely observed in the experiments the reference cases are based on. At the same time there is a qualitative correspondence of reference cases and results of simulations : wave input grows at short fetches (5/3 law by Hasselmann et al., 1976), reaches a stationary state for intermediate fetches (3/2 regime by Toba, 1972) and then decays as Zakharov & Zaslavsky (1983b) predict. Note that for the reference cases, we used net wave input parameterizations of Table 1 with  $\alpha_{ss}(p_\chi = 1) = 0.62$  (Hasselmann et al., 1976),  $\alpha_{ss}(p_\chi = 3/4) = 0.68$  (Toba, 1972) and  $\alpha_{ss}(p_\chi = 4/7) = 0.74$  (Zakharov & Zaslavsky, 1983b). The corresponding estimates are based on results of simulations and will be detailed below.

Link between instantaneous wave inputs and instantaneous wave parameters  $H_{m0}$  and  $T_p$ , as defined by the weakly turbulent asymptotic law (4.19), is well illustrated by figure 4.6. For short and intermediate fetches ( $X < 500 \text{ km}$ ) net wave input by Snyder at  $30 \text{ m s}^{-1}$  and Janssen at  $26 \text{ m s}^{-1}$  differ by several tens of percents while the resulting wave height (figure 4.6b) and period  $T_p$  (figure 4.6 c) are quite close. This does not look surprising if we look at weakly turbulent relationship (4.19) where wave energy depends on energy flux  $dE/dt$  in power 1/3. For older waves ( $500 < X < 3000 \text{ km}$ ) where wave inputs by Snyder and Janssen coincide,  $H_{m0}$  and  $T_p$  are tending to coincide as well which is not a trivial fact because for shorter fetches the input functions differ significantly. This illustrates an important point : waves forget their previous history remarkably fast. From ‘weakly turbulent viewpoint’ such behavior looks natural : wave parameters follow instantaneous wave input with rather short delay and do not depend (or depend slightly) on previous evolution.

Figure 4.7 shows the governing role of total wave input when lower wind speed and different approaches for  $S_{nl}$  are used. At  $U_{10} = 10 \text{ m s}^{-1}$  difference of net wave inputs using Snyder’s and Janssen’s parameterizations are not so pronounced as in previous case. Additionally, the inputs’ magnitudes appear to be closer to reference cases of Table 4.2 (two to three times vs almost one order for  $U_{10} = 30 \text{ m s}^{-1}$ ). The tendency of our results to be closer to reference cases for lower winds looks logical : experimental data these reference parameterizations are based on were obtained for low or moderate winds (or for laboratory

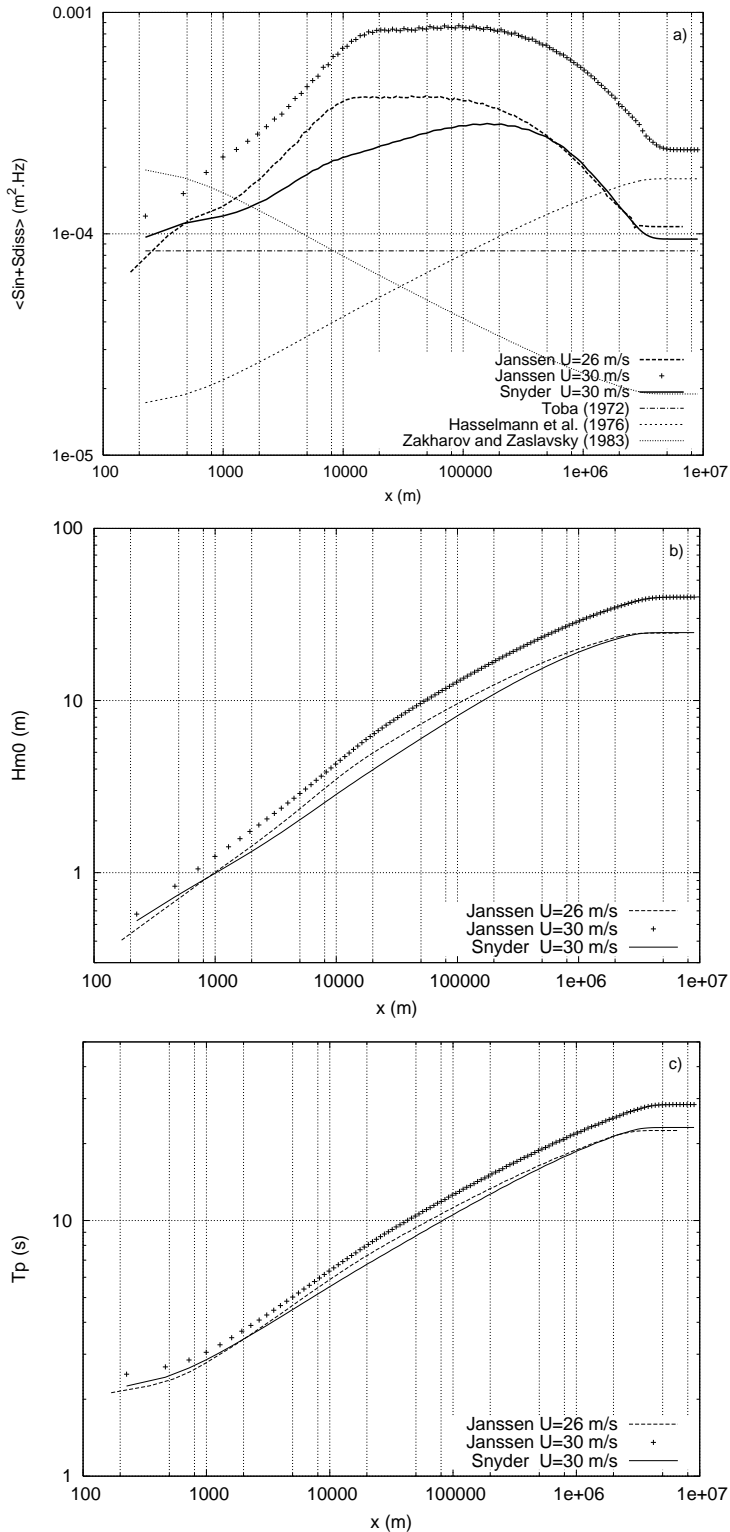


FIGURE 4.6 – a) – Net wave forcing  $\langle S_{in} + S_{diss} \rangle$  as function of the dimensional fetch  $X$  and reference cases of Table 4.1; b) – wave height and c) – wave period. Snyder's input term  $S_{in}$  at wind speed  $U_{10} = 30 \text{ m s}^{-1}$  is compared with Janssen's input term at  $U_{10} = 26 \text{ m s}^{-1}$  and  $U_{10} = 30 \text{ m s}^{-1}$ . Results for DIA method for  $S_{nl}$  term are shown.

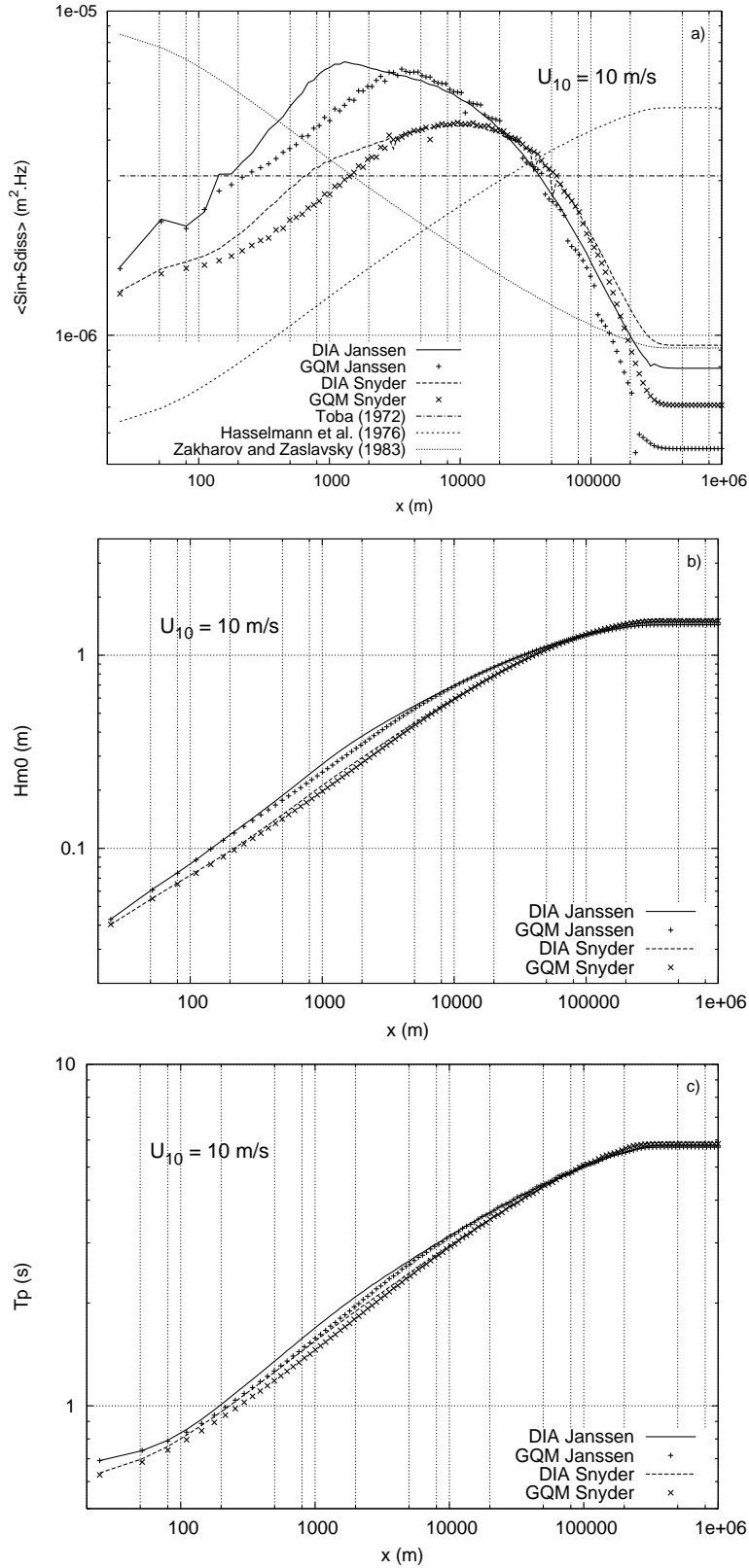


FIGURE 4.7 – a) – Net wave forcing  $\langle S_{in} + S_{diss} \rangle$  as function of the dimensional fetch  $X$  and reference cases of Table 4.1; b) – wave height and c) – wave period at wind speed  $U_{10} = 10 \text{ m s}^{-1}$  for Snyder and Janssen parameterizations of  $S_{in}$ . Results for DIA and GQM methods are shown.

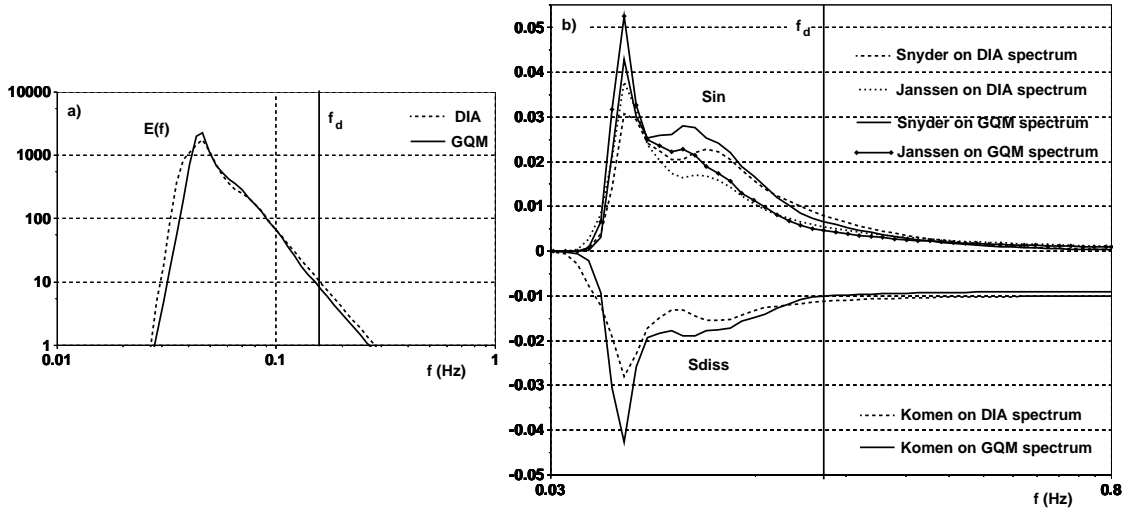


FIGURE 4.8 – a) 1D-spectra  $E(f)$  ( $\text{m}^2 \text{Hz}^{-1}$ ) as functions of frequency  $f$  ( $\text{Hz}$ ) at a large fetch (2400 km) calculated with the GQM and DIA methods, Snyder's source term and wind speed  $U_{10} = 30 \text{ m s}^{-1}$ ; b)  $S_{in}$  functions of Snyder et al. (1981) and Janssen (1989, 1991) and  $S_{diss}$  function of Komen et al. (1984) applied for these two spectra.

tank waves). This illustrates once more insufficiency of wind speed for scaling wind-wave evolution.

Difference of net wave input for different methods for  $S_{nl}$  is fairly well seen in figure 4.7. For short and long fetches (less than 2 km and more than 100 km, respectively) DIA enhances total wave input (up to 50% for Janssen's formulation). It leads to visible effect on wave height  $H_{m0}$  and  $T_p$  at short fetches. The mechanism of influence of method used for  $S_{nl}$  on wave input and, thus, on the resulting wave growth is illustrated by figure 4.8. Wave input and dissipation functions depend on spectral distributions since they are quasi-linear in spectral densities. These distributions can differ significantly for DIA and GQM approaches as it is seen in figure 4.8a. This mechanism is not easy to assess as far as nonlinear transfer and external forcing appear to be closely linked.

Figure 4.8 shows the effect of spectral shape on wave input and dissipation. The instantaneous spectra (figure 4.8a) are taken at dimensional fetch  $X = 2400 \text{ km}$  for  $U_{10} = 30 \text{ m s}^{-1}$ , i.e. for mature sea state where total energy and peak frequency of spectra obtained with GQM and DIA methods are identical. Input functions of Snyder et al. (1981) and Janssen (1989, 1991) and dissipation of Komen et al. (1984) are applied for these two spectra. The effect of the spectral shape on the  $S_{in}$  and  $S_{diss}$  functions is seen fairly well (figure 4.8b).

The black vertical line in figure 4.8 shows the frequency above which the diagnostic tail is imposed. At the right side of this line, the obtained  $S_{in}$  and  $S_{diss}$  functions have no influence on the evolution of the spectrum and must not be considered in the calculation

of the total net wave forcing. Nevertheless, it is interesting to note the strong dissipation in high frequencies obtained with the Komen et al. (1984)  $S_{diss}$  function when imposing a  $f^{-4}$  high-frequency tail (see e.g. Banner & Young, 1994; Gagnaire-Renou et al., in press, for analysis of the influence of the constrained tail).

Despite these ‘shape-to-input’ effects, we saw that differences between DIA and GQM growth curves are still very small in figures 4.3, 4.4. This implies that shape-to-input effects are likely in counterbalance with direct effects of the method for calculating  $S_{nl}$ .

#### 4.4.2.2 Dominating nonlinear transfer and self-similarity of wave spectra

The asymptotic split balance model (4.18) is based on a hypothesis of dominating nonlinear transfer as compared with wave input and dissipation. A straightforward way to justify this hypothesis is a term-to-term comparison of all the constituents of wind-wave balance (e.g. § 3.4 Badulin et al., 2005). Such comparison can lead to misleading results if arbitrary instantaneous spectra and external forcing functions are taken for the comparison. Magnitudes of nonlinear transfer term and external forcing are, in fact, linked to each other because of essential nonlinearity of the Hasselmann equation.

Terms of nonlinear transfer and net wave input for a solution of the Hasselmann equation are shown in figure 4.9 at different non-dimensional fetches. The behavior is typical for all the simulations presented in this study. Wave input can dominate at relatively short fetches, then nonlinear transfer becomes stronger. The excess of the term  $S_{nl}$  is not so pronounced : about 2 to 4 times only for rather long fetches. In fact, such a comparison is not representative for two reasons. First, nonlinear transfer competes with wave input accompanied by dissipation that enhances relative effect of  $S_{nl}$ . Secondly, the leading role of the nonlinear transfer is not determined by  $S_{nl}$  itself but a ‘fine structure’ of the term (see § 2.4 in Badulin et al., 2005, for discussion). The true nonlinear relaxation time is determined by this structure and is much shorter than one derived from the full term  $S_{nl}$ . In many cases, e.g. for mixed seas, the smallness of the nonlinear relaxation scale makes questionable the validity itself of statistical description of water waves (Badulin et al., 2008b).

The true role of nonlinear transfer and its predominant role in wind-wave evolution can be demonstrated in terms of properties of self-similarity of solutions of the Hasselmann equation.

#### 4.4.3 Energy-flux diagrams and self-similarity parameter of growing wind waves

Weakly turbulent approach is based on asymptotic split balance model (4.18). This model predicts self-similar behavior of solutions and rigid link between solutions and spectral fluxes. This link in the form of relationship between total energy and integral flux (4.19) can be used as a test for self-similarity or, more generally, as a test for dominating nonlinear transfer. This idea has been exploited by Badulin et al. (2007) as method of energy-flux

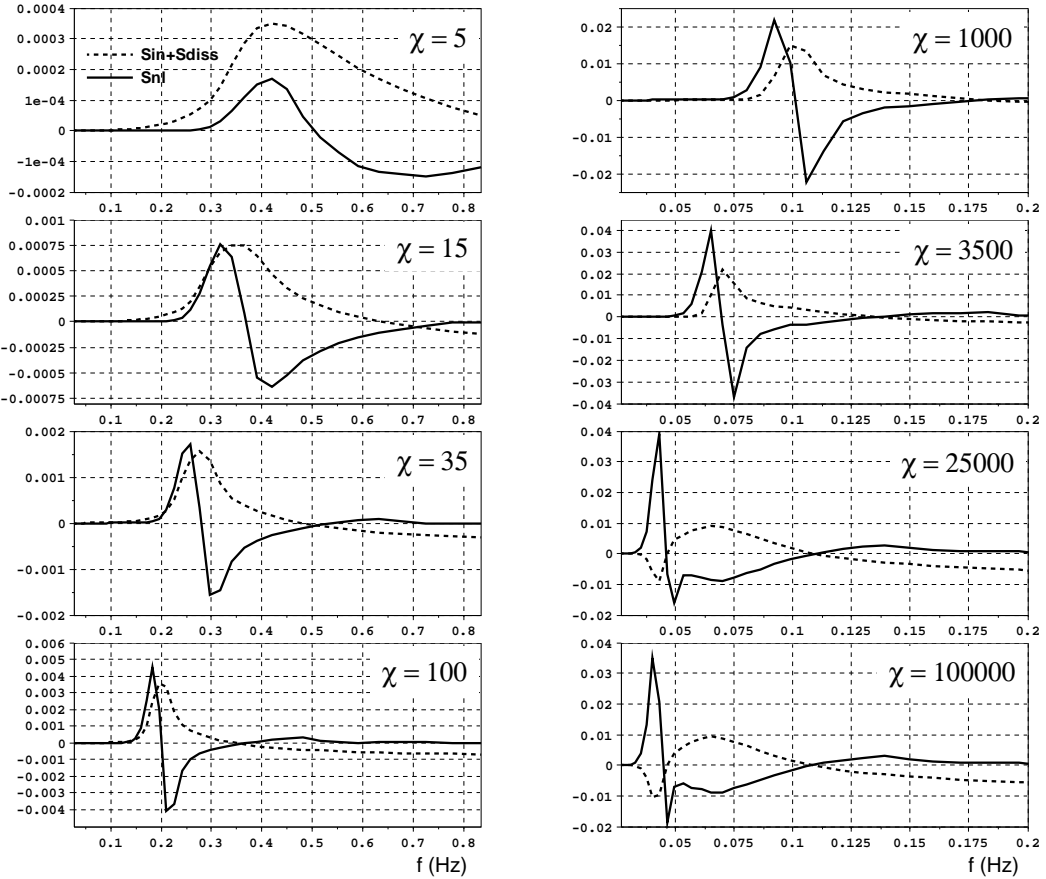


FIGURE 4.9 –  $S_{nl}$  ( $\text{m}^2$ ) (solid lines) and  $S_{in} + S_{diss}$  ( $\text{m}^2$ ) (dashed lines) curves, as functions of frequency  $f$  ( $\text{Hz}$ ), for different non-dimensional fetches  $\chi$ . Wind speed  $U_{10} = 30 \text{ m s}^{-1}$ , Snyder's wind input  $S_{in}$  and GQM method for the  $S_{nl}$ . Note the change of frequency range in the right panels.

diagrams. In this paper, we use the same idea to describe wave spectra evolution from initial growth to the mature sea state.

Figure 4.10 presents energy-flux diagram as proposed by Badulin et al. (2007) for numerical simulation of fetch-limited growth. All cases (different wind speeds, models of  $S_{in}$ , methods for  $S_{nl}$ ) are plotted on this figure intentionally. One can see an asymptotic stage of weakly turbulent wave development fairly well as linear dependence of non-dimensional wave energy (or wave steepness squared) on non-dimensional total net wave input in power 1/3. This is in perfect agreement with the asymptotic relationship (4.21). We added the three dependencies selected in the ‘cleanest’ group (Table 4.2) for comparison. Deviations

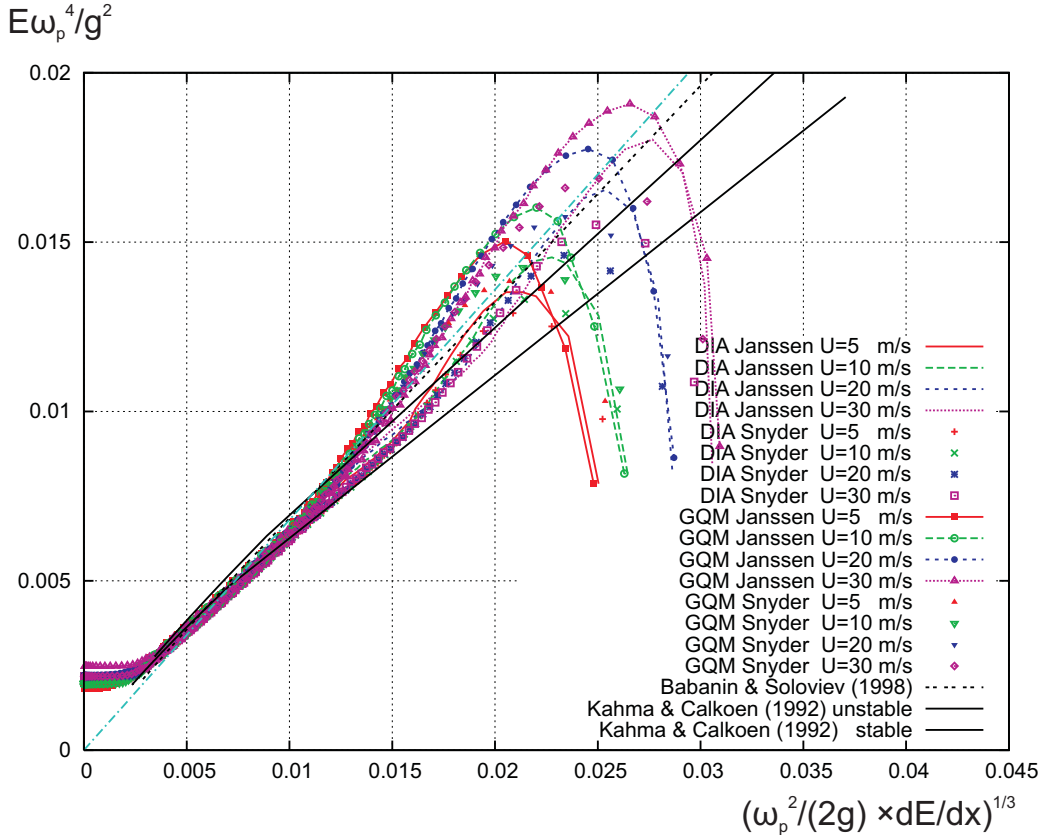


FIGURE 4.10 – Energy-flux dependencies in fetch-limited simulations :  $E\omega_p^4/g^2$  versus  $(\omega_p^2/(2g) \times \partial E/\partial x)^{1/3}$ . Curves for the four wind speeds  $U_{10} = 5, 10, 20, 30 \text{ m s}^{-1}$ , the two parameterizations of the wave input  $S_{in}$  (Snyder and Janssen), and the DIA and GQM methods for the  $S_{nl}$  computation are superimposed. Comparison with the experimental results of Kahma & Calkoen (1992); Babanin & Soloviev (1998b) is carried out. The light-blue curve represents the estimate of  $\alpha_{ss} = 0.68$ .

from the asymptotic regime are seen as different stages of wind-sea evolution. The different regimes (initial wave growth, growing wind-sea and mature wind-sea) are described consecutively in the following sub-section.

The self-similarity parameter  $\alpha_{ss}$  controls the ratio of instantaneous wave steepness (squared) to non-dimensional net wave input (in power 1/3). Results of our numerical study show that a straight line  $y = \alpha_{ss}x$  is tangent to the bundle of curves (light-blue curve in figure 4.10) and consequently  $\alpha_{ss} = 0.68$  can be taken as a representative estimate of the self-similarity parameter. In fact, parameter  $\alpha_{ss}$  depends on wave growth rate  $p_\chi$  (see 4.20). Trying to determine a confidence interval for  $\alpha_{ss}$ , we fix the Toba case as reference one, representative for much of the observed wave growth. Value of  $\alpha_{ss}$  for Toba's reference case is fixed based on our estimate :  $\alpha_{ss}(p_\chi = 3/4) = 0.68$ . Then value of  $\alpha_{ss}$  for two other reference cases of Table 4.1 can be easily deduced from approximate pro-

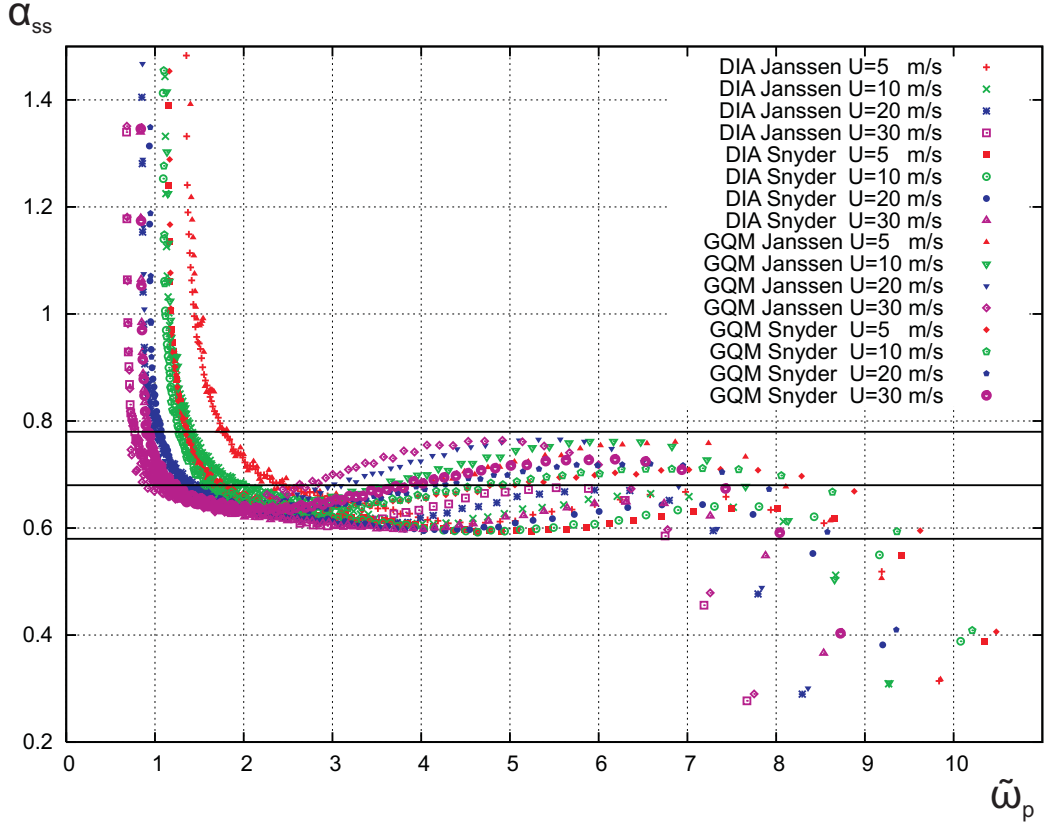


FIGURE 4.11 – Self-similarity parameter  $\alpha_{ss}$  as a function of the inverse wave age  $\tilde{\omega}_p = U_{10}/C_p$ , obtained with wind speeds  $U_{10} = 5, 10, 20, 30 \text{ m s}^{-1}$ , the two parameterizations of the wave input  $S_{in}$  (Snyder and Janssen), and the DIA and GQM methods for the  $S_{nl}$  computation. The horizontal lines  $\alpha_{ss} = 0.58$ ,  $\alpha_{ss} = 0.68$ , and  $\alpha_{ss} = 0.78$  are drawn for a better visualization of the estimated coefficient  $\alpha_{ss} = 0.68 \pm 0.1$ .

portionality  $\alpha_{ss} \sim p_\chi^{-1/3}$  (see 4.20) :  $\alpha_{ss}(p_\chi = 1) = 0.62$  (Hasselmann et al., 1976) and  $\alpha_{ss}(p_\chi = 4/7) = 0.74$  (Zakharov & Zaslavsky, 1983b). Estimates of  $\alpha_{ss}$  for reference cases of Hasselmann et al. (1976) and Zakharov & Zaslavsky (1983b) differ from the Toba value by less than 10 %. The two bounds of the stage of self-similar development can, thus, be fixed by departure  $\pm 0.1$  from the value  $\alpha_{ss} = 0.68$  (which give less than 15 % error, consistent with reference cases estimates). Estimate  $\alpha_{ss} = 0.68 \pm 0.1$  is represented in figures 4.11 and 4.12 where lines  $\alpha_{ss} = 0.58$ ,  $\alpha_{ss} = 0.68$  and  $\alpha_{ss} = 0.78$  are plotted for a better visualization.

Figures 4.11 and 4.12 present ratio  $\alpha_{ss}$  for the different numerical runs as function of inverse wave age (figure 4.11) and wave steepness (figure 4.12). In figure 4.11, we used a ‘mixed’ representation : the self-similarity parameter  $\alpha_{ss}$  (from weakly turbulent theory) is plotted as a function of peak frequency scaled by wind speed. This explains the larger dispersion of the results.

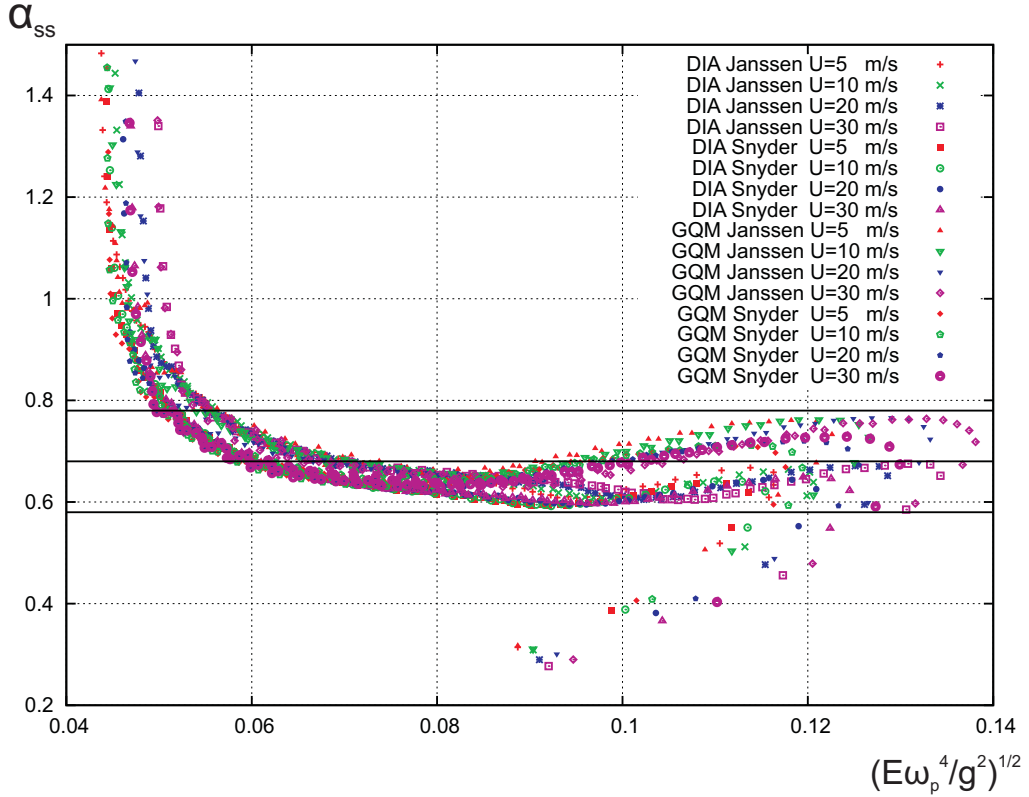


FIGURE 4.12 – Self-similarity parameter  $\alpha_{ss}$  as a function of the wave steepness  $\sqrt{E\omega_p^4/g^2}$  obtained with wind speeds  $U_{10} = 5, 10, 20, 30 \text{ m s}^{-1}$ , the two parameterizations of the wave input  $S_{in}$  (Snyder and Janssen), and the DIA and GQM methods for the  $S_{nl}$  computation. The horizontal lines  $\alpha_{ss} = 0.58$ ,  $\alpha_{ss} = 0.68$ , and  $\alpha_{ss} = 0.78$  are drawn for a better visualization of the estimated coefficient  $\alpha_{ss} = 0.68 \pm 0.1$ .

#### 4.4.4 Stages of wind-wave growth

##### 4.4.4.1 Initial wave growth

Note that wave parameters in figures 4.10, 4.11 and 4.12 start to evolve from right parts of panels : from low initial steepness, maximal non-dimensional wave input or from maximal inverse wave age. In this stage of initial wave growth, the self-similarity parameter  $\alpha_{ss}$  of the asymptotic law (4.19), corresponding to the tangent through points of the trajectory in the energy-flux diagram (figure 4.10), is growing with fetch. The first points on the right side of figure 4.10 correspond to non-dimensional fetch  $\chi = 2.5$ . The wave steepness grows up to a maximum and then starts to decay for rather short non-dimensional fetch  $\chi \approx 10 - 15$ . We see quite strong dispersion of trajectories for different wave input functions, methods for  $S_{nl}$  and wind speeds and no manifestations of self-similar behavior at this stage. It is useful to specify this stage as *non-self-similar stage of initial wave growth* and to define  $\chi^*$  – non-dimensional fetch of the end of this stage. Note the relatively low dispersion of

$\chi^*$  for different wind speeds that makes sense for such demarcation of the state of initially growing wind sea in terms of conventional wind speed scaling. In terms of dimensional fetches this stage is longer for higher winds.

The high dispersion of trajectories at the initial stage for different wind speeds and methods for  $S_{nl}$  and  $S_{in}$  finds its evident explanation in dominating effect of external forcing as illustrated by figure 4.9. Details of distributions of external forcing in frequency and angle play an important role at this stage as well as features of nonlinear transfer functions provided by DIA or any other method for  $S_{nl}$ .

The effect is seen in maximal values of steepness and non-dimensional net wave input that depend on the wind speed and method for calculating  $S_{in}$  and  $S_{nl}$ . Maximal steepness is lower for low winds, for Snyder et al. (1981) input term (as compared with Janssen's one) and when using DIA (as compared with GQM). It is interesting to note that DIA method reduces a bit the duration of this non-asymptotic stage.

Significant dispersion of curves for different wind speeds and methods for  $S_{in}$  is also seen at the initial stage in plots of non-dimensional energy and peak frequency scaled by wind speed (figures 4.3, 4.4). At the same time, as already mentioned above, the wind speed scaling (in contrast to the weakly turbulent approach) does not allow for relating this dispersion with particular physics.

#### 4.4.4.2 Mature wind sea

The well-known stage of mature sea is also identified quite naturally in figure 4.10 as a pronounced deviation of trajectories above an asymptotic straight line. Wave steepness (ordinate axis) is tending to a limiting value, while net wave input (abscissa) is vanishing. This stage can also be observed easily in figures 4.11 and 4.12 when inverse wave age and wave steepness are tending to their limits asymptotically while  $\alpha_{ss} \rightarrow +\infty$ .

The limiting value of steepness  $\varepsilon = \sqrt{E\omega_p^4/g^2}$  depends on the model for the wind input term and on the wind speed. This is in contrast to the case of the classic Pierson-Moskowitz spectrum (Pierson & Moskowitz, 1964) for which steepness is a universal value :

$$\varepsilon_{PM}^2 = \frac{E_{PM}\omega_{PM}^4}{g^2} = \frac{\alpha}{5} \approx 0.0016$$

Here  $\alpha = 0.0081$  is the Phillips's constant in the Pierson-Moskowitz spectrum. Nevertheless, our results give values in a range  $\varepsilon^2 = 0.0018 - 0.0024$ , which are a bit higher but still close to the Pierson-Moskowitz value, especially for low winds  $5$  and  $10$  m s $^{-1}$  ( $\varepsilon < 0.002$ ). Higher winds give 'more severe' mature sea with higher steepness  $\varepsilon$ .

Note that the dependence of the limiting steepness of mature sea on the method for calculating  $S_{nl}$  is very weak. Quite similarly to the case of initially growing waves, the evolution of mature sea is not self-similar and details of particular wave input and dissipation functions  $S_{in}$ ,  $S_{diss}$  are also important. At the same time, the effect of the 'non-self-similarity' is much smaller due to the weakness of the net wave forcing.

We should stress, that the inverse wave age of mature sea obtained for high winds (20 and  $30 \text{ m s}^{-1}$ ) (figure 4.11) is close to the Pierson-Moskowitz value  $(\omega_p U_{10})/g \approx 0.82$ . In our opinion, qualitative correspondence of the Pierson-Moskowitz model and results of our simulations is of much greater importance than this simple quantitative coincidence : the spectral peak component in mature sea is riding faster than wind. It implies that nonlinear transfer is still playing a key role in the mature stage, transferring energy to waves running faster than wind.

#### 4.4.4.3 Growing wind sea as a reference stage of wind-sea evolution

The energy-flux plots in figure 4.10 give an idea to delimit different stages of wave development quantitatively. It is useful to consider the maximum of wave steepness as a starting point of the second stage of wave evolution – *the growing wind sea stage*. The growing wind sea stage is related to the asymptotic split balance model and the resulting self-similarity features.

At the beginning of the stage, the non-self-similar background of wave spectra can contaminate significantly inherent features of the self-similar evolution of wave spectra. It can explain a slight decrease of our estimates of self-similarity parameter  $\alpha_{ss}$  with fetch (or wave age). Self-similarity features at the very beginning of the stage of growing wind sea manifest themselves as rapid collapsing of trajectories to an asymptotic curve irrespective of particular wave input function and wind speed. At the same time, the pronounced dependence on method for  $S_{nl}$  is clearly seen : GQM and DIA form two separate bundles of trajectories. These bundles merge together later on when effect of nonlinear transfer becomes stronger. The trajectories for GQM and DIA become remarkably close but presence of the two bundles is still visible in figure 4.12.

The similarity of GQM and DIA results for the growing wind sea is explained quite naturally by homogeneity property (4.16) of the collision integral  $S_{nl}$ . Minor deviations are dealing, evidently, with the effect of different shaping of wave spectra within GQM and DIA.

The self-similarity parameter  $\alpha_{ss}$  starts to grow slowly when the two bundles in figure 4.10 collapse to a single one. The later behavior appears to be in perfect agreement with the proposed scheme of wave development through a sequence of reference cases of spatial growth (Table 4.1) : increase of  $\alpha_{ss}$  from  $p_\chi = 1$  by Hasselmann et al. (1976), to  $p_\chi = 3/4$  by Toba (1972) and further to Zakharov & Zaslavsky (1983b) regime ( $p_\chi = 4/7$ ). Thus, one can specify sub-stages of wave evolution within the stage of growing wind sea.

These sub-stages are seen perfectly well in figure 4.13 with a ‘mixed’ representation of wave steepness (weakly turbulent scale) vs inverse wave age (conventional wind wave scaling). Three reference curves show different slopes for reference cases of Table 4.1 and fairly good correspondence of these slopes to our simulation results. Gentle slope of the Hasselmann et al. (1976) regime is seen as the first sub-stage of growing wind-sea (inverse wave age  $\tilde{\omega}_p = \omega_p U_{10}/g$  higher than  $2.5 - 3$ ). The Toba (1972) second sub-stage covers relatively narrow range of inverse wave age  $1.5 - 2.5$ . The further steepening of trajectories can be

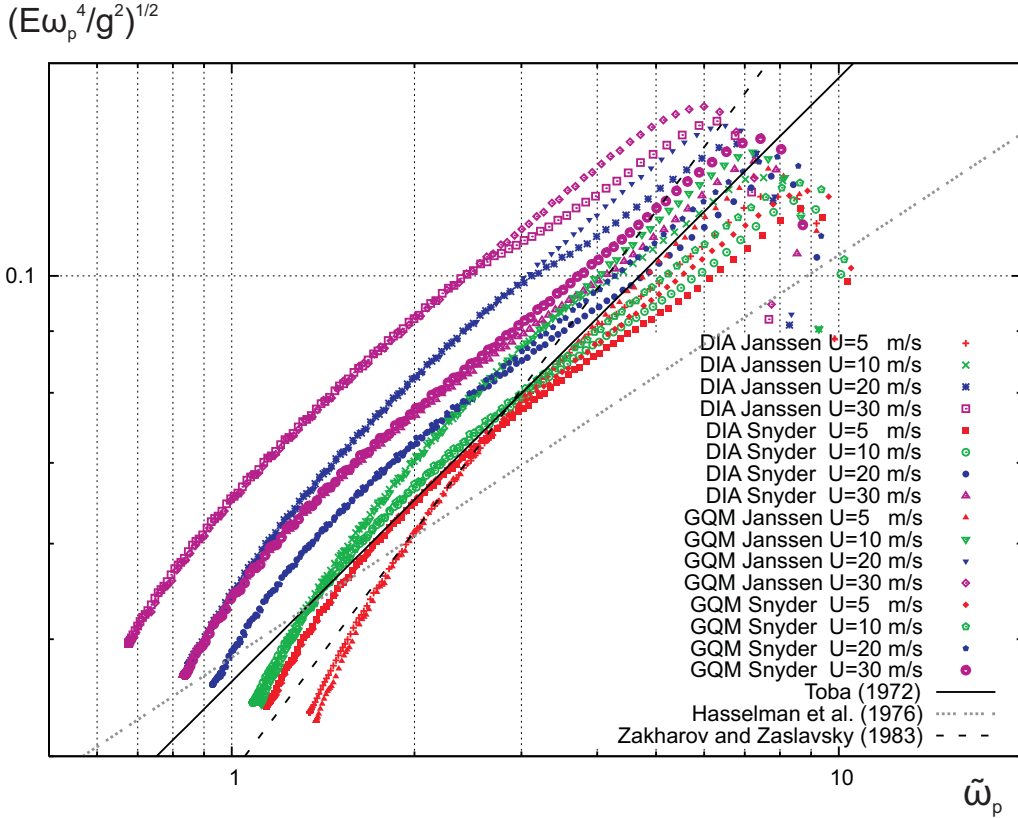


FIGURE 4.13 – Steepness  $\sqrt{E\omega_p^4/g^2}$  as function of inverse wave age  $\tilde{\omega}_p = U_{10}/C_p$  in log-space. Reference regimes give tangents 1/2 for Toba, 1/3 for Hasselmann, 2/3 for Zakharov & Zaslavsky

treated as quite short sub-stage by Zakharov & Zaslavsky (1983b) just before reaching mature sea where inverse wave age  $\tilde{\omega}_p$  is tending to be constant.

Thus, universality of wind-wave growth in the sense of weakly turbulent theory is demonstrated fairly well at this self-similar stage of wave development. Simulation results show that weakly turbulent scaling is a good and proactive tool for analysis of physics of growing wind sea.

## 4.5 Discussion and Conclusions

Summarizing results of the paper, we start by stressing that our simulations followed conventional approaches to wind wave modeling. Thus, key results can be reproduced quite easily, at least, within the well-known Discrete Interaction Approximation (DIA) for  $S_{nl}$ . More expensive ‘exact’ methods of simulation of nonlinear transfer are now available in a number of research groups (e.g. Hasselmann & Hasselmann, 1981, 1985; Resio & Perrie,

1991; Komatsu & Masuda, 1996; Polnikov, 1997; Hashimoto et al., 1998; Lavrenov, 2001, 2003b; Pushkarev et al., 2003; Van Vledder, 2006) and, in principle, reproduction of our results is feasible in its full.

The goal of our extensive numerical study was a physical analysis rather than development of new numerical approach. Calculation of  $S_{nl}$  by two methods was targeted to the question of great physical and practical importance : when does the use of exact nonlinear transfer term make sense in spite of significant increase of simulation time ? Simulations were carried out in a wide range of wind speeds and for two different wave input functions by Snyder et al. (1981) and Janssen (1989, 1991). The goal of the intercomparison was to show how different the wave evolution can be for the same wind conditions and, at the same time, how robust inherent features of wind-wave evolution can be irrespective of this difference.

These inherent features can be observed quite easily if and only if an adequate physical approach is used for analysis of results of simulations. This approach, an asymptotic weakly turbulent theory, the so-called split balance model, showed its power as an effective tool of physical analysis. On the contrary, conventional similarity approach based on wind speed scaling appears to be rather restrictive. Physical roots of these restrictions should be realized definitely : wind over waves is a too complex phenomenon to be described by the wind speed as the only physical parameter. At the same time, the long-lived tradition of wind speed scaling gives us, in many cases, a good vision of diversity of rates of wave growth, and, hence, mechanisms of air-sea interaction. The weakly turbulent approach allows one to make the first step in specifying these mechanisms.

The key point of the approach is the dominance of nonlinear transfer for growing wind sea. This hypothesis and the resulting split balance model propose an alternative physical scaling where total fluxes of energy, wave momentum and wave action play a key role. The use of energy, or for instance, wave momentum flux is a matter of habit as soon as the growing wind sea is self-similar. We introduce total energy flux as physical scale of our approach and use the asymptotic law of wind-wave growth (Badulin et al., 2007) in terms of this quantity.

The use of energy-flux diagrams (see § 3.2 in Badulin et al., 2007, and § 4.4.3 in this paper) as a graphical representation of the weakly turbulent law (4.19) makes the analysis of results of simulations physically transparent. The qualitatively different stages of wave growth can be delimited quite naturally in these diagrams. Initial growth and fully developed (mature) sea are seen as non-self-similar regimes and give a rather high dispersion of simulation curves for different wave input functions and methods for  $S_{nl}$ . At the self-similar stage of growing sea these curves are collapsing to a quite narrow strip irrespective of wind speed, particular wave input function and method for  $S_{nl}$ . Thus, the self-similarity of wind wave growth can be regarded as a really robust feature of wave evolution.

This robustness is demonstrated here for integral parameters of wind wave growth, total energy  $E$  and spectral peak frequency  $\omega_p$ , but not for spectral distributions, and especially, for directional spreading. The latter can be a subject of further study.

In terms of energy-flux trajectories, the surprising quality of DIA for growing sea is ensured by homogeneity property of the collision integral (4.16) that is also respected in DIA

calculations. In terms of explicit dependencies on time or fetch, we showed in this study that difference of results for DIA and GQM can be due to effects of feedback of spectral shapes on total wave input (see § 4.4.2.1 and figure 4.8). But direct effect of the method of calculation certainly compensates these shape-to-input effects since differences are quite small and only visible at intermediate fetches. Evidently, dependence of total wave input on particular method of wave modeling is not a good thing. Necessity to control this important physical quantity is our main recommendation for improving the modeling of wind wave growth.

In some cases of non-self-similar development, especially, for fully developed sea one can also see rather good coincidence of DIA and GQM results. Delusiveness of good quality of DIA in this case should be realized quite clearly : the smallness of net wave input hides principal deficiency of DIA in simulation of spectral distributions. Again, we are forced to leave this topic for further studies

The qualitative features of mature seas observed within the weakly turbulent approach are also very informative. First of all, we showed that the mature state is reached in simulations for all the cases under study as a state with constant total energy and spectral peak frequency. This result extends essentially results by Komen et al. (1984) on balance of mature sea. Steepness of the mature sea appears to depend mainly on wave forcing. This result is not consistent with the classical Pierson & Moskowitz (1964) parameterization of spectra of fully developed sea but does not contradict available experimental and modeling results. The fully developed sea was not a point of our particular interest. A number of delicate questions concerning this state of wave field, first of all, spectral distributions, require thorough analysis.

Our theoretical analysis allows for advancing essentially in analysis of the growing sea stage where the asymptotic split balance model shows its perfect performance. Self-similarity relationships being formulated for different physical quantities (energy, momentum or action) give us an idea to associate wind-wave growth with different regimes of air-sea coupling and, thus, try to delimit sub-stages of growing wind sea. We introduced a set of reference cases that correspond to constancy of fluxes of basic physical quantities to waves : wave energy, wave momentum and wave action. The experimental evidences of these reference regimes have been found long time ago in terms of explicit fetch dependencies (4.17) or single-parameter dependencies (see § 4.4.1.2). Toba (1972) and Hasselmann et al. (1976) gave these dependencies with no reference to weakly turbulent nature of growing wind sea. Zakharov & Zaslavsky (1983b) developed a theoretical model for the regime of constant flux of wave action but their experimental arguments were questionable (see figures 5-8 in Zakharov & Zaslavsky, 1983b).

The rich physics of these three reference cases becomes evident when we use our weakly turbulent wave growth law (4.19) in its full power and convert the single-parameter dependencies (4.26, 4.29, 4.32) into energy fluxes  $dE/dt$  (see Table 4.1). The reference cases give us a consistent picture of wave development as a consequences of stages where energy is delivered to waves in qualitatively different ways.

Relatively young waves at the beginning of growing sea stage are governed mostly by momentum flux of turbulent wind ; the corresponding flux of energy is growing with wave

phase speed (5/3 law by Hasselmann et al., 1976). The wave momentum flux can be associated quite naturally with momentum flux (wind stress) produced by turbulent wind. Thus, under permanent wind conditions the ratio of these two fluxes (wind stress and wave momentum) remains constant while energy flux to waves is growing (due to increase of spectral peak phase velocity  $C_p$ ). The next sub-stage is associated with the well-known 3/2 Toba's law. The energy flux to waves becomes constant in this case (logically, one can use Toba's term 'saturation' of wave growth in this case). The wave momentum is decaying with wave growth that means decaying of turbulent wind stress coming to waves. The last reference case of Zakharov & Zaslavsky (1983b) gives decaying of both wave momentum and wave energy fluxes while wave action flux remains constant.

Non-trivial dependence of total wave input on stage of wave development is well-known and quite often taken into account by combinations of two velocity scales  $u_*$  and  $C_p$  (e.g. Resio et al., 2004). Note that our reference cases propose theoretical background for such parameterizations.

Important quantitative results were formulated in this study. First of all, we estimated key parameter of our asymptotic theory  $\alpha_{ss}$  and its dependence on the rate of wave growth  $p_\chi$ . The reference cases listed in Table 4.1 were used to treat dependence  $\alpha_{ss}(p_\chi)$  in a physically consistent way based on clear physical criteria. Our estimate of self-similarity parameter  $\alpha_{ss}(3/4) = 0.68$  (the Toba sub-stage of growing sea) appears to be consistent

- with previous numerical results on duration-limited growth (Badulin et al., 2008a) ;
- wind sea experiments (Badulin et al., 2007) ;
- wind-wave tank experiments (Badulin & Caulliez, 2009) ;

Further delimitation of sub-stages of self-similar wave growth can be made quantitatively, not only qualitatively. Figure 4.13 gives such estimates of stages of wave development in terms of 'mixed' presentation : steepness (weakly turbulent scaling) and inverse wave age (conventional wind speed scaling). The sub-stage curves (laws 5/3, 3/2, 4/3) give remarkable references, first of all, for slopes of simulation curves and, in less degree, for magnitudes. The better consistency of results at low winds to the reference cases look reasonable : experimental dependencies generally correspond to conditions of low winds (less than 10 m s<sup>-1</sup>).

We see many good perspectives to develop wind-wave studies within the weakly turbulent approach. Two questions are of primary importance, in our opinion. First, spectral and angular distributions at different stages of wave development should be studied in more details. Spectral distributions manifest self-similarity properties only partially (see discussion of the problem of 'magic circle' in § 6.1.2 in Badulin et al., 2005), which can be taken into account for correct assessment of their feedback on total wave input. The study of this effect is a very delicate theoretical and numerical problem.

The second question that should be mentioned here deals with alternative models of wave dissipation. The introduction of these models will very likely not change key results on self-similar stage of wave growth but can affect heavily the state of mature seas.

# Chapitre 5

## Modeling wave growth in fetch-limited and slanting fetch conditions

### 5.1 Introduction

In this chapter, the investigations carried out in chapter 3 in the homogeneous case are extended to include the effect of propagation on the dynamics of the wave spectrum. Two one-dimensional configurations are examined : the wind-driven wave growth with fetch (i.e. the so-called fetch-limited situation), and the slanting fetch conditions. Results using the GQM method for computing nonlinear transfers are compared to DIA results, showing the evolution of the wave spectrum when a quasi-exact method, GQM here, is applied to more realistic situations.

In comparison to the previous chapter, where results of extensive numerical simulations of fetch-limited growth were analyzed within two approaches, wind-speed scaling (Kitaigorodskii, 1962) and alternative weakly turbulent approach (Zakharov, 2005; Badulin et al., 2007), we rely here on a more traditional approach. Our main interest is the analysis of spectral shape and directional properties of the spectrum. In this perspective, a continuum of wind directions (from 0 to 90° with respect to the cross-shore direction) is simulated, showing the effects of the slanting wind on the structure of the wave spectrum.

The well known case of fetch-limited wave growth has been extensively studied over the past decades (e.g. Hasselmann et al., 1973; CERC, 1977; Donelan et al., 1985; Kahma & Calkoen, 1992; Young, 1999). The development of many sensors and measurement techniques to obtain higher accuracy in measured directional properties of ocean waves in the last 20 years allowed for a better understanding of the directional distribution of the wave spectrum in fetch-limited conditions (e.g. Young et al., 1995; Ewans, 1998; Long & Resio, 2007). Nevertheless, directional properties of the wave field are still problematic to measure and quantify, especially for low energy levels. Modeling of these properties requires an accurate

calculation of the nonlinear wave-wave interactions, but also depends on the source/sink terms considered.

Interest of the scientific community in the modeling of wind waves in slanting fetch conditions has grown in the last few years. Indeed, the obliquity of the wind from the cross-shore direction can influence the angular distribution of wave energy, resulting in the fact that long waves are not propagating in the wind direction but in a more alongshore direction (e.g. Holthuijsen, 1983; Pettersson, 2004; Long & Resio, 2007). This effect is generally called wave steering. But wind direction can also have a large effect on wave height, leading to significant consequences for coastal shipping or flooding prevention (Bottema & Van Vledder, 2008).

The first section of this chapter briefly describes the numerical features of the simulations and the various combinations of source terms used in the wave model. In the second section, the ideal fetch-limited case is studied, focusing on the spectral and angular distribution of the spectrum and its evolution with fetch. Dependence of the results on the modeling of the source and transfer terms is analyzed and discussed. Effects of the slanting wind on the modeled spectra are addressed in the third section, trying to understand the role of nonlinear wave-wave interactions in the strong angular wave steering effect in alongshore direction. Some of the results are compared with field measurements of the SHOWEX campaign (Ardhuin et al., 2007).

## 5.2 Description of the set of simulations

### 5.2.1 General layout of the cases

As we consider only deep water conditions without ambient flow and one-dimensional cases (all quantities are uniform along the  $y$  axis), equation (1.47) reduces to :

$$\frac{\partial F(f, \theta)}{\partial t} + C_{gx} \frac{\partial F(f, \theta)}{\partial x} = S_{in}(f, \theta) + S_{diss}(f, \theta) + S_{nl}(f, \theta) \quad (5.1)$$

A constant and homogeneous wind  $U_{10} = 10 \text{ m s}^{-1}$  blows offshore with a direction varying from  $\theta_u = 0^\circ$  from the cross-shore direction (fetch-limited case) to  $\theta_u = 90^\circ$  (wind blowing alongshore), depending on the numerical runs.

### 5.2.2 Modeling of the source and transfer terms

We considered three combinations of source/sink terms (hereafter called sets I, II and III) and two methods for the nonlinear transfer term  $S_{nl}$ .

- Set I corresponds to the WAM-Cycle 3 physics with the wind parameterization of Snyder et al. (1981) (equation 1.54) and the whitecapping dissipation of Hasselmann (1974) as formulated by Komen et al. (1984) (equation 1.61).

- Set II combines the expression of Yan (1987) (equation 1.57) for  $S_{in}$  with the values of parameters proposed by Van der Westhuysen et al. (2007) with the whitecapping model of Van der Westhuysen et al. (2007); Van der Westhuysen (2008) (equation 1.63).
- Set III corresponds to the WAM-Cycle 4 physics, with the Janssen (1989, 1991) wind input model (equation 1.58) and the  $S_{diss}$  model of Komen et al. (1984) (equation 1.61) with the coefficient values proposed in WAM-Cycle 4 (Günther et al., 1992; Komen et al., 1994). As established in chapter 3, in order to obtain acceptable results with set III, a parametric high-frequency tail  $f^{-4}$  needs to be imposed over the frequency range  $[f_d, f_{max}]$  (see equation 1.78).

Results obtained using GQM (medium resolution) and DIA are compared. As in the previous chapters, the parameters of the source and sink terms are not retuned when changing the method for calculating the  $S_{nl}$  term. The model of Van der Westhuysen et al. (2007) for  $S_{diss}$  (see equation (1.62)) was computed with the coefficients  $C_{ds} = 5.0 \cdot 10^{-5}$  and  $B_r = 1.75 \cdot 10^{-3}$ , calibrated for DIA simulations.

### 5.2.3 Numerical aspects

We consider a spatial domain of length 100 km. The spatial grid is logarithmic in  $\Delta X$  ( $\Delta X_{n+1}/\Delta X_n = 1.055$ ) and includes 101 points. The size of the first mesh is  $\Delta X_1 = 25$  m and the size of the last one  $\Delta X_{100} \approx 5300$  km.

The discrete frequency-direction grid is composed of 51 frequencies with logarithmic distribution from  $f_1 = 0.08$  Hz to  $f_{51} = 2.5$  Hz ( $f_{n+1}/f_n = 1.071$ ) and 36 directions with a constant spacing of  $10^\circ$ .

Time integration of the source terms is performed with a semi-implicit scheme (WAMDI Group, 1988) with a constant time-step  $\Delta t = 10$  s. The duration of the simulations is set to 24 hours of physical time so that a quasi-steady state is reached at the end of the runs. In the following, results are given at the final simulation time.

The wave growth limiter used in these simulations is the WAM-Cycle 4 modified expression by Hersbach & Janssen (1999) (eq. 1.77).

In these computations, the diagnostic high-frequency tail of the spectrum is only used for set III with tail exponent  $m$  equal to 4.

### 5.2.4 Initial conditions

The initial wave spectrum (at  $t = 0$ ) is set to zero. The linear source term of Cavaleri & Malanotte-Rizzoli (1981) (eq. 1.52) has been added to the source function so that the waves may start to grow from this zero-energy initial state.

### 5.3 Results on fetch-limited growth

One of the motivations for this case is to compare model results with established growth curves for non-dimensional energy  $\tilde{E} = Eg^2/U_{10}^4$  and non-dimensional peak frequency  $\tilde{\omega}_p = \omega_p U_{10}/g$  (also called ‘inverse wave age’). Another motivation is to analyze precisely the directional distribution of the spectrum, as in chapter 3, in order to see if bimodality is a persistent feature when adding propagation and how it can be influenced by geometric considerations such as the distance from the coastline.

#### 5.3.1 Growth curves

The growth curves of non-dimensional energy  $\tilde{E}$  and non-dimensional peak frequency  $\tilde{\omega}_p$  versus non-dimensional fetch  $\chi = Xg/U_{10}^2$  are plotted in Figure 5.1, using sets I to III, and GQM and DIA methods for computing  $S_{nl}$ . They are compared with the growth curves of Sverdrup-Munk-Bretschneider (SMB) (CERC, 1977), JONSWAP (Hasselmann et al., 1973), Kahma & Calkoen (1992) (stable and unstable conditions) and Babanin & Soloviev (1998b).

Figure 5.1 shows that the global tendency of simulated growth curves is in general agreement with experimental growth curves, which themselves show some dispersion depending on the formula. This is not in contradiction with results of chapter 4 : simulations for  $U_{10} = 10 \text{ m}\cdot\text{s}^{-1}$  are quite close to measurements as they correspond to wind speed currently measured during field campaigns. Results are quite close to the curves of Babanin & Soloviev (1998b) or Kahma & Calkoen (1992) for stable atmospheric conditions, particularly at large fetches. The growth curve of Kahma & Calkoen (1992) with unstable conditions gives a higher energy estimate at large fetch. The JONSWAP measurements (Hasselmann et al., 1973) show smaller energy and larger peak frequency at small and intermediate fetches. SMB curves (CERC, 1977) give smaller  $\tilde{\omega}_p$  estimate at small fetches.

Some discrepancies between results obtained with different forcing terms (sets I, II, III) can be observed at small and intermediate fetches, but curves are closer at large fetches.

Differences between GQM and DIA results are not really significant. At intermediate fetches,  $\tilde{E}$  curves obtained using GQM are lower than DIA curves but they all collapse at large fetches. Note that wind input and dissipation functions were originally calibrated to ensure that growth curves calculated with DIA were close to experimental curves. Therefore, the source terms ( $S_{in}$  and  $S_{diss}$ ) may have to be recalibrated a little when using a quasi-exact method for evaluating the transfer term  $S_{nl}$ .

Comparison of the mean angular spreading  $\sigma$  (eq. 1.29) obtained with the different methods as a function of  $\chi$  (Figure 5.2) shows that DIA systematically gives a larger angular spreading than GQM for all sets. This is a known bias of DIA (see fig. 12 of Hasselmann et al., 1985; Forristall & Ewans, 1998) which spreads energy to much larger angle from the wind direction than predicted by exact calculations of  $S_{nl}$ . Differences between the three sets are also clear and show that the WAM-Cycle 3 parameterization of the forcing terms (set I) gives a much larger angular spreading, whereas WAM-Cycle 4 (set III) gives

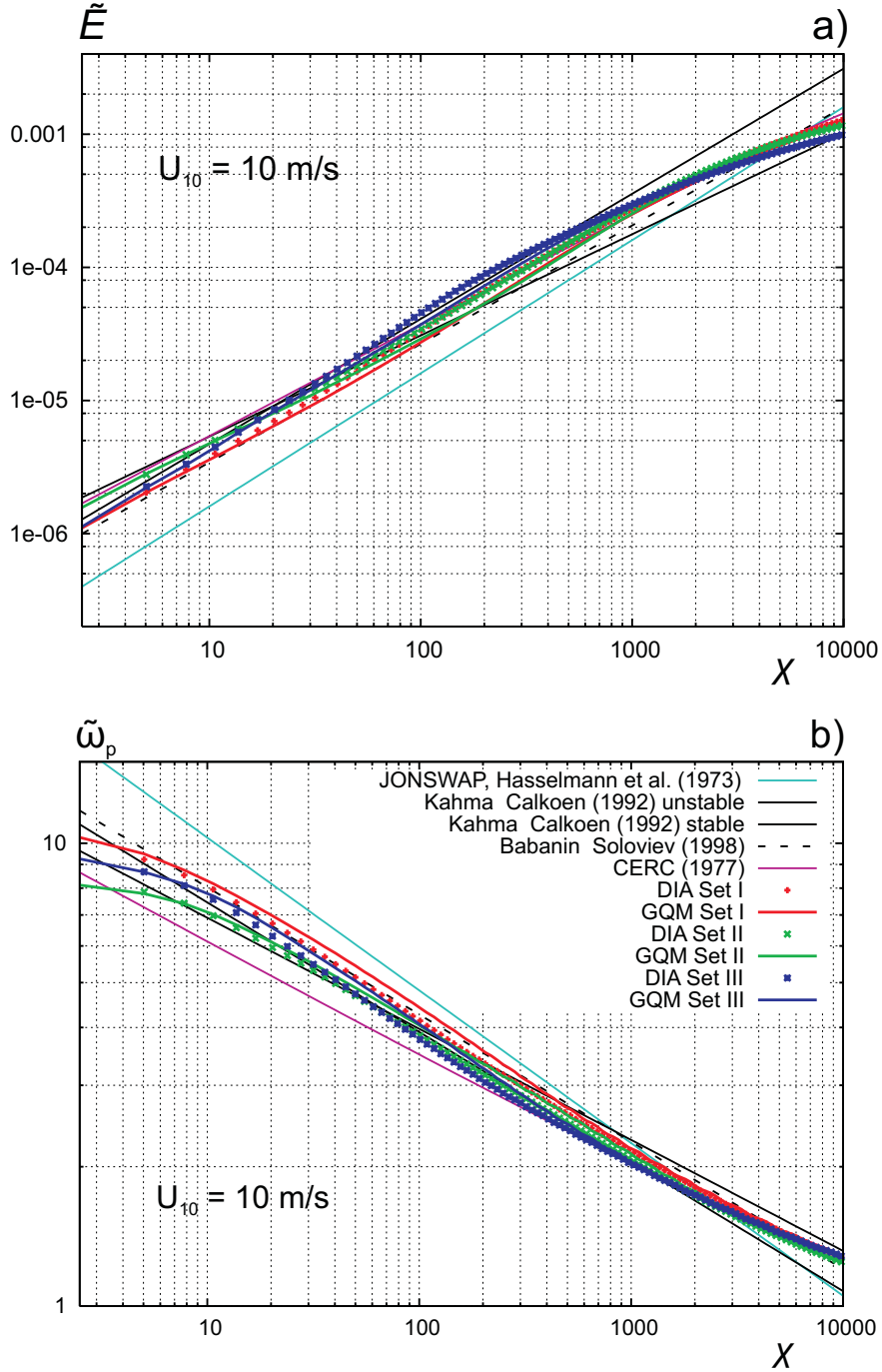


FIGURE 5.1 – Evolution of a)  $\tilde{E}$  and b)  $\tilde{\omega}_p$  with non-dimensional fetch  $\chi$ , for the different sets (I, II and III), DIA and GQM methods for calculating  $S_{nl}$ . Results are given at the final simulation time  $t = 24$  h. Published growth curves of CERC (1977), JONSWAP (Hasselmann et al., 1973), Kahma & Calkoen (1992) (stable and unstable) and Babanin & Soloviev (1998b) are plotted for comparison.

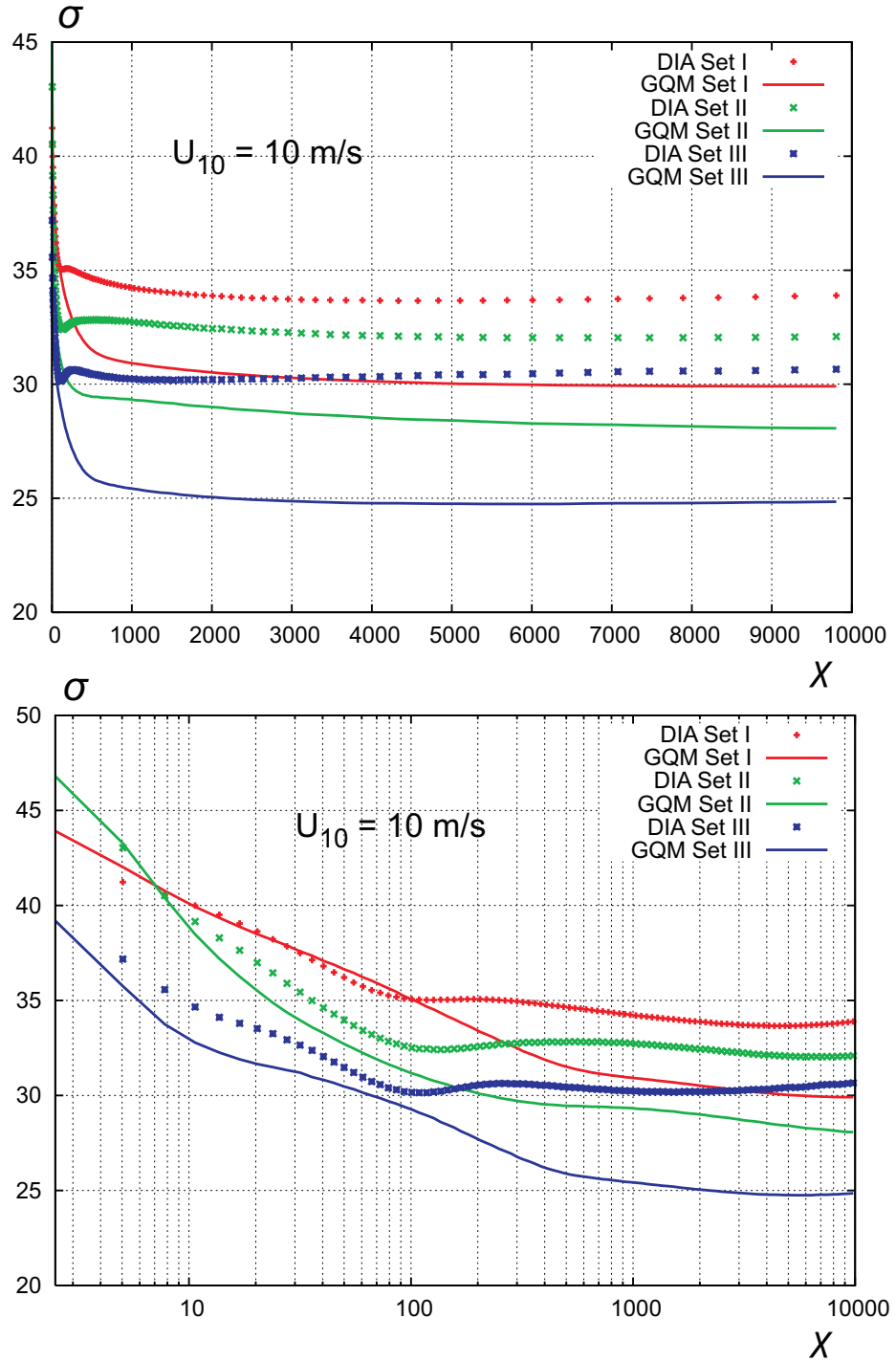


FIGURE 5.2 – Evolution of mean angular spreading  $\sigma$  ( $^{\circ}$ ) with non-dimensional fetch  $\chi$  for different options for source (sets I to III) and transfer terms (DIA and GQM), at the final simulation time  $t = 24$  h. a) Linear scale. b) Logarithmic scale in  $\chi$ .

the smallest one (see chapter 3 for an analysis of the influence of the forcing terms on the directional structure of the spectrum). Only refined measurements could enable to determine the most accurate directional spreading. One difficulty is that the angular spreading is still problematic to measure and data from different field campaigns are not always in agreement. Forristall & Ewans (1998) (fig. 3) compare  $\sigma$  as a function of wave age obtained from Mitsuyasu et al. (1975), Hasselmann et al. (1980), Donelan et al. (1985) and Ewans (1998) directional distributions with DIA (WAM-Cycle 3 parameterization of the source terms) and EXACT-NL (Hasselmann & Hasselmann, 1981, 1985) computations. The Maui parameterization of Ewans (1998) and the Donelan et al. (1985) distribution give a sigma around  $27.5^\circ$  that does not depend on the wave age. This is quite close to results of set II using GQM. The Mitsuyasu et al. (1975) and Hasselmann et al. (1980) values of  $\sigma$  are decreasing with increasing wave age. They are between  $31$  and  $36^\circ$  for Hasselmann et al. (1980) and in a much larger range ( $14$  to  $50^\circ$ ) for Mitsuyasu et al. (1975). Our results show a weak dependence on fetch which means a weak dependence on wave age. Variations of  $\sigma$  are only seen at small fetches.

### 5.3.2 Shape of the frequency spectrum

1D (frequency) spectra are plotted in Figure 5.3 at five fetches (1 km, 5 km, 20 km, 50 km and 100 km from the shoreline) for sets I, II and III combined with the two methods for calculating  $S_{nl}$  (DIA and GQM).

Figure 5.3 shows how spectra evolve with fetch, their maximum value increasing and their peak frequency decreasing with increasing fetch (or in a similar way with increasing wave age). The peakedness of the spectra seems to increase a little with fetch. A high frequency tail close to  $f^{-4}$  is well visible for all the simulated spectra. We recall that this tail is not imposed, except for the simulations of set III (above the diagnostic frequency  $f_d$ ).

Differences between the three sets are mostly observed at small fetches (1-5 km) where set III gives a higher energy level. For all fetches, the peak frequency given by set I is a little higher. At high frequencies, results from set I show a higher energy level with a tail close to  $f^{-3.96}$ , set II gives a tail close to  $f^{-4.2}$ . For set III, the  $f^{-4}$  tail is imposed. Higher spectral peak frequency and overprediction of energy level at high frequencies given by the WAM 3 source terms (set I) have already been pointed out by, e.g., Van der Westhuyzen (2008).

The DIA method produces broader and less peaked spectra than the GQM method. The maximum value of the DIA spectra is higher at short fetches (1 km) and smaller at large fetches (100 km) for the three sets. At short fetches, the peak frequency of DIA spectra is smaller.

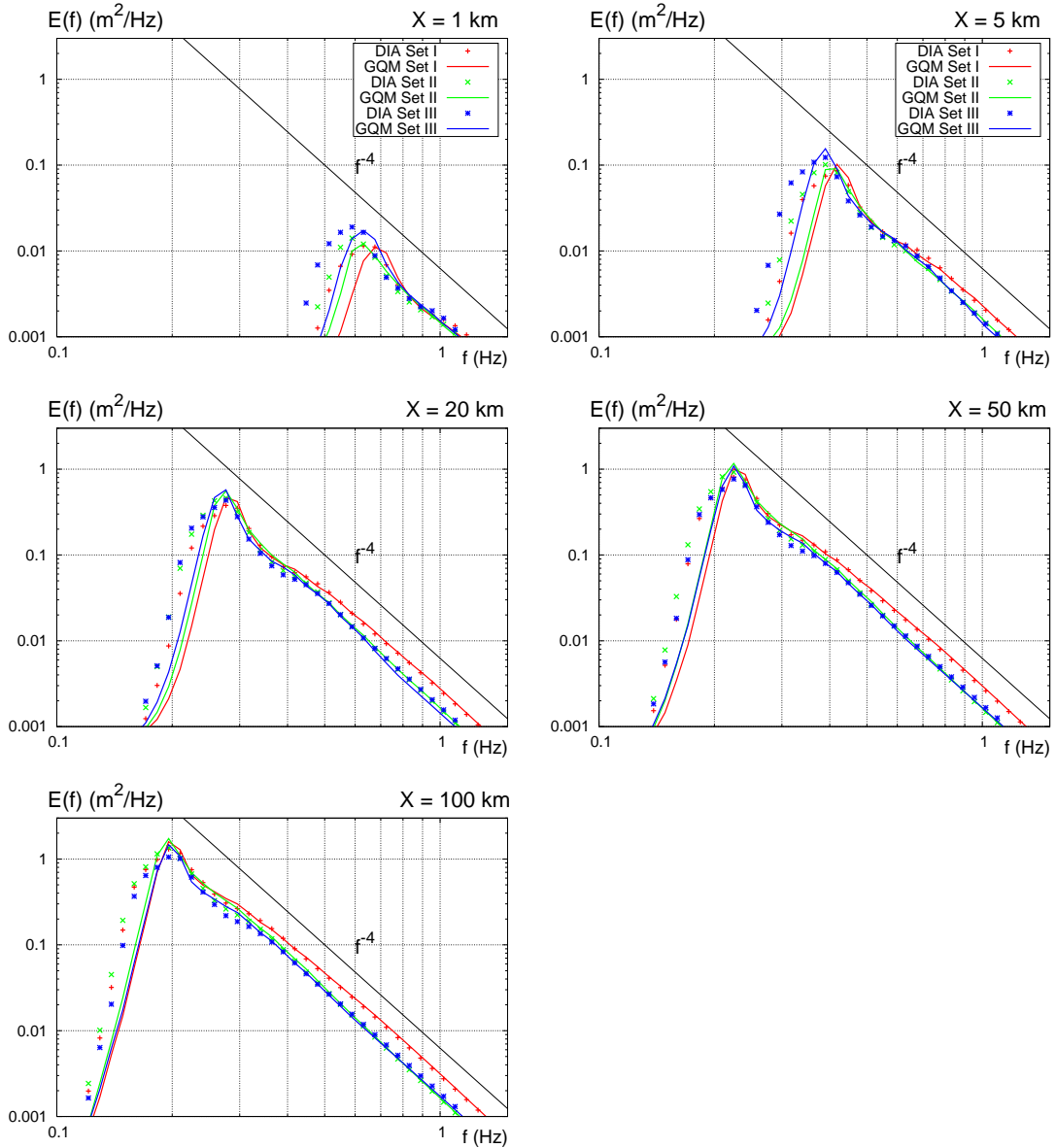


FIGURE 5.3 – 1D-spectra at fetches 1 km, 5 km, 20 km, 50 km and 100 km and different options for source and transfer terms. Results are given at the final simulation time  $t = 24$  h.

### 5.3.3 Directional distribution of the spectrum

#### 5.3.3.1 A complex structure

In chapter 3, we showed that bimodality is a persistent feature of the ocean wave spectrum that is created by non-linear wave-wave interactions. Here the study is extended to fetch limited conditions.

Figures 5.4, 5.5, 5.6 present the angular distribution of spectral energy normalized by its maximum value at each frequency for the three sets. DIA and GQM results are plotted in each figure. The white dotted circles correspond to  $f = f_p$ . The darkest shade indicates the angular position of the maxima. This representation of the directional distribution allows to have a good idea of the main directions of wave propagation.

As the frequency scale is quite large to observe precisely the directional distribution near the spectral peak, Figures 5.22, 5.23 and 5.24 have been included in Appendix B and show a zoom for  $f \leq 0.7$  Hz.

We observe that the results given by the three sets are quite different from each other. Similar features can be noted : they all show high and low frequency bimodality for fetches larger than 5 km when source terms are combined with the quasi-exact GQM method. But the precise form of the distribution, the angle between the two symmetric lobes (lobe angle) and the lobe ratio<sup>1</sup> depend on the source/sink terms considered, which is consistent with the results of Banner & Young (1994).

Bimodality of wave spectra was already observed on fetch-limited wave data (Young et al., 1995; Ewans, 1998; Long & Resio, 2007). Our results confirm the observed structure : the directional distribution is symmetric about wind direction, unimodal and narrow near the spectral peak, and broader at lower and higher frequencies with two (bimodal) lobes. Although low frequency bimodality is still a subject of discussion and requires further research, existence of bimodality above the spectral peak in real sea states is now widely accepted.

Some of the measurements show asymmetry in the directional distribution (Young et al., 1995; Ewans, 1998; Wang & Hwang, 2001). Data from heave-pitch-roll buoys of Lake Michigan (Wang & Hwang, 2001) show a marked asymmetry mostly at the nearshore buoy which may be caused by slanting fetch effects or inhomogeneous wind field due to land proximity. Ewans (1998) assumes that the asymmetry of Maui data is due to low frequency swell or asymmetry in the fetch. Slight asymmetry is also observed by Young et al. (1995) (Lake George measurements) who suggest it is due to sampling variability. Despite these observations, it thus seems tenable to assume the fetch limited directional distribution is symmetrical. Effects due to slanting fetch are analyzed in section 5.4.

Results using set I and GQM show a quite pronounced high frequency bimodality for all represented fetches. For fetch  $X = 100$  km, bimodality starts at  $f \approx 1.7 - 1.8f_p$  and the maximum lobe ratio  $r_{lobe}$  is equal to 1.22 at  $f = 4.5f_p$  (see also Figure 5.8 for a plot in Cartesian coordinates). The maximum lobe angle is close to  $140^\circ$ , which means that each

---

1. Ratio of the maximum value of  $D(f, \theta)$  to its value at the dominant wave direction.

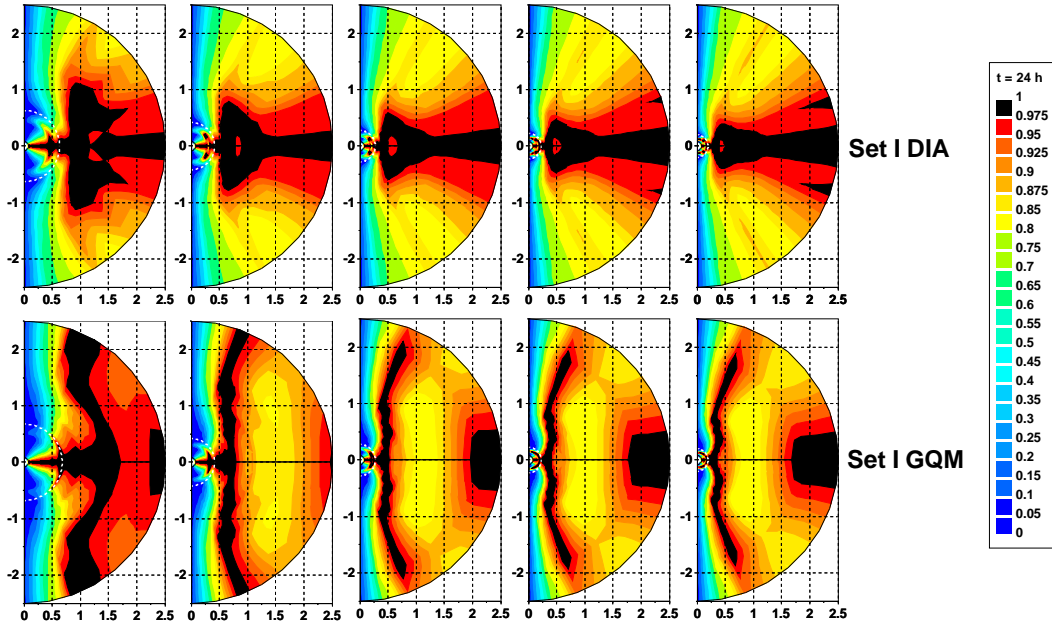


FIGURE 5.4 – Angular distribution normalized by the maximum value at each frequency at different fetches (1 km, 5 km, 20 km, 50 km, 100 km), using DIA (upper panels) and GQM (lower panels) methods for  $S_{nl}$  and set I for the source and sink terms. Results are represented in polar coordinates at  $t = 24$  h. The white dotted circles indicate the peak frequency  $f_p$ .

lobe is about  $70^\circ$  away from the wind direction. The angular spreading is much larger than for the two other sets. For  $f \geq 8.5f_p$ , a transition to unimodality can be noticed.

For sets II and III, bimodality is seen for fetches  $X \geq 5$  km. For fetch  $X = 100$  km, the distributions become bimodal at  $f \approx 1.4f_p$  and  $f \approx 1.6f_p$ , respectively. The maximum lobe ratio obtained with set II at  $X = 100$  km is comparable to set I ( $r_{lobe} = 1.21$ ), but for a much smaller frequency ( $f = 2.3f_p$ ). The lobe angle  $\theta_l$  reach  $90\text{--}100^\circ$  and then decreases. High frequency unimodality is seen from  $f = 4.2f_p$ . For set III, a high frequency  $f^{-4}$  tail is imposed, which means for frequencies above  $f_d$  (for  $X = 100$  km,  $f_d = 3.2f_p$ ) the directional distribution remains equal to the one obtained at  $f = f_d$ . This has a pronounced influence on the directional structure of the spectrum, as already noticed in Chapter 3. Consequently, no transition to unimodality occurs and the maximum lobe ratio and lobe angle are smaller than for the two other sets :  $r_{lobe} = 1.1$  at  $f = 2.3f_p$ ,  $\theta_{l,max} = 55\text{--}60^\circ$ .

Directional distributions obtained with DIA in figures 5.4, 5.5, 5.6 are completely different. They do not show clear bimodality at high frequencies. Some broadening or slight bimodality can be seen around  $2f_p$  for sets I and II (at fetches 50 and 100 km).

Low frequency bimodality is obtained in all our simulations at fetches  $X \geq 20$  km ( $U_{10}/C_p \leq 1.8$ ), even when using DIA. For a discussion on this subject, please refer to chapter 3 section 3.4.6. It is shown that low frequency bimodality has already been observed on measure-

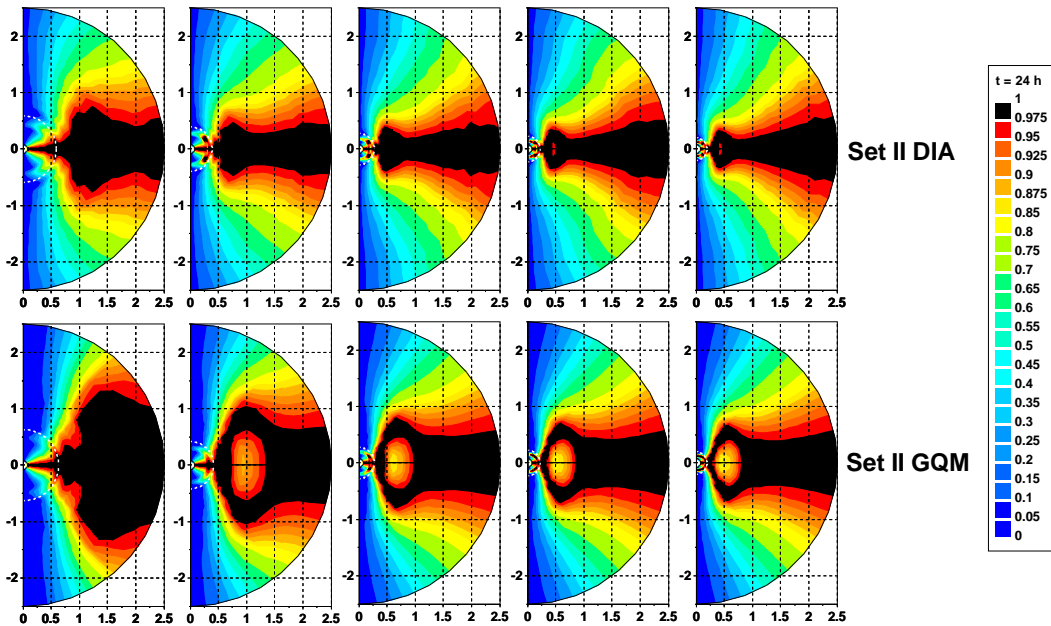


FIGURE 5.5 – Same figure as figure 5.4, but for set II.

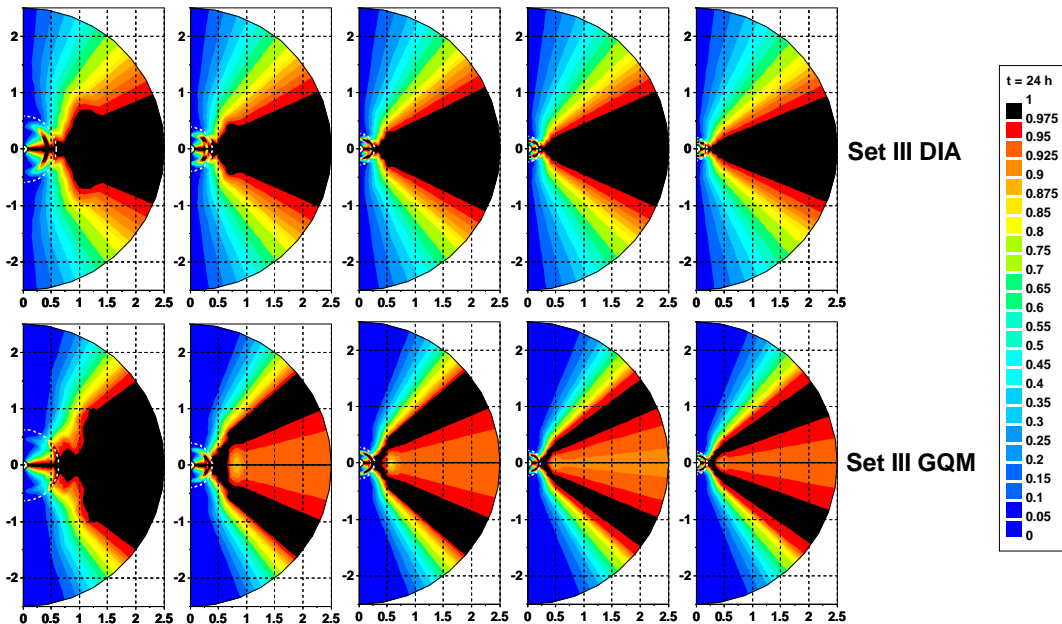


FIGURE 5.6 – Same figure as figure 5.4, but for set III.

ments (Ewans, 1998; Hwang et al., 2000a,b; Wang & Hwang, 2001) and is a persistent feature of simulated spectra. This suggests that it could be a real feature of sea states under certain conditions (for example, conditions close to duration or fetch-limited conditions); at least, this possibility should not be neglected and should be a subject of further studies, in particular on the basis of well defined and controlled field campaigns.

### 5.3.3.2 Influence of the fetch

The distance from the coastline seems to have a relatively small influence on the global structure of the directional distribution (figures 5.4, 5.5, 5.6), except at small fetches (e.g.  $X = 1$  km). For  $X \geq 5$  km, a small dependence of the lobe ratio and lobe angle on the fetch, and consequently on the wave age, can be observed, but all the sets do not show a similar tendency.  $r_{lobe}$  slightly increases with fetch for sets I and II, while the largest lobe ratio is obtained at  $X \approx 20$  km for set III and then  $r_{lobe}$  decreases. This suggests that the constrained high frequency tail could be responsible for the decreasing of  $r_{lobe}$ , its influence being strongest with increasing fetch ( $f_d$  decreases with fetch).  $\theta_l$  decreases a little with  $X$  for all sets, being almost constant for set I. These results are consistent with Ewans (1998); Wang & Hwang (2001); Long & Resio (2007). Ewans (1998) and Wang & Hwang (2001) show that no clear dependence of bimodality parameters on wave age can be concluded. Nevertheless, Long & Resio (2007)'s observations in Currituck Sound combined with the data of Ewans (1998) seem to show a modest dependence of lobe angle on wave age : distributions tend to narrow with increasing wave age.

### 5.3.3.3 Comparison with the expression of Hasselmann et al. (1980)

To make a link with chapter 3, we briefly compare our GQM results (sets I to III) with the  $\cos^{2s}((\theta - \theta_m)/2)$  expression of Hasselmann et al. (1980). Parameter  $s$  is plotted in Figure 5.7 for directional distributions obtained at fetch  $X = 50$  km, and compared with Hasselmann et al. (1980)'s curve. Three main features should be noted. First, the maximum of  $s$  is observed at the peak frequency (narrowing of the directional distribution near the spectral peak) for the three sets, whereas the maximum given by Hasselmann et al. (1980) is slightly above  $f_p$ . Secondly, we can notice that the slope of our simulated curves is sharper than the one of Hasselmann et al. (1980)'s curve at low frequencies, but the  $s$  values around  $f = 0.75f_p$  are close. Finally, at frequencies higher than  $f_p$ , our results gives a much slower decrease of  $s$  with a stabilization above  $f \approx 4f_p$ . Of course, this comparison is made for the only purpose of showing some main trends. The next paragraph gives comparison with bimodal model and measurements.

### 5.3.3.4 Comparison with the bimodal parameterization of Ewans (1998)

Figure 5.8 presents a comparison of our normalized angular distributions at fetch  $X = 100$  km (sets I, II, III with GQM method) with Ewans (1998)'s symmetric double Gaussian

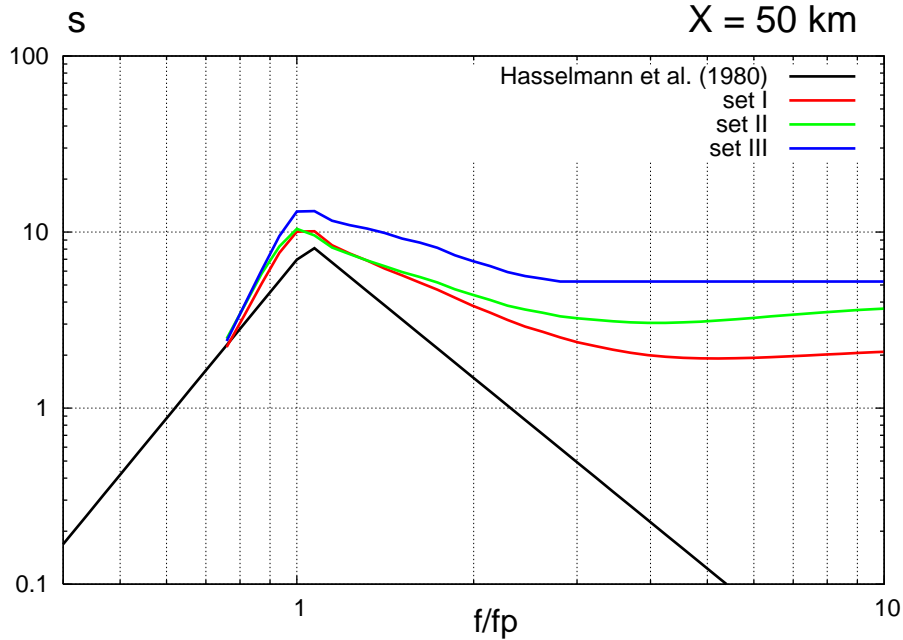


FIGURE 5.7 – The parameter  $s$  of the  $\cos^{2s}((\theta - \theta_m)/2)$  model (cardioid model) for directional distributions at fetch  $X = 50$  as a function of  $f/f_p$ . GQM method, sets I, II and III,  $t = 24$  h. Comparison with the expression of Hasselmann et al. (1980).

parameterization of the Maui data (measurements at large fetch  $X \approx 200$  km). Qualitatively, the directional distributions show similar features. The more significant difference with our results is a lobe ratio increasing to a much higher value :  $r_{lobe}$  is equal to 1.1 at  $f = 2.3f_p$  but reaches 3.7 at  $f = 4.5f_p$ . The distribution is bimodal from  $f = 2f_p$ , with an increasing angle between the two lobes :  $\theta_l$  reaches  $130 - 140^\circ$  at  $f = 5f_p$ , which is quite close to results of set I.

The double Gaussian parameterization of Ewans (1998) was established on the basis of MEM (Maximum Entropy Method, Lygre & Krogstad (1986)) and MLM (Maximum Likelihood Method, Isobe et al. (1984)) estimates of the Maui spectra. These estimates show quantitative differences : MLM estimate becomes bimodal at  $f \approx 2f_p$  (consistent with measurements of Young et al. (1995)) and MEM estimate at  $f \approx 1.4f_p$  (close to set II results). Moreover, sections of the directional distribution in figure 8 of Ewans (1998) show significant differences in lobe ratio obtained with MEM and MLM. Therefore, comparison with double Gaussian parameterization should be more qualitative than quantitative and conclusions concerning the ‘best’ set for predicting directional distribution should not be made too quickly on the basis of this single comparison.

Furthermore, results should not be compared with measurements for frequencies greater than  $4 - 5f_p$  (high-frequency limit of the measurement arrays). Consequently, transition to unimodality is unlikely to be observed in measurement data. Due to very small energy level at these frequencies, possibility of modeling error should also be considered.

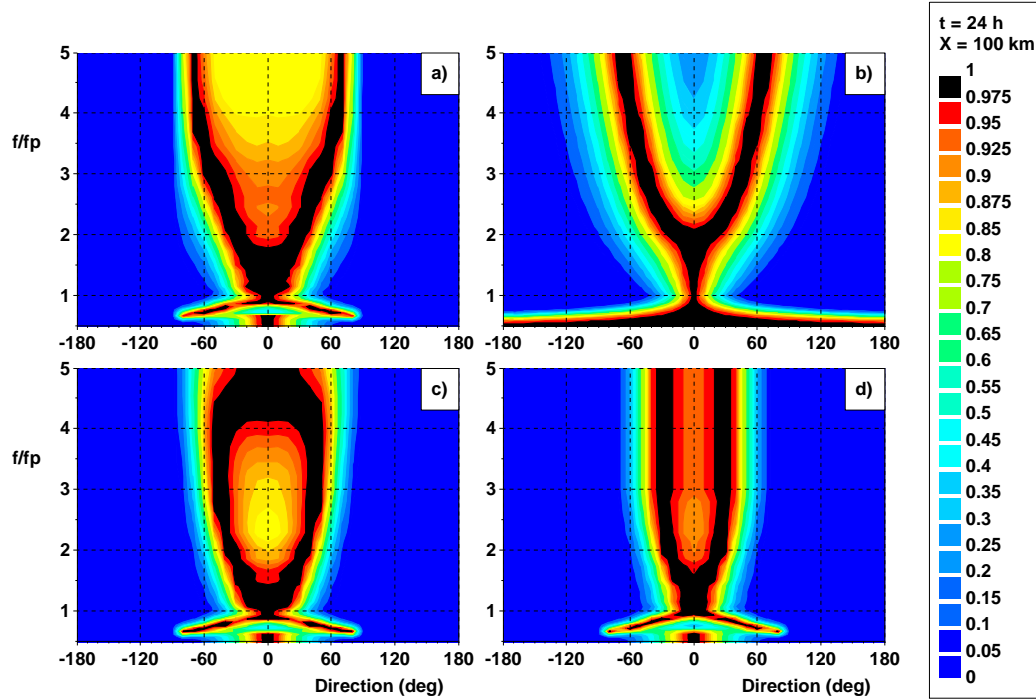


FIGURE 5.8 – Angular distribution normalized by the maximum value at each frequency at fetch  $X = 100$  km a) Set I b) Ewans (1998) bimodal parameterization c) Set II d) Set III. GQM method. Cartesian coordinates.  $t = 24$  h.

Differences between measured and simulated lobe ratios are also observed in Young et al. (1995) (Plate 1), who compared Lake George measurements with simulations (sources terms correspond to our set I with exact computation of the nonlinear interactions). The authors show that bimodality is a robust feature of fetch-limited waves for frequencies above  $f > 2f_p$  (directional distribution is flat-topped from  $f > 1.7f_p$ ).

## 5.4 Slanting fetch conditions

In this section, we focus on the influence of the wind direction on the results : wind blows obliquely from the shore with a direction varying from  $\theta_u = 0^\circ$  to  $90^\circ$  relative to cross-shore direction ( $\Delta\theta_u = 10^\circ$ ). Results of the simulations are compared with some data of the SHOWEX campaign (Ardhuin et al., 2007). The non-dimensional slanting fetch is defined by the simple formula  $\chi = Xg/(\cos(\theta_u)U_{10}^2)$ , as in Arduin et al. (2007), using the wind direction relative to the shore-normal.

The fetch concept in slanting wind conditions is not simple. The pronounced influence of the fetch geometry on the wave growth was shown by, e.g., Schwab et al. (1984); Liu et al. (1984); Donelan et al. (1985); Pettersson (2004); Forget et al. (2006). Different formulations

were proposed by Donelan et al. (1985) and Walsh et al. (1989), based on a re-scaling of the fetch by the cosine of the wave direction relative to the shore-normal. The concept of effective fetch is further investigated in Bottema & Van Vledder (2008).

#### 5.4.1 The SHOWEX campaign

The Shoaling Waves Experiment (SHOWEX) was conducted from September to December 1999 in the North Carolina (USA) continental shelf. A transect of six Datawell Directional Waverider buoys (X1 to X6) situated between 5 and 80 km from the coastline was deployed (see Figure 5.9). Additional wave data were also available during this time period, as measurements from the 3-m discus buoy 44014 of the National Data Buoy Center (NDBC). Wind data were recorded from six NDBC stations ; locations of 44014, CHLV2 and DSNL7 stations are indicated in Figure 5.9. For a complete description of the SHOWEX measurement campaign, please refer to Arduin et al. (2003b,a), Watts (2003) and Arduin et al. (2007).

Measurements over a 5 hours period (12-17h EST time) on 3 November 1999 show nearly ideal deep water wave growth conditions. This event was selected and analyzed in Arduin et al. (2007). The wind blows offshore with a moderate fairly uniform speed  $U_{10} \approx 9.5 \text{ m s}^{-1}$  and a relatively steady direction close to  $\theta_u = 20^\circ$  from the shore-normal. Atmospheric boundary layer conditions are unstable as air temperature is colder than the ocean. During this period, an onshore swell with a peak frequency  $f_p$  close to 0.1 Hz and a significant wave height  $H_s \approx 1 \text{ m}$  is nearly opposing the wind.

The five hour averaged wave observations are compared with our simulations in the next subsections. We did not include opposing swell in our simulations since results of Arduin et al. (2007) showed that a moderate swell opposing wind does not significantly impact the wind sea. Moreover, they also showed that WAM 3 parameterization of the source terms (set I), and, to a less degree WAM-Cycle 4 parameterization (set III), do not give correct results in the presence of opposing swell. Nevertheless, we think that the impact of the swell on wind-wave growth deserves to be further analyzed. Van der Westhuysen (2008) provides some comparisons of X3 and X6 buoy data during this event with simulated spectra using WAM 3 and their saturation-based model (Van der Westhuysen et al., 2007) (set II) combined with DIA. His results indicate that the saturation-based model reproduces spectra under mixed swell and wind-sea conditions much more accurately than WAM 3 source terms.

#### 5.4.2 Influence of the wind obliquity on the growth curves

The obliquity of the wind strongly influences the parameters  $\tilde{E}$  and  $\tilde{\omega}_p$ , as shown in figures 5.10 and 5.11. The wave energy is higher in slanting fetch conditions than in situations with wind blowing perpendicularly off the coast, and the peak frequency is smaller. Major differences are observed at short fetches. The larger the incidence of the wind, the higher the wave energy and the smaller the peak frequency. At large fetches, the curves tend to become similar. These conclusions are consistent with the modeling results of Arduin

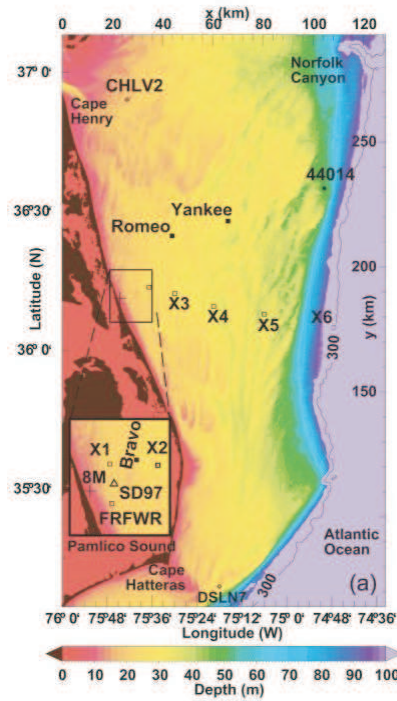


FIGURE 5.9 – Bathymetry of the North Carolina shelf and instrument location during SHOWEX (1999). This image is taken from Ardhuin et al. (2007) (their figure 1 a).

et al. (2007) that show the wind angle is a very sensitive parameter. Their simulations indicate that a  $10^\circ$  error in the wind direction is as important as a 10 % change in the wind speed.

Figures 5.10 and 5.11 show that a  $10^\circ$  slanting wind does not give very strong deviation of the  $\tilde{E}$  and  $\tilde{\omega}_p$  curves from the fetch-limited growth curves (the largest deviation is observed with set II). For an incidence larger than  $20^\circ$ , differences are very significant. For  $\theta_u = 80^\circ$  (wind is almost alongshore), curves are close to horizontal lines, which means that results are close to unlimited fetch conditions and the coast has a small influence. We recall here that in the wave model used for these simulations, reflexion of waves on the coastline is not modeled, all boundaries absorb waves. Energy and peak frequency values for  $\theta_u = 90^\circ$  have not been included because the non-dimensional fetch cannot be defined from  $\chi = Xg/(\cos(\theta_u)U_{10}^2)$  formula.

Differences between results of the three sets can be noticed in figures 5.10 and 5.11 : effect of the slanting wind seems to be enhanced or reduced by the source/sink terms. Discrepancies between the results of the different sets appear to be much more important in slanting fetch conditions than for shore-normal wind. At small fetches, effects of the slanting wind are more pronounced with set II. For larger fetches, set I gives the highest energy levels and set III the smallest. When the DIA method is used, influence of the obliquity of the wind is more pronounced than when GQM is used, for all sets.

Simulated growth curves for a  $20^\circ$  oblique wind (green curves) can be compared with SHOWEX measurements (buoys X1 to X6) obtained under similar slanting fetch conditions (Ardhuin et al., 2007). Parameters  $\tilde{E}$  and  $\tilde{\omega}_p$  are calculated from the measured spectra considering only the wind sea part of  $E(f)$  : energy of the low frequency swell peak is removed from our calculation (see figure 3 of Ardhuin et al., 2007). At large fetches ( $\chi \geq 5000$ ), we see important differences between our results and the field data. This is most probably explained by unstable atmospheric conditions observed in the North Carolina shelf at this time period. Ardhuin et al. (2007) show that the SHOWEX data agree well with the growth curves of Kahma (1981) or Kahma & Calkoen (1992) (unstable) obtained with similar unstable boundary layer and slanting fetches of about  $20^\circ$ . Our results for  $\chi \geq 5000$  are much closer to the Kahma & Calkoen (1992) curve measured in stable atmospheric stratification (see figure 5.1). At smaller fetches, curves are closer to the data (more or less close depending on the set considered).

In figure 5.11, it can be observed that for obliquity higher than  $20^\circ$  (mainly at  $\theta_u = 20^\circ$ ,  $30^\circ$  or  $40^\circ$ ),  $\tilde{\omega}_p$  increases first at small distance from the coastline (first few fetch points) and then decreases. Analysis of the spectra at these small fetches shows that a distinct slanting-fetch component can be seen at lower frequencies : at these small fetches, spectra have two peaks, one slanting fetch component and one wind-sea component. Sometimes, the lower frequency peak can take close or higher values than the wind sea peak, which leads to small values of  $\tilde{\omega}_p$ , then the wind sea starts dominating and  $\tilde{\omega}_p$  increases. This feature depends quite significantly on the set considered, and is also much more pronounced when using DIA. Analysis of the  $S_{nl}$  terms shows that nonlinear interactions are largely responsible for the formation of these peaks, they transfer energy from the components in the wind direction toward the lower frequency component. Measurements presented in Ardhuin et al. (2007) indicate that spectra observed at relatively short distance from the coastline (Waverider buoy FRFWR at about 1 km from the coast, buoy X2) can contain a distinct slanting fetch component (see figure 3 of Ardhuin et al., 2007), but with a smaller peak value than the wind sea component. This would require additional investigations and comparison with measurements at very small fetches, in particular, to address the following issues : does the nonlinear transfer term  $S_{nl}$  calculated with the DIA method enhance this feature, transferring too much energy to the lower frequency component ? which set gives the more accurate  $\tilde{\omega}_p$  calculation ?

### 5.4.3 Frequency spectra and frequency dependent wave parameters

#### 5.4.3.1 Analysis of 1D frequency spectra

1D-spectra, plotted in Figure 5.12, show differences induced by the slanting wind. Note that we compare spectra for different distances from the coastline (1, 5, 20, 50 and 100 km). If the fetch is defined by the distance from the coastline in the direction where the wind blows (which is consistent with our definition of non-dimensional fetch), then spectra are compared for same distance from the shore (say, at a same wave buoy), but not for the same fetch.

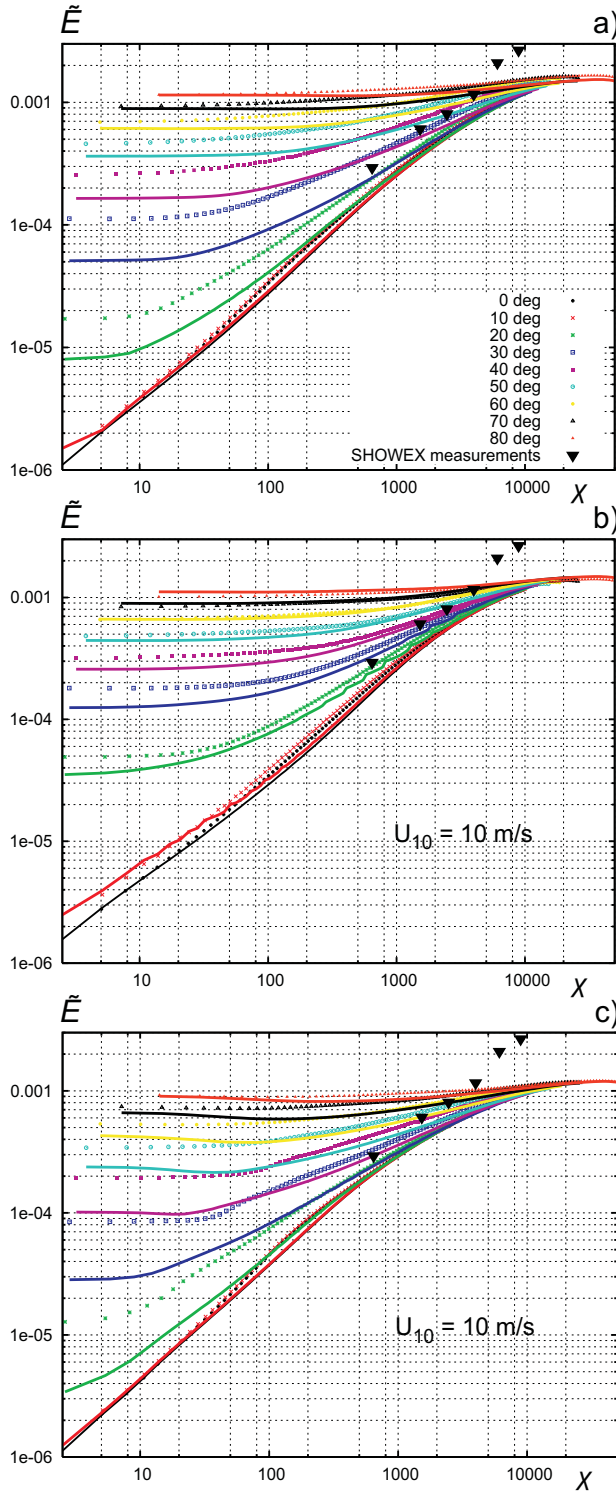


FIGURE 5.10 – Evolution of non-dimensional energy  $\tilde{E}$  with non-dimensional fetch  $\chi$ , for slanting directions  $0 - 80^\circ$  (colors are indicated in the figure). a) set I, b) set II and c) set III. DIA (points) and GQM (solid lines) methods for calculating  $S_{nl}$ .  $t = 24 \text{ h}$ . SHOWEX measurements (buoys X1 to X6) on 3 November 1999 : data averaged over the 12-17h EST time interval (EST=UTC-5 h).

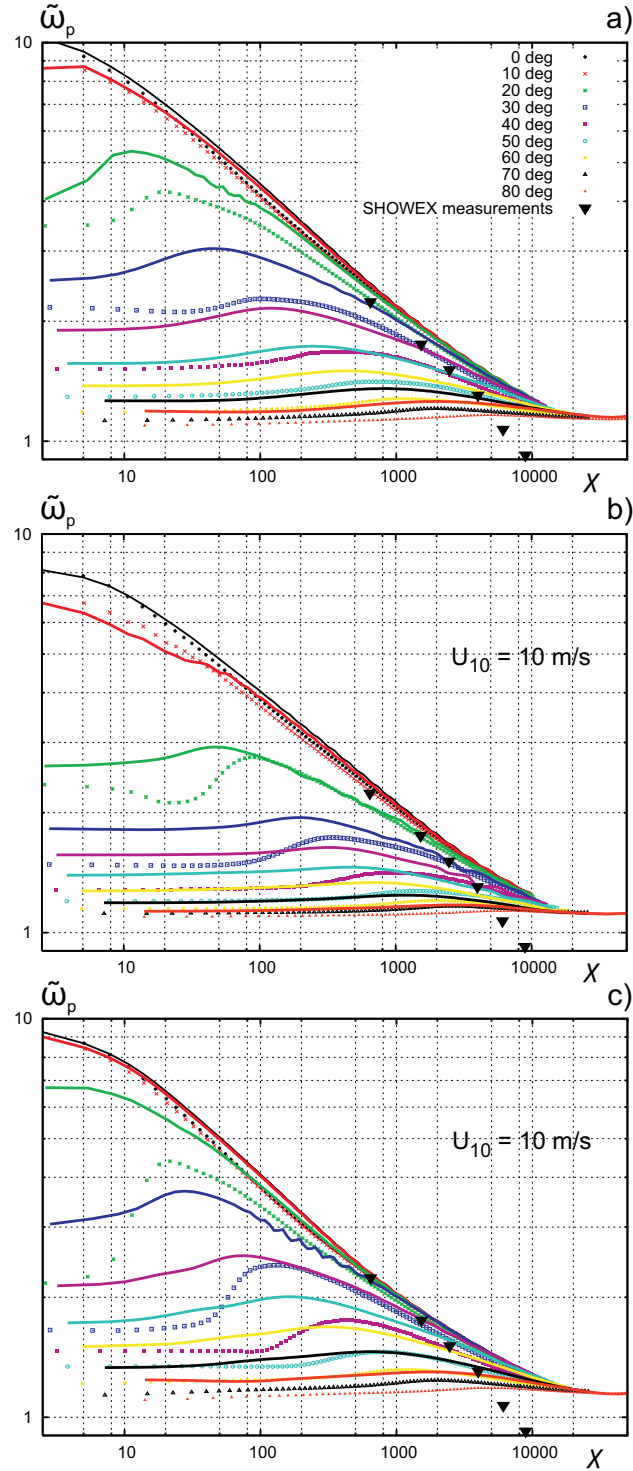


FIGURE 5.11 – Evolution of non-dimensional peak frequency  $\tilde{\omega}_p$  (inverse wave age) with non-dimensional fetch  $\chi$ , for slanting directions from  $0 - 80^\circ$  (colors are indicated in the figure). a) set I, b) set II and c) set III. DIA (points) and GQM (solid lines) methods for calculating  $S_{nl}$ .  $t = 24$  h. SHOWEX measurements (buoys X1 to X6) on 3 November 1999 : data averaged over the 12-17h EST time interval (EST=UTC-5 h).

Globally, spectra are broader in frequency when the wind is slanting. The flattest spectra are observed for 30-40° incidence. For 20 and 30° oblique wind, spectra with two peaks (one smaller slanting peak and one wind-sea peak) are obtained when using DIA ( $X = 1$  km). Maximum value of the spectra is higher and peak frequency is smaller for larger obliquity, as we already observed in subsection 5.4.2. These features are clearly observed at small and intermediate distance from the coastline. At large distance (100 km), curves are merging and only small differences can be noticed. For  $\theta_u = 90^\circ$ , spectra show almost no dependence on the distance from the shore. These spectra are in conditions close to an unlimited fetch, except at very short distance from the coast.

There is a pronounced dependence of the results on the method for computing the nonlinear interactions, especially at small distance from the coast and for wind direction between 20 and 60° where effects of the slanting wind are the most significant. This means that nonlinear interactions have a major effect on the spectra obtained in slanting wind conditions. For all fetches and wind directions, spectra given by the GQM method are more peaked than the DIA spectra.

For practical reasons, only spectra obtained with set II are included in this chapter. Spectra obtained with sets I and II are presented in Appendix B. Same global features are observed for the effects of the slanting wind but source terms have a quite significant influence.

Measurements of the SHOWEX campaign on 3 November 1999 (5 hour averaged data) are compared with 20° oblique wind simulations at 5 km (buoy X1), 20 km (buoy X3) and 50 km (buoy X5) (see figures 5.12, 5.25 and 5.26). Note that large measured values of  $E(f)$  at low frequencies are due to the swell component. All sets give results fairly close to measurements at 5 and 20 km from the coast (buoys X1 and X3). In particular, sets I and III with DIA provide good estimation of X1 buoy data and set II results seem closer with GQM. Accurate estimation of buoy X3 measurements is given by set II with DIA. At larger distance from the shore (50 km), all sets underestimate the energy level and overestimate the peak frequency of buoy X5. This is consistent with results of subsection 5.4.2 and is probably due to unstable atmospheric conditions. We think it could also be related to the swell component that is not included in our model. As shown by Ardhuin et al. (2007) or Van der Westhuysen (2008), inclusions of a swell component in some models (WAM 3, WAM 4 and to a less extent the saturation-based model of Van der Westhuysen (2008)) increases the wave growth. The possible interactions of swell and wind sea components have to be further studied and confirmed. Globally, sets II and III give a good estimation of the high frequency tail, especially at 20 and 50 km from the coast. We recall that the high-frequency tail is imposed for set III. Set I overestimates energy in the high frequency tail.

#### 5.4.3.2 Analysis of the directional spreading

Influence of the wind direction on the directional spreading  $\sigma(f)$  (equation 1.28) is shown in figure 5.13 and figures 5.27, 5.28, 5.29 of Appendix B. Differences between normal and slanting fetch conditions mainly occur at low frequencies, where  $\sigma$  is generally reduced by the wind obliquity, except at short distance from the coast for  $\theta_u = 10 - 30^\circ$  where it can

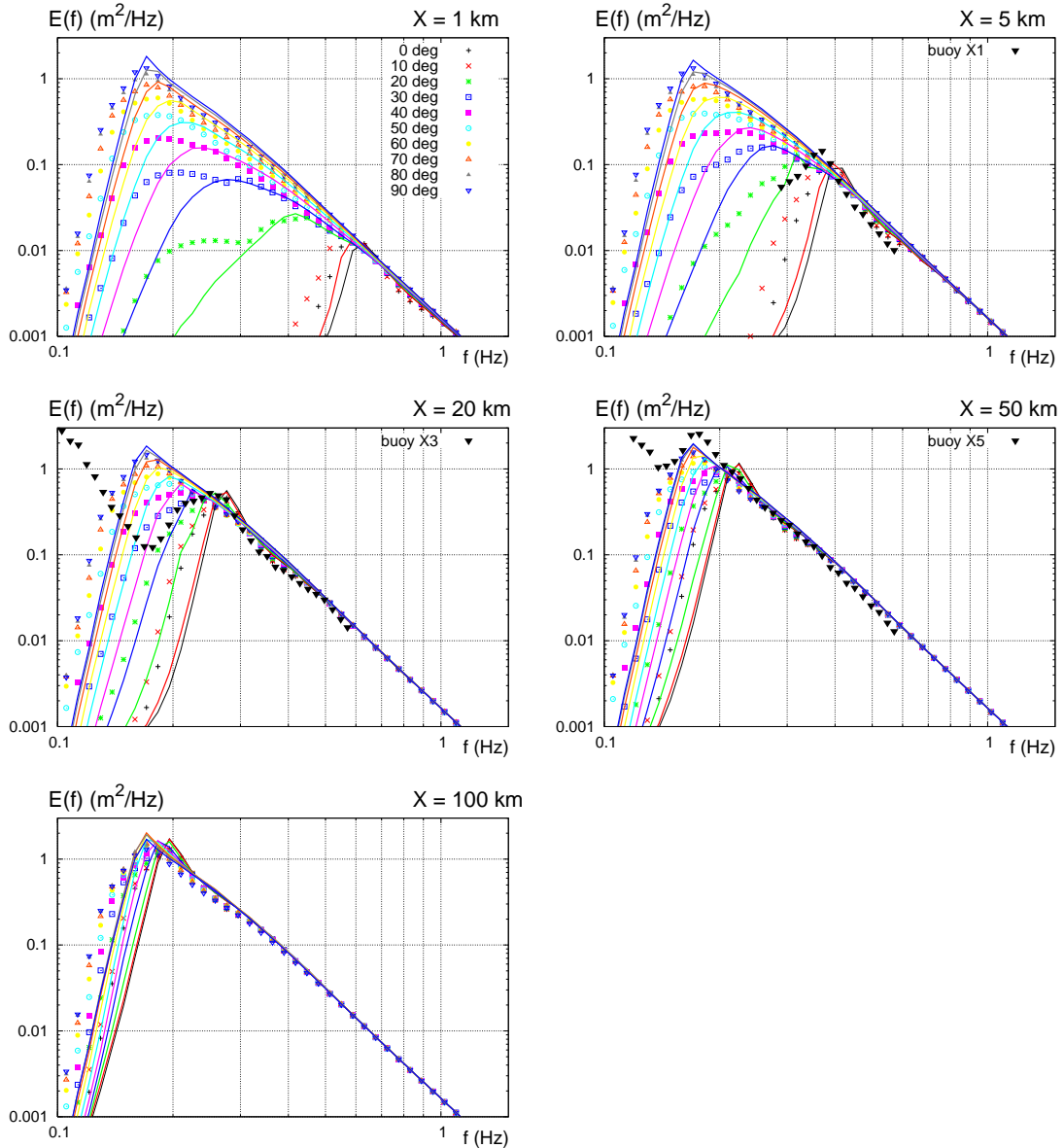


FIGURE 5.12 – 1D-spectra for different distances from the coast (1 km, 5 km, 20 km, 50 km and 100 km) and different oblique wind directions (from  $0^\circ$  to  $90^\circ$ ). Set II. GQM (solid lines) and DIA (points) methods.  $t = 24 \text{ h}$ . Some of the SHOWEX measurements are plotted for comparison with  $\theta_u = 20^\circ$  results (green curve) : buoys X1, X3 and X5 on 3 November 1999 (average over time period 12-17h EST).

take higher values. At high frequencies, the wind angle has little or no effect. This is in agreement with the results of Bottema & Van Vledder (2008) (figure 9 b and 11 a). At 100 km from the shore, low frequency maxima of  $\sigma(f)$  are between  $50^\circ$  (shore-normal wind) and  $30^\circ$  (alongshore wind).

Note that maximum and minimum values of  $\sigma(f)$  (minimum value correspond to the peak frequency) are shifted toward lower frequencies when the obliquity increases since the peak frequency is smaller for larger slanting wind direction (especially near the coastline).

Results for the three sets are globally consistent. Some differences are seen at low frequencies for  $X = 1 - 5$  km. At high frequencies, set I gives the highest  $\sigma(f)$  close to  $47^\circ$  (in fair agreement with Pettersson (2004)'s observations), set II is about  $40^\circ$  and set III provides the smallest angular spreading ( $32^\circ$ ). At intermediate and high frequencies, when differences are noticed, we observe that larger obliquity from the shore-normal direction gives higher  $\sigma(f)$  for set I. For sets II and III, this tendency is not so clear. Set II shows a small decrease of  $\sigma(f)$  for  $\theta_u = 10 - 40^\circ$  and then it increases.

DIA results have not been plotted in 5.13 for readability reasons. Globally, features are comparable except that DIA gives a higher angular spreading at intermediate (and high) frequencies (see figure 5.28 of Appendix B).

Comparison with SHOWEX measurements shows that our simulations underestimate the directional spreading. This is consistent with the results of Ardhuijn et al. (2007). As set I gives the highest spreading, it is closer to measurements ; similarly, DIA results are closer than GQM (except at  $X = 100$  km). At  $X = 5$  km, buoy X1 shows two peaks of  $\sigma(f)$ , which is not obtained in simulations.

#### 5.4.3.3 Analysis of the mean wave direction

The mean direction of the waves  $\theta_m(f)$  (equation 1.30) is shown in figure 5.14 for set II and GQM (see also figures 5.30, 5.31 and 5.32 of Appendix B for comparison with sets I and III and DIA results with set II). At high frequencies, waves are roughly aligned with the wind. At low frequencies,  $\theta_m(f)$  deviates considerably from the wind direction. The wave directions appear to be ‘steered’ by the coastline, which means they propagate in directions much closer to the coastline, or even a little onshore, despite the offshore wind. Observation of wave steering have been reported by Holthuijsen (1983); Donelan et al. (1985) and more recently by Pettersson (2004) and Long & Resio (2007). They all show that in slanting fetch conditions, peak directions tend to align with the longer fetch direction (direction of the coast) while mean direction of the high frequency waves is close to the wind direction. Similar tendencies have also been reported by Bottema & Van Vledder (2008) in simulations using DIA and WRT methods for  $S_{nl}$ .

In our simulation, the largest deviations are seen at small distance from the coast, for  $\theta_u = 20 - 30^\circ$  : mean direction of the waves can deviate up to  $80^\circ$  from the wind direction. This leads to wave going onshore ( $\theta_m > 90^\circ$ ). Even for small wind angles ( $\theta_u = 20^\circ$ ), mean direction of the low frequency waves can be slightly onshore. At large distance from

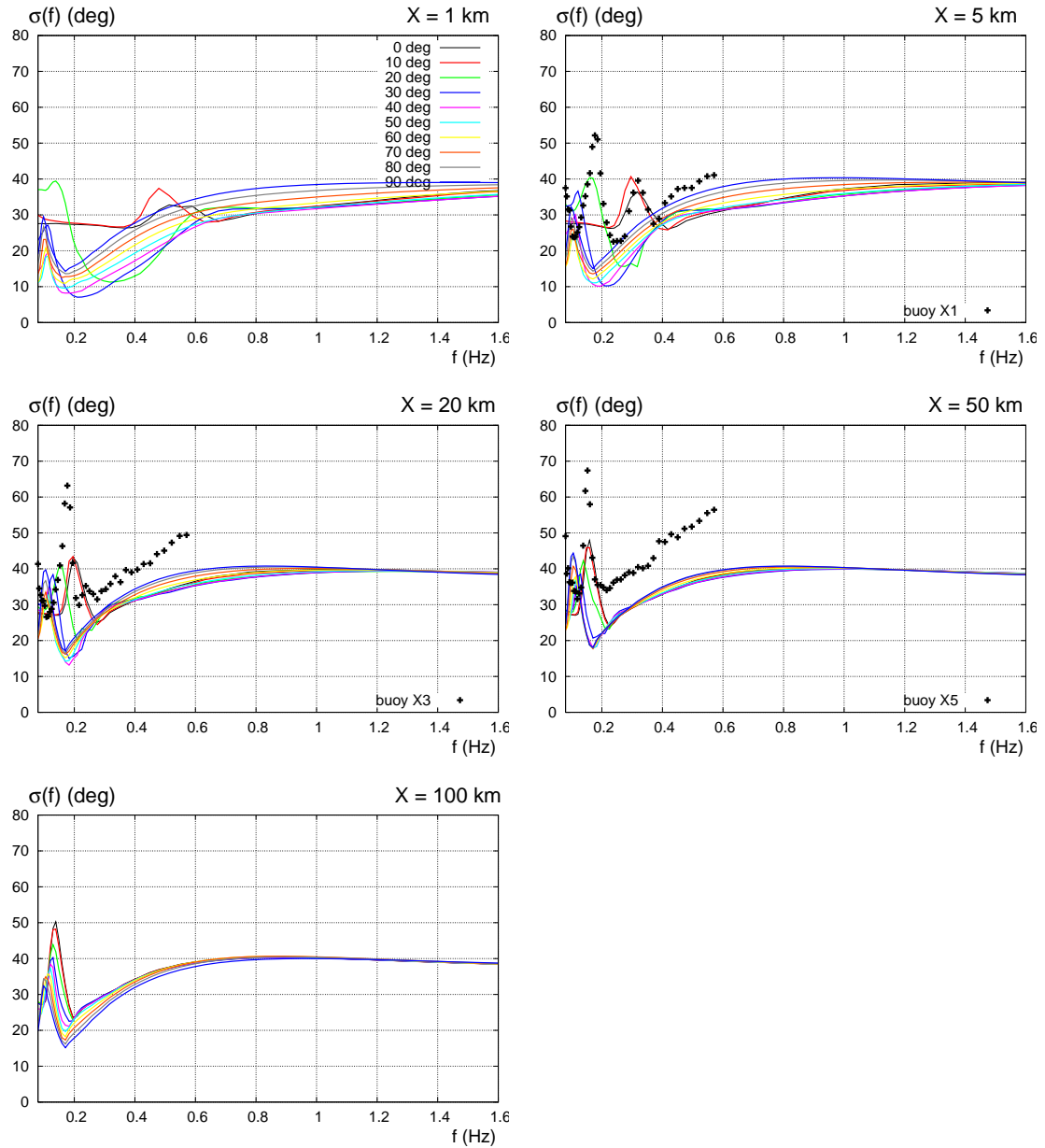


FIGURE 5.13 – Frequency-dependent directional spreading  $\sigma(f)$  ( $^{\circ}$ ) for different distances from the coast (1 km, 5 km, 20 km, 50 km and 100 km) and different oblique wind directions (from  $0^{\circ}$  to  $90^{\circ}$ ). Set II. GQM method.  $t = 24$  h. Some of the SHOWEX measurements are plotted for comparison with  $\theta_u = 20^{\circ}$  results (green curve) : buoys X1, X3 and X5 on 3 November 1999 (average over time period 12-17h EST).

the coast, the wave steering is much smaller but still clearly visible, except for the largest incidences (i.e. wind direction close to shore direction).

All the sets exhibit the same tendencies, but differences can be noticed : set II globally predicts more wave steering than the two other sets. DIA simulations (figure 5.31) gives fairly close results compared to GQM although we may notice that the low frequency wave are more deviated by the coast when using DIA.

SHOWEX measurements at buoys X1, X3 and X5 also seem to confirm these features. Note that the last low frequency measurement point represented in each figures should not be considered, as it shows change of the mean direction due to the onshore swell component.

Measurements at buoy X1 (5 km) show an abrupt shift in direction from  $110^\circ$  at 0.27 Hz to  $20^\circ$  at 0.33 Hz and some sort of plateau around 0.2-0.3 Hz at  $110^\circ$  ( $90^\circ$  from the wind direction) (see description in Arduin et al., 2007). Our simulation with set II and GQM (green curve corresponding to  $\theta_u = 20^\circ$ ) also indicates an abrupt shift in direction from  $95^\circ$  to  $23^\circ$  and a plateau near 0.2-0.3 Hz, although  $\theta_m$  is quite underestimated. The sharp separation in two wind-sea systems described by Arduin et al. (2007) is reproduced fairly well.

Buoy X3 also shows a short plateau around 0.2 Hz with waves propagating  $70^\circ$  from the wind direction. The simulation using set II (and GQM) reproduces quite well the observed wave steering, although the shift in direction is still a little underestimated. Buoy X5 gives  $25^\circ$  wave steering at about 0.17 Hz, which is overestimated by our simulated results (from 40 to  $50^\circ$  of wave steering).

#### 5.4.4 Directional wave spectrum and nonlinear interactions

Figures 5.15 and 5.16 represent directional spectra normalized by their maximum value at relatively short ( $X = 5$  km) and relatively long ( $X = 50$  km) distance from the coastline, for wind directions  $0-90^\circ$ . The wave ‘steering’ illustrated with  $\theta_m(f)$  in the above subsection is seen very well.

Figure 5.15 confirms that at short fetch, the low frequency components of the waves are strongly influenced by the coastline. For  $\theta_u = 20$  to  $90^\circ$ , the peak of the spectrum is in the direction of the coast or a little onshore ( $10-20^\circ$  onshore). For  $\theta_u = 10^\circ$ , the peak is at  $30^\circ$  from the wind direction. This means that a change of wind direction from  $\theta_u = 10^\circ$  to  $\theta_u = 20^\circ$  have a very strong impact on the wave steering. High frequency components are more aligned with the wind, which shows that two different wave systems are coexisting.

At larger fetch (figure 5.16), the wave steering is less pronounced, although it is still present at the peak of the spectrum. For a  $10^\circ$  slanting wind, the peak of the spectrum is at  $10^\circ$  more oblique direction ; for  $\theta_u = 20^\circ$ , waves are propagating at  $30^\circ$  from the wind direction. The spectrum for  $\theta_u = 30^\circ$  shows two peaks, one alongshore and one at  $\theta = 55^\circ$ . For incidence higher than  $40^\circ$ , waves are propagating alongshore or slightly onshore ( $5^\circ$ ). Spectrum for  $\theta_u = 90^\circ$  is symmetric with respect to wind direction (unlimited fetch case). At frequencies above the peak, most of the waves are roughly propagating in the wind direction.

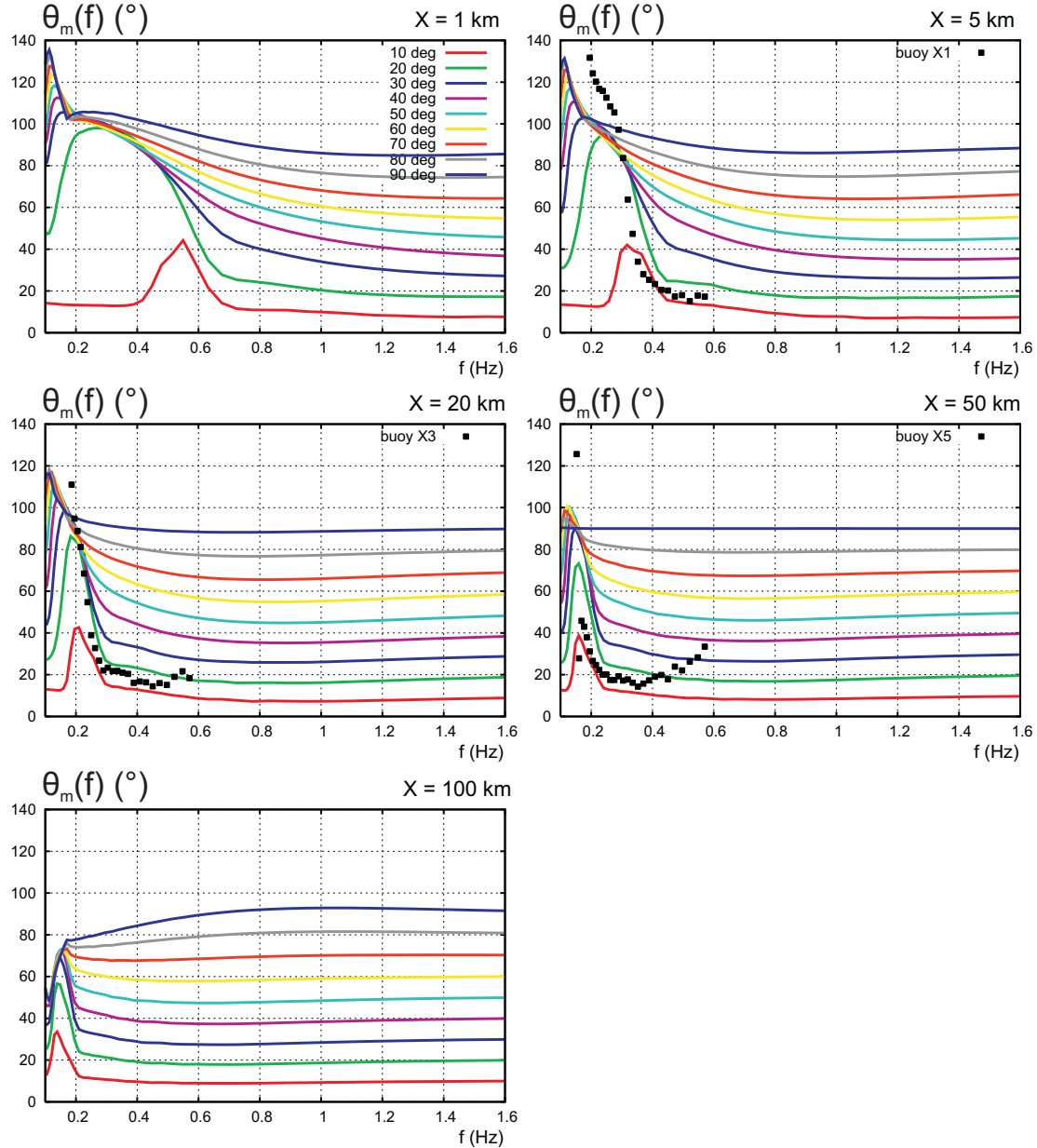


FIGURE 5.14 – Mean wave direction  $\theta_m(f)$  ( $^{\circ}$ ) for different distances from the coast (1 km, 5 km, 20 km, 50 km and 100 km) and different oblique wind directions (from  $0^{\circ}$  to  $90^{\circ}$ ). Set II. GQM method.  $t = 24$  h. Some of the SHOWEX measurements are plotted for comparison with  $\theta_u = 20^{\circ}$  results (green curve) : buoys X1, X3 and X5 on 3 November 1999 (average over time period 12-17h EST).

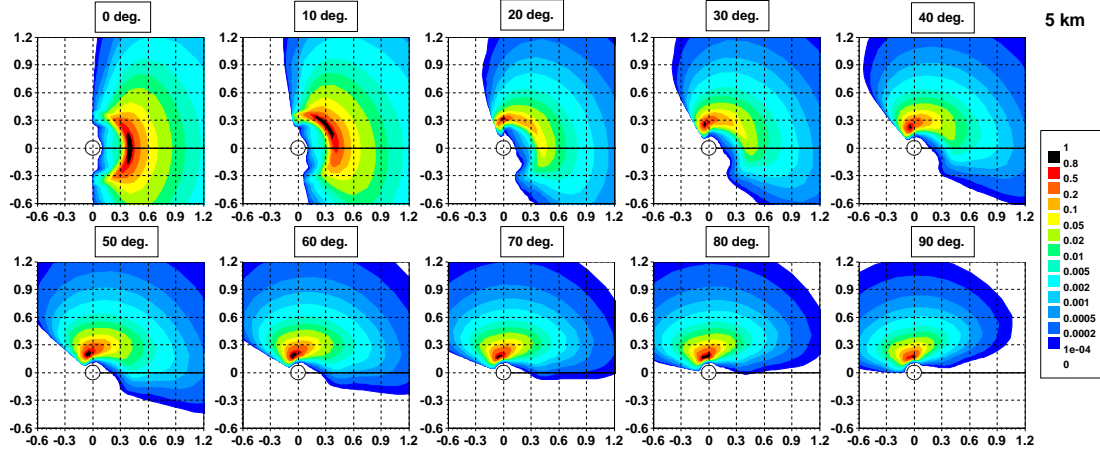


FIGURE 5.15 – Normalized spectra  $E(f, \theta)/E_{max}$  for  $X = 5$  km and different oblique wind directions (from  $0^\circ$  to  $90^\circ$ ), using the GQM method for  $S_{nl}$  and set II for the source and sink terms.  $t = 24$  h.

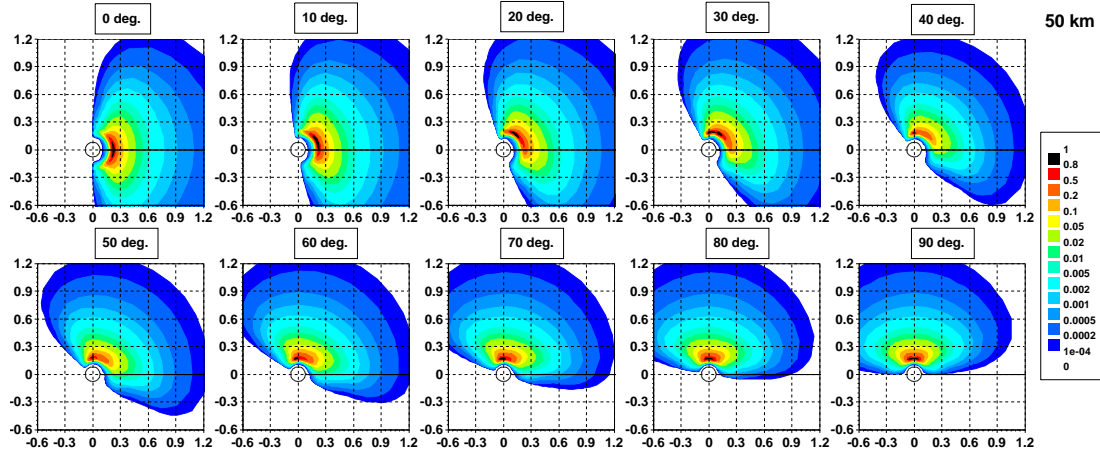


FIGURE 5.16 – Normalized spectra  $E(f, \theta)/E_{max}$  for  $X = 50$  km and different oblique wind directions (from  $0^\circ$  to  $90^\circ$ ), using the GQM method for  $S_{nl}$  and set II for the source and sink terms.  $t = 24$  h.

Figures 5.17 and 5.18 present the nonlinear transfer term  $S_{nl}(f, \theta)$  at  $X = 5$  and  $50$  km. It is clear from these two figures that the peak of the spectrum is deviated from the wind direction by the nonlinear wave-wave interactions. These interactions transfer energy from wind direction to directions more aligned with the coastline (or a little onshore). The low frequency peak of the spectrum seems to match quite well with the maximum positive transfer of the  $S_{nl}$  term. At high frequencies, the  $S_{nl}$  term provides negative transfers in the wind direction. This is in agreement with recent observations of Pettersson (2004)

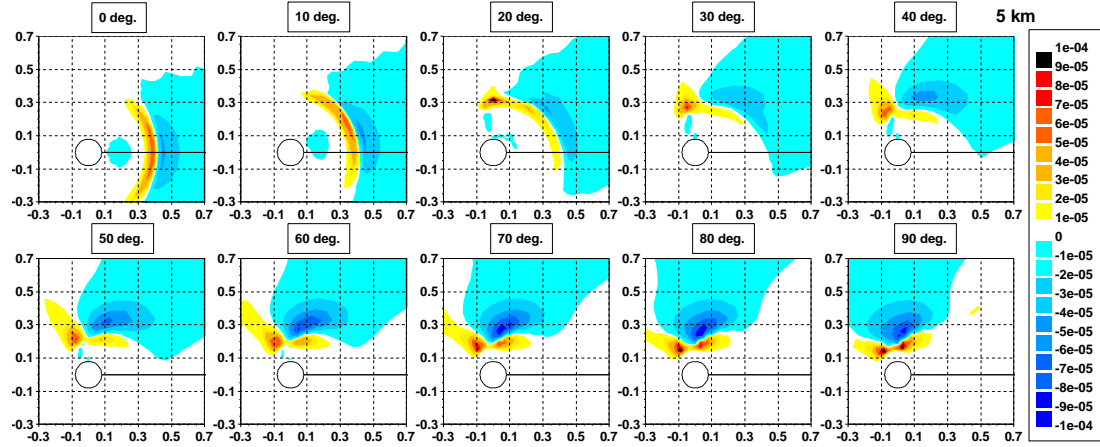


FIGURE 5.17 – Nonlinear transfer term  $S_{nl}(f, \theta)$  for  $X = 5$  km and different oblique wind directions (from  $0^\circ$  to  $90^\circ$ ), using the GQM method for  $S_{nl}$  and set II for the source and sink terms.  $t = 24$  h.

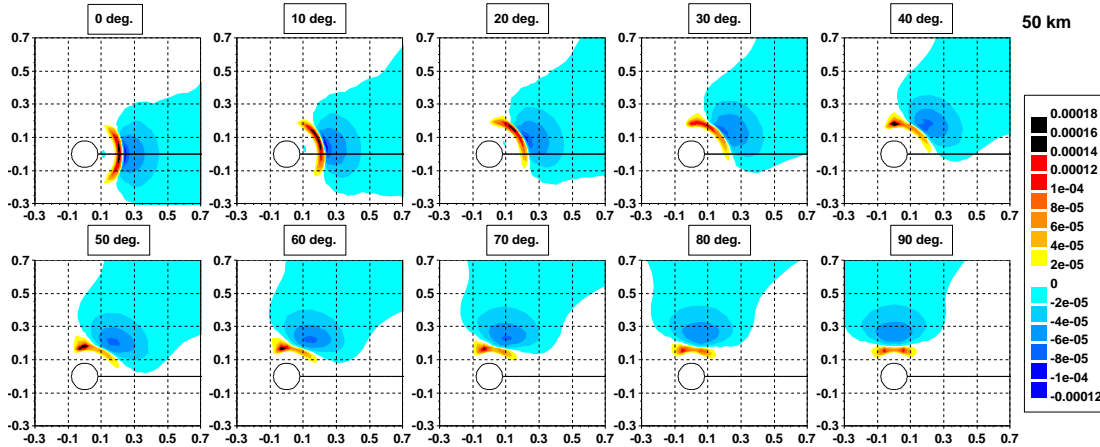


FIGURE 5.18 – Nonlinear transfer term  $S_{nl}(f, \theta)$  for  $X = 50$  km and different oblique wind directions (from  $0^\circ$  to  $90^\circ$ ), using the GQM method for  $S_{nl}$  and set II for the source and sink terms.  $t = 24$  h.

that showed nonlinear four-wave interactions play a major role in the evolution of wave spectrum under slanting fetch conditions.

#### 5.4.5 Directional distribution of the spectrum

Figure 5.20 represents the directional distribution of the wave spectrum normalized by its maximum value at each frequency obtained with set II and the GQM method ( $X = 50$

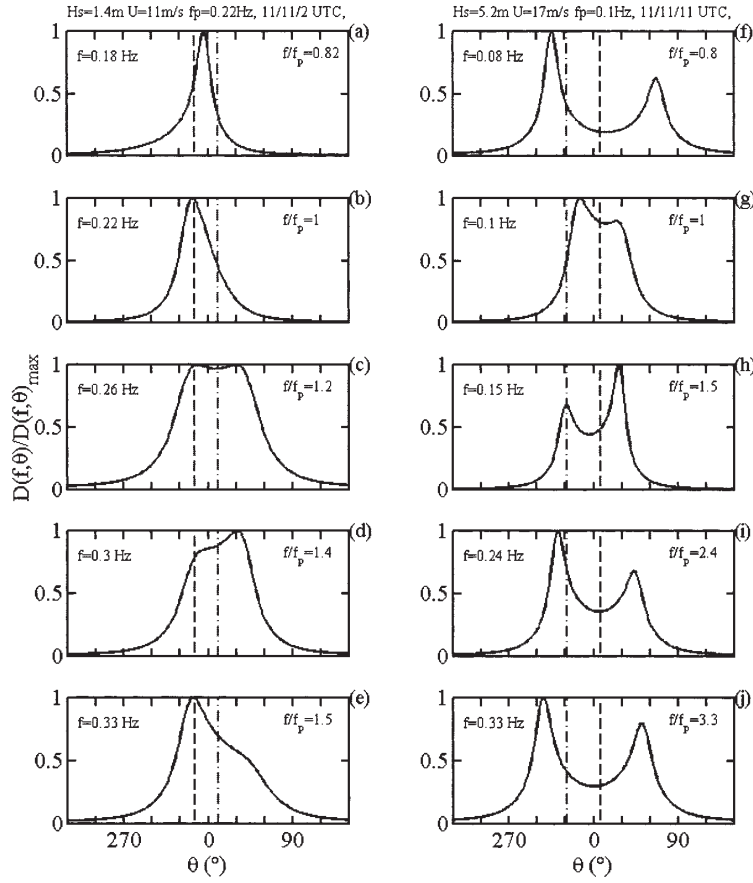


FIGURE 5.19 – This figure is extracted from Wang & Hwang (2001) (their figure 9) and represents sections of two directional distributions at different frequencies. Measurements are acquired by an offshore buoy. Dashed-dotted lines correspond to the wind direction, dashed lines to the peak wave direction.

km, wind directions  $0 - 90^\circ$ ). The white dotted circles correspond to  $f_p$ ,  $2f_p$  and  $4f_p$ . This figure illustrates quite well the evolution of the directional distribution of the spectrum for a continuum of wind directions from shore-normal to alongshore.

We see that some main characteristics of the fetch-limited directional distributions can be also observed when the wind is slanting. The directional distributions are narrow at the spectral peak and broader at frequencies lower and higher than the peak. The transition to unimodality is observed above  $4 - 5f_p$ .

For frequencies higher than  $4 - 5f_p$ , the distributions are all unimodal whatever the wind direction is. At these frequencies, the main direction is aligned with the wind (it can be  $5^\circ$  more slanted than the wind, but globally direction is very similar).

For  $f_p < f < 4f_p$ , the directional distribution is bimodal for shore normal wind and  $10^\circ$  slanting wind, then for angle greater than  $60^\circ$  the bimodality is seen again. It is not very

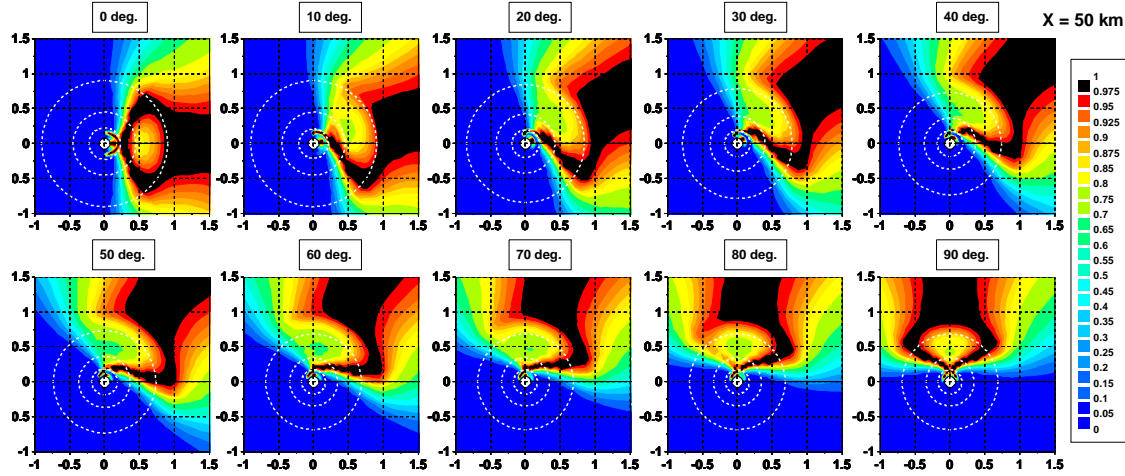


FIGURE 5.20 – Angular distribution normalized by the maximum value at each frequency  $D(f, \theta)/D_{max}(f)$  for  $X = 50$  km. Set II. GQM method.  $t = 24$  h. The white dotted circles indicate  $f_p$ ,  $2f_p$  and  $4f_p$ .

pronounced for  $\theta_u = 60-70^\circ$  (small lobe ratio) but become significant for  $\theta_u = 80$  and most of all  $90^\circ$  (unlimited fetch conditions). For  $\theta_u = 90^\circ$ , the bimodality above  $f_p$  is even more pronounced than for  $\theta_u = 0^\circ$ , with a lobe ratio equal to 1.29. The lobe angle is similar to the one calculated in fetch-limited conditions ( $\theta_l = 90-100^\circ$ ). For  $10 \leq \theta_u \leq 80^\circ$ , the directional distribution is very asymmetric with respect to the wind direction. As described in subsection 5.3.3, most of the directional distributions observed in conditions close to fetch-limited growth are asymmetric (Young et al., 1995; Ewans, 1998; Wang & Hwang, 2001). Our results present similarities with observations of Wang & Hwang (2001) (see figure 5.19 or their figures 8, 9 (offshore buoy), 11 and 12 (nearshore buoy)). Their sections of directional distributions show that there may be very pronounced differences between amplitudes of the two bimodal lobes : one can be very smooth and the other very sharp.

Our slanting wind simulations give us clue to analyze this asymmetry. Indeed, for  $\theta_u = 10^\circ$ , the distribution is strongly asymmetric and for  $\theta_u = 20^\circ$ , bimodality is not present any more in these simulations. With set I (and GQM) some slight bimodality is still seen for  $\theta_u = 20^\circ$  (not shown here), but globally results point out that wind direction is a very sensitive parameter and recommendation should be done for all high resolution measurements of directional spectra to try to have wind measurements as accurate as possible.

Results of Long & Resio (2007) (their figures 12 and 13) also indicate asymmetry in the directional distribution for the different wind incidences, but asymmetry seems less pronounced than in our simulations.

At frequencies below the peak, bimodality can be seen in fetch-limited conditions and for alongshore wind (some low-frequency bimodality is also seen for  $\theta_u = 80^\circ$ ). Wind incidence have clear effect on the low frequency bimodality : low frequency bimodality is not seen as

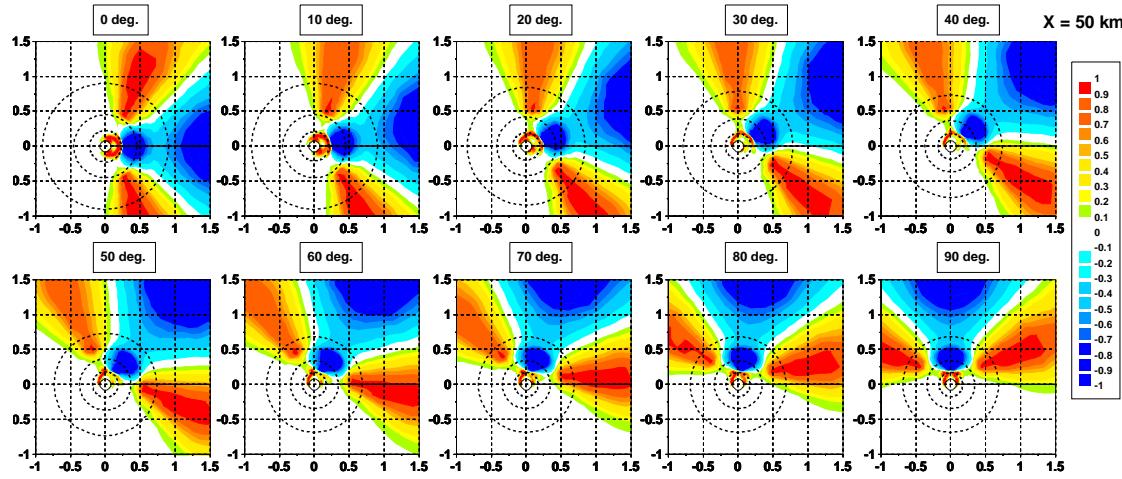


FIGURE 5.21 – Nonlinear transfer term normalized by its maximum absolute value at each frequency  $S_{nl}(f, \theta) / |S_{nl,max}(f)|$  for  $X = 50$  km and different oblique wind directions (from  $0^\circ$  to  $90^\circ$ ). Set II. GQM method.  $t = 24$  h. The black dotted circles indicate  $f_p$ ,  $2f_p$  and  $4f_p$ .

soon as the wind is slanting.

Figure 5.33 of Appendix B shows the directional distribution at shorter distance from the coastline ( $X = 5$  km). Directional distributions are more asymmetric and do not show clear bimodality at low frequencies.

Nonlinear transfer terms normalized by their maximum absolute value at each frequency are plotted in figure 5.21 for  $X = 50$  km and wind directions  $0-90^\circ$ . At frequencies higher than  $f_p$ , the  $S_{nl}$  term send energy to oblique directions relative to wind direction. The ten panels show very similar features with a  $S_{nl}$  term turning with wind obliquity. However, when the wind is slanting, the energy transfers are not symmetric with respect to the wind direction : one directional positive peak of  $S_{nl}$  is higher than the other one, so that one direction gets more energy. This creates the asymmetry of the directional distributions observed in figure 5.20.

## 5.5 Conclusions

In this chapter, we investigated the effect of wind direction on fetch-limited wave growth at different distances from a straight coastline. Two cases were considered separately, fetch-limited and slanting fetch conditions, paying particular attention to the two-dimensional wave spectrum and its directional distribution. Effect of the substitution of the DIA method by a quasi-exact algorithm for computing four-wave nonlinear interactions, the GQM method, was studied and three combinations of the dissipation and input terms were tested and compared.

Our analysis suggests that the nonlinear transfers play a major role in the evolution of the directional spectrum under fetch-limited and slanting fetch conditions, since they create bimodality and may be partly responsible of the wave steering for slanting wind directions.

In the fetch-limited case, few differences are observed between DIA and GQM results as long as we consider  $\tilde{E}$  and  $\tilde{f}_p$  growth curves. However, the predicted angular spreading is significantly reduced when the GQM method is used and the frequency spectra are more peaked. Improvement brought by GQM can be particularly seen on the directional structure of the spectrum which appears to be bimodal at frequencies lower and higher than the peak frequency.

Differences induced by the use of three combinations of the source and sink terms are mainly seen on the directional properties of the spectrum :

- Set I gives a larger directional spreading and a much broader bimodal directional distribution.
- The use of the diagnostic tail with set III has a clear effect on the bimodality of the modeled directional distribution.

Effects of the source/sink terms are also visible on the frequency spectrum : set I was shown to produce higher energy levels at high frequencies, together with a higher peak frequency.

The slanting fetch case showed interesting features. At short fetches, the larger the angle between the wind and the shore normal direction, the higher the wave energy and the lower the peak frequency. The steering of the wave direction is clearly observed on the mean wave direction and on the directional spectra. The low frequency waves are strongly influenced by the coastline while the high frequency waves behave similarly to locally generated wind waves. This is consistent with the results of Holthuijsen (1983); Pettersson (2004); Long & Resio (2007); Bottema & Van Vledder (2008).

The role of the quadruplet interactions during slanting fetch was investigated by Bottema & Van Vledder (2008). They found that the method for computing  $S_{nl}$  mainly influences the amount of wave steering. Our analysis confirms that nonlinear interactions have significant effects on the amount of wave steering (even if our conclusion are quite the opposite, as Bottema & Van Vledder (2008) found that DIA gives less steering) but other parameters where shown to be also impacted. Difference between  $\tilde{E}$  and  $\tilde{\omega}_p$  obtained with DIA and GQM can be quite significant at small fetches. Moreover, we saw that the method for computing  $S_{nl}$  has a pronounced influence on the shape of the frequency spectrum and its directional distribution : results with DIA were only presented for fetch-limited simulations, but our investigations showed that directional distribution is also highly influenced by the method for  $S_{nl}$  in slanting fetch conditions. However, DIA was shown to reproduce fairly well the wave steering phenomenon, even if it overestimates the amount of wave steered by the coastline compared to GQM simulations.

Discrepancies between the results of the different sets for source/sink terms appear to be much more important in slanting fetch conditions than for shore-normal wind when looking at the growth curves at small fetches. Differences in the amount of wave steering and for the frequency distribution of the spectrum are also quite significant. This suggests that the nonlinear wave-wave interaction is not the only term in the balance equation responsible for the wave steering and that simultaneous accuracy in calculation of nonlinear interactions

and source terms is necessary to obtain reliable results, in agreement with the conclusions of Ardhuin et al. (2007) and Bottema & Van Vledder (2008).

In this chapter, we compared our results with some of the SHOWEX measurement for a 20° slanting wind and an opposing swell. Nevertheless, our simulations did not include swell as Ardhuin et al. (2007) showed that a moderate swell opposing wind does not significantly impact the evolution of wind waves. Masson (1993) analyzed the coupling between swell and wind sea and showed the strong influence of nonlinear wave-wave interactions on this coupling. Based on simulations and laboratory experiments, Masson (1993) shows that the strength of the interaction depend on the ratio of the swell frequency and the wind sea peak frequency, and on the angle between mean directions of the two systems. Masson (1993) concludes that the coupling decreases significantly when peak frequencies of the swell and wind sea are well apart (for a ratio of the swell and wind sea peak frequencies smaller than 0.6, no significant coupling is visible). We think further investigation of this aspect by simulating the evolution of swell and wind sea for different ratios of energy, peak frequency and mean direction of the two systems would be an interesting perspective for the present work.

## Acknowledgments

We acknowledge the National Data Buoy Center (NDBC) for data from buoy 44014 and stations DSLN7 and CHLV2. SHOWEX buoys X1 to X6 were deployed by staff from the Naval Postgraduate School and the Scripps Institution of Oceanography Center for Coastal Studies.

# Conclusion générale - Perspectives

Dans cette thèse, les objectifs principaux ont été (i) de traiter le calcul des interactions non-linéaires au sein du spectre d'énergie des vagues en recherchant le meilleur compromis possible entre une grande précision des résultats et un temps de calcul acceptable, et (ii) d'étudier les effets associés à ces interactions non-linéaires sur la dynamique d'évolution du spectre d'état de mer dans différents cas de figure. Nous nous sommes limités au cas de grande profondeur d'eau (i.e. profondeur supposée « infinie »), pour lequel la relation de dispersion peut être simplifiée.

Pour l'évaluation numérique du terme d'interactions non-linéaires entre quadruplets de fréquences ( $S_{nl}$ ), nous avons utilisé et optimisé la méthode GQM (Gaussian Quadrature Method), qui repose sur une intégration numérique à l'aide de quadratures de Gauss. Elle a été développée en s'appuyant sur le travail de Lavrenov (2001) et donne un calcul « exact » (ou plutôt quasi-exact) de ces interactions. La précision du calcul dépend bien entendu de la résolution de la méthode et du nombre de configurations considérées.

Dans ce travail, la méthode GQM a été comparée avec des méthodes actuellement implémentées dans les modèles de troisième génération (par exemple WAM, WAVEWATCH III, SWAN, TOMAWAC, CREST) : la méthode DIA, et occasionnellement MDIA. Plusieurs formulations pour modéliser la génération des vagues par le vent ( $S_{in}$ ) et la dissipation par moutonnement ( $S_{diss}$ ) ont également été utilisées et comparées dans différentes situations (cas de durée limitée, fetch limité ou oblique).

## Synthèse des principales conclusions

Les conclusions principales de la thèse sont les suivantes :

- La méthode GQM permet d'avoir une approche à la fois précise et possédant des temps de calcul raisonnables. Il est ainsi possible d'envisager dans un futur proche son implantation dans des modèles opérationnels puisque les temps de calcul pour la résolution la plus grossière parmi les trois considérées (nommée résolution « rough ») sont seulement :
  - 100 fois supérieurs à ceux de la méthode DIA pour des simulations en un seul point avec uniquement les interactions non-linéaires vague-vague,

- 50 fois supérieurs à ceux de la méthode DIA pour des simulations en un seul point (durée-limitée) prenant en compte également les termes  $S_{in}$  et  $S_{diss}$ ,
- 25 fois supérieurs à ceux de la méthode DIA pour des simulations prenant en compte les trois termes sources et la propagation des vagues (modèle à une dimension d'espace).
- En mer ouverte, l'intérêt d'un calcul (quasi-)exact des interactions non-linéaires entre quadruplets de fréquences n'est pas forcément évident pour une estimation des paramètres intégrés du spectre comme la hauteur significative  $H_{m0}$  ou la fréquence de pic  $f_p$ , mais les différences sont claires lorsqu'on regarde les paramètres directionnels, le spectre d'énergie des vagues et en particulier sa distribution angulaire.
- L'évolution auto-similaire du spectre fréquentiel  $E(f)$  a été vérifiée avec les méthodes GQM et DIA dans le cas de simulations sans action du vent ni dissipation (cas où seules les interactions non-linéaires interviennent). Lorsqu'on simule l'équation cinétique complète (avec vent, dissipation et propagation éventuelle), des propriétés d'auto-similarité asymptotique ont été démontrées par Badulin et al. (2007) pour les situations de durée et fetch limités. Ces propriétés sont utilisées dans le chapitre 4 sans qu'on les ait prouvées à nouveau.
- Un des aspects principaux de ce travail a porté sur l'étude de la structure directionnelle du spectre, et en particulier ce que l'on nomme bimodalité : les composantes de certaines fréquences se propagent dans deux directions principales, généralement symétriques par rapport à la direction du vent. On a montré que la bimodalité dans les fréquences supérieures à la fréquence de pic était une caractéristique majeure du spectre directionnel d'énergie de l'état de mer. Elle est obtenue dans les cas d'évolution sans vent ni dissipation, et dans des conditions de durée limitée et de fetch limité. Dans ce dernier cas, la bimodalité hautes fréquences est présente quelles que soient les formulations utilisées pour les termes  $S_{in}$  et  $S_{diss}$  et de façon quasi-indépendante de la distance à la côte, mais uniquement lorsque le calcul des interactions non-linéaires est effectué de façon quasi-exacte. Cela montre que les interactions non-linéaires constituent le mécanisme clef responsable de la bimodalité du spectre des vagues. Une structure commune se dégage de tous ces cas : le spectre est étroit au niveau de la fréquence de pic et son étalement angulaire augmente dans les fréquences en dessous et au-dessus de la fréquence de pic  $f_p$ . Dans les fréquences supérieures à  $f_p$ , la bimodalité est constatée à partir de  $f = 1$  à  $1.8 f_p$  selon les cas, et l'on remarque généralement un retour à l'unimodalité dans les plus hautes fréquences ( $f \geq 4 - 5f_p$ ).

Lorsque le calcul des interactions non-linéaires est effectué avec une méthode approchée, comme DIA (ou également MDIA), on n'observe pas (ou très peu) de bimodalité dans les fréquences supérieures à la fréquence de pic. Néanmoins, une structure étroite au niveau du pic spectral avec un étalement angulaire plus important dans les fréquences inférieures et supérieures à  $f_p$  est aussi obtenue.

L'influence des termes de génération par le vent et de dissipation sur la structure di-

rectionnelle du spectre dans les hautes fréquences est observée dans les conditions de durée-limitée (chapitre 3), de fetch limité (chapitre 5), et également pour le cas de fetch oblique même si ces derniers résultats ne sont pas inclus dans le présent mémoire. Les termes sources et puits ont un effet quantitatif sur l'étalement directionnel du spectre, sur l'angle entre les deux lobes et sur le fait que la bimodalité soit plus ou moins prononcée. Ils influent aussi sur la fréquence à partir de laquelle la bimodalité apparaît et sur la transition dans les hautes fréquences vers un spectre à nouveau unimodal.

Une dépendance des paramètres représentant la bimodalité en fonction de l'âge des vagues n'a pas pu être clairement établie, ni dans le chapitre 3, ni dans le chapitre 5, même si une telle corrélation ne peut pas être totalement écartée.

Dans le cas de fetch oblique, la distribution directionnelle du spectre est fortement asymétrique et la bimodalité n'est plus visible pour certains angles d'incidence du vent. Pour des angles de 10 à 80° par rapport à la normale à la côte (et même jusqu'à 90° lorsqu'on se place à proximité de la côte), la distribution directionnelle du spectre est très asymétrique. La bimodalité est visible pour des angles de 10° et environ jusqu'à 20°, puis pour des angles supérieurs à 60°, avec une forte différence d'amplitude entre les deux lobes. Cet aspect devra être encore être approfondi, par une comparaison avec des mesures à haute précision de spectres directionnels pour différentes incidences (voir notamment Long & Resio, 2007). Ces simulations d'un continuum de directions entre 0 et 90° nous donnent des éléments intéressants pour analyser l'asymétrie des spectres observés dans des conditions proches du cas de fetch limité (Young et al., 1995; Ewans, 1998; Wang & Hwang, 2001). En effet, pour un angle faible de 10° par rapport à la côte, l'asymétrie de la distribution directionnelle des spectres simulés est déjà assez prononcée. Les mesures n'étant jamais réalisées dans des conditions de vent totalement stable et perpendiculaire à la côte (même dans des conditions proches de cas idéaux !), cela peut expliquer l'asymétrie observée dans les spectres issus de mesures *in situ*. La direction du vent est un paramètre très sensible qui doit être attentivement contrôlé lors de campagnes de mesures *in situ*.

La bimodalité basses fréquences (en dessous du pic spectral) est obtenue dans toutes les simulations effectuées pour des cas de durée et fetch limité ainsi que dans les simulations prenant en compte uniquement les transferts non-linéaires. On l'observe pour tous les termes de génération par le vent et de dissipation considérés, avec la méthode GQM, mais aussi la méthode DIA bien que les résultats soient parfois moins prononcés ou plus bruités. L'existence de la bimodalité dans les basses fréquences est encore aujourd'hui sujet à débat, malgré certaines mesures en nature sur lesquelles on peut la constater (Ewans, 1998; Hwang et al., 2000a,b; Wang & Hwang, 2001). En effet, les fréquences en dessous du pic spectral correspondant à des faibles niveaux d'énergie, les mesures sont délicates et manquent souvent de précision. Il est ainsi généralement estimé que cette bimodalité provient d'artéfacts de mesures. Néanmoins, nous pensons qu'ayant à l'appui mesures et simulations, ce sujet mérite discussion. De plus, l'étude des conditions de fetch oblique a montré que la bimodalité n'était pas ou faiblement observée lorsque le vent souffle avec une incidence non nulle par rapport à la côte. Un faible fetch oblique

peut donc diminuer fortement la possibilité d'observer la bimodalité basses fréquences. Les cas idéaux de fetch limité ou durée limitée étant rarement observés, cela pourrait aussi expliquer la difficulté à constater son existence.

- Un autre point qui a retenu notre intérêt au cours de ce travail est l'influence de l'imposition dans les codes de calcul d'une forme spectrale donnée dans les hautes fréquences, appelée communément queue diagnostique. Une queue diagnostique en  $f^{-4}$  ou  $f^{-5}$  est couramment appliquée au-dessus d'une fréquence  $f_d$  (fréquence diagnostique) dans les modèles d'état de mer de troisième génération. Cet artifice permet de pallier les déficiences des formulations utilisées pour les termes  $S_{in}$  et  $S_{diss}$  (WAMDI Group, 1988; Komen et al., 1994), notamment lorsqu'une forte dissipation est appliquée dans les hautes fréquences (cas de la dissipation par moutonnement utilisée dans WAM-Cycle 4), amenant un déséquilibre entre les termes  $S_{in}$  et  $S_{diss}$ . Nous avons pu montrer que cette queue diagnostique avait des conséquences majeures sur la distribution fréquentielle et directionnelle du spectre et notamment la bimodalité, mais également sur l'évolution de paramètres intégrés comme  $H_{m0}$  ou  $f_p$ . L'usage de la queue diagnostique est ainsi à proscrire tant que possible (voir par exemple Banner & Young, 1994; Van der Westhuysen et al., 2007). Lorqu'un bon équilibre entre les termes  $S_{in}$  et  $S_{diss}$  est respecté dans les hautes fréquences, les transferts non-linéaires permettent d'obtenir la queue spectrale en  $f^{-4}$  observée (au moins jusqu'à  $2 - 3f_p$ ) ou obtenue théoriquement par Zakharov & Filonenko (1966), Kahma (1981), Kitaigorodskii (1983), Phillips (1985), Resio et al. (2001), etc.
- L'influence des termes source  $S_{in}$  (Snyder et al., 1981; Yan, 1987; Janssen, 1991) et puits  $S_{diss}$  (Komen et al., 1984, 1994; Van der Westhuysen, 2008) sur les courbes de croissance de l'énergie  $E$  (ou de  $H_{m0}$ ) et de la fréquence de pic en fonction du temps ou du fetch n'a pas été analysée de manière identique dans chaque chapitre. Dans les chapitres 3 et 5, les résultats de simulations avec différents modèles combinés pour un vent de  $10 \text{ m s}^{-1}$  ( $36 \text{ km h}^{-1}$ ) se sont avérés assez proches (sauf lorsqu'on utilise les paramétrisations de WAM-4 sans queue diagnostique!). Seul le cas de fetch oblique a montré des écarts assez significatifs. A l'inverse, dans le chapitre 4, nous avons souligné les grandes disparités entre les simulations obtenues avec deux formulations du terme de génération par le vent  $S_{in}$ , en particulier pour de forts vents ( $20 \text{ à } 30 \text{ m s}^{-1}$ ). Ceci s'explique en partie par le fait qu'une vitesse de  $10 \text{ m s}^{-1}$  est représentative de vitesses couramment mesurées lors de campagnes *in situ*. Les formulations de  $S_{in}$  et  $S_{diss}$  sont donc généralement calibrées pour que les valeurs de  $E$  et  $f_p$  simulées soient proches de ces observations.
- Dans le chapitre 4, l'étude de la modélisation des états de mer a été abordée à l'aide d'une approche originale, qui diffère essentiellement de l'approche 'traditionnelle' basée sur un adimensionnement des paramètres intégrés (énergie et fréquence de pic) par la vitesse du vent  $U_{10}$  (ou  $u_*$ ) (Kitaigorodskii, 1962). Cette approche a été développée récemment par Badulin et al. (2007) et s'appuie sur des résultats de la théorie de la turbulence faible. Elle utilise les flux spectraux d'énergie, de quantité de mouvement et d'action comme échelles physiques du problème et permet une analyse physique qualitative et quantitative approfondie de la croissance de la mer de vent et des caractéristiques des

interactions atmosphère-océan.

Trois stades de développement des vagues ont pu être identifiés à l'aide de cette approche : le stade initial correspondant aux vagues jeunes, le stade de croissance des vagues (ou stade auto-similaire), et la mer pleinement développée. Ils correspondent à différents équilibres des termes de vent, dissipation et transfert non-linéaire vague-vague.

Cette approche s'appuie sur un modèle appelé « split balance », qui sépare l'équation cinétique en deux équations, considérant d'une part, l'évolution du spectre due aux transferts non-linéaires d'énergie vague-vague (équation conservative de Hasselmann), et d'autre part, l'effet des forçages intégrés  $\langle S_{in} + S_{diss} \rangle$  sur l'évolution de l'énergie totale  $E$ . Ce modèle permet de démontrer des propriétés d'auto-similarité asymptotique dans les cas de durée et de fetch limités et fait ressortir certaines caractéristiques du développement des vagues ne dépendant pas du choix particulier des modèles de génération par le vent et de dissipation. La validité de cette approche est démontrée pour le stade de croissance des vagues. Elle se base sur l'hypothèse de prédominance des termes non-linéaires par rapport aux termes de vent et de dissipation qui permet d'obtenir des résultats d'auto-similarité pour le stade de croissance des vagues. Il en résulte un lien de proportionnalité entre les forçages intégrés  $\langle S_{in} + S_{diss} \rangle$  (ou flux d'énergie), la fréquence de pic et l'énergie totale des vagues.

Cette approche a été validée numériquement dans le cas de durée limitée et en se basant sur des données de mesures *in situ* dans le cas de fetch limité dans une précédente étude menée par Badulin et al. (2007). Ici, notre travail a permis de donner une nouvelle justification numérique à cette approche dans le cas de fetch limité par l'analyse d'un grand nombre de simulations pour une large gamme de vitesses de vent ( $5$  à  $30$  m s $^{-1}$ ).

Nos simulations ont montré une très bonne adéquation des résultats obtenus lors du stade de croissance des vagues, quelle que soit la formulation du terme  $S_{in}$ , la méthode de calcul du terme  $S_{nl}$  (DIA et GQM) et la vitesse de vent. Ainsi, la méthode DIA donne également des résultats tout à fait convenables pour ce stade asymptotique, car elle vérifie les propriétés d'homogénéité du terme non-linéaire  $S_{nl}$  et l'auto-similarité du spectre de vagues en découlant.

Le stade de croissance des vagues est étudié en détail. A l'intérieur de ce stade, trois étapes sont à nouveau distinguées et comparées à trois cas de référence correspondant à différents couplages entre l'atmosphère et les vagues (Toba, 1972; Hasselmann et al., 1976; Zakharov & Zaslavsky, 1983b).

Le paramètre d'auto-similarité  $\alpha_{ss}$  est estimé à  $\alpha_{ss} = 0.68 \pm 0.1$ . Cette valeur apparaît tout à fait cohérente avec les précédents résultats de simulation concernant le cas de durée limitée, avec l'estimation donnée par les mesures *in situ* dans le cas de fetch limité ( $\alpha_{ss} = 0.55 \pm 0.25$ ) (Badulin et al., 2007) et avec les récentes expériences en canal à houle de Badulin & Caulliez (2009).

- Dans le chapitre 5, l'analyse des conditions de fetch oblique a montré quelques résultats bien spécifiques. A faible distance de la côte, l'énergie et la fréquence de pic sont fortement impactées par l'incidence oblique du vent. Plus l'angle est important, plus l'énergie augmente et la fréquence de pic diminue (ce qui signifie que l'âge des vagues augmente). Lorsqu'on s'éloigne de la côte, les effets sont moins notables.

Le spectre d'énergie et sa répartition selon les fréquences et directions est lui-aussi largement influencé par l'incidence du vent. A faible distance de la côte, le spectre fréquentiel est plus étalé, en particulier pour des directions de vent de 30-40°. Au-dessus de 50° d'incidence, la direction du vent se rapproche de la direction de la côte et l'on tend vers un cas de fetch illimité. Le spectre redevient alors plus étroit et pointu. Dans les basses fréquences, la direction des vagues est fortement influencée par la proximité de la côte. Les vagues sont déviées et la direction du pic spectral avoisine celle de la côte. Les vagues de plus haute fréquence ont une direction proche de celle du vent.

Les écarts entre les résultats obtenus à l'aide des différents modèles de génération par le vent et de dissipation semblent nettement plus importants lorsque le vent est oblique (par rapport à un vent normal à la côte). Comme nous l'avons dit précédemment, la direction du vent doit être contrôlée avec vigilance, notamment lors de mesures *in situ*.

## Perspectives de prolongement et d'exploitation des travaux de recherche

Les travaux de cette thèse peuvent trouver des applications ou des prolongements dans plusieurs directions. On donne ci-après quelques éléments sur ces perspectives futures.

### 1 Optimisation de l'algorithme GQM

Des améliorations du temps de calcul de la méthode GQM peuvent encore être proposées. Deux axes ont été identifiés. Nous souhaiterions tout d'abord travailler sur l'optimisation de la troisième intégration (sur  $\omega_1$ ), qui n'est pas effectuée par quadrature de Gauss mais par une simple intégration par la méthode des trapèzes. Nous pensons aussi qu'il serait utile de perfectionner le filtrage des configurations qui ont une faible contribution au calcul global du terme  $S_{nl}$ , en optimisant la méthode ou le niveau de filtrage (seuils choisis, nombre de configurations éliminées, etc.).

### 2 Implémentation de la méthode GQM dans un modèle de troisième génération et tests en deux dimensions d'espace (2DH).

Les développements seront implémentés dans le code TOMAWAC pour une validation finale. La nouvelle version comprendra la méthode GQM, mais aussi les termes de génération par le vent de Yan (1987) et de dissipation de Van der Westhuysen et al. (2007); Van der Westhuysen (2008). La possibilité d'utiliser un pas de temps dynamique sera également ajoutée. Les résultats des cas tests en 2DH devront être comparés à des mesures. Les données de la campagne SHOWEX (Ardhuin

et al., 2007) nous paraissent tout à fait adaptées à ce type de validation, car elles ont l'avantage de pouvoir être modélisées en conservant l'hypothèse de profondeur infinie.

### 3 Extensions des résultats du chapitre 4

Nous pensons qu'il existe de nombreuses perspectives d'extension et d'amélioration des résultats du chapitre 4. Tout d'abord, les résultats doivent être confirmés en utilisant d'autres termes de dissipation. Nous pourrions commencer par valider cette approche en utilisant la combinaison II (cf. chapitres 3 et 5) des modèles de Yan (1987) et Van der Westhuysen et al. (2007), puis implémenter de nouveaux modèles de dissipation (voir notamment Zakharov et al., 2007; Korotkevich et al., 2008; Ardhuin et al., 2008, 2009). Nous pensons que les résultats principaux concernant le stade auto-similaire (stade de croissance des vagues) ne seront pas affectés par les nouvelles formulations du terme  $S_{diss}$ . Néanmoins, il se pourrait que le terme de dissipation influe fortement sur le stade de mer pleinement développée.

La distribution fréquentielle et directionnelle du spectre devra être étudiée en détail avec cette nouvelle approche. Il serait intéressant de regarder les propriétés du spectre directionnel à chaque étape de développement des vagues. En effet, dans le chapitre 4, seuls les paramètres intégrés ont été analysés. Les propriétés d'auto-similarité obtenues dans les cas de durée et de fetch limités pour les paramètres intégraux ne sont pas applicables de façon immédiate à la distribution du spectre d'énergie suivant les fréquences et les directions (voir §6.1.2 de Badulin et al., 2005). En particulier, l'impact de la distribution fréquentielle et directionnelle du spectre sur le forçage total devra être observée attentivement.

Une autre idée que nous aimerais creuser serait d'utiliser la méthode GQM pour tester plus avant le modèle de « split balance », en étudiant l'évolution d'un spectre sous l'action séparée du forçage intégré  $\langle S_{in} + S_{diss} \rangle$  et des interactions non-linéaires (terme  $S_{nl}$ ). Le forçage total  $\langle S_{in} + S_{diss} \rangle$  serait appliqué au spectre avec une répartition quelconque en début de pas de temps. On regarderait ensuite comment les interactions non-linéaires transfèrent l'énergie pour donner à nouveau au spectre une forme auto-similaire. Ce test nous permettrait de vérifier que l'influence de la répartition en  $(f, \theta)$  du forçage intégral sur le spectre est faible et a notamment peu d'effet sur les courbes de croissance de l'énergie et de la fréquence de pic.

### 4 Interaction houle - mer de vent et stabilité des états de mer complexes (multipics)

Pour compléter l'étude des conditions de fetch limité et de fetch oblique effectuée au chapitre 5, nous voudrions traiter des cas où une houle est présente. Pour cela, nous pourrions à nouveau nous appuyer sur des comparaisons avec les mesures de la campagne SHOWEX. Il serait intéressant de quantifier l'influence de différents paramètres sur l'interaction entre la houle et la mer de vent, en prolongement des travaux de Masson (1993) : angle entre les directions de la houle et du vent (ou la direction moyenne de la mer du vent), ratio des fréquences de pic et des hauteurs significatives de la houle et de la mer du vent.

**5 Extension de la méthode GQM au cas de la profondeur finie**

Pour le moment, la méthode GQM ne peut être appliquée qu'à des situations en grande profondeur d'eau. La méthode devra donc être étendue au cas de la profondeur finie. Cette extension n'est pas immédiate. En effet, la relation de dispersion est compliquée par l'introduction de la profondeur. Les développements exposés dans le chapitre 2, nous permettant d'obtenir une forme adaptée à l'intégration par quadrature de Gauss, dépendent fortement de la relation de dispersion et doivent donc être revus. On pourra entre autre s'inspirer des travaux de Polnikov (1997) qui utilise une expression approchée explicite de la relation de dispersion.

**6 Comparaison des équations de Hasselmann (1962) et de Zakharov (1968)**

Pour finir, nous pensons qu'il pourrait être intéressant d'effectuer une comparaison entre les résultats donnés par l'équation de Hasselmann (1962) (interactions résonnantes, équation 1.64), calculée avec la méthode GQM, et ceux obtenus en utilisant l'équation de Zakharov (1968) (qui n'a pas été abordée dans la thèse), dans laquelle les interactions non-résonnantes sont aussi incluses. Cela nous permettrait de quantifier les importances relatives des interactions résonnantes et non-résonnantes dans différents cas.

# Annexe A : supplement to chapter 5

This annexe is dedicated to figures corresponding to Chapter 5 that were not considered essential but may nevertheless provide some clarification.

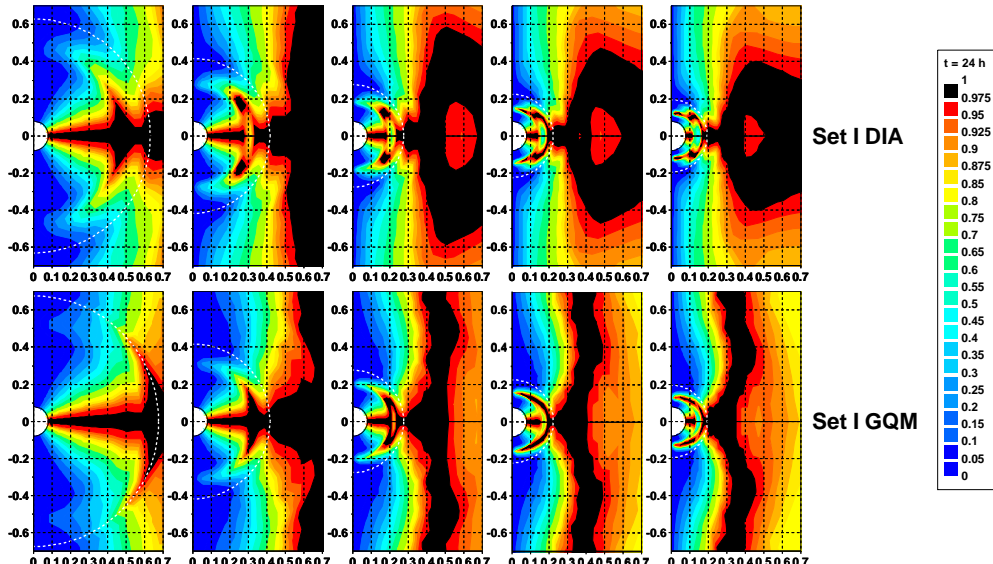


FIGURE 5.22 – Angular distribution normalized by the maximum value at each frequency for different fetches (1 km, 5 km, 20 km, 50 km, 100 km). DIA and GQM methods. Set I. Polar coordinates. The dotted white circle indicates the peak frequency  $f_p$ .

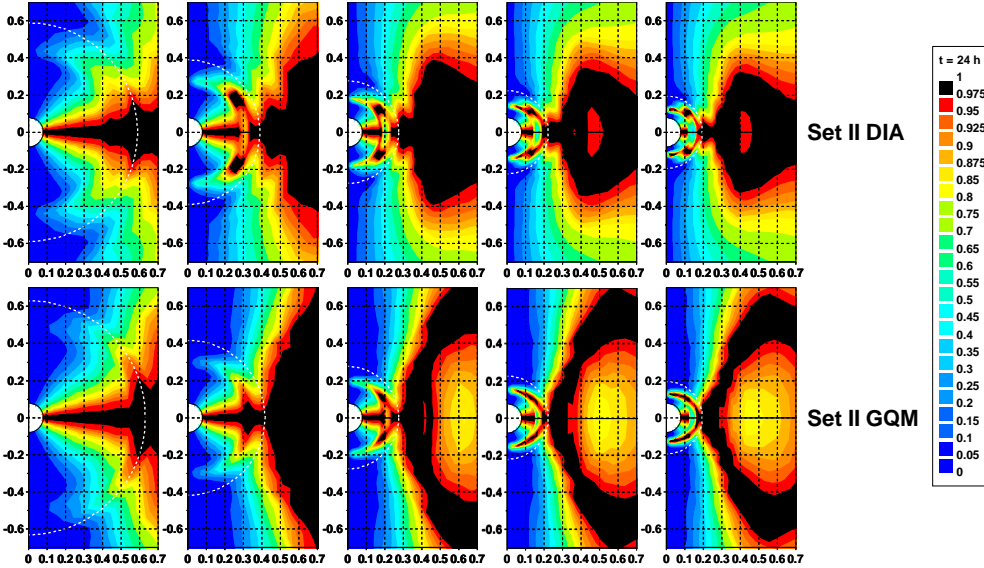


FIGURE 5.23 – Angular distribution normalized by the maximum value at each frequency for different fetches (1 km, 5 km, 20 km, 50 km, 100 km). DIA and GQM methods. Set II. Polar coordinates. The dotted white circle indicates the peak frequency  $f_p$ .

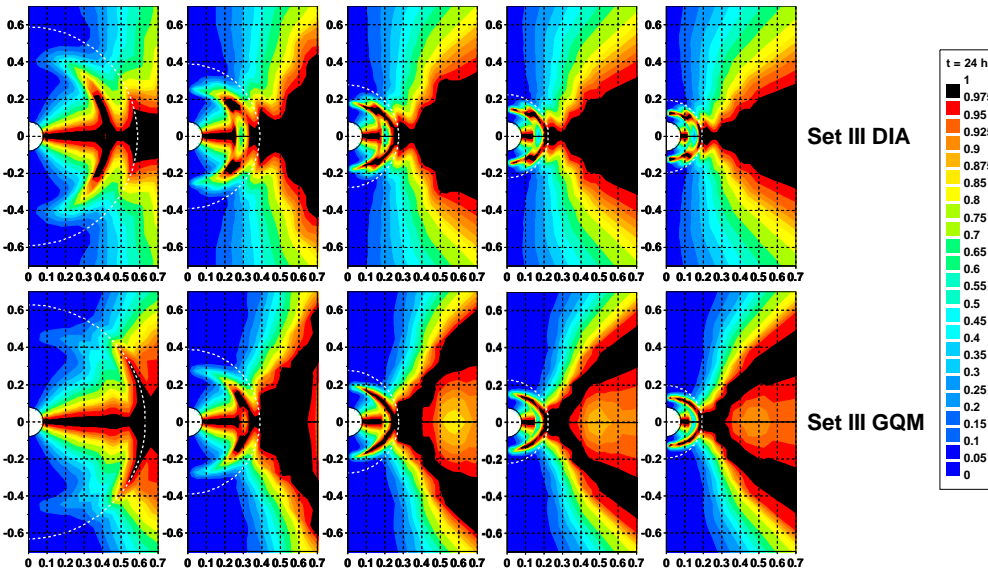


FIGURE 5.24 – Angular distribution normalized by the maximum value at each frequency for different fetches (1 km, 5 km, 20 km, 50 km, 100 km). DIA and GQM methods. Set III. Polar coordinates. The dotted white circle indicates the peak frequency  $f_p$ .

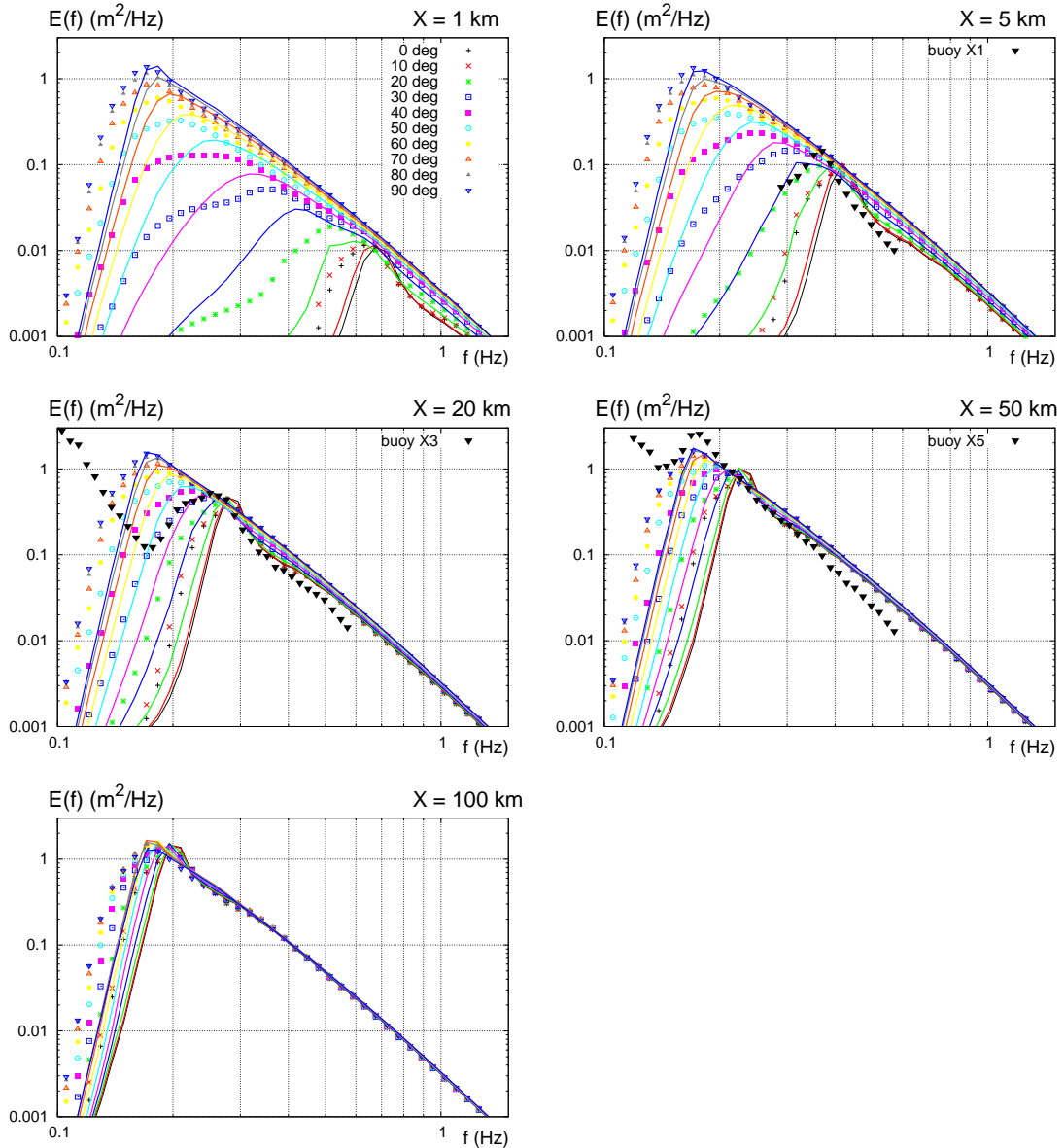


FIGURE 5.25 – 1D-spectra for different distances from the coast (1 km, 5 km, 20 km, 50 km and 100 km) and different oblique wind directions (from  $0^\circ$  to  $90^\circ$ ). Set I. GQM (solid lines) and DIA (points) methods. Some of the SHOWEX measurements are plotted for comparison with  $\theta = 20^\circ$  results (green curve) : buoys X1, X3 and X5 on 3 November 1999 (average over time period 12-17h EST).

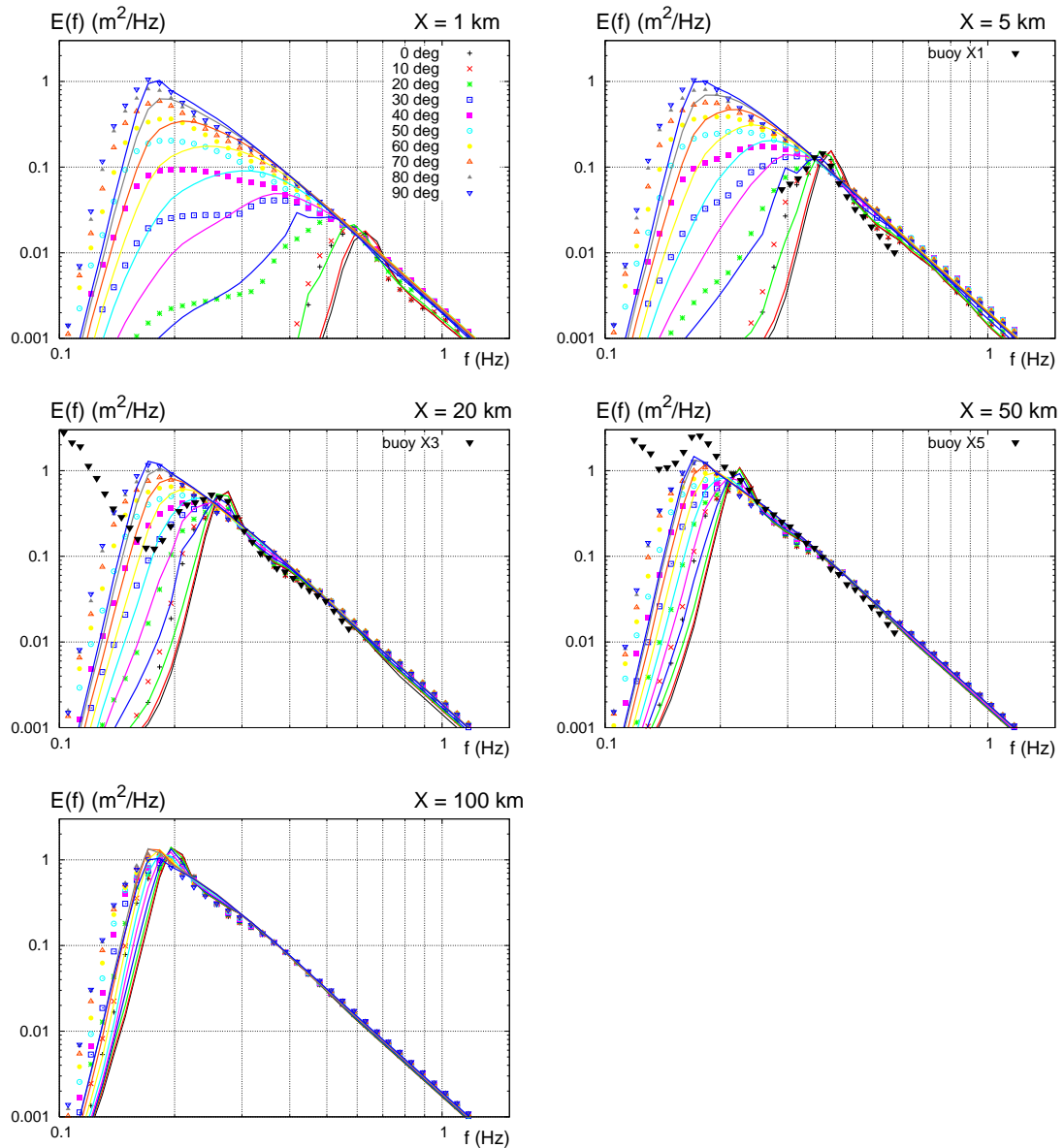


FIGURE 5.26 – 1D-spectra for different distances from the coast (1 km, 5 km, 20 km, 50 km and 100 km) and different oblique wind directions (from  $0^\circ$  to  $90^\circ$ ). Set III. GQM (solid lines) and DIA (points) methods. Some of the SHOWEX measurements are plotted for comparison with  $\theta = 20^\circ$  results (green curve) : buoys X1, X3 and X5 on 3 November 1999 (average over time period 12-17h EST).

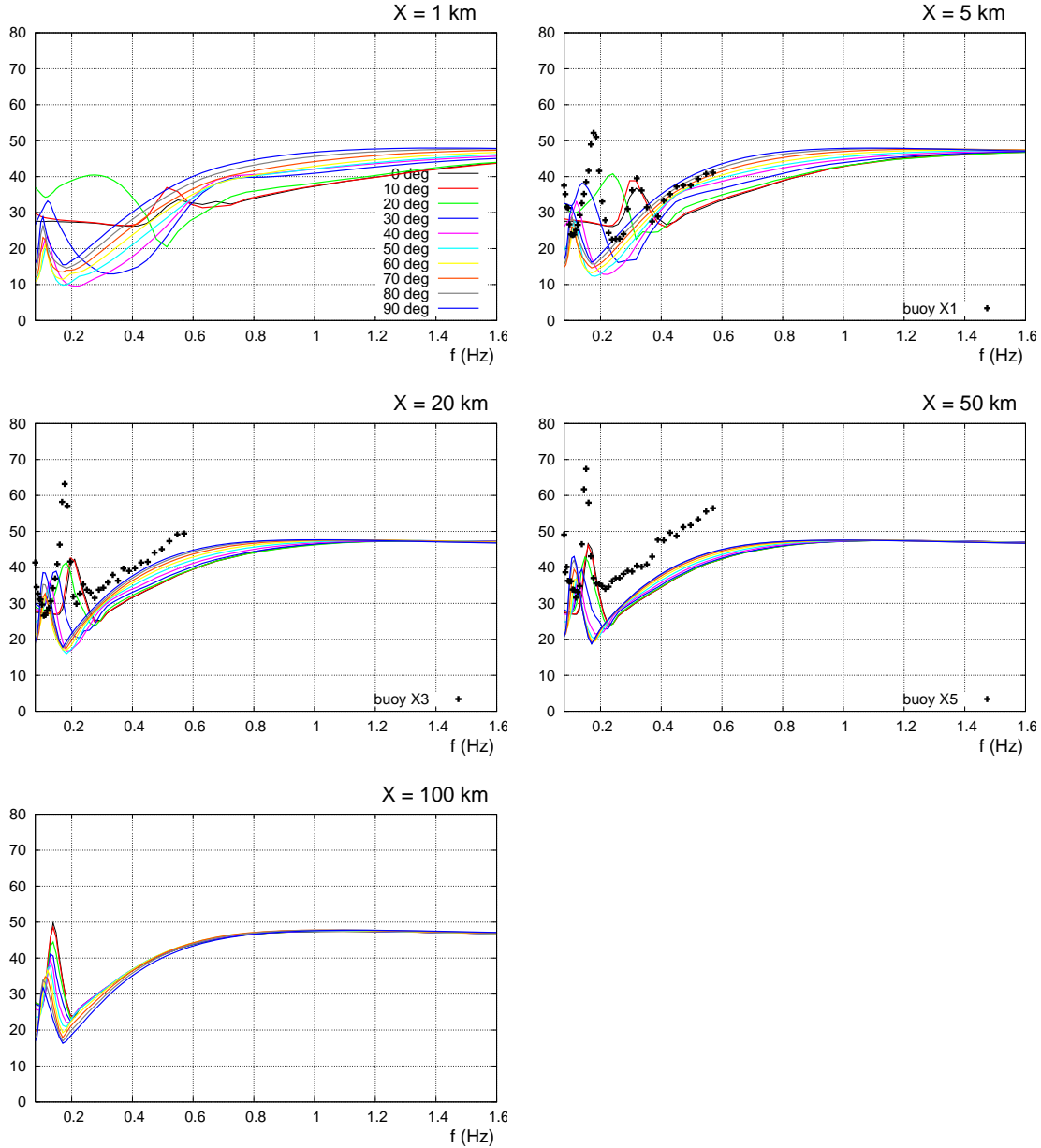


FIGURE 5.27 – Frequency-dependent directional spreading  $\sigma(f)$  for different distances from the coast (1 km, 5 km, 20 km, 50 km and 100 km) and different oblique wind directions (from  $0^\circ$  to  $90^\circ$ ). Set I. GQM method. Some of the SHOWEX measurements are plotted for comparison with  $\theta = 20^\circ$  results (green curve) : buoys X1, X3 and X5 on 3 November 1999 (average over time period 12-17h EST).

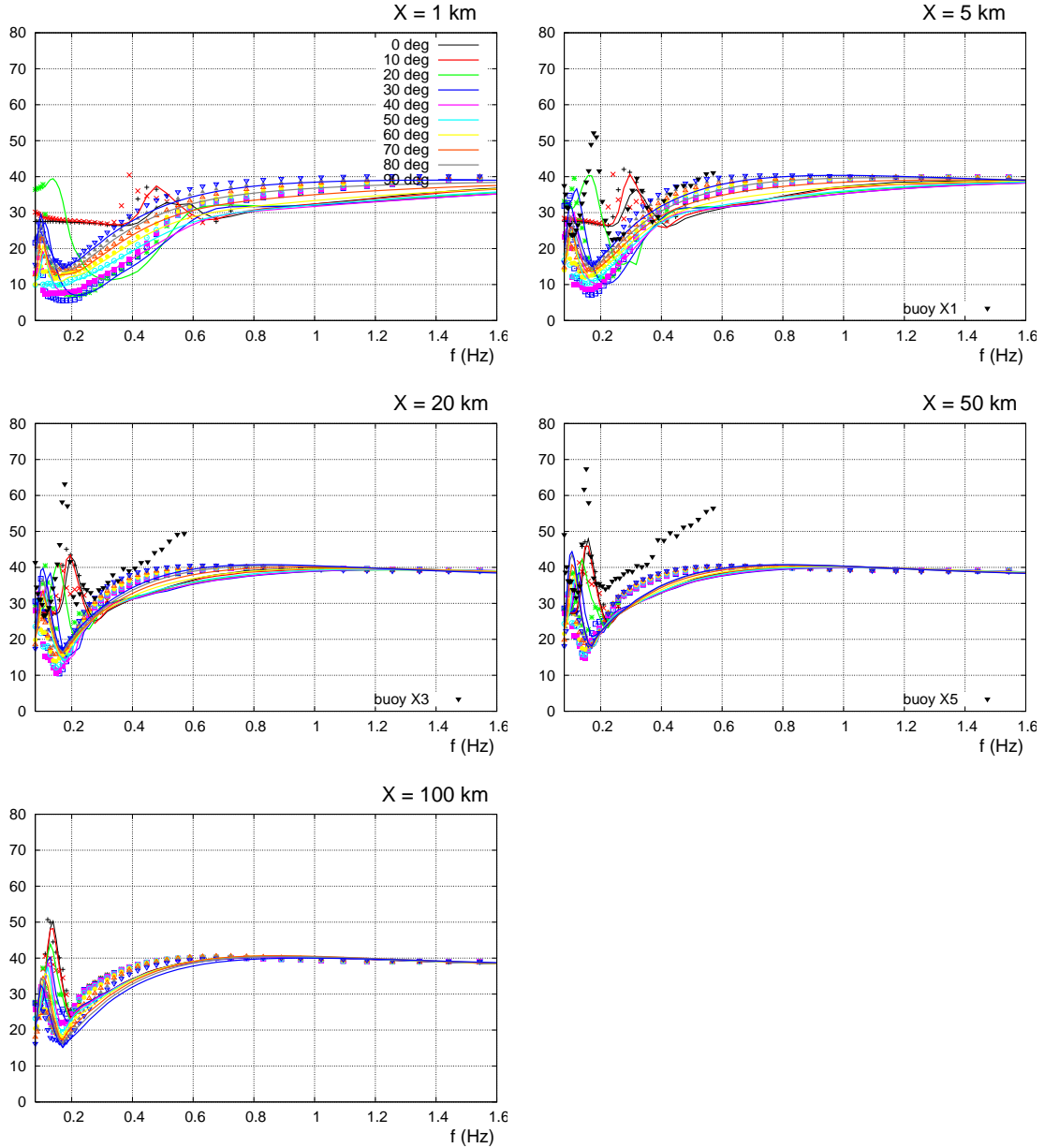


FIGURE 5.28 – Frequency-dependent directional spreading  $\sigma(f)$  for different distances from the coast (1 km, 5 km, 20 km, 50 km and 100 km) and different oblique wind directions (from  $0^\circ$  to  $90^\circ$ ). Set II. DIA (points) and GQM (solid lines) methods. Some of the SHO-WEX measurements are plotted for comparison with  $\theta = 20^\circ$  results (green curve) : buoys X1, X3 and X5 on 3 November 1999 (average over time period 12-17h EST).

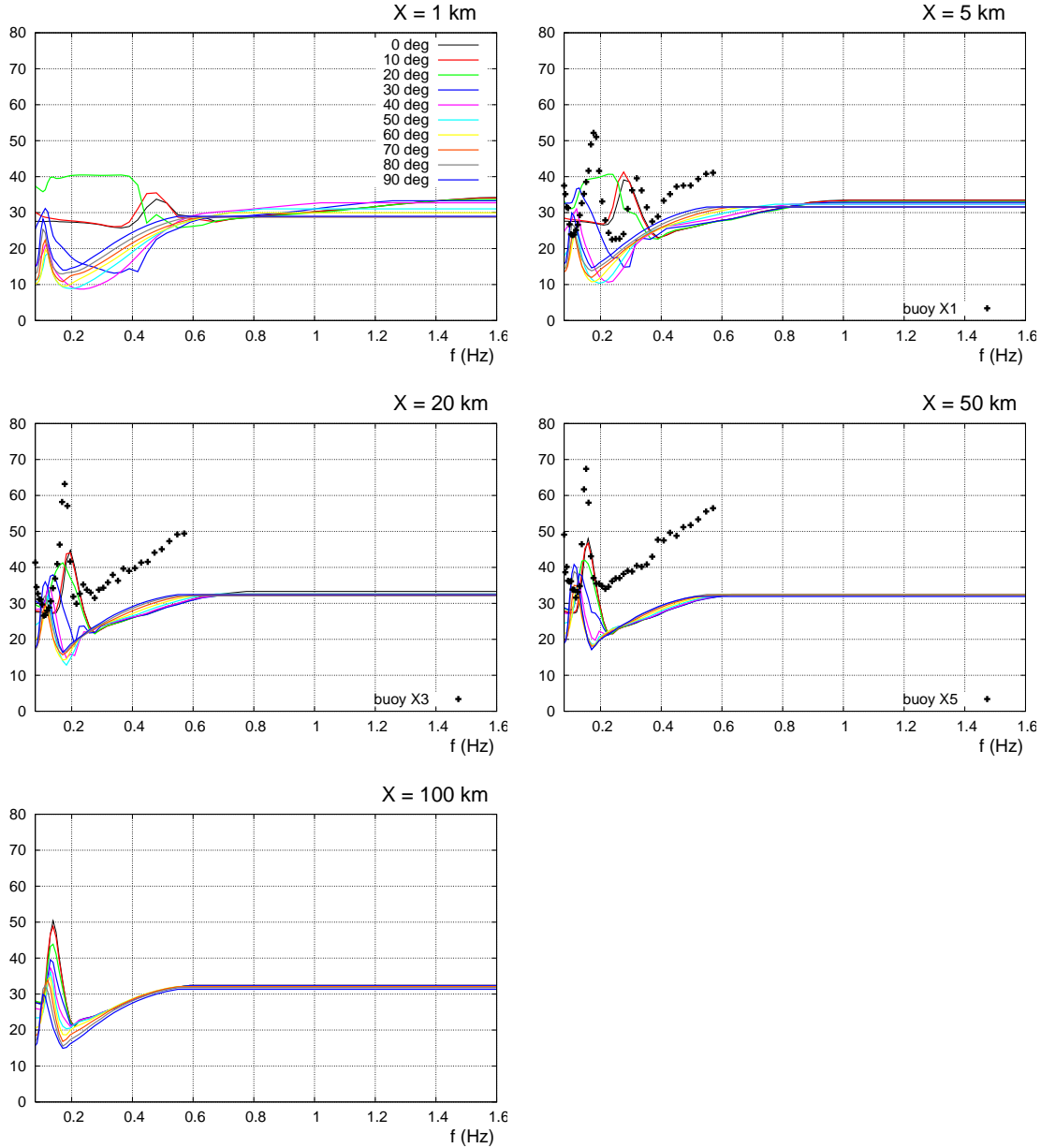


FIGURE 5.29 – Frequency-dependent directional spreading  $\sigma(f)$  for different distances from the coast (1 km, 5 km, 20 km, 50 km and 100 km) and different oblique wind directions (from  $0^\circ$  to  $90^\circ$ ). Set III. GQM method. Some of the SHOWEX measurements are plotted for comparison with  $\theta = 20^\circ$  results (green curve) : buoys X1, X3 and X5 on 3 November 1999 (average over time period 12-17h EST).

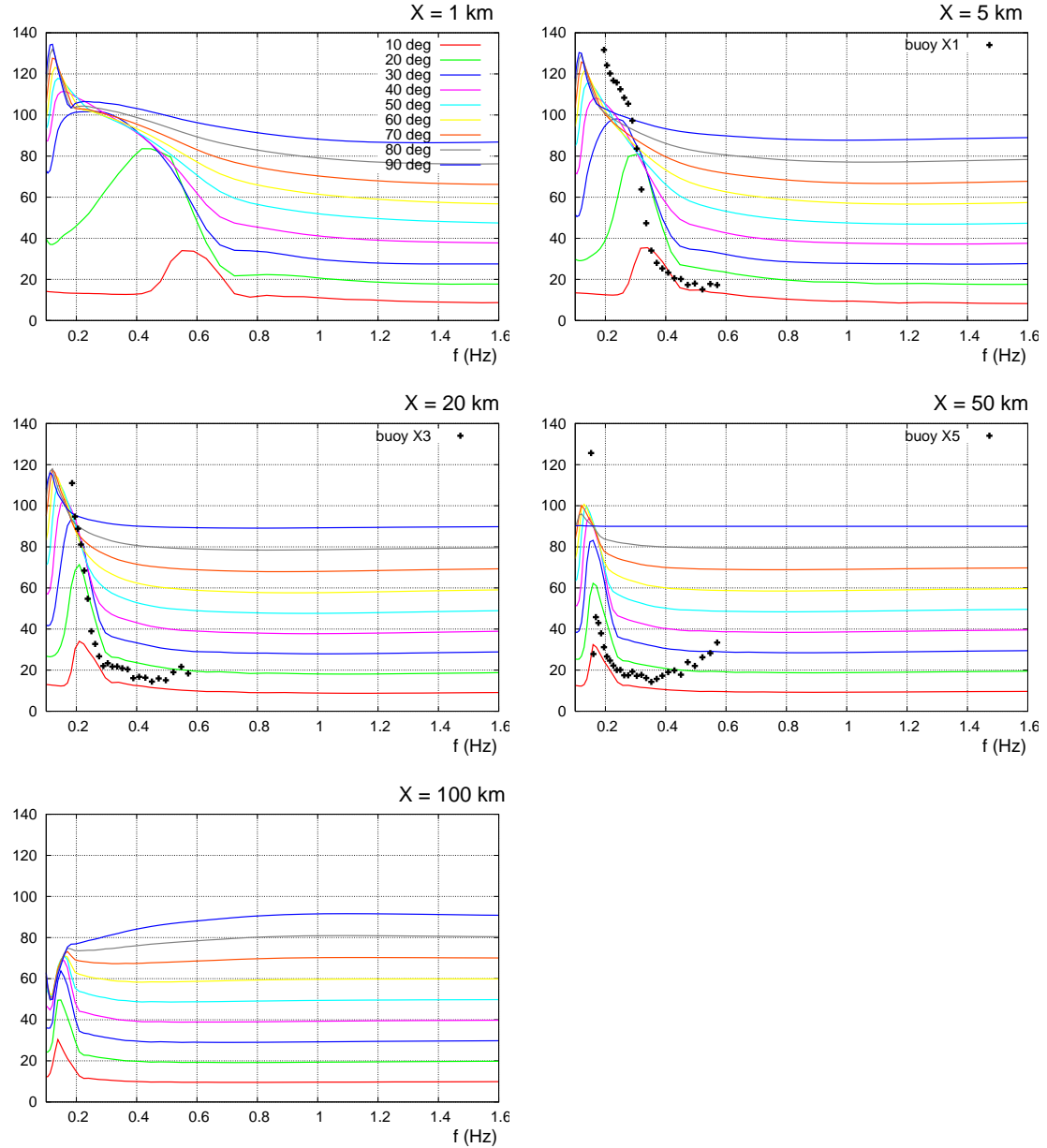


FIGURE 5.30 – Mean wave direction  $\theta_m(f)$  for different distances from the coast (1 km, 5 km, 20 km, 50 km and 100 km) and different oblique wind directions (from  $0^\circ$  to  $90^\circ$ ). Set I. GQM method. Some of the SHOWEX measurements are plotted for comparison with  $\theta = 20^\circ$  results (green curve) : buoys X1, X3 and X5 on 3 November 1999 (average over time period 12-17h EST).

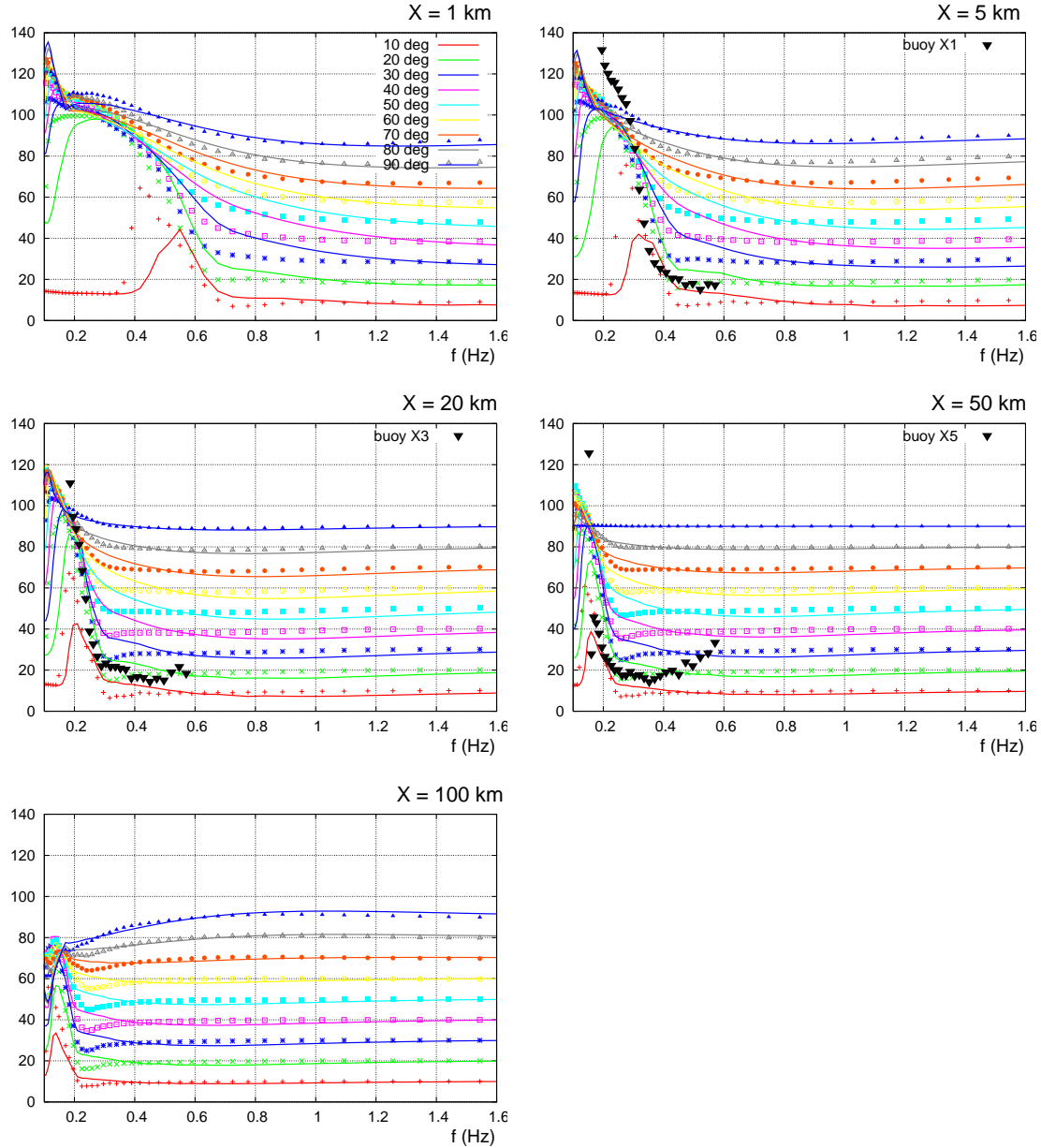


FIGURE 5.31 – Mean wave direction  $\theta_m(f)$  for different distances from the coast (1 km, 5 km, 20 km, 50 km and 100 km) and different oblique wind directions (from  $0^\circ$  to  $90^\circ$ ). Set II. GQM and DIA methods. Some of the SHOWEX measurements are plotted for comparison with  $\theta = 20^\circ$  results (green curve) : buoys X1, X3 and X5 on 3 November 1999 (average over time period 12-17h EST).

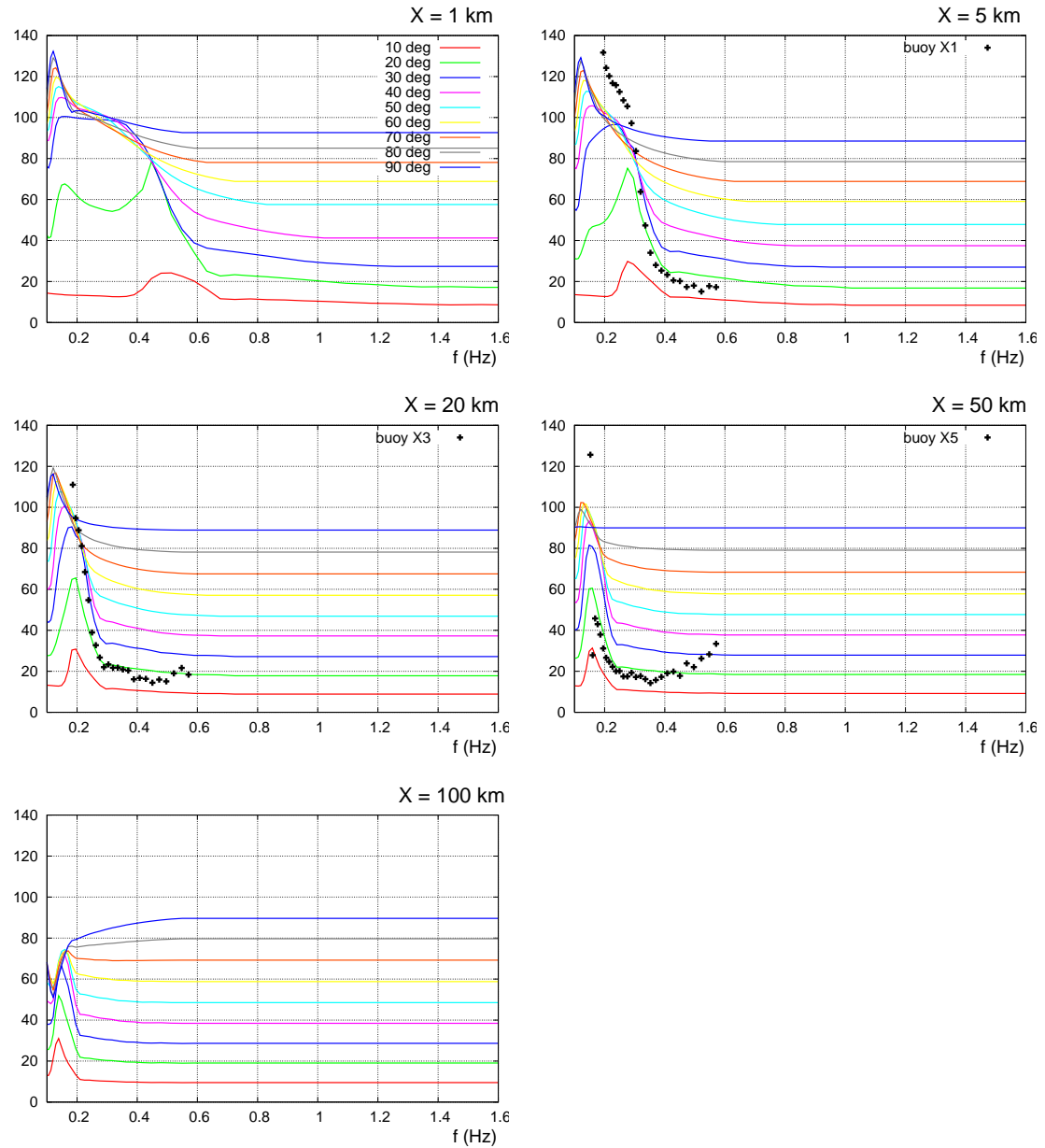


FIGURE 5.32 – Mean wave direction  $\theta_m(f)$  for different distances from the coast (1 km, 5 km, 20 km, 50 km and 100 km) and different oblique wind directions (from  $0^\circ$  to  $90^\circ$ ). Set III. GQM method. Some of the SHOWEX measurements are plotted for comparison with  $\theta = 20^\circ$  results (green curve) : buoys X1, X3 and X5 on 3 November 1999 (average over time period 12-17h EST).

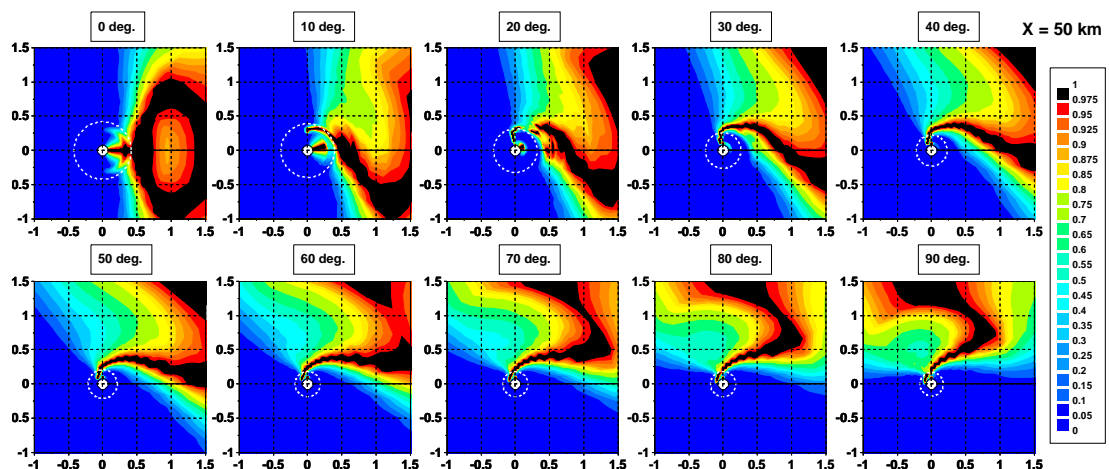


FIGURE 5.33 – Angular distribution normalized by the maximum value at each frequency  $D(f, \theta)/D_{max}(f)$  for  $X = 5$  km. Set II. GQM method. The white dotted circles indicate the peak frequency  $f = f_p$ .



# Annexe B : Valorisation et publications issues des travaux de thèse

## Articles de revues scientifiques

Gagnaïre-Renou E., Benoit M., Badulin S. (2010) On weakly turbulent scaling of wind sea in simulations of fetch-limited growth. *Manuscrit soumis à Journal of Fluid Mechanics le 30/09/2009, demande de révisions le 18/01/2010*, réf. JFM-09-S-0809.

Gagnaïre-Renou E., Benoit M., Forget Ph. (2010) Ocean wave spectrum properties as derived from quasi-exact computations of nonlinear wave-wave interactions. *Journal of Geophysical Research - C (Oceans)*, doi :10.1029/2009JC005665, *in press*.

## Articles de conférences internationales avec comité de lecture et actes

Gagnaïre-Renou E., Benoit M., Forget P. (2008) Modeling waves in fetch-limited and slanting fetch conditions using a quasi-exact method for nonlinear four-wave interactions. *Proc. 31st Int. Conf. on Coastal Eng. (ICCE'2008)*, 1-5 Septembre 2008, Hambourg (Allemagne), 496-508

Benoit M., Gagnaïre-Renou E. (2007) Interactions vague-vague non-linéaires et spectre d'équilibre pour les vagues de gravité en grande profondeur d'eau. *Actes du 18ième Congrès Français de Mécanique 2007 - Session S19 "Ondes et écoulements à surface libre"*, 27-31 Août 2007, Grenoble (France).

## **Communications dans des colloques et séminaires internationaux (sans actes)**

Gagnaire-Renou E., Benoit M., Badulin S. (2009) On weakly turbulent scaling of wind sea in simulations of fetch-limited growth. *Annual WISE meeting (Waves In Shallow-water Environments)*, 27-30 April 2009, Ensenada (Mexico).

Gagnaire-Renou E., Benoit M., Forget P. (2008) Analysis of the structure of ocean wave directional spectrum from quasi-exact computations of nonlinear wave-wave interactions. *Annual WISE meeting (Waves In Shallow-water Environments)*, 2-5 June 2008, Helsinki (Finland).

Gagnaire-Renou E., Benoit M., Forget P. (2007) Etude du rôle des interactions non-linéaires dans l'évolution d'un spectre d'états de mer en conditions instationnaires. *Séminaire "Hydrodynamique et Océano-Météorologie" du CLAROM*, 29 Novembre 2007, Bougival (France).

Gagnaire-Renou E., Abonnel C., Benoit M., Buvat C. (2007) Mesure et caractérisation des conditions de courants et de vagues dans le Raz de Barfleur (Manche) pour mieux apprécier la ressource en énergie hydraulienne. *Journées OCOSS'2007*, 26-27 Juin 2007, Paris (France).

Gagnaire-Renou E., Benoit M., Buvat C., Abonnel C. (2006) Some lessons from tidal current and wave measurements at sea. Feedback of experience and analysis of measurements. *Concerted Action on Ocean Energy (CA-OE), Workshop WS4*, 16-17 November 2006, Lisbon (Portugal).

# Table des figures

2.1	Integration bounds of $w_2$ versus $\varepsilon_a$ . . . . .	43
2.2	Factor $1/\sqrt{\tilde{B}_0(\varepsilon_a, w_2)\tilde{B}_1(\varepsilon_a, w_2)\tilde{B}_2(\varepsilon_a, w_2)}$ versus $w_2 = \omega_2/\omega_a$ for three values of $\varepsilon_a : 0.8, 1, 1.2$ . . . . .	44
2.3	Nonlinear transfer term $S_{nl}$ computed using the GQM method (rough, medium and fine resolutions) and applied to a JONSWAP-type spectrum with usual features ( $f_p = 1$ Hz, $\sigma = 0.07$ if $f \leq f_p$ , $\sigma = 0.09$ if $f > f_p$ , $\gamma = 3.0$ ) combined with a $\cos^6(\theta/2)$ directional distribution. . . . .	50
2.4	Variance frequency spectrum $E(f)$ at six times (5 s, 1 min, 15 min, 2 h, 16 h, 128 h) computed with the rough, medium and fine resolutions of the GQM method. . . . .	51
2.5	Directional spectrum $F(f, \theta)$ at $t = 128$ h computed with the GQM method, resolution a) fine, b) medium, and c) rough. . . . .	51
2.6	Nonlinear transfer term $S_{nl}$ computed with the GQM method (rough, medium and fine resolutions) with and without filtering. . . . .	53
2.7	Nonlinear transfer term $S_{nl}$ computed using DIA, MDIA, and GQM (fine resolution) and applied to a JONSWAP-type spectrum with usual features ( $f_p = 1$ Hz, $\sigma = 0.07$ if $f \leq f_p$ , $\sigma = 0.09$ if $f > f_p$ , $\gamma = 3.0$ ) combined with a $\cos^6(\theta/2)$ directional distribution function. . . . .	54
2.8	Variance frequency spectrum $E(f)$ at six times (5 s, 1 min, 15 min, 2 h, 16 h, 128 h) computed with the methods DIA, MDIA, and GQM (medium resolution). . . . .	55
2.9	Directional spectrum $F(f, \theta)$ at $t = 128$ h computed with the methods a) DIA, b) MDIA, and c) GQM (medium resolution). . . . .	56
3.1	Angular integrated nonlinear transfer terms $S_{nl}(f)$ computed with various methods : EXACT-NL, DIA, GQM-fine, GQM-rough for the spectrum of case 3 of Hasselmann & Hasselmann (1981). The frequency spectrum $E(f)$ is superimposed. . . . .	65

3.2 Initial conditions : a) three different frequency spectra : step, Gaussian and Jonswap combined with b) three different distribution $D(\theta)$ : half-plane, broad and narrow cardioids. . . . .	68
3.3 Time evolution of $H_{m0}/H_{m0,init}$ . GQM method : eight test-cases. DIA : Case C3.b. Comparison to the law in $t^{-1/22}$ (Badulin et al., 2005). . . . .	69
3.4 Time evolution of the peak period of the wave spectrum $T_p$ . GQM method : eight test-cases. DIA : Case C3.b. Comparison to the law in $t^{1/11}$ (Badulin et al., 2005). . . . .	70
3.5 Time evolution of the wave spectrum mean angular width $\sigma$ . GQM method : eight test-cases. DIA : Case C3.b. . . . .	71
3.6 Evolution of the frequency spectrum $E(f)$ (from 0 to 128 h), using the GQM method. Initial case C1.b. a) Short term evolution (from 0 to 15 min). b) Long term evolution (from 30 min to 128 h). . . . .	72
3.7 Variation of the shape function $U_\beta(y, \theta = 180^\circ)$ with $y$ (equation 3.8), as computed using the GQM method between $t = 2$ h and $t = 128$ h. Initial spectrum C3.b. . . . .	73
3.8 Time evolution of the frequency spectrum, using the DIA method. Initial case C1.b. a) Short term evolution (from 0 to 15 min). b) Long term evolution (from 30 min to 128 h). . . . .	74
3.9 Variation of the shape function $U_\beta(y, \theta = 180^\circ)$ with $y$ (equation 3.8), as computed using DIA between $t = 2$ h and $t = 128$ h. Initial spectrum C3.b. . . . .	74
3.10 Normalized directional spreading function $\tilde{D}(f/f_p, \theta)$ at $t = 128$ h. Case C2.b. a) GQM method. b) DIA method. . . . .	75
3.11 Nonlinear transfer term $S_{nl}$ calculated by the GQM method at $t = 0.01$ s (first time step) for case C3.b. a) $S_{nl}(f, \theta)$ in polar coordinates, b) $S_{nl}(f/f_p, \theta)/ Q_{nl4,max}(f/f_p) $ in Cartesian coordinates. . . . .	76
3.12 Angle between the lobes of the wave directional distribution, $2\theta_l$ , versus $f/f_p$ at $t = 128$ h for the eight simulated cases. GQM method. . . . .	77
3.13 Sections of the directional spreading function $D(f, \theta)$ at $t = 128$ h, at six frequencies ( $f = 0.7f_p$ , $f = f_p$ , $f = 1.5f_p$ , $f = 2f_p$ , $f = 3f_p$ and $f = 5f_p$ ) for case C3.b. GQM (solid lines) and DIA (dashed lines) methods. . . . .	78
3.14 Time evolution of the wave height $H_{m0}$ , the peak period $T_p$ and the mean angular width $\sigma$ for the 4 initial cases. Set II, GQM and DIA methods, linear scale (left column), logarithmic scale (right column). . . . .	80
3.15 Time evolution of the wave height $H_{m0}$ , the peak period $T_p$ and the mean angular width $\sigma$ . Initial case C3.a, GQM and DIA methods. Comparison of sets I, II, III-ft and III-it. . . . .	81

3.16 Evolution of the frequency spectrum $E(f)$ (from 0 to 96 h). Initial case C1.a. a), c), e), g) : GQM method with sets I, II, III-ft and III-it, respectively. b), d), f), h) : DIA method with sets I, II, III-ft and III-it, respectively. . . . .	83
3.17 Influence of the HF tail on the evolution of the spectrum : effect of the dissipation term $S_{diss}$ . a) The frequency spectrum $E(f)$ simulated with set III-ft and GQM at $t = 6$ h is considered (dotted line). A $f^{-4}$ tail is applied to this spectrum (solid line). b) $S_{in}$ (Janssen, 1989, 1991) and $S_{diss}$ (Komen et al., 1984; Günther et al., 1992) are calculated from both spectra. c) $S_{in} + S_{diss}$ . d) $S_{nl}$ (GQM method). e) Relative nonlinear transfer term $S_{nl}/E(f)$ . f) Total source term $S_{in} + S_{diss} + S_{nl}$ . . . . .	85
3.18 Normalized directional spreading function $\tilde{D}(f/f_p, \theta)$ at $t = 96$ h. Initial case C2.a. a), b), c), d) : GQM method with source terms I, II, III-ft and III-it, respectively. e), f), g), h) : DIA method with source terms I, II, III-ft and III-it, respectively. . . . .	87
3.19 The parameter $s$ of the cardioid model for the directional distribution as a function of $f/f_p$ at $t = 96$ h. GQM method, sets I, II and III-ft and III-it, initial case C2.a. Comparison with Mitsuyasu et al. (1975) and Hasselmann et al. (1980) . . . . .	90
3.20 Normalized directional spreading function $\tilde{D}(f/f_p, \theta)$ at $t = 96$ h. a) GQM method, source terms II, initial case C2.a. b) $A \cos^{2s}((\theta - \theta_0)/2)$ . c) Ewans (1998) model. d) Hwang et al. (2000b) (FFT, 9 terms). . . . .	91
3.21 a) Angle between the lobes and the main direction $-\theta_l, \theta_l$ , b) Lobe ratio $r_{lobe}$ versus $f/f_p$ at $t = 96$ h. Initial case C2.a, GQM method, source terms I, I and III-ft and III-it. Comparison with Hwang et al. (2000a,b) (measurements with an airborne scanning lidar system, Fourier decomposition with 9 components $D_{k,FFT9}$ and polynomial fitting not degraded (see Fig.10 and Table 2 of their paper)) and the Ewans (1998) parameterization. . . . .	93
3.22 Lobe ratio $r_{lobe}$ versus inverse wave age $U_{10}/C_p$ for $f = 2.5f_p$ . Initial case C2.a, GQM method, source terms I, II and III-ft and III-it. . . . .	94
4.1 Non-dimensional growth rate $S_{in}(f)/(fE(f))$ as function of the inverse wave age $\omega U_{10}/g$ for parameterizations of the input term $S_{in}$ by Snyder et al. (1981) and Janssen (1989, 1991). Wind speed $U_{10} = 10 \text{ m s}^{-1}$ . . . . .	107
4.2 Nonlinear transfer term $S_{nl}$ computed with a) the method DIA, MDIA, and GQM (fine resolution), and b) the GQM method (rough, medium and fine resolutions) . . . . .	110
4.3 Non-dimensional energy $\tilde{E} = Eg^2/U_{10}^4$ as function of non-dimensional fetch $\chi = Xg/U_{10}^2$ , for different wind speeds $U_{10} = 5, 10, 20, 30 \text{ m s}^{-1}$ , parameterizations of wave input term $S_{in}$ by Snyder et al. (1981) and Janssen (1989, 1991), DIA and GQM methods for calculating $S_{nl}$ (shown in legends). ‘The cleanest’ experimental dependencies of Table 4.2 are given for comparison. . . . .	120

4.4 Inverse wave age $\tilde{\omega}_p = \omega_p U_{10}/g$ as function of non-dimensional fetch $\chi = Xg/U_{10}^2$ , for different wind speeds $U_{10} = 5, 10, 20, 30 \text{ m s}^{-1}$ , parameterizations of wave input term $S_{in}$ by Snyder et al. (1981) and Janssen (1989, 1991), DIA and GQM methods for calculating $S_{nl}$ (see legends). ‘The cleanest’ experimental dependencies of Table 4.2 are given for comparison. . . . .	121
4.5 Non-dimensional energy $\tilde{E}$ vs non-dimensional peak frequency $\tilde{\omega}_p$ . Straight lines – ‘the cleanest’ experimental dependencies, Toba’s 3/2 law for the reference case $dE/dt = \text{const}$ , the Hasselmann et al. (1976) 5/3 law for $\omega_p dE/dt = \text{const}$ and the Zakharov & Zaslavsky (1983b) 4/3 law for the case $\omega_p^{-1} dE/dt = \text{const}$ . . . . .	122
4.6 a) – Net wave forcing $\langle S_{in} + S_{diss} \rangle$ as function of the dimensional fetch $X$ and reference cases of Table 4.1; b) – wave height and c) – wave period. Snyder’s input term $S_{in}$ at wind speed $U_{10} = 30 \text{ m s}^{-1}$ is compared with Janssen’s input term at $U_{10} = 26 \text{ m s}^{-1}$ and $U_{10} = 30 \text{ m s}^{-1}$ . Results for DIA method for $S_{nl}$ term are shown. . . . .	125
4.7 a) – Net wave forcing $\langle S_{in} + S_{diss} \rangle$ as function of the dimensional fetch $X$ and reference cases of Table 4.1; b) – wave height and c) – wave period at wind speed $U_{10} = 10 \text{ m s}^{-1}$ for Snyder and Janssen parameterizations of $S_{in}$ . Results for DIA and GQM methods are shown. . . . .	126
4.8 a) 1D-spectra $E(f)$ ( $\text{m}^2 \text{ Hz}^{-1}$ ) as functions of frequency $f$ ( $\text{Hz}$ ) at a large fetch (2400 km) calculated with the GQM and DIA methods, Snyder’s source term and wind speed $U_{10} = 30 \text{ m s}^{-1}$ ; b) $S_{in}$ functions of Snyder et al. (1981) and Janssen (1989, 1991) and $S_{diss}$ function of Komen et al. (1984) applied for these two spectra. . . . .	127
4.9 $S_{nl}$ ( $\text{m}^2$ ) (solid lines) and $S_{in} + S_{diss}$ ( $\text{m}^2$ ) (dashed lines) curves, as functions of frequency $f$ ( $\text{Hz}$ ), for different non-dimensional fetches $\chi$ . Wind speed $U_{10} = 30 \text{ m s}^{-1}$ , Snyder’s wind input $S_{in}$ and GQM method for the $S_{nl}$ . Note the change of frequency range in the right panels. . . . .	129
4.10 Energy-flux dependencies in fetch-limited simulations : $E\omega_p^4/g^2$ versus $(\omega_p^2/(2g) \times \partial E/\partial x)^{1/3}$ . Curves for the four wind speeds $U_{10} = 5, 10, 20, 30 \text{ m s}^{-1}$ , the two parameterizations of the wave input $S_{in}$ (Snyder and Janssen), and the DIA and GQM methods for the $S_{nl}$ computation are superimposed. Comparison with the experimental results of Kahma & Calkoen (1992); Babanin & Soloviev (1998b) is carried out. The light-blue curve represents the estimate of $\alpha_{ss} = 0.68$ . . . . .	130
4.11 Self-similarity parameter $\alpha_{ss}$ as a function of the inverse wave age $\tilde{\omega}_p = U_{10}/C_p$ , obtained with wind speeds $U_{10} = 5, 10, 20, 30 \text{ m s}^{-1}$ , the two parameterizations of the wave input $S_{in}$ (Snyder and Janssen), and the DIA and GQM methods for the $S_{nl}$ computation. The horizontal lines $\alpha_{ss} = 0.58$ , $\alpha_{ss} = 0.68$ , and $\alpha_{ss} = 0.78$ are drawn for a better visualization of the estimated coefficient $\alpha_{ss} = 0.68 \pm 0.1$ . . . . .	131

4.12 Self-similarity parameter $\alpha_{ss}$ as a function of the wave steepness $\sqrt{E\omega_p^4/g^2}$ obtained with wind speeds $U_{10} = 5, 10, 20, 30 \text{ m s}^{-1}$ , the two parameterizations of the wave input $S_{in}$ (Snyder and Janssen), and the DIA and GQM methods for the $S_{nl}$ computation. The horizontal lines $\alpha_{ss} = 0.58$ , $\alpha_{ss} = 0.68$ , and $\alpha_{ss} = 0.78$ are drawn for a better visualization of the estimated coefficient $\alpha_{ss} = 0.68 \pm 0.1$ . . . . .	132
4.13 Steepness $\sqrt{E\omega_p^4/g^2}$ as function of inverse wave age $\tilde{\omega}_p = U_{10}/C_p$ in log-space. Reference regimes give tangents 1/2 for Toba, 1/3 for Hasselmann, 2/3 for Zakharov & Zaslavsky . . . . .	135
5.1 Evolution of a) $\tilde{E}$ and b) $\tilde{\omega}_p$ with non-dimensional fetch $\chi$ , for the different sets (I, II and III), DIA and GQM methods for calculating $S_{nl}$ . Results are given at the final simulation time $t = 24 \text{ h}$ . Published growth curves of CERC (1977), JONSWAP (Hasselmann et al., 1973), Kahma & Calkoen (1992) (stable and unstable) and Babanin & Soloviev (1998b) are plotted for comparison. . . . .	143
5.2 Evolution of mean angular spreading $\sigma$ ( $^\circ$ ) with non-dimensional fetch $\chi$ for different options for source (sets I to III) and transfer terms (DIA and GQM), at the final simulation time $t = 24 \text{ h}$ . a) Linear scale. b) Logarithmic scale in $\chi$ . . . . .	144
5.3 1D-spectra at fetches 1 km, 5 km, 20 km, 50 km and 100 km and different options for source and transfer terms. Results are given at the final simulation time $t = 24 \text{ h}$ . . . . .	146
5.4 Angular distribution normalized by the maximum value at each frequency at different fetches (1 km, 5 km, 20 km, 50 km, 100 km), using DIA (upper panels) and GQM (lower panels) methods for $S_{nl}$ and set I for the source and sink terms. Results are represented in polar coordinates at $t = 24 \text{ h}$ . The white dotted circles indicate the peak frequency $f_p$ . . . . .	148
5.5 Same figure as figure 5.4, but for set II. . . . .	149
5.6 Same figure as figure 5.4, but for set III. . . . .	149
5.7 The parameter $s$ of the $\cos^{2s}((\theta - \theta_m)/2)$ model (cardioid model) for directional distributions at fetch $X = 50$ as a function of $f/f_p$ . GQM method, sets I, II and III, $t = 24 \text{ h}$ . Comparison with the expression of Hasselmann et al. (1980). . . . .	151
5.8 Angular distribution normalized by the maximum value at each frequency at fetch $X = 100 \text{ km}$ a) Set I b) Ewans (1998) bimodal parameterization c) Set II d) Set III. GQM method. Cartesian coordinates. $t = 24 \text{ h}$ . . . . .	152
5.9 Bathymetry of the North Carolina shelf and instrument location during SHOWEX (1999). This image is taken from Ardhuin et al. (2007) (their figure 1 a). . . . .	154

5.10 Evolution of non-dimensional energy $\tilde{E}$ with non-dimensional fetch $\chi$ , for slanting directions $0 - 80^\circ$ (colors are indicated in the figure). a) set I, b) set II and c) set III. DIA (points) and GQM (solid lines) methods for calculating $S_{nl}$ . $t = 24$ h. SHOWEX measurements (buoys X1 to X6) on 3 November 1999 : data averaged over the 12-17h EST time interval (EST=UTC-5 h). . . . .	156
5.11 Evolution of non-dimensional peak frequency $\tilde{\omega}_p$ (inverse wave age) with non-dimensional fetch $\chi$ , for slanting directions from $0 - 80^\circ$ (colors are indicated in the figure). a) set I, b) set II and c) set III. DIA (points) and GQM (solid lines) methods for calculating $S_{nl}$ . $t = 24$ h. SHOWEX measurements (buoys X1 to X6) on 3 November 1999 : data averaged over the 12-17h EST time interval (EST=UTC-5 h). . . . .	157
5.12 1D-spectra for different distances from the coast (1 km, 5 km, 20 km, 50 km and 100 km) and different oblique wind directions (from $0^\circ$ to $90^\circ$ ). Set II. GQM (solid lines) and DIA (points) methods. $t = 24$ h. Some of the SHOWEX measurements are plotted for comparison with $\theta_u = 20^\circ$ results (green curve) : buoys X1, X3 and X5 on 3 November 1999 (average over time period 12-17h EST). . . . .	159
5.13 Frequency-dependent directional spreading $\sigma(f)$ ( $^\circ$ ) for different distances from the coast (1 km, 5 km, 20 km, 50 km and 100 km) and different oblique wind directions (from $0^\circ$ to $90^\circ$ ). Set II. GQM method. $t = 24$ h. Some of the SHOWEX measurements are plotted for comparison with $\theta_u = 20^\circ$ results (green curve) : buoys X1, X3 and X5 on 3 November 1999 (average over time period 12-17h EST). . . . .	161
5.14 Mean wave direction $\theta_m(f)$ ( $^\circ$ ) for different distances from the coast (1 km, 5 km, 20 km, 50 km and 100 km) and different oblique wind directions (from $0^\circ$ to $90^\circ$ ). Set II. GQM method. $t = 24$ h. Some of the SHOWEX measurements are plotted for comparison with $\theta_u = 20^\circ$ results (green curve) : buoys X1, X3 and X5 on 3 November 1999 (average over time period 12-17h EST). . . . .	163
5.15 Normalized spectra $E(f, \theta)/E_{max}$ for $X = 5$ km and different oblique wind directions (from $0^\circ$ to $90^\circ$ ), using the GQM method for $S_{nl}$ and set II for the source and sink terms. $t = 24$ h. . . . .	164
5.16 Normalized spectra $E(f, \theta)/E_{max}$ for $X = 50$ km and different oblique wind directions (from $0^\circ$ to $90^\circ$ ), using the GQM method for $S_{nl}$ and set II for the source and sink terms. $t = 24$ h. . . . .	164
5.17 Nonlinear transfer term $S_{nl}(f, \theta)$ for $X = 5$ km and different oblique wind directions (from $0^\circ$ to $90^\circ$ ), using the GQM method for $S_{nl}$ and set II for the source and sink terms. $t = 24$ h. . . . .	165
5.18 Nonlinear transfer term $S_{nl}(f, \theta)$ for $X = 50$ km and different oblique wind directions (from $0^\circ$ to $90^\circ$ ), using the GQM method for $S_{nl}$ and set II for the source and sink terms. $t = 24$ h. . . . .	165

5.19 This figure is extracted from Wang & Hwang (2001) (their figure 9) and represents sections of two directional distributions at different frequencies. Measurements are acquired by an offshore buoy. Dashed-dotted lines correspond to the wind direction, dashed lines to the peak wave direction. . . . .	166
5.20 Angular distribution normalized by the maximum value at each frequency $D(f, \theta)/D_{max}(f)$ for $X = 50$ km. Set II. GQM method. $t = 24$ h. The white dotted circles indicate $f_p$ , $2f_p$ and $4f_p$ . . . . .	167
5.21 Nonlinear transfer term normalized by its maximum absolute value at each frequency $S_{nl}(f, \theta)/ S_{nl,max}(f) $ for $X = 50$ km and different oblique wind directions (from $0^\circ$ to $90^\circ$ ). Set II. GQM method. $t = 24$ h. The black dotted circles indicate $f_p$ , $2f_p$ and $4f_p$ . . . . .	168
5.22 Angular distribution normalized by the maximum value at each frequency for different fetches (1 km, 5 km, 20 km, 50 km, 100 km). DIA and GQM methods. Set I. Polar coordinates. The dotted white circle indicates the peak frequency $f_p$ . . . . .	179
5.23 Angular distribution normalized by the maximum value at each frequency for different fetches (1 km, 5 km, 20 km, 50 km, 100 km). DIA and GQM methods. Set II. Polar coordinates. The dotted white circle indicates the peak frequency $f_p$ . . . . .	180
5.24 Angular distribution normalized by the maximum value at each frequency for different fetches (1 km, 5 km, 20 km, 50 km, 100 km). DIA and GQM methods. Set III. Polar coordinates. The dotted white circle indicates the peak frequency $f_p$ . . . . .	180
5.25 1D-spectra for different distances from the coast (1 km, 5 km, 20 km, 50 km and 100 km) and different oblique wind directions (from $0^\circ$ to $90^\circ$ ). Set I. GQM (solid lines) and DIA (points) methods. Some of the SHOWEX measurements are plotted for comparison with $\theta = 20^\circ$ results (green curve) : buoys X1, X3 and X5 on 3 November 1999 (average over time period 12-17h EST). . . . .	181
5.26 1D-spectra for different distances from the coast (1 km, 5 km, 20 km, 50 km and 100 km) and different oblique wind directions (from $0^\circ$ to $90^\circ$ ). Set III. GQM (solid lines) and DIA (points) methods. Some of the SHOWEX measurements are plotted for comparison with $\theta = 20^\circ$ results (green curve) : buoys X1, X3 and X5 on 3 November 1999 (average over time period 12-17h EST). . . . .	182
5.27 Frequency-dependent directional spreading $\sigma(f)$ for different distances from the coast (1 km, 5 km, 20 km, 50 km and 100 km) and different oblique wind directions (from $0^\circ$ to $90^\circ$ ). Set I. GQM method. Some of the SHOWEX measurements are plotted for comparison with $\theta = 20^\circ$ results (green curve) : buoys X1, X3 and X5 on 3 November 1999 (average over time period 12-17h EST). . . . .	183

5.28 Frequency-dependent directional spreading $\sigma(f)$ for different distances from the coast (1 km, 5 km, 20 km, 50 km and 100 km) and different oblique wind directions (from $0^\circ$ to $90^\circ$ ). Set II. DIA (points) and GQM (solid lines) methods. Some of the SHOWEX measurements are plotted for comparison with $\theta = 20^\circ$ results (green curve) : buoys X1, X3 and X5 on 3 November 1999 (average over time period 12-17h EST). . . . .	184
5.29 Frequency-dependent directional spreading $\sigma(f)$ for different distances from the coast (1 km, 5 km, 20 km, 50 km and 100 km) and different oblique wind directions (from $0^\circ$ to $90^\circ$ ). Set III. GQM method. Some of the SHOWEX measurements are plotted for comparison with $\theta = 20^\circ$ results (green curve) : buoys X1, X3 and X5 on 3 November 1999 (average over time period 12-17h EST). . . . .	185
5.30 Mean wave direction $\theta_m(f)$ for different distances from the coast (1 km, 5 km, 20 km, 50 km and 100 km) and different oblique wind directions (from $0^\circ$ to $90^\circ$ ). Set I. GQM method. Some of the SHOWEX measurements are plotted for comparison with $\theta = 20^\circ$ results (green curve) : buoys X1, X3 and X5 on 3 November 1999 (average over time period 12-17h EST). . . . .	186
5.31 Mean wave direction $\theta_m(f)$ for different distances from the coast (1 km, 5 km, 20 km, 50 km and 100 km) and different oblique wind directions (from $0^\circ$ to $90^\circ$ ). Set II. GQM and DIA methods. Some of the SHOWEX measurements are plotted for comparison with $\theta = 20^\circ$ results (green curve) : buoys X1, X3 and X5 on 3 November 1999 (average over time period 12-17h EST). . . . .	187
5.32 Mean wave direction $\theta_m(f)$ for different distances from the coast (1 km, 5 km, 20 km, 50 km and 100 km) and different oblique wind directions (from $0^\circ$ to $90^\circ$ ). Set III. GQM method. Some of the SHOWEX measurements are plotted for comparison with $\theta = 20^\circ$ results (green curve) : buoys X1, X3 and X5 on 3 November 1999 (average over time period 12-17h EST). . . . .	188
5.33 Angular distribution normalized by the maximum value at each frequency $D(f, \theta)/D_{max}(f)$ for $X = 5$ km. Set II. GQM method. The white dotted circles indicate the peak frequency $f = f_p$ . . . . .	189

# Liste des tableaux

3.1	Description of the initial spectra : cases C1 to C4 . . . . .	67
3.2	Description of the sets (I, II, III) and options (free tail or imposed tail). . . . .	79
4.1	Summary of reference regimes of wind wave growth. Exponents $p_\chi, q_\chi$ are given for explicit dependencies on fetch (4.17). $\tilde{B}$ and $T$ are parameters in energy-to-frequency relationship $\tilde{E} = \tilde{B}\tilde{\omega}_p^{-2T}$ . Last column is parameterization of net wave forcing $dE/dt$ in accordance with weakly turbulent relationship (4.19). . . . .	117
4.2	Summary of experimental cases of wind wave growth. Exponents $p_\chi, q_\chi$ are given for explicit dependencies on fetch (4.17). $\tilde{B}$ and $T$ are parameters in the corresponding energy-to-frequency relationship $\tilde{E} = \tilde{B}\tilde{\omega}_p^{-2T}$ . Last column is the theoretical estimate of exponent $T$ in the energy-to-frequency relationship (Badulin et al., 2007) for given value of $p_\chi$ . . . . .	118



# Bibliographie

- Alves, J.-H. G. M., 2000 : A saturation-dependant dissipation source function for wind-wave modelling applications. Ph.D. thesis, University of New South Wales, Australia.
- Alves, J.-H. G. M. & M. L. Banner, 2003 : Performance of a saturation-based dissipation-rate source term in modeling the fetch-limited evolution of wind waves. *J. Phys. Oceanogr.*, **33**, 1274–1298.
- Alves, J. H. G. M., M. L. Banner, & I. R. Young, 2003 : Revisiting the Pierson-Moskowitz asymptotic limits for fully developed wind waves. *J. Phys. Oceanogr.*, **33**, 1301–1323.
- Andrews, D. G. & M. E. McIntyre, 1978 : On wave action and its relatives. *J. Fluid Mech.*, **89**, 647–664, corrigendum : vol. 95, p. 796.
- Ardhuin, F. & A. L. Boyer, 2006 : Numerical modelling of sea states : validation of spectral shapes. *Navigation*, **54** (216), 55–71.
- Ardhuin, F., B. Chapron, & F. Collard, 2009 : Observation of swell dissipation across oceans. *Geophys. Res. Lett.*, **36**, L06607, doi :10.1029/2008GL037030.
- Ardhuin, F., F. Collard, B. Chapron, P. Queffeulou, J.-F. Filipot, & M. Hamon, 2008 : Spectral wave dissipation based on observations : a global validation. *Proceedings of Chinese-German Joint Symposium on Hydraulics and Ocean Engineering*, Darmstadt, Germany, 391–400.
- Ardhuin, F., T. H. C. Herbers, & W. C. O'Reilly, 2001 : A hybrid Eulerian-Lagrangian model for spectral wave evolution with application to bottom friction on the continental shelf. *J. Phys. Oceanogr.*, **31** (6), 1498–1516.
- Ardhuin, F., T. H. C. Herbers, W. C. O'Reilly, & P. F. Jessen, 2003a : Swell transformation across the continental shelf. part II : validation of a spectral energy balance equation. *J. Phys. Oceanogr.*, **33**, 1940–1953.
- Ardhuin, F., T. H. C. Herbers, G. P. Van Vledder, K. P. Watts, R. Jensen, & H. C. Gruber, 2007 : Swell and slanting-fetch effects on wind wave growth. *J. Phys. Oceanogr.*, **37**, 908–931.
- Ardhuin, F., W. C. O'Reilly, T. H. C. Herbers, & P. F. Jessen, 2003b : Swell transformation across the continental shelf. part I : Attenuation and directional broadening. *J. Phys. Oceanogr.*, **33**, 1921–1939.

- Babanin, A. V., M. Banner, I. Young, & M. Donelan, 2007a : Wave follower field measurements of the wind input spectral function. part iii : Parameterization of the wind input enhancement due to wave breaking. *J. Phys. Oceanogr.*, **37**, 2764–2775.
- Babanin, A. V., D. Chalikov, I. Young, & I. Savelyev, 2007b : Predicting the breaking onset of surface water waves. *Geophys. Res. Lett.*, **34**, L07605, doi :10.1029/2006GL029135.
- Babanin, A. V. & Y. P. Soloviev, 1998a : Field investigation of transformation of the wind wave frequency spectrum with fetch and the stage of development. *J. Phys. Oceanogr.*, **28**, 563–576.
- Babanin, A. V. & Y. P. Soloviev, 1998b : Variability of directional spectra of wind-generated waves, studied by means of wave staff arrays. *Mar. Freshwater Res.*, **49**, 89–101.
- Badulin, S. I., A. V. Babanin, D. Resio, & V. Zakharov, 2007 : Weakly turbulent laws of wind-wave growth. *J. Fluid Mech.*, **591**, 339–378.
- Badulin, S. I., A. V. Babanin, D. Resio, & V. Zakharov, 2008a : Numerical verification of weakly turbulent law of wind wave growth. *IUTAM Symposium on Hamiltonian Dynamics, Vortex Structures, Turbulence. Proceedings of the IUTAM Symposium held in Moscow, 25-30 August, 2006*, A. V. Borisov, V. V. Kozlov, I. S. Mamaev, & M. A. Sokolovskiy, Eds., IUTAM Bookseries, Vol. 6, 175–190, ISBN : 978-1-4020-6743-3.
- Badulin, S. I. & G. Caulliez, 2009 : Significance of laboratory observations for modeling wind-driven seas. *Geophysical Research Abstracts*, EGU General Assembly 2009, Vol. 11, EGU2009-12 694.
- Badulin, S. I., A. O. Korotkevich, D. Resio, & V. E. Zakharov, 2008b : Wave-wave interactions in wind-driven mixed seas. *Proceedings of the Rogue Waves 2008 Workshop, October 13-15, 2008, Brest, France*, M. Olagnon & M. Prevosto, Eds., IFREMER, Brest, France, 77–86.
- Badulin, S. I., A. N. Pushkarev, D. Resio, & V. E. Zakharov, 2005 : Self-similarity of wind-driven seas. *Nonl. Proc. Geophys.*, **12**, 891–946.
- Banner, M. L., I. S. F. Jones, & J. C. Trinder, 1989 : Wavenumber spectra of short gravity waves. *J. Fluid Mech.*, **198**, 321–344.
- Banner, M. L. & I. R. Young, 1994 : Modeling spectral dissipation in the evolution of wind waves. part I : assessment of existing model performance. *J. Phys. Oceanogr.*, **24**, 1550–1570.
- Barnett, T. P., 1968 : On the generation, dissipation and prediction of ocean wind wave. *J. Geophys. Res.*, **73 (2)**, 513–529.
- Becq, F., 1998 : Extension de la modélisation spectrale des états de mer vers le domaine côtier. Ph.D. thesis, Université de Toulon et du Var (France).
- Benoit, M., 2005 : Evaluation of methods to compute the non-linear quadruplet interactions for deep-water wave spectra. *Proc. 5th Int. Symp. on Ocean Wave Measurement and Analysis (WAVES 2005)*, Madrid (Spain), Paper 52.

- Benoit, M., 2006 : Implementation and test of improved methods for evaluation of non-linear quadruplet interactions in a third generation wave model. *Proc. 30th Int. Conf. on Coastal Eng.*, San Diego (California, USA), 526–538.
- Benoit, M. & E. Gagnaire-Renou, 2007 : Interactions vague-vague non-linéaires et spectre d'équilibre pour les vagues de gravité en grande profondeur d'eau. *Proc. 18th Congrès Français de Mécanique*, Grenoble (France), in French.
- Benoit, M. & F. Lafon, 2004 : A nearshore wave atlas along the coasts of france based on the numerical modelling of wave climate over 25 years. *Proc. 29th Int. Conf. on Coastal Eng.*, Lisbonne (Portugal), 714–726.
- Benoit, M., F. Marcos, & F. Becq, 1996a : Development of a third generation shallow-water wave model with unstructured spatial meshing. *Proc. 25th Int. Conf. on Coastal Eng.*, Orlando (Florida, USA), 465–478.
- Benoit, M., F. Marcos, F. Becq, & P. Thellier, 1996b : Tomawac v1.0 - note de validation. Tech. rep., EDF R&D - LNHE, Chatou, France.
- Bidlot, J., S. Abdalla, & P. Janssen, 2005 : A revised formulation for ocean wave dissipation in CY25R1. Tech. Rep. Memorandum R60.9/JB/0516, Research Department, ECMWF, Reading, U. K.
- Booij, N., R. C. Ris, & L. H. Holthuijsen, 1999 : A third-generation wave model for coastal regions. part i. model description and validation. *J. Geophys. Res.*, **104 (C4)**, 7649–7666.
- Bottema, M. & G. P. Van Vledder, 2008 : Effective fetch and non-linear four-wave interactions during wave growth in slanting fetch conditions. *Coastal Eng.*, **55**, 261–275.
- Bretschneider, C., 1952 : The generation and decay of wind waves in deep water. *Trans. Am. Geophys. Union*, **33 (3)**, 381–389.
- Cavaleri, L. & P. Malanotte-Rizzoli, 1981 : Wind wave prediction in shallow water : theory and applications. *J. Geophys. Res.*, **86 (C5)**, 10,961–10,975.
- Cavaleri, L., et al., 2007 : Wave modelling – the state of the art. *Progr. Ocean.*, **75**.
- CERC, 1977 : *Shore Protection Manual*, Vol. 3. U. S. Army Coastal Engineering Research Center.
- Donelan, M., M. Skafel, H. Gruber, P. Liu, D. Schwab, & S. Venkatesh, 1992 : On the growth rate of wind-generated waves. *Atmosphere Ocean*, **30 (3)**, 457–478.
- Donelan, M. A., J. Hamilton, & W. H. Hui, 1985 : Directional spectra of wind-generated waves. *Phil. Trans. Roy. Soc. Lond. A*, **315**, 509–562.
- Donelan, M. A. & W. J. Pierson-jr., 1987 : Radar scattering and equilibrium ranges in wind-generated waves with application to scatterometry. *J. Geophys. Res.*, **92 (C5)**, 4971–5029.

- Elfouhaily, T., B. Chapron, K. Katsaros, & D. Vandemark, 1997 : A unified directional spectrum for long and short wind-driven waves. *J. Geophys. Res.*, **102** (C7), 15 781–15 796.
- Ewans, K. C., 1998 : Observations of the directional spectrum of fetch-limited waves. *J. Phys. Oceanogr.*, **28**, 495–512.
- Ewing, J., 1971 : A numerical wave prediction method for the North Atlantic ocean. *Deut. Hydrogr. Z.*, **24**, 241–261.
- Forget, P., M. Saillard, & P. Broche, 2006 : Observations of the sea surface by coherent L band radar at low grazing angles in a nearshore environment. *J. Geophys. Res.*, **111**, C09015, doi :10.1029/2005JC002900.
- Forristall, G. Z. & K. C. Ewans, 1998 : Worldwide measurements of directional wave spreading. *J. Atmos. Ocean Technol.*, **15**, 440–469.
- Gagnaire-Renou, E., M. Benoit, & P. Forget, 2008 : Modeling waves in fetch-limited and slanting fetch conditions using a quasi-exact method for nonlinear four-wave interactions. *Proc. 31th Int. Conf. on Coastal Eng.*, Hamburg (Germany), 496–508.
- Gagnaire-Renou, E., M. Benoit, & P. Forget, in press : Ocean wave spectrum properties as derived from quasi-exact computations of nonlinear wave-wave interactions. *J. Geophys. Res.*, doi :10.1029/2009JC005665.
- Gelci, R., H. Cazalé, & J. Vassal, 1957 : Prévision de la houle. La méthode des densités spectroangulaires. *Bulletin d'information du Comité d'Océanographie et d'Etude des Côtes*, **9**, 416–435, in French.
- Günther, H., S. Hasselmann, & P. A. E. M. Janssen, 1992 : The WAM model cycle 4 (revised version). Tech. Rep. 4, Deutsch. Klimatol. Rechenzentrum, Hamburg, Germany.
- Hara, T. & S. E. Belcher, 2002 : Wind forcing in the equilibrium range of wind-wave spectra. *J. Fluid Mech.*, **470**, 223–245.
- Hashimoto, N. & K. Kawaguchi, 2001 : Extension and modification of discrete interaction approximation (dia) for computing nonlinear energy transfer of gravity wave spectrum. *Proc. 4th Int. Symp. on Ocean Waves Measurement and Analysis (WAVES 2001)*, San Francisco (California), 530–539.
- Hashimoto, N., H. Tsuruya, & Y. Nakagawa, 1998 : Numerical computations of the nonlinear energy transfer of gravity-wave spectra in finite water depths. *Coastal Eng. Journal*, **40**, 23–40.
- Hasselmann, D. & J. Bösenberg, 1991 : Field measurements of wave-induced pressure over wind-sea and swell. *J. Fluid Mech.*, **230**, 391–428.
- Hasselmann, D. E., M. Dunkel, & J. A. Ewing, 1980 : Directional wave spectra observed during JONSWAP 1973. *J. Phys. Oceanogr.*, **10**, 1264–1280.

- Hasselmann, K., 1962 : On the nonlinear energy transfer in a gravity wave spectrum. Part 1. General theory. *J. Fluid Mech.*, **12**, 481–500.
- Hasselmann, K., 1963a : On the nonlinear energy transfer in a gravity wave spectrum. evaluation of the energy flux and swell-sea interaction for a neumann spectrumP. 3. *J. Fluid Mech.*, **15**, 385–398.
- Hasselmann, K., 1963b : On the nonlinear energy transfer in a gravity wave spectrum. Part 2 Conservation theorems; wave-particle analogy; irreversibility. *J. Fluid Mech.*, **15**, 273–281.
- Hasselmann, K., 1974 : On the spectral dissipation of ocean waves due to white capping. *Boundary-Layer Meteorol.*, **6**, 107–127.
- Hasselmann, K., D. B. Ross, P. Müller, & W. Sell, 1976 : A parametric wave prediction model. *J. Phys. Oceanogr.*, **6**, 200–228.
- Hasselmann, K., et al., 1973 : Measurements of wind-wave growth and swell decay during the Joint North Sea Wave Project (JONSWAP). *Dtsch. Hydrogr. Zeitschr. Suppl.*, **12 (A8)**.
- Hasselmann, S. & K. Hasselmann, 1981 : A symmetrical method of computing the nonlinear transfer in a gravity wave spectrum. *Hamburger Geophysikalische Einzelschriften, Reihe A, Heft 52, Max-Planck-Institut für Meteorologie, Hamburg*, **A52**.
- Hasselmann, S. & K. Hasselmann, 1985 : Computations and parametrizations of the non-linear energy transfer in a gravity-wave spectrum. Part I. A new method for efficient computations of the exact nonlinear transfer integral. *J. Phys. Oceanogr.*, **15**, 1369–1377.
- Hasselmann, S., K. Hasselmann, J. H. Allender, & T. P. Barnett, 1985 : Computations and parametrizations of the nonlinear energy transfer in a gravity-wave spectrum. part ii. parameterizations of the nonlinear energy transfer for application in wave models. *J. Phys. Oceanogr.*, **15**, 1378–1391.
- Hersbach, H. & P. Janssen, 1999 : Improvement of the short-fetch behavior in the wave ocean model (wam). *J. Atm. Oceanic Tech.*, **16**, 884–892.
- Herterich, K. & K. Hasselmann, 1980 : A similarity relation for the non-linear energy transfer in a finite-depth gravity-wave spectrum. *J. Fluid Mech.*, **97**, 215–224.
- Hisaki, Y., 2007 : Directional distribution of the short wave estimated from HF ocean radars. *J. Geophys. Res.*, **112**, C10014, doi :10.1029/2007JC004296.
- Holthuijsen, L. H., 1983 : Observations of the directional distribution of ocean wave energy. *J. Phys. Oceanogr.*, **13**, 191–207.
- Holthuijsen, L. H., 2007 : *Waves in Oceanic and Coastal Waters*. Cambridge Univ. Press, 387 pp.

- Hsiao, S. V. & O. H. Shemdin, 1983 : Measurements of wind velocity and pressure with a wave follower during MARSEN. *J. Geophys. Res.*, **88** (C14), 9841–9849.
- Hwang, P. A. & D. W. Wang, 2004 : Field measurements of duration-limited growth of wind-generated ocean surface waves at young stage of development. *J. Phys. Oceanogr.*, 2316–2326.
- Hwang, P. H., D. W. Wang, E. J. Walsh, W. B. Krabill, & R. N. Swift, 2000a : Airborne measurement of the wavenumber spectra of ocean surface waves. Part I : spectral slope and dimensionless spectral coefficient. *J. Phys. Oceanogr.*, **30**, 2753–2767.
- Hwang, P. H., D. W. Wang, E. J. Walsh, W. B. Krabill, & R. N. Swift, 2000b : Airborne measurement of the wavenumber spectra of ocean surface waves. Part II : directional distribution. *J. Phys. Oceanogr.*, **30**, 2768–2787.
- Isobe, M., K. Kondo, & K. Horikawa, 1984 : Extension of MLM for estimating directional wave spectrum. *Symp. on Description and Modelling of Directional Seas*, DHI and MMI, Copenhagen, 1–15.
- Janssen, P. A. E. M., 1989 : Wave-induced stress and the drag of air flow over sea waves. *J. Phys. Oceanogr.*, **19**, 745–754.
- Janssen, P. A. E. M., 1991 : Quasi-linear theory of wind-wave generation applied to wave forecasting. *J. Phys. Oceanogr.*, **21**, 1631–1642.
- Janssen, P. A. E. M., 2004 : *The Interaction of Ocean Waves and Wind*. Cambridge Univ. Press, New York, 300 pp.
- Jenkins, A. & O. Phillips, 2001 : A simple formula for nonlinear wave-wave interaction. *Int. J. Offshore Polar Engng*, **11**(2), 81–86.
- Kahma, K. K., 1981 : A study of the growth of the wave spectrum with fetch. *J. Phys. Oceanogr.*, **11**, 1503–1515.
- Kahma, K. K. & C. J. Calkoen, 1992 : Reconciling discrepancies in the observed growth of wind-generated waves. *J. Phys. Oceanogr.*, **22**, 1389–1405.
- Kitaigorodskii, S. A., 1962 : Applications of the theory of similarity to the analysis of wind-generated wave motion as a stochastic process. *Bull. Acad. Sci. USSR, Geophys. Ser., Engl. Transl.*, **N1**, 105–117.
- Kitaigorodskii, S. A., 1983 : On the theory of the equilibrium range in the spectrum of wind-generated gravity waves. *J. Phys. Oceanogr.*, **13**, 816–827.
- Komatsu, K. & A. Masuda, 1996 : A new scheme of nonlinear energy transfer among wind waves : RIAM method. algorithm and performance. *J. Oceanogr. Soc. Japan*, **52**, 509–537.
- Komen, G. J., L. Cavaleri, M. Donelan, K. Hasselmann, S. Hasselmann, & P. A. E. M. Janssen, 1994 : *Dynamics and modelling of ocean waves*. Cambridge University Press, New York, 532 pp.

- Komen, G. J., S. Hasselmann, & K. Hasselmann, 1984 : On the existence of a fully developed wind-sea spectrum. *J. Phys. Oceanogr.*, **14**, 1271–1285.
- Korotkevich, A. O., A. N. Pushkarev, D. Resio, & V. E. Zakharov, 2008 : Numerical verification of the weak turbulent model for swell evolution. *Eur. J. Mech. B/Fluids*, **27**, 361–387.
- Krasitskii, V. P., 1994 : On reduced Hamiltonian equations in the nonlinear theory of water surface waves. *J. Fluid Mech.*, **272**, 1–20.
- Kudryavtsev, V. N., V. K. Makin, & B. Chapron, 1999 : Coupled sea surface–atmosphere model. 2. spectrum of short wind waves. *J. Geophys. Res.*, **104** (C4), 7625–7639.
- Lavrenov, I. V., 2001 : Effect of wind wave parameter fluctuation on the nonlinear spectrum evolution. *J. Phys. Oceanogr.*, **31**, 861–873.
- Lavrenov, I. V., 2003a : A numerical study of a non-stationary solution of the Hasselmann equation. *J. Phys. Oceanogr.*, **33**, 499–511.
- Lavrenov, I. V., 2003b : *Wind-waves in oceans : dynamics and numerical simulations*. Springer, Berlin, 376 pp.
- Lin, R. & W. Perrie, 1998 : On the mathematics and approximation of the nonlinear wave-wave interactions. *Nonlinear ocean waves*, W. Perrie, Ed., Computational Mechanics Publications, Advances in Fluid Mechanics, 61–88.
- Liu, P., D. Schwab, & J. Bennett, 1984 : Comparison of a two-dimensional wave prediction model with synoptic measurements in Lake Michigan. *J. Phys. Oceanogr.*, **14**, 1514–1518.
- Liu, P. C. & D. Ross, 1980 : Airborne measurements of wave growth for stable and unstable atmospheres in lake Michigan. *J. Phys. Oceanogr.*, **10**, 1842–1853.
- Long, C. & D. Resio, 2007 : Wind wave spectral observations in currituck sound, north carolina. *J. Geophys. Res.*, **112**, C05001, doi :10.1029/2006JC003835.
- Longuet-Higgins, M. S., D. E. Cartwright, & N. D. Smith, 1963 : Observations of the directional spectrum of sea waves using the motions of a floating buoy. *Ocean Wave Spectra, proceedings of a conference, Easton, Maryland*, Prentice-Hall, National Academy of Sciences, 111–136.
- Lygre, A. & H. E. Krogstad, 1986 : Maximum entropy estimation of the directional distribution in ocean wave spectra. *J. Phys. Oceanogr.*, **16**, 2,052–2,060.
- Masson, D., 1993 : On the nonlinear coupling between swell and wind waves. *J. Phys. Oceanogr.*, **23**, 1249–1258.
- Masuda, A., 1980 : Nonlinear energy transfer between wind waves. *J. Phys. Oceanogr.*, **10**, 2082–2093.

- Masuda, A., 1986 : Nonlinear energy transfer between random gravity waves. *Waves Dynamics and Radio Probing of the Ocean Surface*, O. Phillips & K. Hasselmann, Eds., Plenum Press, New-York, 136–149.
- Miles, J. W., 1957 : On the generation of surface waves by shear flows. *J. Fluid Mech.*, **3**, 185–204.
- Mitsuyasu, H., F. Tasai, T. Suhara, S. Mizuno, M. Onkusu, T. Honda, & T. Rukiiski, 1975 : Observations of the directional spectrum of ocean waves using a cloverleaf buoy. *J. Phys. Oceanogr.*, **5**, 751–761.
- Monbaliu, J., J. Hargreaves, J.-C. Carretero, H. Gerritsen, & R. Flather, 1999 : Wave modelling in the PROMISE project. *Coastal Eng.*, **37**, 379–407.
- Monbaliu, J., R. Padilla-Hernández, J. C. Hargreaves, J. C. Carretero Albiach, W. Luo, M. Sclavo, & H. Günther, 2000 : The spectral wave model, WAM, adapted for applications with high spatial resolution. *Coastal Eng.*, **41**, 41–62.
- Perrie, W. A. & D. T. Resio, 2009 : A two-scale approximation for efficient representation of nonlinear energy transfers in a wind wave spectrum. part ii : Application to observed wave spectra. *J. Phys. Oceanogr.*, **39**, 2451–2476.
- Pettersson, H., 2004 : Wave growth in a narrow bay. Ph.D. thesis, University of Helsinki, URL <http://ethesis.helsinki.fi/julkaisut/mat/fysik/vk/pettersson/>, [ISBN 951-53-2589-7 (Paperback) ISBN 952-10-1767-8 (PDF)].
- Phillips, O., 1958 : The equilibrium range in the spectrum of wind-generated waves. *J. Fluid Mech.*, **4**, 426–434.
- Phillips, O. M., 1957 : On the generation of waves by turbulent wind. *J. Fluid Mech.*, **2**, 415–417.
- Phillips, O. M., 1977 : *The dynamics of the upper ocean*. Cambridge University Press.
- Phillips, O. M., 1985 : Spectral and statistical properties of the equilibrium range in wind-generated gravity waves. *J. Fluid Mech.*, **156**, 505–531.
- Pierson, W. J. & L. A. Moskowitz, 1964 : A proposed spectral form for fully developed wind seas based on the similarity theory of S. A. Kitaigorodskii. *J. Geophys. Res.*, **69**, 5181–5190.
- Plant, W. J., 1982 : A relationship between wind stress and wave slope. *J. Geophys. Res.*, **87 (C3)**, 1961–1967.
- Polnikov, V., 1997 : Nonlinear energy transfer through the spectrum of gravity waves for the finite depth case. *J. Phys. Oceanogr.*, **27**, 1481–1491.
- Polnikov, V. G., 1990 : Numerical solution of the kinetic equation for surface gravity waves. *Izv. Atmos. Ocean. Phys.*, **26 (2)**, 168–176.

- Polnikov, V. G. & L. Farina, 2002 : On the problem of optimal approximation of the four-wave kinetic integral. *Nonl. Proc. Geophys.*, **9**, 497–512.
- Press, W., S. A. Teukolsky, W. T. Vetterling, & B. Flannery, 1992 : *Numerical recipes in FORTRAN : the art of scientific computing*. Cambridge University Press, Cambridge, UK.
- Pushkarev, A. N., D. Resio, & V. E. Zakharov, 2003 : Weak turbulent theory of the wind-generated gravity sea waves. *Phys. D : Nonlin. Phenom.*, **184**, 29–63.
- Pushkarev, A. N., D. Resio, & V. E. Zakharov, 2004 : Second generation diffusion model of interacting gravity waves on the surface of deep water. *Nonl. Proc. Geophys.*, **11**, 329–342, sRef-ID : 1607-7946/npg/2004-11-329.
- Pushkarev, A. N. & V. E. Zakharov, 2000 : On conservation of the constants of motion in the models of nonlinear wave interaction. *Proceedings of the Sixth International Workshop on Wave Hindcasting and Forecasting*, Monterey, CA, 456–469.
- Resio, D. T., C. E. Long, & C. L. Vincent, 2004 : Equilibrium-range constant in wind-generated wave spectra. *J. Geophys. Res.*, **109**, C01018, doi :1029/2003JC001788.
- Resio, D. T. & W. Perrie, 1991 : A numerical study of nonlinear energy fluxes due to wave-wind interactions. *J. Fluid Mech.*, **223**, 603–629.
- Resio, D. T. & W. A. Perrie, 2008 : A two-scale approximation for efficient representation of nonlinear energy transfers in a wind wave spectrum. part I : Theoretical development. *J. Phys. Oceanogr.*, **38**, 2801–2816.
- Resio, D. T., J. Pihl, B. Tracy, & C. L. Vincent, 2001 : Nonlinear energy fluxes and the finite depth equilibrium range in wave spectra. *J. Geophys. Res.*, **106** (C4), 6985–7000.
- Ris, R. C., 1997 : Spectral modelling of wind waves in coastal areas. Ph.D. thesis, Delft University of Technology.
- Ross, D. B., 1978 : On the use of aircraft in the observation of one- and two-dimensional ocean wave spectra. *Ocean Wave Climate*, M. D. Earle & A. Malahoff, Eds., Plenum Press, 253–267.
- Schwab, D., J. Bennett, P. Liu, & M. Donelan, 1984 : Application of a simple numerical wave prediction model to Lake Erie. *J. Geophys. Res.*, **89** (C3), 3586–3592.
- Snyder, R. L., F. W. Dobson, J. A. Elliot, & R. B. Long, 1981 : Array measurements of atmospheric pressure fluctuations above surface gravity waves. *J. Fluid Mech.*, **102**, 1–59.
- Stewart, R. W., 1974 : The air-sea momentum exchange. *Boundary-Layer Meteorol.*, **6**, 151–167.
- Sverdrup, H. U. & W. H. Munk, 1947 : Wind, sea, and swell : theory of relations for forecasting. Tech. Rep. 601, U. S. Hydrographic Office.

- SWAMP Group, 1985 : *Ocean wave modelling*. Plenum Press, New York, 256 pp.
- Tanaka, M., 2001 : Verification of Hasselmann's energy transfer among surface gravity waves by direct numerical simulations of primitive equations. *J. Fluid Mech.*, **444**, 199–221.
- Toba, Y., 1972 : Local balance in the air-sea boundary processes. I. on the growth process of wind waves. *J. Oceanogr. Soc. Japan*, **28**, 109–121.
- Toba, Y., 1973a : Local balance in the air-sea boundary processes. II. partition of wind stress to waves and current. *J. Oceanogr. Soc. Japan*, **29**, 70–75.
- Toba, Y., 1973b : Local balance in the air-sea boundary processes. III. on the spectrum of wind waves. *J. Oceanogr. Soc. Japan*, **29**, 209–220.
- Toba, Y., 1978 : Stochastic form of the growth of wind waves in a single-parameter representation with physical implementations. *J. Phys. Oceanogr.*, **8**, 494–507.
- Toba, Y., 1997 : Wind-wave strong wave interactions and quasi-local equilibrium between wind and wind sea with the friction velocity proportionality. *Nonlinear ocean waves*, W. Perrie, Ed., Computational Mechanics Publications, Advances in Fluid Mechanics, Vol. 17, 1–59.
- Tolman, H. L., 1991 : A third generation model for wind on slowly varying, unsteady and inhomogeneous depth and currents. *J. Phys. Oceanogr.*, **21**, 766–781.
- Tolman, H. L., 1992 : Effects of numerics on the physics in a third-generation wind-wave model. *J. Phys. Oceanogr.*, **22**, 1095–1111.
- Tolman, H. L., 2002 : User manual and system documentation of WAVEWATCH-III version 2.22. Tech. Rep. 222, NOAA/NWS/NCEP/MMAB.
- Tolman, H. L., 2004 : Inverse modeling of discrete interaction approximations for nonlinear interactions in wind waves. *Ocean Modelling*, **6**, 405–422.
- Tolman, H. L. & D. Chalikov, 1996 : Source terms in a third-generation wind wave model. *J. Phys. Oceanogr.*, **26**, 2497–2518.
- Tolman, H. L., V. M. Krasnopolsky, & D. V. Chalikov, 2005 : Neural network approximations for nonlinear interactions in wind wave spectra : direct mapping for wind seas in deep water. *Ocean Modelling*, **8**, 253–278.
- Tracy, B. & D. Resio, 1982 : Theory and calculation of the nonlinear energy transfer between sea waves in deep water. WES Rep. 11, US Army, Engineer Waterways Experiment Station, Vicksburg, MS.
- Trizna, D., R. Bogle, J. Moore, & C. Howe, 1980 : Observation by hf radar of the phillips resonance mechanism for generation of wind waves. *J. Geophys. Res.*, **85 (C9)**, 4946–4956.

- Van der Westhuysen, A. J., 2008 : Advances in the spectral modelling of wind waves in the nearshore. Ph.D. thesis, Delft University of Technology, The Netherlands.
- Van der Westhuysen, A. J., M. Zijlema, & J. A. Battjes, 2007 : Nonlinear saturation-based whitecapping dissipation in swan for deep and shallow water. *Coastal Eng.*, **54**, 151–170.
- Van Vledder, G. P., 2001 : Extension of the discrete interaction approximation for computing nonlinear quadruplet wave-wave interactions in operational wave prediction models. *Proc. 4th Int. Symp. on Ocean Waves, Measurements and Analysis (WAVES2001)*, San-Francisco, CA (USA), 540–549.
- Van Vledder, G. P., 2006 : The WRT method for the computation of non-linear four-wave interactions in discrete spectral wave models. *Coastal Eng.*, **53**, 223–242.
- Van Vledder, G. P., T. Herbers, R. Jensen, D. Resio, & B. Tracy, 2000 : Modelling of non-linear quadruplet wave-wave interactions in operational wave models. *Proc. 27th Int. Conf. on Coastal Eng.*, Sydney (Australia), 797–811.
- Wahle, K., H. Günther, & H. Schiller, 2009 : Neural network parameterisation of the mapping of wave spectra onto nonlinear four-wave interactions. *Ocean Modelling*, **30**, 48–55.
- Walsh, E. J., D. W. Hancock, III, D. E. Hines, R. N. Swift, & J. F. Scott, 1989 : An observation of the directional wave spectrum evolution from shoreline to fully developed. *J. Phys. Oceanogr.*, **19**, 1288–1295.
- WAMDI Group, 1988 : The WAM model - a third generation ocean wave prediction model. *J. Phys. Oceanogr.*, **18**, 1775–1810.
- Wang, D. W. & P. A. Hwang, 2001 : Evolution of the bimodal directional distribution of ocean waves. *J. Phys. Oceanogr.*, **31**, 1200–1221.
- Watts, K. P., 2003 : Fetch-limited wind wave generation on the continental shelf. M.S. thesis, Naval Postgraduate School, Monterey, CA.
- Webb, D. J., 1978 : Non-linear transfers between sea waves. *Deep Sea Res.*, **25**, 279–298.
- Whitham, G. B., 1974 : *Linear and nonlinear waves*. Wiley, New York, 636 p.
- Yan, L., 1987 : An improved wind input source term for third generation ocean wave modelling. Tech. Rep. 8, Royal Dutch Meteor. Inst.
- Young, I., S. Hasselmann, & K. Hasselmann, 1987 : Computations of the response of a wave spectrum to a sudden change in the wind direction. *J. Phys. Oceanogr.*, **17**, 1317–1338.
- Young, I. R., 1994 : On the measurement of directional wave spectra. *Appl. Ocean Res.*, **16**, 283–294.
- Young, I. R., 1995 : The determination of confidence limits associated with estimates of the spectral peak frequency. *Ocean Eng.*, **22 (7)**, 669–686.

- Young, I. R., 1999 : *Wind Generated Ocean Waves*. Elsevier.
- Young, I. R., 2006 : Directional spectra of hurricane wind waves. *J. Geophys. Res.*, **111**, doi :10.1029/2006JC003540.
- Young, I. R. & A. V. Babanin, 2006 : The form of the asymptotic depth-limited wind wave frequency spectrum. *J. Geophys. Res.*, **111**, C06031, doi :10.1029/2005JC003398.
- Young, I. R. & G. Van Vledder, 1993 : A review of the central role of nonlinear interactions in wind-wave evolution. *Phil. Trans. Roy. Soc. London*, **342**, 505–524.
- Young, I. R., L. A. Verhagen, & M. L. Banner, 1995 : A note on the bimodal directional spreading of fetch-limited wind waves. *J. Geophys. Res.*, **100 (C1)**, 773–778.
- Zakharov, V. E., 1966 : Problems of the theory of nonlinear surface waves. Ph.D. thesis, Budker Institute for Nuclear Physics, Novosibirsk, USSR.
- Zakharov, V. E., 1968 : Stability of periodic waves of finite amplitude on the surface of a deep fluid. *J. Appl. Mech. Tech. Phys.*, **9 (2)**, 190–194.
- Zakharov, V. E., 1999 : Statistical theory of gravity and capillary waves on the surface of a finite-depth fluid. *Eur. J. Mech. B/Fluids*, **18**, 327–344.
- Zakharov, V. E., 2005 : Theoretical interpretation of fetch limited wind-driven sea observations. *Nonl. Proc. Geophys.*, **12**, 1011–1020.
- Zakharov, V. E., G. Falkovich, & V. Lvov, 1992 : *Kolmogorov spectra of turbulence. Part I*. Springer, Berlin.
- Zakharov, V. E. & N. N. Filonenko, 1966 : Energy spectrum for stochastic oscillations of the surface of a fluid. *Soviet Phys. Dokl.*, **160**, 1292–1295.
- Zakharov, V. E., A. O. Korotkevich, A. N. Pushkarev, & D. Resio, 2007 : Coexistence of weak and strong wave turbulence in a swell propagation. *Phys. Rev. Lett.*, **99 (164501)**.
- Zakharov, V. E. & A. N. Pushkarev, 1999 : Diffusion model of interacting gravity waves on the surface of deep fluid. *Nonl. Proc. Geophys.*, **6**, 1–10.
- Zakharov, V. E. & M. M. Zaslavsky, 1982a : Integrals of input and dissipation in the weak-turbulence theory of wind-generated waves. *Izv. Atmos. Ocean. Phys.*, **18 (10)**, 1066–1076.
- Zakharov, V. E. & M. M. Zaslavsky, 1982b : Kinetic equation and Kolmogorov spectra in the weak-turbulence theory of wind waves. *Izv. Atmos. Ocean. Phys.*, **18 (9)**, 970–980.
- Zakharov, V. E. & M. M. Zaslavsky, 1983a : Shape of spectrum of energy carrying components of a water surface in the weak-turbulence theory of wind waves. *Izv. Atmos. Ocean. Phys.*, **19 (3)**, 207–212.
- Zakharov, V. E. & M. M. Zaslavsky, 1983b : Dependence of wave parameters on the wind velocity, duration of its action and fetch in the weak-turbulence theory of water waves. *Izv. Atmos. Ocean. Phys.*, **19 (4)**, 300–306.

Zaslavsky, M. M., 1984 : Wind-wave forecasting as a problem of the weak turbulence theory. thesis for doctor of science degree, P.P. Shirshov Institute of Oceanology of the Academy of Sciences of the USSR, Moscow, Russia.

# AMELIORATION DE LA MODELISATION SPECTRALE DES ETATS DE MER PAR UN CALCUL QUASI-EXACT DES INTERACTIONS NON-LINEAIRES VAGUE-VAGUE

## RESUME

Les modèles numériques d'état de mer décrivent l'évolution du spectre d'énergie de l'état de mer sous l'action conjointe de plusieurs processus physiques qui apportent, dissipent ou transfèrent de l'énergie. Une meilleure prise en compte des interactions non-linéaires entre quadruplets de fréquences de vagues est essentielle à l'amélioration des modèles d'état de mer.

Sur la base d'une approche proposée par Lavrenov (2001), nous avons développé et optimisé une méthode de calcul quasi-exacte des interactions non-linéaires vague-vague en grande profondeur d'eau. Cette approche, nommée GQM (« Gaussian Quadrature Method »), est basée sur l'utilisation de quadratures de Gauss, et permet d'obtenir des estimations très précises du terme de transfert non-linéaire à des coûts de calcul raisonnables.

A l'aide de cette méthode, nous nous sommes d'abord intéressés à la modélisation de l'évolution temporelle du spectre des vagues dans un cas homogène et sans forçage. Dans un second temps, l'introduction de différents termes de forçage par le vent et de dissipation par moutonnement nous a permis de montrer la sensibilité du spectre des vagues aux modèles choisis. Des situations plus proches de la réalité mais conservant une géométrie simple (fetch limité, fetch oblique) ont ensuite été modélisées en prenant en compte la propagation spatiale des vagues. Nous avons notamment comparé les résultats du modèle à des mesures issues de la campagne SHOWEX de 1999 (Duck, NC, USA).

Les travaux effectués confirment d'une part la nécessité de modéliser de façon précise les interactions non-linéaires dans les modèles spectraux d'états de mer et montrent d'autre part la faisabilité de ces améliorations grâce à la méthode GQM et l'algorithme de calcul mis au point au cours de la thèse.

## PROGRESS IN SPECTRAL WAVE MODELING USING A QUASI-EXACT METHOD FOR NONLINEAR WAVE-WAVE INTERACTIONS

## ABSTRACT

Numerical wave models describe the evolution of the wave energy spectrum under the combined action of several physical processes that generate, transfer or dissipate energy. A more accurate modeling of nonlinear four-wave interactions is necessary to improve sea state models.

Based on a method introduced by Lavrenov (2001), we developed and optimized a quasi-exact method for computing the non-linear four-wave interactions in deep water. This method, called GQM ('Gaussian Quadrature Method'), uses Gaussian quadrature formulas for the different integrations and provides very accurate estimates of the nonlinear transfer term with acceptable CPU times.

In the present study, we first consider the temporal evolution of a homogeneous wave field when there is no energy input from the wind or dissipation. In a second step, wind input and whitecapping dissipation are also taken into account and results show the influence of the forcing terms on the evolution of the wave spectrum. In the last step, we consider two more realistic situations with a simple geometry, including wave propagation, namely the fetch-limited case and the slanting fetch case. Model results are compared to measurements from the SHOWEX campaign (1999, Duck, NC, USA).

The work presented in this thesis confirms the need to accurately model the nonlinear wave-wave interactions in spectral wave models and shows that these improvements are now feasible, thanks to the GQM method and the algorithm developed in this thesis.